National Technical University of Athens
School of applied mathematical and physical sciences
Department of Physics

Noise effects in the Large Hadron Collider (LHC) and its High-Luminosity upgrade (HL-LHC)

SOFIA KOSTOGLOU

A dissertation submitted in fulfillment of the requirements
for the degree of Doctor of Philosophy in Physics

ATHENS, March 2020

ΕΘΝΙΚΟ ΜΕΤΣΟΒΙΟ ΠΟΛΥΤΕΧΝΕΙΟ
ΣΧΟΛΗ ΕΦΑΡΜΟΣΜΕΝΩΝ ΜΑΘΗΜΑΤΙΚΩΝ ΚΑΙ ΦΥΣΙΚΩΝ ΕΠΙΣΤΗΜΩΝ
ΤΟΜΕΑΣ ΦΥΣΙΚΗΣ

Φαινόμενα θορύβου στον Μεγάλο Επιταχυντή Αδρονίων και στον αναβαθμισμένο Επιταχυντή Υψηλής Φωτεινότητας

ΔΙΔΑΚΤΟΡΙΚΗ ΔΙΑΤΡΙΒΗ

ΣΟΦΙΑΣ ΚΩΣΤΟΓΛΟΥ

Διπλωματούχου Ηλεκτρολόγου Μηχανικού και Μηχανικού Υπολογιστών Ε.Μ.Π.

Επιβλέπων: Ε. Γαζής
Καθηγητής Ε.Μ.Π.

ΑΘΗΝΑ, Μάρτιος 2020

Εθνικο Μετσοβιο Πολυτεχνειο
Σχολη Εφαρμοσμενων Μαθηματικων και Φυσικων Επιστημων
Τομεας Φυσικης

Φαινόμενα θορύβου στον Μεγάλο Επιταχυντή Αδρονίων και στον αναβαθμισμένο Επιταχυντή Υψηλής Φωτεινότητας

ΔΙΔΑΚΤΟΡΙΚΗ ΔΙΑΤΡΙΒΗ

ΣΟΦΙΑΣ ΚΩΣΤΟΓΛΟΥ

Διπλωματούχου Ηλεκτρολόγου Μηχανικού και Μηχανικού Υπολογιστών Ε.Μ.Π.

ΤΡΙΜΕΛΗΣ ΣΥΜΒΟΥΛΕΥΤΙΚΗ ΕΠΙΤΡΟΠΗ:

1. Ε. Γαζής, Καθ. Ε.Μ.Π.
2. Ι. Παπαφιλίππου, Ερευνητής CERN
3. Θ. Αλεξόπουλος, Καθ. Ε.Μ.Π.

ΕΠΤΑΜΕΛΗΣ ΕΞΕΤΑΣΤΙΚΗ ΕΠΙΤΡΟΠΗ:

1. Ε. Γαζής, Καθ. Ε.Μ.Π.
2. Ι. Παπαφιλίππου, Ερευνητής CERN
3. Θ. Αλεξόπουλος, Καθ. Ε.Μ.Π.
4. Μ. Κόκκορης, Καθ. Ε.Μ.Π.
5. Ν. Κατσαρός, Διευθ. Ερευνών ΕΚΕΦΕ «Δημόκριτος»
6. Γ. Τσιρώνης, Καθ. Πανεπ. Κρήτης
7. G. Sterbini, Ερευνητής CERN

ΑΘΗΝΑ, Μάρτιος 2020

Εθνικό Μετσόβιο Πολυτεχνείο
Σχολή Εφαρμοσμένων Μαθηματικών και Φυσικών Επιστημών
Τομέας Φυσικής

To Serafeim, Evgenia, Kostas, Kiki and Nikos,
my biggest supporters and the most important people in my life

Abstract

In order to optimize the performance of a high-energy particle collider such as the Large Hadron Collider (LHC) and its high-luminosity upgrade (HL-LHC), a thorough understanding of all the phenomena that can act as a luminosity degradation mechanism is required. A major concern for the transverse single-particle beam dynamics is the presence of noise, a mechanism that can impact the long term stability of the circulating particles. From the plethora of noise sources that are present in the accelerator, this thesis investigates the impact of a modulation in the strengths of the dipole and quadrupole magnets of the lattice due to power converter noise. In the presence of non-linearities, depending on the spectral components of the noise and the nature of the source, such a mechanism can increase the diffusion of the particles in the distribution through the excitation of additional resonances in the vicinity of the ones driven by the lattice non-linearities. As this effect can have severe implications on the beam performance, it is important to understand and control the noise mechanisms that have been observed in the LHC and that are anticipated in the HL-LHC era. To this end, this thesis presents the investigation of the 50 Hz harmonics that have been observed in the beam spectrum since the beginning of the LHC operation. Based on several observations and dedicated experiments, the source of this perturbation is identified and its impact on the beam performance is quantified with single-particle tracking simulations. For the HL-LHC, the reduction of the beam size in the interaction points of the high luminosity experiments will lead to an increase of the maximum β-functions in the quadrupoles of the inner triplet. The expected increase of the sensitivity to noise, combined with the new hardware that is currently implemented, justifies the need to investigate the impact of tune modulation effects on the beam performance. The modulation that may arise from the power supply ripples in the high β-function regimes will be combined with the tune modulation that intrinsically emerges from the coupling of the transverse and longitudinal plane for off-momentum particles through chromaticity. The aim of the thesis is to determine whether tune modulation effects will pose a limitation in the luminosity production of the HL-LHC.

Acknowledgments

This thesis would not have been possible without the help, support and guidance of several individuals. I am deeply grateful to all the people who have helped me throughout this long, challenging but amazing journey.

First and foremost, I would like to sincerely thank my CERN supervisor, Dr. Yannis Papaphilippou for his faith and confidence in me. His guidance, constant support and immense expertise have guided and inspired me to discover the world of particle accelerators. Thank you for the opportunity to embark on this adventure, for your unique ideas and for always finding solutions to any problem that I encountered along the way. It has been a privilege being a Ph.D. student under your supervision and I am thankful for the excellent example you have provided not only as a researcher and a mentor but also as a person full of understanding, enthusiasm and kindness.

I would like to express my sincere gratitude to my university supervisor, Prof. Evangelos Gazis, for giving me the unique opportunity to start my journey at CERN five years ago and for introducing me to the field of accelerator physics. He has always been there to support, assist and encourage since my early years as an undergraduate student. I greatly appreciate his excitement in regard to teaching, his moral support and advice throughout this dissertation.

I am deeply grateful to Guido Sterbini as my knowledge on the field has exponentially increased from the moment our paths crossed. Thanks to his immense patience and amazing ideas I learned the meaning of systematic and in-depth research. He guided, motivated and encouraged me especially in difficult times when nothing was working, always in a good mood even in very stressful times. For all these reasons (and for proofreading all of my manuscripts, even the very long ones), this Ph.D. would not have been possible without your help.

My sincere gratitude also goes to the other members of my examining committee: Theodoros Alexopoulos, Michalis Kokkoris, Nikolaos Katsaros and George Tsironis for accepting to be part of my committee and for their helpful comments on this work. I am also extremely grateful to Manolis Dris, Stavros Maltezos and George Koutsoumbas for their understanding and for helping me prepare for the course examinations in the context of the Ph.D program.

I would like to recognize the invaluable assistance of Hannes Bartosik and Natalia Triantafyllou as an important part of this thesis was done thanks to their amazing ideas and help.

I am extremely thankful to Dario Pellegrini for his help during my first research steps. Thank you for being so patient and for the many hours spent answering all my questions. Your help was essential to this Ph.D.

I gratefully acknowledge Gianluigi Arduini, Riccardo De Maria, Miriam Fitterer, Davide Gamba, Xavier Buffat and Nicolas Mounet for valuable suggestions and discussions on this work. I would like to thank Daniel Valuch and Martin Soderen for all ADT related measurements and experiments and Tom Levens for the MIM measurements and discussions. I am grateful to all EPC colleagues who have contributed to these studies and especially to Michele Martino and Miguel Cerqueira Bastos for all the power converter related measurements and discussions.

My warmest thanks goes to my fellow office mates and friends, Stefania, Michalis and Kostas for always helping and supporting me through my ups and downs (especially with coffee discussions).

Τέλος αλλά πιο σημαντικά, ϑα ήϑελα να ευχαριστήσω τους αγαπημένους μου συνοδοιπόρους σε αυτό το ταξίδι. Ευχαριστώ τους γονείς μου, Κώστα και Ευγενία, για την παντοτινή τους αγάπη, στήριξη και έμπνευση και τα αδέλφια μου, Κική και Νίκο, για τις αμέτρητες στιγμές γέλιου (beam-beam, beam-beam). Σας ευχαριστώ που δίνετε χρώμα στην καϑημερινότητά μου.

Κυρίως όμως ϑα ήϑελα να ευχαριστήσω τον καλύτερο μου φίλο και σύζυγο μου, Σεραφείμ. Σε ευχαριστώ που ομορφαίνεις τις καλές αλλά και τις λιγότερα όμορφες, γεμάτες άγχος, στιγμές μου. Ελπίζω με τον καιρό να πάρω λίγη από την ψυχραιμία, την αποφασιστικότητα και την οργανωτικότητα σου. Εύχομαι αυτό να είναι το πρώτο βήμα μεταξύ πολλών που ϑα κάνουμε μαζί και ανυπομονώ να δω τι μας επιφυλάσσει το μέλλον.

Contents

Περίληψη

Ο Μεγάλος Επιταχυντής Αδρονίων (LHC) ολοκλήρωσε με επιτυχία το δεύτερο κύκλο λειτουργίας του έπειτα από τρία χρόνια πειραμάτων (2015-2018), επιτυγχάνοντας πρωτοφανείς τιμές ολοκληρωμένης φωτεινότητας (160 fb^{-1}) και ενέργειας κέντρου μάζας (13 TeV). Για τα επόμενα δύο χρόνια προβλέπονται εκτεταμένες τροποποιήσεις με σκοπό την προετοιμασία του επιταχυντή για τη μελλοντική του αναβάθμιση σε επιταχυντή Υψηλής Φωτεινότητας (HL-LHC). Αυτή η αναβάθμιση της Υψηλής Φωτεινότητας στοχεύει στην επίτευξη μιας άνευ προηγουμένου ολοκληρωμένης φωτεινότητας των 250 fb^{-1} ανά έτος.

Η βελτιστοποίηση της απόδοσης του επιταχυντή απαιτεί, παράλληλα, την κατανόηση όλων των μηχανισμών που μπορούν να συντελέσουν στη μείωση ή υποβάθμιση της τιμής της φωτεινότητας.

Ένας μηχανισμός που μπορεί να επηρεάσει την εγκάρσια κίνηση των σωματιδίων της δέσμης πρωτονίων, οδηγώντας σε χαοτικές τροχιές και κατ΄ επέκταση σε απώλειες πρωτονίων, είναι τα φαινόμενα θορύβου στη δυναμική των φορτισμένων σωματιδίων. Ανάμεσα στις πολλαπλές πηγές θορύβου που υπάρχουν σε έναν επιταχυντή, η παρούσα διδακτορική διατριβή επικεντρώνεται στις επιπτώσεις αρμονικών διαταραχών στην τάση των πηγών τροφοδοσίας των μαγνητικών διπόλων και τετραπόλων, ένα φαινόμενο που οδηγεί σε διαμόρφωση συχνότητας του μαγνητικού πεδίου. Ανάλογα με τις συχνότητες και το πλάτος των φασματικών συνιστωσών του θορύβου, που εξαρτώνται από το είδος του μαγνήτη και τον τύπο της πηγής τροφοδοσίας, οι επιπτώσεις στην εγκάρσια κίνηση των σωματιδίων της δέσμης ποικίλουν. Ο θόρυβος από τις πηγές τροφοδοσίας, σε συνδυασμό με τα μη-γραμμικά μαγνητικά πεδία του επιταχυντή, που είτε είναι απαραίτητα για τον έλεγχο της χρωματικότητας και την απόσβεση της συλλογικής κίνησης των σωματιδίων είτε απορρέουν από τη σύγκρουση των δύο δεσμών, μπορεί να αυξήσει τη διάχυση της κατανομής των σωματιδίων, μέσω της εμφάνισης και διέγερσης των επιπλέον συχνοτήτων συντονισμού πέρα από τις προβλεπόμενες λόγω της μη-γραμμικότητας των επί μέρους μαγνητικών πεδίων. Η ύπαρξη ενός τέτοιου φαινομένου είναι ιδιαιτέρως κρίσιμη για τη διατήρηση του συνολικού χρόνου ζωής της δέσμης. Η παρούσα έρευνα παρουσιάζει τη μελέτη αυτών των φαινομένων πρώτα στα δίπολα, ένα φαινόμενα που έχει παρατηρηθεί στον επιταχυντή, και στη συνέχεια στα τετράπολα, ένα είδος θορύβου που είναι ιδιαίτερα κρίσιμο για τον επιταχυντή Υψηλής Φωτεινότητας.

Από την έναρξη της λειτουργίας του επιταχυντή, αρμονικές των 50 Hz έχουν παρατηρηθεί στο φάσμα της δέσμης με άγνωστη προέλευση. Εφόσον πολλαπλές φασματικές συνιστώσες βρίσκονται στην εγγύτητα της βητατρονικής συχνότητας, η παρουσία τους μπορεί να περιπλέξει

τη μέτρηση της συχνότητας της δέσμης και ενδεχομένως να οδηγήσει σε απώλειες πρωτονίων. Η δυσκολία αυτού του πεδίου έγκειται πρώτα, στο να αποδειχθεί ότι οι συχνότητες αυτές είναι συζευγμένες με τη δέσμη και δεν απορρέουν ως αποτέλεσμα σφάλματος στα όργανα μέτρησης και στη συνέχεια, στον εντοπισμό της πηγής της διαταραχής. Στο Σχήμα 1 παρουσιάζεται η εξέλιξη του φάσματος της μιας δέσμης στο οριζόντιο επίπεδο και στη μέγιστη ενέργεια, πριν την έναρξη των συγκρούσεων. Οι αρμονικές στο φάσμα είναι εμφανείς σε όλα τα στάδια της λειτουργίας του επιταχυντή. Ο χρωματικός κώδικας απεικονίζει τη φασματική πυκνότητα ισχύος. Ιδιαίτερα σημαντικό είναι το γεγονός ότι στη μέση του χρονικού διαστήματος, όπου γίνεται η αλλαγή της εγκάρσιας συχνότητας (μαύρη διακεκομμένη γραμμή), οι συχνότητες των αρμονικών δεν μεταβάλλονται. Η παρατήρηση αυτή αποδεικνύει ότι ο θόρυβος πηγάζει από ένα δίπολο και όχι λόγω διαταραχών στο πεδίο ενός τετραπόλου.

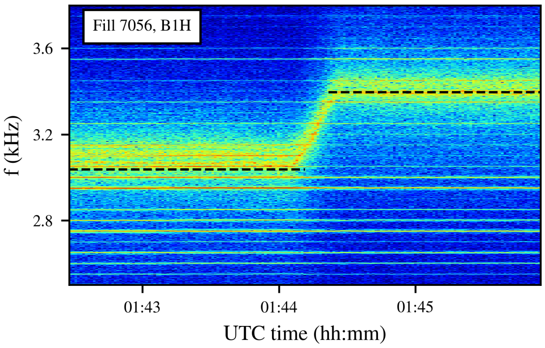

Σχήμα 1: Η χρονική εξέλιξη του φάσματος της δέσμης στο οριζόντιο επίπεδο. Ο χρωματικός κώδικας απεικονίζει τη φασματική πυκνότητα ισχύος. Η αλλαγή της βητατρονικής συχνότητας παρουσιάζεται με τη μαύρη διακεκομμένη γραμμή.

Μέσω μετρήσεων υψηλής δειγματοληψίας των θέσεων των σωματιδίων ανά στροφή, το φάσμα της δέσμης επεκτείνεται μέχρι υψηλές συχνότητες (10 kHz). Το φάσμα παρουσιάζεται στο Σχήμα 2 και εκτείνεται έως τα 100 nm σε πλάτος. Από το φάσμα διακρίνονται δύο περιοχές στο χώρο των συχνοτήτων όπου αρμονικές είναι εμφανείς. Αρχικά πολλαπλές αρμονικές των 50 Hz παρουσιάζονται έως και 3.6 Hz (μπλε περιοχή), μια περιοχή που σε αυτήν τη μελέτη αποκαλείται το σύμπλεγμα χαμηλών συχνοτήτων. Στη συνέχεια, άλλο ένα σύμπλεγμα αρμονικών εκτείνεται γύρω από τα 7-8 kHz (κίτρινη περιοχή), το οποίο καλείται σύμπλεγμα υψηλών συχνοτήτων.

Η ακριβής τοποθεσία του συμπλέγματος υψηλών συχνοτήτων είναι η περιοχή $\mathrm{f_{rev}} - \mathrm{f_x}$ όπου $\mathrm{f_{rev}}, \mathrm{f_x}$ είναι η συχνότητα περιστροφής στον επιταχυντή και η βητατρονική συχνότητα, αντίστοιχα. Το συμπέρασμα αυτό προκύπτει από το Σχήμα 3 (πάνω) που παρουσιάζει το φάσμα λίγο πριν (μπλε γραμμή) και μετά (μαύρη γραμμή) την αλλαγή της βητατρονικής συχνότητας. Οι κάθετες γραμμές αντιπροσωπεύουν τα πολλαπλάσια των 50 Hz. Δίνοντας έμφαση στην περιοχή των συμπλέγματος υψηλών συχνοτήτων (κάτω) γίνεται αντιληπτό ότι και στις δύο περιπτώσεις πρόκειται για θόρυβο προερχόμενο από ένα δίπολο, εφόσον οι γραμμές συμπίπτουν με τα πολλαπλάσια των 50 Hz. Ωστόσο, το κέντρο του συμπλέγματος υψηλών συχνοτήτων

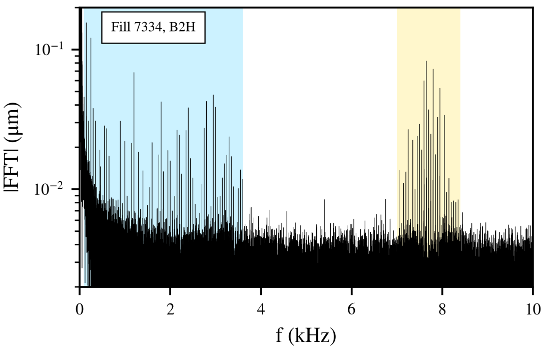

Σχήμα 2: Το φάσμα της δέσμης στο οριζόντια επίπεδο κατά τη διάρκεια των συγκρούσεων. Το σύμπλεγμα των αρμονικών χαμηλών (μπλε) και υψηλών συχνοτήτων (κίτρινο) απεικονίζεται.

εξαρτάται από τη βητατρονική συχνότητα.

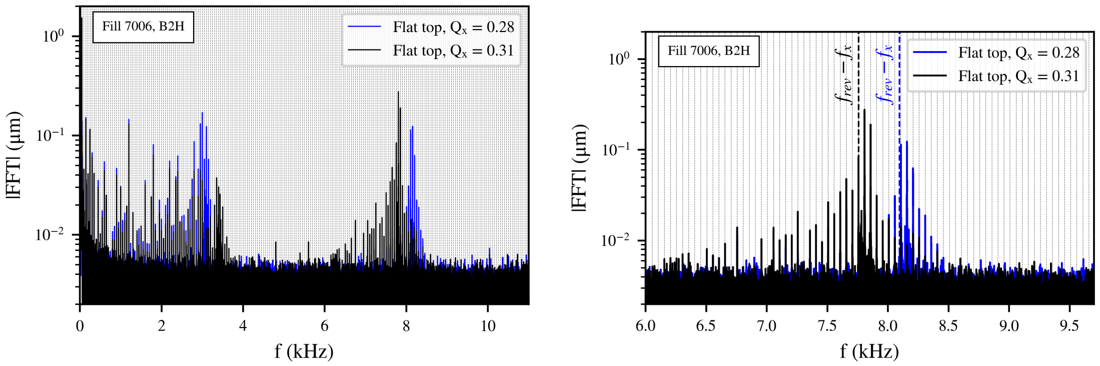

Σχήμα 3: Το φάσμα της δέσμης στο οριζόντια επίπεδο πριν (μπλε γραμμή) και μετά (μαύρη γραμμή) την αλλαγή της βητατρονικής συχνότητας για εύρος συχνοτήτων μέχρι 10 kHz (αριστερά) και γύρω από το σύμπλεγμα υψηλών συχνοτήτων (δεξιά). Οι κάθετες γραμμές απεικονίζουν τα πολλαπλάσια των 50 Hz.

Οι αρμονικές στο φάσμα της δέσμης δεν είναι ένα σφάλμα των συστημάτων μέτρησης. Πολλαπλές παρατηρήσεις αποδεικνύουν πως πρόκειται για συχνότητες που υπεισέρχονται στην κίνηση των σωματιδίων της δέσμης. Το συμπέρασμα αυτό γίνεται κατανοητό με τον υπολογισμό της εξέλιξης της φάσης του θορύβου. Συγκεκριμένα, υπολογίζεται η φάση του θορύβου από πειραματικές μετρήσεις μεταξύ δύο σημείων παρατήρησης σε μικρή απόσταση και η τιμή αυτή συγκρίνεται με τη βητατρονική φάση, μια παράμετρος που καθορίζεται από την οπτική. Το Σχήμα 4 παρουσιάζει τη μέση τιμή της φασικής εξέλιξης μεταξύ των δύο κοντινών τοποθεσιών στον τομέα του επιταχυντή για τις πιο σημαντικές αρμονικές και των δύο συμπλεγμάτων, η γραμμή σφάλματος υποδηλώνει μία τυπική απόκλιση και η οριζόντια γραμμή απεικονίζει τη βητατρονική φάση. Σε κάθε περίπτωση, εντός του σφάλματος της ανάλυσης, οι φάσεις του θορύβου συμπίπτουν με τη βητατρονική, μια παρατήρηση η οποία αποδεικνύει ότι ο θόρυβος είναι συζευγμένος με τη δέσμη.

Στη συνέχεια, με βάση τα πειραματικά δεδομένα που συλλέχθηκαν, οι έρευνες επικε-

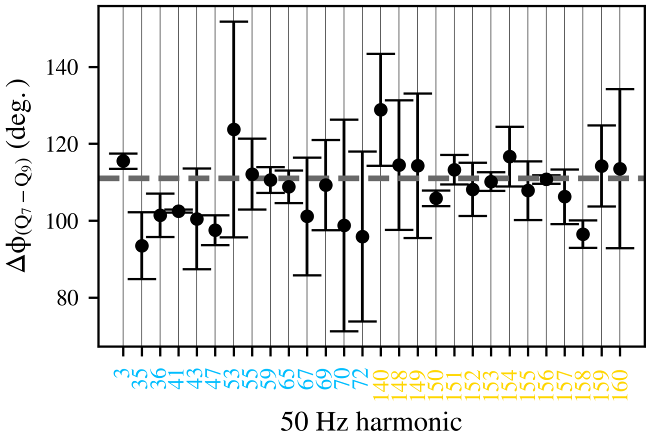

Σχήμα 4: Η εξέλιξη της φάσης του θορύβου για τις αρμονικές του συμπλέγματος χαμηλών (μπλε) και υψηλών (κίτρινο) συχνοτήτων και της βητατρονικής συχνότητας (γκρι οριζόντια γραμμή).

ντρώθηκαν στα δίπολα ως πηγή της διαταραχής. Ο επιταχυντής αποτελείται από οκτώ τομείς με οκτώ πηγές ισχύος που τροφοδοτούν 154 δίπολα ανά τομέα συνδεδεμένα σε σειρά. Η τάση παροχής περιλαμβάνει ένα ενεργό φίλτρο για την εξασθένηση των αρμονικών στην πηγή τροφοδοσίας. Με ειδικά πειράματα, το κάθε φίλτρο ενεργοποιήθηκε και απενεργοποιήθηκε, μια διαδικασία που επηρέασε την εξέλιξη του πλάτους των αρμονικών της δέσμης. Οι διακριτές αλλαγές στο φάσμα της δέσμης κατά τη διάρκεια αυτών των πειραμάτων εμφανίζεται στο Σχήμα 5 (πάνω) καθώς και η κατάσταση των φίλτρων για το ίδιο χρονικό διάστημα (κάτω). Αυτή η πειραματική διαδικασία απέδειξε ότι οι αρμονικές του συμπλέγματος χαμηλών συχνοτήτων είναι το αποτέλεσμα θορύβου που πηγάζει και από τις οκτώ πηγές τροφοδοσίας και κατ΄ επέκταση μεταδίδεται σε όλα δίπολα του επιταχυντή. Όσον αφορά την πηγή του συμπλέγματος υψηλών συχνοτήτων, πειραματικές παρατηρήσεις δείχνουν πως η πηγή είναι επίσης τα δίπολα αλλά επιπρόσθετα υπάρχει και η αλληλεπίδραση του θορύβου με έναν μηχανισμό που προέρχεται από τη δέσμη.

Οι επιπτώσεις του θορύβου στη διάχυση των σωματιδίων και στην απώλεια πρωτονίων ερευνάται με προσομοιώσεις. Στο Σχήμα 6 παρουσιάζονται οι συχνότητες και οι αρχικές συνθήκες των σωματιδίων με το χρωματικό κώδικα να αντιστοιχεί στη διάχυση των σωματιδίων. Η πρώτη μελέτη αφορά των Μεγάλο Επιταχυντή Αδρονίων με παραμέτρους που αντιστοιχούν στη λειτουργία του επιταχυντή το 2018 χωρίς να συμπεριλαμβάνονται φαινόμενα θορύβου (Σχήμα 6α΄). Το διάγραμμα συντονισμού απεικονίζεται στο χώρο των συχνοτήτων (γκρι γραμμή). Στη συνέχεια, συμπεριλαμβάνεται το φάσμα του συμπλέγματος χαμηλών (Σχήμα 6β΄) και υψηλών (Σχήμα 6γ΄) συχνοτήτων και τελικά, και το συνολικό φάσμα (Σχήμα 6δ΄). Οι διαταραχές στα δίπολα οδηγούν στην εμφάνιση επιπλέον συχνοτήτων συντονισμού (μαύρες και μπλε γραμμές) σε σταθερές συχνότητες ίσες με τη συχνότητα των αρμονικών που βρίσκονται στην εγγύτητα της βητατρονικής συχνότητας, οδηγώντας στην αύξηση της διάχυσης των σωματιδίων.

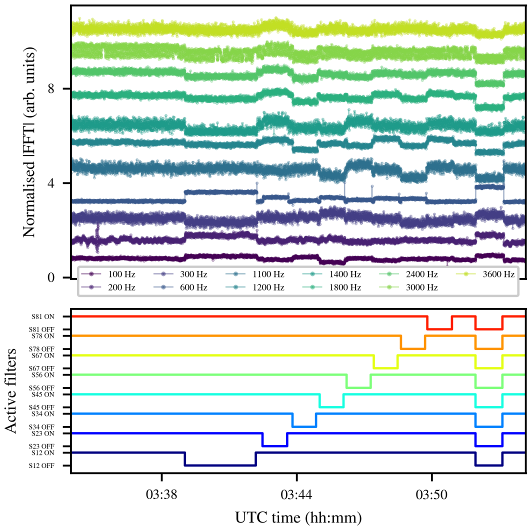

Σχήμα 5: Η εξέλιξη του πλάτους των αρμονικών του συμπλέγματος χαμηλής συχνότητας (πάνω) κατά τη διάρκεια της ενεργοποίησης και απενεργοποίησης των ενεργών φίλτρων των οκτώ τομέων (κάτω).

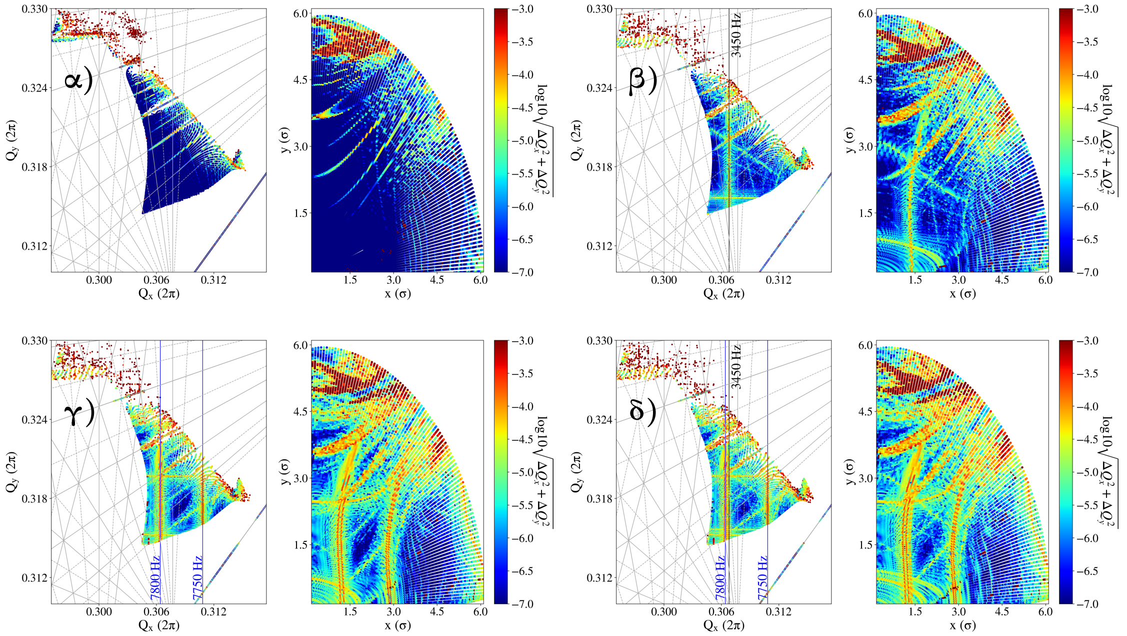

Σχήμα 6: Απεικονίσεις συχνοτήτων και αρχικές συνθήκες των σωματιδίων της κατανομής (α) χωρίς θόρυβο, (β) συμπεριλαμβάνοντας το σύμπλεγμα των χαμηλών ή (γ) υψηλών συχνοτήτων και (δ) περιλαμβάνοντας και τις δύο περιοχές στις προσομοιώσεις. Το διάγραμμα συχνοτήτων συντονισμού λόγω των μη-γραμμικών πεδίων του επιταχυντή (γκρι γραμμές) και οι επιπλέον συχνότητες συντονισμού (μπλε και μαύρες γραμμές) απεικονίζονται.

Τα φάσμα θορύβου, όπως υπολογίστηκε από τις πειραματικές μετρήσεις, οδηγεί σε αύξηση στις απώλειες πρωτονίων και στη μείωση του χρόνου ζωής. Στο Σχήμα 7 παρουσιάζεται η εξέλιξη της έντασης της δέσμης για την κάθε περίπτωση. Η αύξηση της απώλειας πρωτονίων οφείλεται κυρίως στο σύμπλεγμα υψηλών συχνοτήτων (κίτρινη γραμμή).

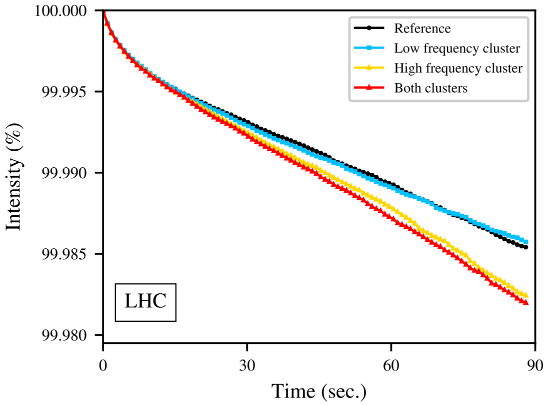

Σχήμα 7: Οι απώλειες των πρωτονίων στη δέσμη όπως υπολογίστηκε με προσομοιώσεις για 10^6 στροφές χωρίς θόρυβο (μαύρη γραμμή), συμπεριλαμβάνοντας το σύμπλεγμα των χαμηλών (μπλε γραμμή) ή υψηλών συχνοτήτων (κίτρινη γραμμή) και περιλαμβάνοντας και τις δύο περιοχές (κόκκινη γραμμή).

Για τον επιταχυντή Υψηλής Φωτεινότητας, η μείωση του μεγέθους της δέσμης στις περιοχές αλληλεπίδρασης των πειραμάτων υψηλής φωτεινότητας, ATLAS και CMS, οδηγεί σε αύξηση των μέγιστων συναρτήσεων-β στα τετράπολα της εσωτερικής τριπλέτας, που παρέχει την τελική εστίαση της δέσμης στο σημείο της κρούσης. Ως εκ τούτου, αναμένεται αυξημένη ευαισθησία σε φαινόμενα θορύβου σε αυτές τις περιοχές του επιταχυντή. Η διαμόρφωση στις πηγές τροφοδοσίας των τετραπόλων μπορεί να οδηγήσει σε διαμόρφωση συχνότητας στη βητατρονική κίνηση των σωματιδίων. Η διαμόρφωση αυτή συνδυάζεται με τη διαμόρφωση συχνότητας που πηγάζει από τη σύζευξη του εγκάρσιου και διαμήκους επιπέδου μέσω της χρωματικότητας. Τα δύο αυτά φαινόμενα αυξάνουν τον αριθμό των συχνοτήτων συντονισμού στο διάγραμμα. Ωστόσο, σε αντίθεση με τα δίπολα, η διαμόρφωση συχνότητας οδηγεί σε επιπλέον συχνότητες συντονισμού σε απόσταση από τις κύριες συχνότητες ίση με τη συχνότητα διαμόρφωσης. Στο Σχήμα 8 φαίνονται οι συχνότητες και οι αρχικές συνθήκες των σωματιδίων στην κατανομή με το χρωματικό κώδικα να απεικονίζει το ρυθμό διάχυσης. Η διαμόρφωση συχνότητας δημιουργεί έναν μηχανισμό διάχυσης που εξαρτάται από τη συχνότητα. Σε αντίθεση με το θόρυβο στα δίπολα, το φαινόμενο αυτό επηρεάζει την απόδοση της δέσμης ακόμη κι αν η συχνότητα διαμόρφωσης δεν βρίσκεται στην εγγύτητα της βητατρονικής συχνότητας. Επομένως, συγκεκριμένες συχνότητας μπορούν να προκαλέσουν μεγαλύτερη διάχυση και κατ΄ επέκταση περισσότερες απώλειες πρωτονίων ανάλογα με τις βητατρονικές συχνότητες, τα μη-γραμμικά πεδία στον επιταχυντή και την τοποθεσία των επιπλέον συχνοτήτων συντονισμού.

Προκειμένου να καθοριστεί εάν τα φαινόμενα διαμόρφωσης συχνότητας μπορούν να συντελέσουν στη μείωση της φωτεινότητας του επιταχυντή, προσομοιώσεις πραγματοποιούνται

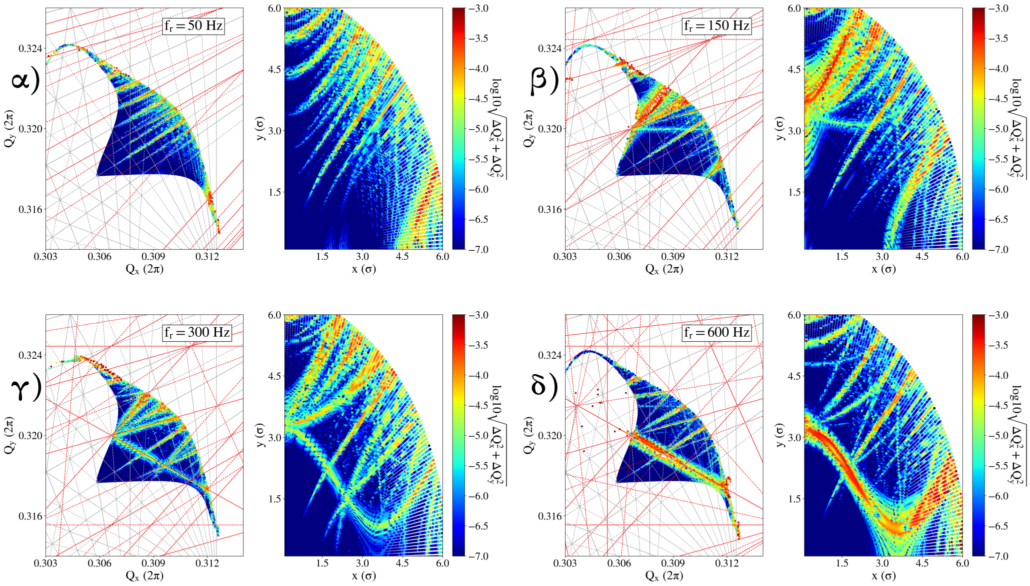

Σχήμα 8: Απεικονίσεις συχνοτήτων και αρχικές συνθήκες των σωματιδίων για συχνότητα διαμόρφωσης ίση με (α) 50 Hz, (β) 150 Hz, (γ) 300 Hz, (δ) 600 Hz και ίσα πλάτη. Οι επιπλέον συχνότητες συντονισμού λόγω θορύβου απεικονίζονται (κόκκινες γραμμές).

για όλες τις αρμονικές των 50 Hz μέχρι τα 10 kHz στα τετράπολα της εσωτερικής τριπλέτας και για αυξανόμενες τιμές του πλάτους. Στο Σχήμα 9, ο χρωματικός κώδικας απεικονίζει την ελάχιστη τιμή του πλάτους της δέσμης με ευσταθείς τροχιές (Δυναμικό Εύρος). Ο συνδυασμός των παραμέτρων θορύβου που οδηγούν σε χαοτικές τροχιές σε μικρότερα πλάτη των σωματιδίων της κατανομής (κόκκινη περιοχή) συγκρίνονται με τις προδιαγραφές των πηγών τροφοδοσίας (μαύρη και κόκκινη γραμμή). Οι προδιαγραφές καθορίζουν τις μέγιστες επιτρεπτές τιμές του θορύβου από τους μετατροπείς ισχύος. Η σύγκριση οδηγεί στο συμπέρασμα ότι η διαμόρφωση συχνότητας δεν θα αποτελέσει παράγοντα μείωσης του χρόνου ζωής της δέσμης στο μέλλον.

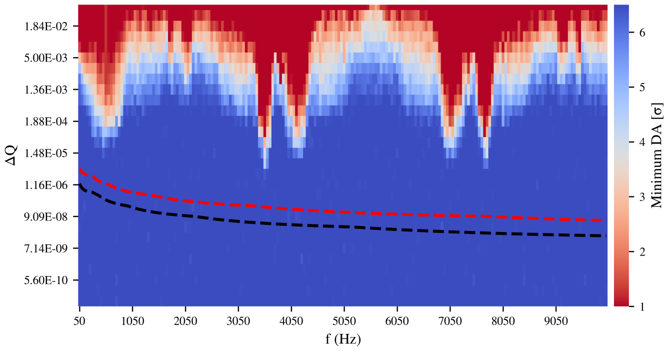

Σχήμα 9: Η συχνότητας διαμόρφωσης συναρτήσει του πλάτους, με το χρωματικό κώδικα να απεικονίζει το πλάτος της δέσμης με ευσταθείς τροχιές (Δυναμικό Εύρος). Η κόκκινη και η μαύρη γραμμή παρουσιάζουν τις προδιαγραφές των πηγών τροφοδοσίας.

Chapter 1

Introduction

The Standard Model (SM) is the theory of the elementary particles of matter and their interaction through four fundamental forces: strong, weak, electromagnetic and gravitational [1–4]. Although the SM has demonstrated a very good agreement with experimental observations, it does not provide a unified theory of all the fundamental interactions. Observations such as the matter-antimatter asymmetry, neutrino oscillations between flavors, the accelerating expansion of the universe and gravitational effects, possibly indicating the existence of dark energy and dark matter, are phenomena which cannot be explained by the SM.

Founded in 1954, the aim of the European Organization for Nuclear Research (CERN) is to investigate some of these fundamental physics phenomena, through high energy particle collisions [5]. The Large Hadron Collider (LHC) is the largest collider in the world, with a circumference of 26.658 km, dedicated to studies in high energy particle physics. Installed in the tunnel built for the Large Electron-Positron collider (LEP) at 100 meters underground [6], the accelerator became operational in 2008, designed to reach an unprecedented energy of 7 TeV per beam and a peak luminosity of 1×10^{34} cm^{-2}s^{-1}. Two counter-rotating beams, consisting either of protons or lead ions, are circulating in two separated rings and, once accelerated, are brought to collision at the locations of the four experiments: ATLAS (A Toroidal LHC ApparatuS) [7], CMS (the Compact Muon Solenoid) [8], ALICE (A Large Ion Collider Experiment) [9] and LHCb (study of physics in B-meson decays at LHC) [10]. During collisions, the particles scatter inelastically, a process that leads to the production of secondary particles. By collecting and reconstructing these events, the main goal is to validate the SM theories and potentially discover particles beyond the SM.

During the first proton run (2010-2012), while operating at a beam energy of 3.5 and 4 TeV, the LHC reached many milestones such as the discovery of a massive 125 GeV boson, predicted in 1964 by Peter Higgs, Francois Englert and Robert Brout, the Higgs boson [11–16]. After the Long Shutdown (LS1), the accelerator restarted with an energy of 6.5 TeV per beam for the whole duration of the second run (2015-2018) to potentially enable the creation of new particles. Apart from the increase of the center-of-mass energy, extensive modifications of the machine configuration took place across the years aiming to increase the luminosity, a parameter which defines the rate of collisions in the detectors [17]. After the successful completion of the second run in 2018, the LHC has reached the LS2, dedicated to the maintenance, the consolidation and the preparation for the third run and the upgrade to the High Luminosity LHC (HL-LHC).

The systematic monitoring of the accelerator's performance across the two runs has revealed that the proton losses exceed the expected intensity decay that intrinsically emerges from the collisions of the two beams. In addition, a growth of the Root Mean Square (RMS) beam size has been reported, which cannot be explained by the current models [18–20]. These observations reveal the existence of mechanisms that enhance the diffusion of the particles, eventually leading to an emittance growth and a reduction of the beam intensity, thus impacting the luminosity.

One issue of major concern for past, current and future particle accelerators is the presence of external noise [21–32]. Noise can arise from several sources such as fluctuations in the current of the magnets in the accelerator's lattice, vibrations of the ground and random kicks induced by the transverse feedback system. Depending on their spectral components and the nature of the source, these effects can perturb the beam motion and eventually prove detrimental for the beam lifetime. In particular, in the presence of non-linearities, noise can act as an additional diffusion mechanism for particles at the tails, as well as the core of the distribution. Subsequently, the potential impact on the beam performance both for LHC and its future upgrade must be investigated.

The scope of this thesis is to study the beam dynamics in the presence of external noise with a spectral density that consists of distinct frequency components. Such a noise spectrum can be injected on the beam due to the variations in the current of the magnets' power converters and it is particularly important as it can potentially result in the excitation of additional resonances. Depending on the type of the power converter, well-defined frequencies or multiple harmonics can appear on the beam spectrum and, depending on the type of the magnet, the repercussions on the transverse motion vary. The aim of the thesis is twofold. First, to examine harmonic dipolar field errors, a study which was driven by experimental observations during the LHC operation. Second, to address mechanisms that cause a modulation on the betatron tunes, usually originating from perturbations in the current of the quadrupoles in the lattice, an effect which will be particularly important for HL-LHC.

This introductory chapter presents a brief overview of the concepts that are relevant to the next sections of the thesis, concerning the performance and the evolution of the LHC. The chapter is divided into five sections. First, section 1.1 describes the CERN accelerator complex, illustrating the passage of the beam through the chain of accelerators until it reaches the LHC. Second, in section 1.2 the main components of the LHC lattice are outlined. Next, in section 1.3 the concept of luminosity is discussed, along with relevant concepts such as beam-beam effects. An overall description of the challenges encountered to increase the luminosity and the evolution of the machine configuration across the years is presented. Section 1.4 contains a brief description of the planned upgrades for the HL-LHC that underlines the necessity for a better understanding of all the mechanisms that can potentially impact the machine performance. Finally, a detailed description of the objective and the outline of the thesis is drawn in section 1.5.

1.1 The CERN Accelerator Complex

The acceleration of the two beams to multiple TeV is not feasible with a single circular accelerator. Consequently, the CERN accelerator complex consists of successive particle accelerators that boost the energy of the particles, before injecting the beam to the next machine in the sequence. Figure 1.1 illustrates the full scheme of the accelerator chain. The LHC is the final element in the sequence of acceleration and the latest addition to the available accelerators [33].

The protons, which are obtained from stripping the electrons of hydrogen atoms through an electric field, are initially injected with an energy of 100 keV in the linear accelerator (Linac2). In this stage, the protons are captured in bunches, followed by an acceleration to 50 MeV. The particles are then transferred through a transfer line in the Proton Synchrotron Booster (PSB), where an energy of 1.4 GeV is reached. The booster is followed by the Proton Synchrotron (PS), where the beam is accelerated to 25 GeV and the final bunch structure is established. During the PS cycle, a series of Radio Frequency (RF) manipulations are employed that determine the longitudinal bunch structure, i.e., the bunch length and spacing. Then, the beam arrives at the Super Proton Synchrotron (SPS), the second largest machine in the accelerator complex with a 7 km circumference. Finally, trains of bunches are injected in the LHC with an energy of 450 GeV. After approximately 20 minutes, the two beams are accelerated up to 6.5 TeV (7 TeV design energy) and eventually brought into collision.

Furthermore, there is a chain of acceleration for physics with lead ions. From vaporized lead, the ions are injected to Linac3 and are then accelerated in the Low Energy Ion Ring (LEIR), before moving to PS, SPS and eventually to LHC.

1.2 LHC lattice layout

The LHC ring is divided into eight segments, as shown in Fig. 1.2. Each octant is composed of an Arc for bending the particles in a circular trajectory, interleaved by eight Long Straight Sections (LSSs).

Each Arc consists of 154 twin aperture superconducting dipole magnets that are electrically powered in series, while each sector is powered independently. The dipoles are kept at a cryogenic temperature of 1.9 K and they can provide a magnetic field up to 8.3 T.

Each insertion contains a part equipped with devices dedicated to specific functions, called Interaction Region (IR), the layout of which depends on the use of the LSS. The IR is surrounded at each end with a Dispersion Suppressor (DS), to reduce the horizontal

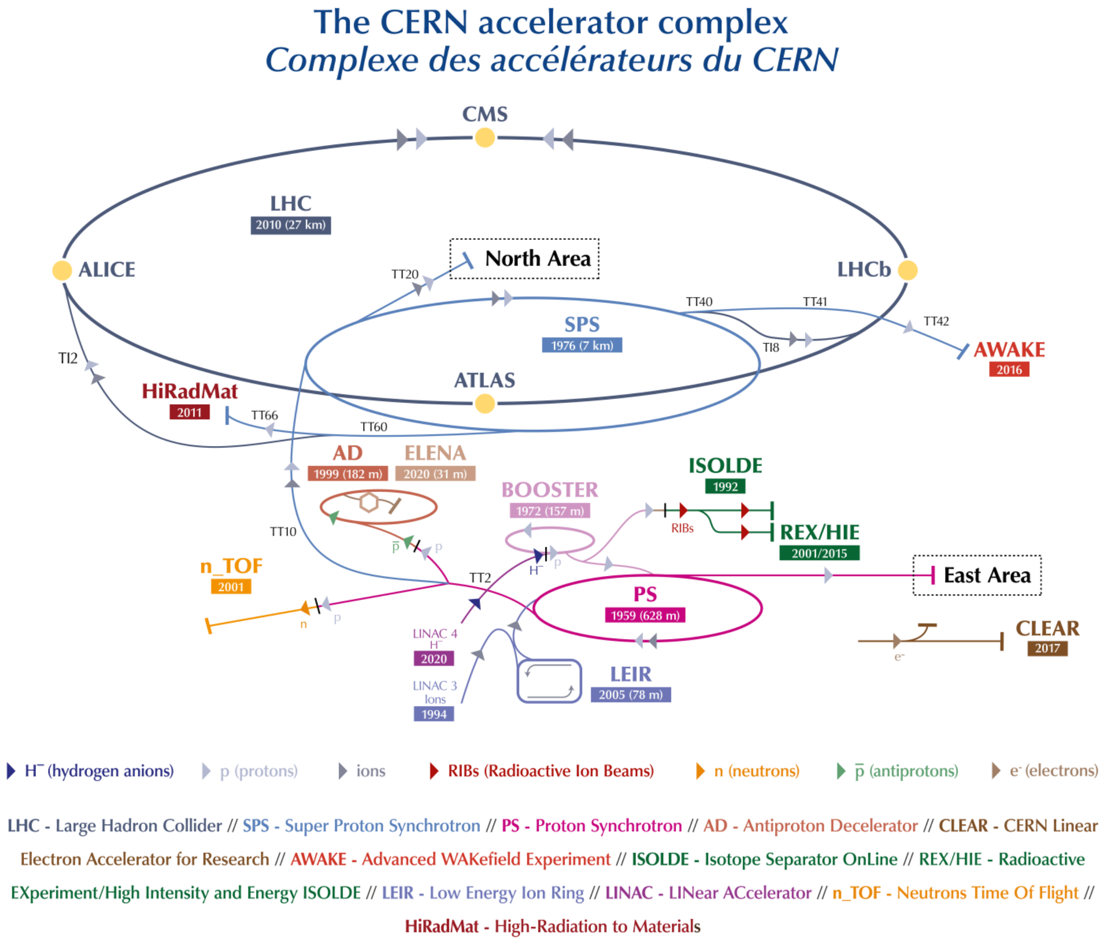

Figure 1.1: The CERN accelerator complex [34].

dispersion during the transition from the Arc to the LSS.

Apart from the DS, the interaction region of the experimental insertions consists of a low-β triplet (Q1, Q2, Q3), a pair of separation/recombination dipoles (D1, D2) and four matching quadrupole magnets, as shown in Fig. 1.3. The Inner Triplet (IT) quadrupoles are employed to minimize the β-function at the interaction points (IPs), where the beam collisions occur and the particle detectors are situated. In this way, the beam size is minimized at the IPs, leading to the maximization of the interaction rate. The separation/recombination magnets are responsible for the guidance of the two beams from the two separated apertures to a common vacuum chamber. In the common aperture, the two counter-rotating beams are subjected to an opposite force from the quadrupoles of the IT. To achieve a simultaneous focusing, the optics left and right of the IPs and between the two beams are anti-symmetrical.

During operation, Beam 1 (blue) and Beam 2 (red) are injected from SPS to LHC with the injection kickers situated in IP2 and IP8, respectively. The two beams circulate clockwise and anti-clockwise in separated apertures and they are independently accelerated

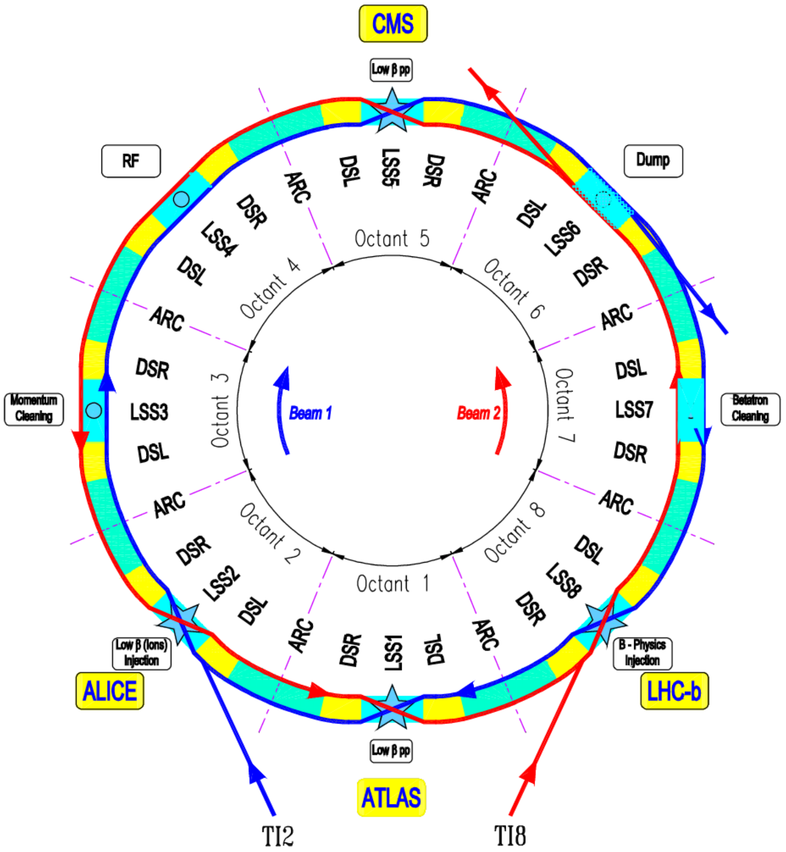

Figure 1.2: Schematic layout of the LHC ring [33].

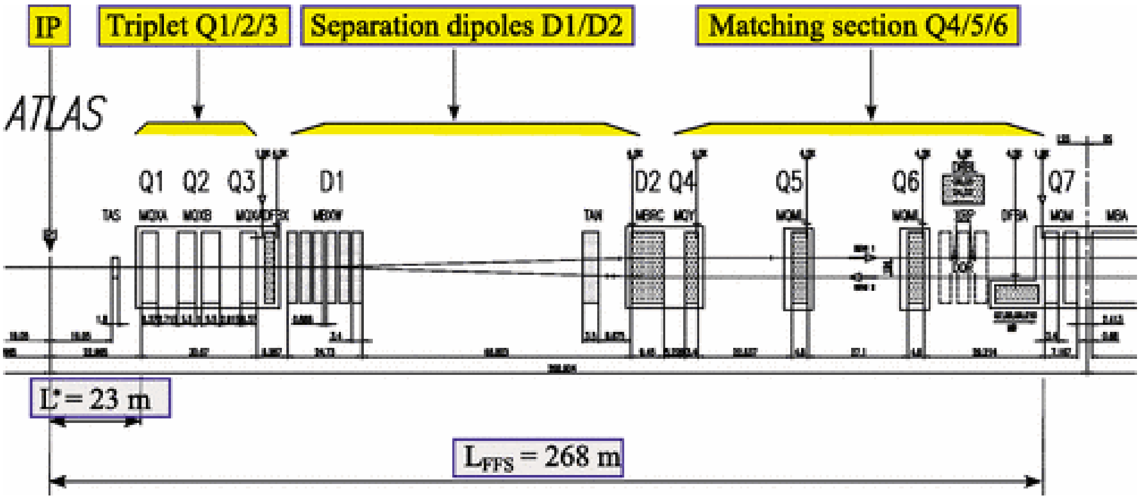

Figure 1.3: A detailed view of the low-β insertion in IR1 [33, 35].

with the Radio Frequency (RF) cavities in IR4, which also contains most of the beam instrumentation. The rest of the insertion regions are dedicated to the collimation system for momentum and betatron cleaning (IR3 and IR7) and the dump of the beams (IR6) when the physics period ends or in case of any failure. The two high luminosity experiments, ATLAS and CMS, are situated in IP1 and IP5 respectively. The two beams are crossing vertically in IR1 and horizontally in IR5. The two other experimental insertions, ALICE and LHCb, are situated in points 2 and 8.

1.3 Luminosity and LHC performance

In particle colliders, the two main figures of merit are the center-of-mass *collision energy* and the *luminosity*. In particular, as the collision energy determines the mass of the produced particles, rare interactions can be investigated with collisions at higher energies. To this end, the center-of-mass energy that can be achieved with circular colliders is orders of magnitude larger than the one of fixed-target experiments [17]. Furthermore, the luminosity defines the collision rate, i.e., the events observed per time. The following section presents the most crucial factors of luminosity reduction.

1.3.1 Beam-beam effects

In a particle collider, the *beam-beam effect* is the result of the interaction between two counter-rotating beams [36]. When the two charged beams are brought in a small separation or collide, they are subjected to strong non-linear forces, originating from the interaction of their electromagnetic fields. Specifically, in a machine with multiple closely spaced bunches such as the LHC, when the beams share a common beam pipe such as the experimental areas, the two beams will experience *head-on* collisions as well as encounters at large separations called *long-range interactions*. The two types of interactions between the bunches of the counter-circulating beams are depicted in Fig. 1.4. For round Gaussian beams, the radial kick experienced by a particle from the opposing beam due to the beam-

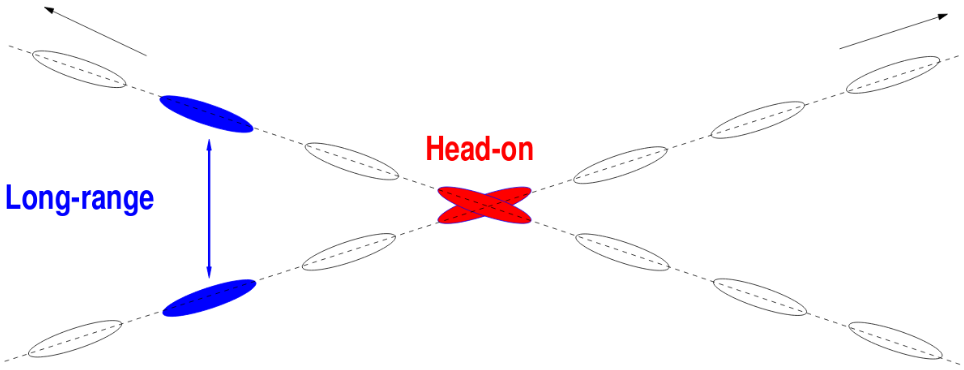

Figure 1.4: The head-on and long-range beam-beam interactions during the collision of two counter-rotating beams [36].

beam force can be expressed as:

$$\Delta r' = \frac{2Nr_p}{\gamma}\frac{1}{r}\left(1 - e^{-\frac{r^2}{2\sigma^2}}\right) \tag{1.1}$$

where:
N is the number of particles in the bunch,
r_p is the classical proton radius,
γ the relativistic Lorentz factor,
σ the separation of the particle with respect to the core of the other beam,
r is the radial distance of the particle.
The beam-beam force of Eq. (1.1) as a function of the separation is illustrated in Fig. 1.5. It must be noted that the linearity of the beam-beam force in head-on encounters, similar to a quadrupole kick, is gradually replaced by a $1/r$ dependence for the long-range interactions.

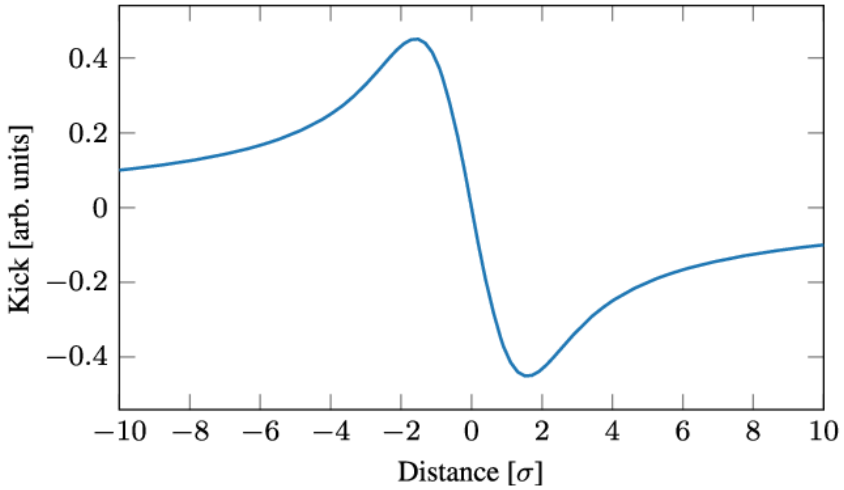

Figure 1.5: The beam-beam force for a round Gaussian beam as a function of the separation of the particle from the core of the other beam [37].

Depending on the separation, the beam-beam force can have an important impact on the motion of the particles, leading to effects such as a tune shift, an amplitude detuning and a perturbation of the closed orbit. Bunches that experience a weaker beam-beam force exhibit a different behavior than the nominal bunches, which leads to the need for a bunch classification. To this end, in the presence of a non-regular filling scheme, bunches next to the gaps will experience less long-range encounters and are characterized as PACMAN bunches. This effect is also observed in the case were head-on encounters are missing, the so-called SUPER PACMAN bunches.

1.3.2 Instantaneous luminosity

In a particle collider, the number of events per second $\frac{dR}{dt}$ is equal to [17]:

$$\frac{dR}{dt} = \mathcal{L} \cdot \sigma_p \tag{1.2}$$

where σ_p is the cross section, measured in units of barn (1b = 10^{-24} cm^2), that represents the probability that an event will occur. $\mathcal{L}$ is the *instantaneous luminosity* in units of cm^{-2}s^{-1}, which describes the ability of a collider to produce the required number of collisions. For Gaussian beams colliding head-on, the instantaneous luminosity is expressed as:

$$\mathcal{L} = \frac{N_1 N_2 f N_b}{4\pi\sigma_x^* \sigma_y^*} \tag{1.3}$$

where:
N_1, N_2 are the number of particles per bunch for the two beams,
f is the revolution frequency (11.245 kHz in the LHC case),
N_b the number of bunches,
σ_x and σ_y are the RMS beam sizes in the absence of dispersion for the horizontal and vertical plane, respectively, equal to $\sigma_{x,y} = \sqrt{\frac{\beta^*_{x,y}\epsilon_n}{\gamma\beta}}$, where β^* is the β-function at the IPs, ϵ_n the normalized emittance and γ, β the relativistic Lorentz factors.

Crossing angle

The introduction of a crossing angle is essential in order to avoid the long-range beam-beam encounters described in the previous section when the two beams are in the same vacuum chamber. The fact that the two beams cross with an angle poses important limitations in the luminosity production, which is expressed through the *luminosity reduction factor S*:

$$\mathcal{L} = \frac{N_1 N_2 f N_b}{4\pi\sigma_x^* \sigma_y^*} S \tag{1.4}$$

For a small angle ϕ and a crossing at the horizontal plane x, the luminosity reduction factor is given by:

$$S \approx \frac{1}{\sqrt{1 + \left(\frac{\sigma_s}{\sigma_x}\frac{\phi}{2}\right)^2}} \tag{1.5}$$

with σ_s the RMS beam size in the longitudinal plane. The concept of the crossing angle ϕ of two bunches in beam 1 (blue) and 2 (red) is depicted in Fig. 1.6.

Beam offset

Another important factor that leads to the reduction of luminosity is the offset between the two colliding beams. In this case, the two beams do not collide head-on, but one is displaced relatively to the other in the transverse plane. The beam separation results either

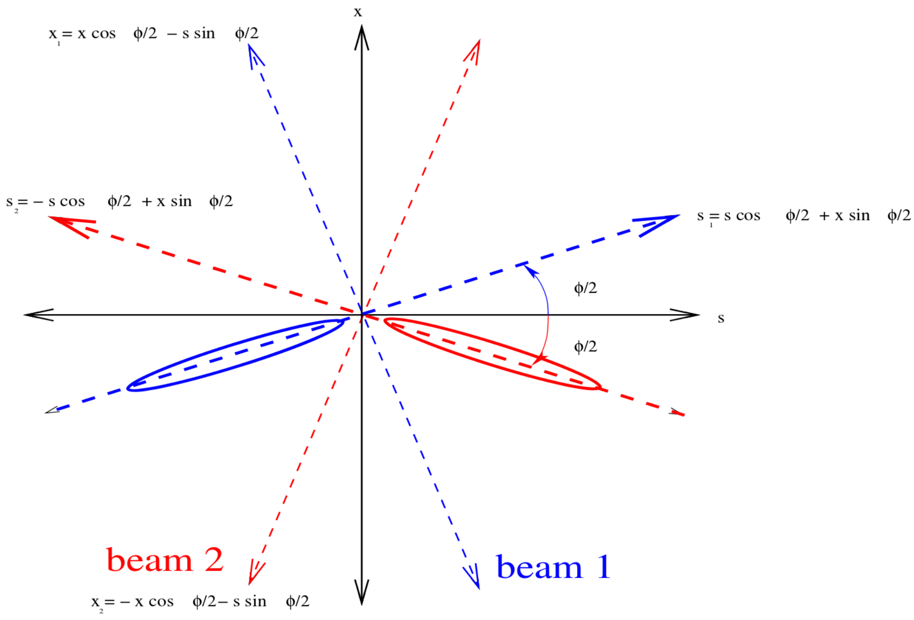

Figure 1.6: The crossing of the two bunches at an angle ϕ [17].

intrinsically by orbit imperfections or intentionally for luminosity control. The combined effect of the crossing angle and the separation is expressed as:

$$\mathcal{L} = \frac{N_1 N_2 f N_b}{4\pi\sigma_x^*\sigma_y^*} S \cdot W \cdot e^{\frac{B^2}{A}} \tag{1.6}$$

with:
$W = e^{-\frac{1}{4\sigma_x^2}(d_2-d_1)^2}$ that expresses the luminosity reduction due to the beam offset with d_1 and d_2 the displacement of the two beams relatively to their reference orbit,
$e^{\frac{B^2}{A}}$ the factor included in the presence of both crossing angle and offset in the same plane with $A = \frac{\sin^2(\frac{\phi}{2})}{\sigma_x^2} + \frac{\cos^2(\frac{\phi}{2})}{\sigma_z^2}$, $B = \frac{(d_2-d_1)\sin\phi/2}{2\sigma_x^2}$, assuming a crossing in the horizontal plane.

Hourglass effect

In the IR, the evolution of the β-function as a function of the distance s from the interaction point is equal to:

$$\beta(s) = \beta^* + \frac{s^2}{\beta^*} \tag{1.7}$$

where β^* is the β-function at the location of the IP. When the two beams are squeezed to small values of β^* and the bunches are longitudinally long, the β-function will rapidly vary as a parabolic function. Consequently, the transverse RMS beam size will change over the length of the bunch. The coupling between the transverse and the longitudinal plane is called *hourglass effect* and it leads to a further reduction of luminosity. The hourglass factor is equal to:

$$H = \sqrt{\pi}\frac{\beta^*}{\sigma_s} e^{\left(\frac{\beta^*}{\sigma_s}\right)^2} \operatorname{erfc}\left(\frac{\beta^*}{\sigma_s}\right) \tag{1.8}$$

where erfc=1-erf denotes the complementary error function. The final expression of luminosity in the presence of crossing angle, offset and hourglass effect is:

$$\mathcal{L} = \frac{N_1 N_2 f N_b}{4\pi\sigma_x^* \sigma_y^*} S \cdot W \cdot e^{\frac{B^2}{A}} \cdot H \tag{1.9}$$

1.3.3 Luminosity lifetime and integrated luminosity

During collisions, the luminosity is not constant due to proton losses originating from the inelastic scattering of the particles, known as *burn-off*. The burn-off decay time can be expressed as [38]:

$$\tau = \frac{N_0}{k\mathcal{L}_0\sigma} \tag{1.10}$$

where N_0 is the initial bunch intensity, $\mathcal{L}_0$ the initial luminosity, σ the total cross section with $\sigma \approx$110 mb for an energy of 6.5 TeV and k the number of IPs. When the burn off is the only mechanism that contributes to the proton losses, the evolution of the beam intensity as a function of time is expressed as:

$$N(t) = \frac{N_0}{1 + t/\tau} \tag{1.11}$$

and the luminosity evolution is equal to:

$$\mathcal{L}(t) = \frac{\mathcal{L}_0}{(1 + t/\tau)^2} \tag{1.12}$$

The *integrated luminosity* over a time period T is computed as:

$$\mathcal{L}_{int} = \int_0^T \mathcal{L}(t)dt \tag{1.13}$$

and, once multiplied by the cross section, returns the total number of events observed for a process p. The integrated luminosity is expressed in units of fb^{-1}. It must be noted that experimental observations indicate that there are additional mechanisms that result in diffusion processes and eventually to losses beyond burn-off.

1.3.4 Luminosity levelling and anti-leveling

Apart from the physical mechanisms that lead to the degradation of the luminosity production, one of the main limiting factors of the luminosity increase is the *pile-up*, i.e., the number of simultaneous events that can be distinguished and reconstructed by the detectors of the experiments. Several modifications of the beam and machine configuration can lead to the increase of the beam intensity and the minimization of the RMS beam size, thus maximizing the instantaneous luminosity. However, in this case, the analysis of the detector data becomes increasingly challenging and for values beyond the maximum acceptable pile-up, a degradation of the data quality is observed. To this end, the main goal is to improve the integrated, rather than the instantaneous luminosity, which can be achieved through the *luminosity levelling* and *anti-leveling*.

During the luminosity levelling, the machine parameters are modified so that the instantaneous luminosity is reduced according to the maximum pile-up defined by the experiments. The simplest method of leveling is achieved through the introduction of an offset between the two beams, independently in each IP, through a local orbit bump. During the physics fills, levelling by separation has been mainly employed for ALICE and LHCb, although it has recently also been applied to ATLAS and CMS.

Furthermore, the anti-leveling techniques aim at increasing the integrated luminosity. During collisions, the intensity decay leads to weaker beam-beam effects over time and therefore, the luminosity reduction due to the geometric factor can be compensated throughout the fill. To this end, the crossing angle or/and the β^* are gradually reduced, leading to an increase of the geometric factor and a decrease in the beam size, respectively. These techniques have been successfully incorporated in operation during the 2017 and 2018 runs and proved beneficial for the integrated luminosity.

1.3.5 LHC operating cycle

During a physics fill, the LHC cycle is organized in several *beam modes*. Overall, the bunches are injected into the machine, followed by the energy ramp and are eventually brought to collision. The operational cycle of the LHC is illustrated for a physics fill in Fig. 1.7. The figure depicts the various beam modes (dashed vertical lines), the energy evolution (black line), the beam intensities (blue and red) and the instantaneous luminosity (orange line).

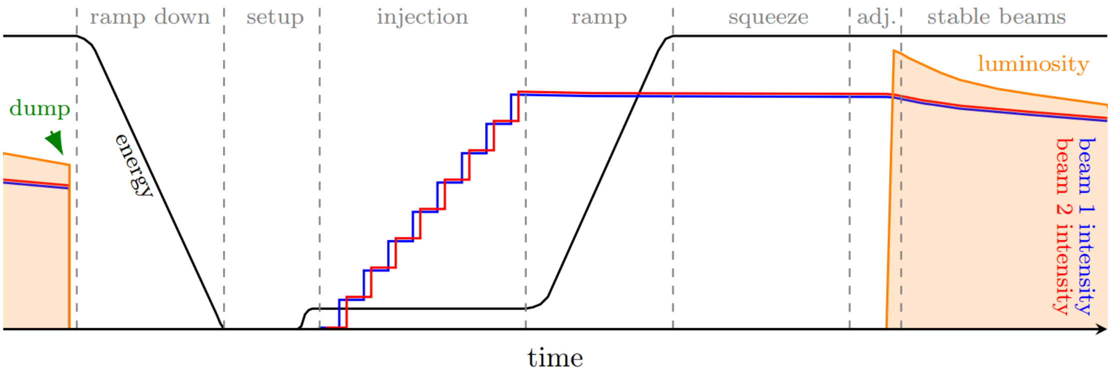

Figure 1.7: Operational cycle of a typical LHC Fill [39].

During the first phase, *Setup*, the current of the main dipoles is ramped to the injection configuration of 450 GeV, the beam dump system is armed in case of failure, while all the interlocks are reset. For machine protection, prior to the injection of high-intensity batches in the machine, a single low-intensity bunch (probe) is injected into each ring. Next, the trains of bunches are injected from SPS to LHC until the designated filling scheme is achieved. Then, during *Ramp*, the RF system accelerates the beams, which reach an energy of 6.5 TeV. In order to constrain the circular trajectory of the particles, the current of the main dipoles is gradually increased. The duration of this beam mode is approximately 20 minutes. Once the beam reaches *Flat Top*, i.e., the maximum energy, the working point is moved from injection to the collision tunes. During *Squeeze*, an interchange between injection and collision optics takes place, while the triplets around the IPs are set to low-β^* operation. During *Adjust*, the separation orbit bumps collapse, to establish collisions and all IPs are optimized for luminosity. If requested by the experiments, luminosity leveling is enabled. *Stable beams* are declared to signal that data taking can be initiated from the experiments. After approximately 10-15 h in Stable beams, the beams are extracted from the LHC dump system. The magnet currents are then ramped down to accept a new beam from the injectors, which defines the start of a new fill. The *Ramp Down* lasts approximately 30 minutes and it is essential to control magnetic hysteresis effects, while a shortened version of this phase is the *Precycle*.

1.3.6 LHC performance

During the operational years, the LHC configuration has significantly evolved, leading to a peak luminosity that exceeded in run II by more than a factor of two its design luminosity. Figure 1.8 depicts the delivered luminosity in ATLAS and CMS across the years. In the following section, a brief overview of run I and II is presented and the various machine and beam configurations are discussed. The evolution of the important parameters is shown in Table 1.1 and Table 1.2 for run I and II, respectively.

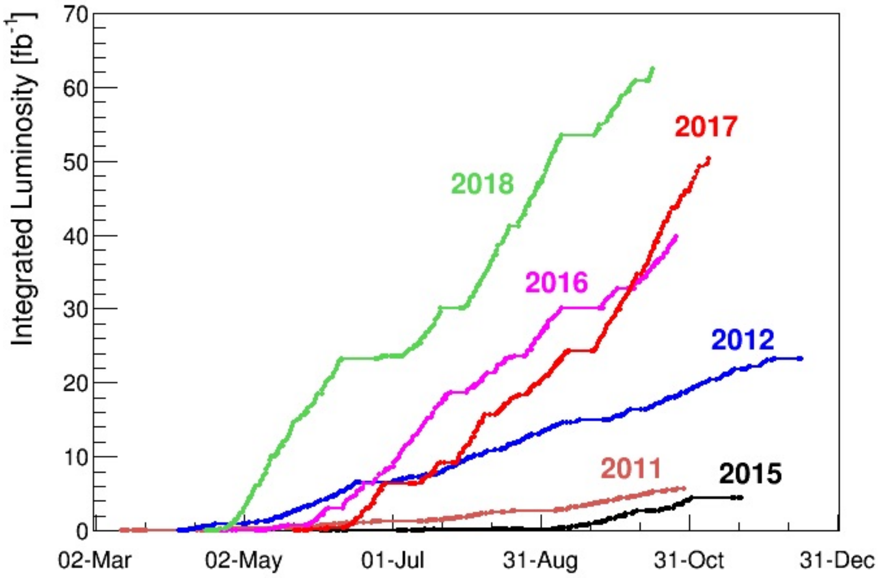

Figure 1.8: Overview of the integrated luminosity per year.

The first operational period of the LHC was very successful and resulted in important physics discoveries. During the first run, the LHC operated with 3.5 TeV (2010 and 2011) and 4 TeV (2012) [40]. The beams consisted of bunches with a longitudinal spacing of 150 ns (2010), 75 ns (2011) and 50 ns (2011 and 2012). The β^* value for ATLAS and CMS was reduced from 3.5 m (2010) to 1 m (2011) and eventually to 0.6 m (2012).

Table 1.1: The LHC machine and beam configuration during run I.

	Run I		
	2010	**2011**	**2012**
Collision energy (TeV)	3.5	3.5	4
Maximum number of bunches	268	1380	1380
IR1/IR5 integrated luminosity (fb^{-1})	0.048	5.6	23.3
Intensity start of Stable Beams (10^{11})	1.2	1.45	1.6
Half crossing angle IR1/IR5 (μrad)	100	120	145
Tunes at collision	64.31,59.32	64.31,59.32	64.31,59.32
Chromaticity	2-3	2-3	2-3/15
IR1/IR5 β^* (cm)	350	150/100	60
Beam type	150/50 ns	75/50/25 ns	50/25 ns
Days of physics operation	-	160	201
Leveling	Offset	Offset	Offset

In 2015, the machine operated for the first time with an energy of 6.5 TeV per beam and with the standard 25 ns bunch spacing [41]. To limit electron-cloud effects, the number of bunches was gradually increased to 2244 per beam. A new high brightness 25 ns beam, based on the Batch Compression Merging and Splitting (BCMS) scheme, developed in 2016, in combination with the reduction of the crossing angle, allowed to reach a peak and integrated luminosity of 1.4×10^{34} $\mathrm{cm}^{-2}\mathrm{s}^{-1}$ and 40 fb^{-1} respectively [42]. In 2017, a variety of beam flavors were employed to reduce the losses induced by electron cloud effects: 8b4e, i.e., a beam structure of eight bunches spaced with four empty slots and its high brightness version based on the Batch Compression and Splitting (8b4e-BCS). Furthermore, a novel optics scheme was employed, the Achromatic and Telescopic Squeeze (ATS), which allowed for the reduction of β^* from 40 cm to 30 cm in the two high luminosity experiments [35]. The combination of high brightness beam and the reduction of the beam size at the interaction points resulted in a peak luminosity of 2.06×10^{34} $\mathrm{cm}^{-2}\mathrm{s}^{-1}$ and due to the limits in the pile-up density of the experiments luminosity leveling by beam separation was necessary for the high luminosity experiments. At the end of 2017, the crossing angle anti-leveling was employed by reducing the half crossing angle from 150 to 120 μrad. In 2018, the machine operated with 2556 BCMS bunches and the crossing-angle anti-leveling was incorporated before the β^* reduction from 30 cm to 25 cm. The 2018 proton run resulted in 65 fb^{-1} of integrated luminosity, signaling the end of the second run.

1.4 The High-Luminosity LHC

The LHC performance across the years has been continuously improving, both in terms of beam energy and luminosity. To further increase the collision rate and extend its dis-

Table 1.2: The LHC machine and beam configuration during run II.

	Run II			
	2015	**2016**	**2017**	**2018**
Collision energy (TeV)	6.5	6.5	6.5	6.5
Maximum number of bunches	2244	2220	2556/1916/1868	2556
IR1/IR5 integrated luminosity (fb^{-1})	4.2	39.7	50.6	66
Intensity start of Stable Beams (10^{11})	1.0-1.25	1.0-1.25	1.0-1.25	1.0-1.25
Half crossing angle IR1/IR5 (μrad)	145	185/140	150-120	160-130
Tunes at collision	62.31,60.32	62.31,60.32	62.312,60.318	62.312,60.318
Chromaticity	15	15	15	15/8
IR1/IR5 β^* (cm)	80	40	40/30	30-27-25
Beam type	Standard 25 ns	Standard 25 ns/BCMS	BCMS/8b4e/BCS	BCMS
Days of physics operation	88	146	140	145
Leveling	Offset	Offset	Offset, Crossing angle anti-leveling	Offset, β^*, Crossing angle anti-leveling

covery potential, the LHC will undergo a major upgrade in LS3 (2023-2025). The goal of the aforementioned upgrade (HL-LHC) is to increase the instantaneous luminosity by a factor of five beyond its design value and the integrated luminosity by a factor of ten, aiming at 3000 fb^{-1} over its lifetime [43].

To reach this challenging task, the beam brightness must be increased, by doubling the beam intensity and minimizing the transverse emittance in the IPs. In view of this upgrade, various components will be replaced or modified. The main focus lies on the LHC Injectors Upgrade (LIU), taking place during LS2, on the replacement of insertion magnets and the compensation of the geometric reduction factor with Crab Cavities (CCs).

In particular, a β^* equal to 15 cm is envisaged in the baseline scenario, which leads to a series of limitations. The first limitation arises from the mechanical aperture of the final focusing quadrupoles in the IT as such small values of β^* result in a very large β-function at the location of the triplet. To overcome this challenge, an increase of the aperture can be achieved with longer and weaker, in terms of gradient, quadrupoles as shown in [35]:

$$\beta_{IT} \propto \frac{1}{\beta^* \sqrt{g}} \tag{1.14}$$

where g is the quadrupole gradient. Apart from the aperture limitations that can be resolved with the installation of new, larger-aperture magnets, additional constraints arise from chromatic aberrations due to the larger β-functions in the quadrupoles. In this case, the strengths of the sextupoles for chromaticity correction pose an additional limitation. These chromatic aberrations can be mitigated with the ATS. A brief overview of the scheme is the following. A pre squeeze β^* is reached with a standard matching procedure that is achievable in terms of quadrupoles strength and chromaticity correction efficiency. Then, with an appropriate phase advance, the β-beat of the adjacent arcs to the low β-insertions reaches its maximum at the location of the sextupoles, an effect which boosts their efficiency in terms of chromaticity correction. Therefore, with the incorporation of the ATS optics and new triplet magnets, the aforementioned limitations can be mitigated.

Moreover, operating with such small values of β^* will require an increase of the crossing angle to minimize the long-range beam-beam effects. Then, the geometric luminosity loss factor becomes important. To overcome this problem, two RF CCs will be installed per beam and side, which will cause a longitudinal rotation of the beams so that the head-on collisions are restored.

1.5 Motivation and thesis outline

Based on the experience gained during the two proton runs of the LHC, it is understood that several single-particle non-linear effects pose limitations on the beam performance. In particular, one of the mechanisms that can affect the transverse beam size and the rate of proton losses, thus leading to the degradation of luminosity, is the presence of external noise. There are several sources of noise that can perturb the transverse beam dynamics. This thesis focuses on the time variation of the dipolar and quadrupolar strengths, arising from perturbations in the power converters of the magnets. Specifically, the aspects that are treated in this thesis are:

- 50 Hz harmonics on the beam spectrum. Since the start of the LHC commissioning, components at harmonics of the mains frequency (50 Hz) have been observed in the beam spectrum. As many of these lines reside in the vicinity of the betatron tune, their presence can complicate the tune measurement and tracking during operation and potentially lead to beam losses and emittance growth. The difficulty of the subject resides in proving that these harmonics are the result of a real beam excitation, rather than an instrumental feature. This thesis provides definitive indications that this noise effect originates from the beam, through a systematic analysis of the experimental data during the proton run of 2018. In addition, based in observations and dedicated experiments, the source of the perturbation is presented. Tracking simulations are employed to define whether these spectral components are harmful to the beam performance.

- Tune modulation. Fluctuations in the current of a quadrupole in the lattice result in a modulation of the normalized focusing strength. Particles traveling turn-by-turn through a modulated quadrupole experience a modulation of their betatron tune, with a peak-to-peak variation proportional to the β-function at the location of the perturbation. In the presence of non-linearities, depending on the modulation frequency and depth, this effect can potentially lead to the excitation of additional sideband resonances in phase space, with a distance between main and sideband resonance equal to the modulation frequency. Therefore, depending on the modulation parameters and the working point, in combination with the potential overlap between resonances, the diffusion of the particles can increase. As there is a sensitivity of this frequency-dependent mechanism on the β-function, tune modulation effects are particularly relevant for the HL-LHC. The reduction of the beam size to a $\beta^* = 15$ cm in the IR, as described in the previous section, leads to an increase of the maximum β-functions in the quadrupoles of the IT by approximately a factor of two, compared to the LHC case. To this end, a more important impact of noise induced by the quadrupoles' power converters is expected for HL-LHC. The scope of this thesis is to provide a power supply noise threshold for acceptable performance in the IT from the transverse beam dynamics point of view. This is achieved by investigating the impact of several modulation frequencies and amplitudes on Dynamic Aperture (DA), lifetime and emittance growth, by employing single-particle tracking code simulations. In this way, the dangerous regimes in the modulation parameter space are defined to avoid performance degradation. Another aspect that is not usually included in the studies for power supply ripples is synchro-betatron coupling. Specifically, the coupling between the transverse and the longitudinal plane in the presence of a non-zero chromaticity is expressed as a tune modulation, with a modulation frequency equal to the synchrotron tune and a depth proportional to the chromaticity and the momentum deviation. A non-zero chromaticity is needed for the mitigation of collective instabilities by introducing a dependence on the particles' momentum. In this thesis, the interplay between power supply ripples and synchro-betatron coupling is also taken into account.

The present thesis is organized in the following way.

Chapter 2 presents a brief overview of the theoretical principles of the single-particle beam dynamics in accelerators. A description of the motion of the particles under the influence of an electromagnetic field is derived through the Hamiltonian formalism. Relevant concepts of the linear beam optics are discussed, along with the implications of linear magnet imperfections on the beam dynamics. A description of the non-linear effects using the canonical perturbation theory is included that leads to the introduction of the concept of resonances. Furthermore, the Hamiltonian formalism in the vicinity of a single resonance is discussed.

Chapter 3 is devoted to the methodology used for the post-processing of the simulation results. Such tools include algorithms for the precise representation of the particles' motion in frequency domain and the determination of the area of stability in phase space, methods that are later applied in noise simulations. The last section of the chapter describes the set of tools that have been developed with the purpose of tracking distributions with a detailed representation of the tails. The scope of this method is to quantify the impact of noise mainly in terms of beam lifetime.

Chapter 4 focuses on the studies concerning the harmonics of 50 Hz that perturb the beam spectrum. First, an analytical formalism for the particles motion under the influence of harmonic dipolar field errors is described. Second, several observations during the proton run of 2018 are presented, which indicate that these spectral components are the result of a real beam excitation, rather than an instrumental artifact. The followed experimental procedures for the investigation of the source of these spectral components are discussed. Finally, based on the findings, simulations including this type of noise effect are presented to determine their impact on the beam performance.

Chapter 5 illustrates the mechanisms underlining the quadrupolar modulation. In this context, a simple one-turn model is employed, including non-linearities and noise. Starting from an instantaneous tune determination, which depicts the concept of the tune modulation, the existence of additional sideband resonances in phase space is demonstrated for various frequencies and strengths. Then, the projections concerning the impact of tune modulation effects on the beam performance in HL-LHC is illustrated. The results of the multi-parametric tracking simulation in the presence of power supply ripples in the ITs of the high-luminosity experiments are shown. The additional modulation induced by synchro-betatron coupling is also taken into account. Tolerances based on dynamic aperture studies are depicted, as well as the impact of different modulation frequencies and depths on the beam distribution.

Finally, Chapter 6 summarizes the conclusions of the thesis and identifies areas for further research.

Chapter 2

Single particle beam dynamics

Single particle dynamics is the mathematical formalism that provides an accurate description of the motion of charged particles in the presence of external electromagnetic fields produced by the accelerator components while neglecting collective effects, i.e., effects that arise from the collective forces generated by the beam such as impedance-driven instabilities and space charge effects. In relativistic circular accelerators, the acceleration of the beam is achieved with electric fields, while magnetic fields are used for steering and focusing the particles.

A lattice that consists of low order field components such as drifts, dipoles and quadrupoles can be approximated by a linear system. In such a system, the equations of motion can be derived analytically. In reality, non-linear effects are an important aspect of particle accelerators, arising either from non-linear magnets to control chromaticity and stabilize the beam motion or intrinsically from beam-beam effects and magnet imperfections. The important contribution of non-linearities to the degradation of the beam performance, through the excitation of resonances, renders the linear formalism insufficient, thus leading to the development of a set of mathematical tools that can accurately treat these effects. In this chapter, a brief overview of the single particle beam dynamics is discussed, starting from the linear approximation and extending to the non-linear formalism as derived in [44–46], unless stated otherwise.

2.1 Hamiltonian formalism in an electromagnetic field

The aim of circular accelerator is to steer and focus the charged particles in a prescribed trajectory, known as the *closed orbit*. The motion of a particle with a charge q, a mass m and a vector velocity $\boldsymbol{v}$ can only be influenced by electric and magnetic fields, as described by the *Lorentz force*:

$$\frac{d\boldsymbol{p}}{\mathrm{dt}} = \boldsymbol{F} = q\boldsymbol{E} + q(\boldsymbol{v} \times \boldsymbol{B}), \tag{2.1}$$

where $\boldsymbol{p}$ is the relativistic kinetic momentum and $\boldsymbol{E}$, $\boldsymbol{B}$ are the electric and magnetic fields, respectively. From Eq. (2.1), it can be shown that a change in the kinetic energy of the particle can only be achieved through the interaction with the electric field, while, in the relativistic regime, the magnetic field is employed for deflecting its trajectory. From the equilibrium of the centrifugal and the Lorentz force, for a magnetic field orthogonal to the particle's velocity, the *radius of curvature* is equal to:

$$\rho = \frac{mv}{qB}. \tag{2.2}$$

From Eq. (2.2), the *magnetic rigidity* of the charged particle is defined as:

$$B\rho = \frac{p}{q}. \tag{2.3}$$

For a particle with charge $q = e$, Eq. (2.3) transforms into:

$$B\rho\ [\mathrm{Tm}] = 3.3357\ p\ [\mathrm{GeV/c}]. \tag{2.4}$$

During the steering of the particle's trajectory to the desired orbit, the *deflection angle* caused by the dipolar magnetic field is equal to:

$$\theta = \int \frac{\mathrm{ds}}{\rho}. \tag{2.5}$$

Equations (2.3) and (2.5) indicate that the bending radius of the particle is inversely proportional to its momentum, i.e., a more rigid beam will be less affected by the magnetic field. To this end, for a constant magnetic field, reaching a higher energy requires increasing the radius of curvature.

The equations of motion as a function of time can be derived from the Lorentz force. However, a general description of the particle's motion is achieved with the *Hamiltonian formalism*, from which, through the transformation to the curved co-ordinate system, the equations of motions are parameterized as a function of the path length, rather than the time.

The total energy E and canonical momentum $\boldsymbol{p}$ of a relativistic particle under the influence of an electromagnetic field can be expressed as:

$$E = \gamma mc^2 + qV, \tag{2.6}$$

$$\boldsymbol{p} = \boldsymbol{\beta}\gamma mc + q\boldsymbol{A}, \tag{2.7}$$

where V is the electric scalar potential, $\boldsymbol{A}$ the magnetic vector potential, $\boldsymbol{\beta} = \frac{\boldsymbol{v}}{c}$ and $\gamma = \frac{1}{\sqrt{1-\beta^2}}$ the Lorentz factors. Combining Eq. (2.6) and (2.7) yields:

$$(E - qV)^2 = (\boldsymbol{p} - q\boldsymbol{A})^2 c^2 + m^2c^4. \tag{2.8}$$

The Hamiltonian for a relativistic particle in a static electromagnetic field is equal to the total energy of the system and from Eq. (2.8) it is expressed as:

$$H = c\sqrt{(\boldsymbol{p} - q\boldsymbol{A})^2 + m^2c^2} + qV. \tag{2.9}$$

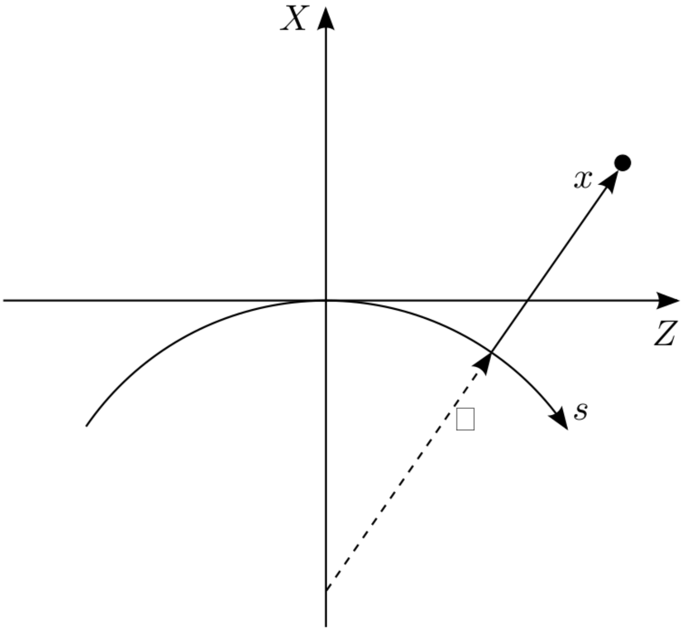

Figure 2.1: The curved co-ordinate system [44].

In order to describe the trajectory of a particle in a dipole with a bending radius ρ in the horizontal plane, a transformation from the Cartesian (X, Y, Z) to the curved co-ordinates (x, y, s) is needed, as depicted in Fig. 2.1:

$$X = (x+\rho)\cos\left(\frac{s}{\rho}\right) - \rho, \tag{2.10}$$

$$Y = y, \tag{2.11}$$

$$Z = (x+\rho)\sin\left(\frac{s}{\rho}\right). \tag{2.12}$$

The canonical transformation for the momenta (P_X, P_Y, P_Z) is derived through a mixed-variable generating function of the third kind (Appendix A.1):

$$F_3 = -\left((x+\rho)\cos\left(\frac{s}{\rho}\right) - \rho\right)P_X - yP_Y - (x+\rho)\sin\left(\frac{s}{\rho}\right)P_Z. \tag{2.13}$$

The new momenta (p_x, p_y, p_s) are expressed as:

$$p_x = P_X\cos\left(\frac{s}{\rho}\right) + P_Z\sin\left(\frac{s}{\rho}\right), \tag{2.14}$$

$$p_y = P_Y, \tag{2.15}$$

$$p_s = P_Z\left(1+\frac{x}{\rho}\right)\cos\left(\frac{s}{\rho}\right) - P_X\left(1+\frac{x}{\rho}\right)\sin\left(\frac{s}{\rho}\right). \tag{2.16}$$

The expression of the magnetic vector potential on the curved reference trajectory is:

$$A_x = A_X \cos\left(\frac{s}{\rho}\right) - A_Z \sin\left(\frac{s}{\rho}\right), \tag{2.17}$$

$$A_y = A_Y, \tag{2.18}$$

$$A_s = A_Z \cos\left(\frac{s}{\rho}\right) - A_X \sin\left(\frac{s}{\rho}\right). \tag{2.19}$$

The new Hamiltonian is:

$$H' = c\sqrt{\left(\frac{p_s}{1+\frac{x}{\rho}} - qA_s\right)^2 + (p_x - qA_x)^2 + (p_y - qA_y)^2 + m^2c^2} + qV. \tag{2.20}$$

Since the machine is periodic in the longitudinal position s, the independent variable in Eq. (2.20) is changed from time to path length, through the *action*. The action of a particle moving in one degree of freedom with $q_1 = x$ and $p_1 = p$ for a time interval (t_0, t_1) is:

$$S = \int_{t_0}^{t_1} p\dot{x} - H'\mathrm{d}t. \tag{2.21}$$

By changing the independent variable of the integration from time to path length:

$$S = \int_{s_0}^{s_1} (-H')\frac{\mathrm{d}t}{\mathrm{d}s} + p\mathrm{d}s, \tag{2.22}$$

the following interchange of variables can be defined:

$$H' \rightarrow (-p_s)\ , \quad t \rightarrow s. \tag{2.23}$$

Using Hamilton's equations (Appendix A.2) with the new set of variables yields:

$$\frac{\mathrm{d}t}{\mathrm{d}s} = \frac{\partial p_s}{\partial H'}, \tag{2.24}$$

$$\frac{\mathrm{d}H'}{\mathrm{d}s} = -\frac{\partial p_s}{\partial t}. \tag{2.25}$$

Based on Eq. (2.23), the conjugate phase-space co-ordinates with s as the independent variable are:

$$(x, p_x);\ (y, p_y);\ (t, -H'). \tag{2.26}$$

Substituting Eq. (2.8) into Eq. (2.20), taking into account Eq. (2.23):

$$H' = -p_s = -\left(1+\frac{x}{\rho}\right)\sqrt{\frac{(E-qV)^2}{c^2} - (p_x - qA_x)^2 - (p_y - qA_y)^2 - m^2c^2} - \left(1+\frac{x}{\rho}\right)qA_s. \tag{2.27}$$

Assuming that only transverse fields are present with $A_x = A_y = 0$, the vector potential can be expressed as a power series:

$$A_s = -B_0\mathrm{Re}\left[\sum_{n=0}^{\infty} \frac{b_n + ia_n}{n+1}(x+iy)^{n+1}\right], \tag{2.28}$$

with $a_n = \frac{1}{B_0 n!}\frac{\partial^n B_x}{\partial x^n}$ the *skew* and $b_n = \frac{1}{B_0 n!}\frac{\partial^n B_y}{\partial x^n}$ the *normal multipole coefficients* and B_0 the main dipolar field strength, which is used as a reference. The magnetic field can be derived from $\boldsymbol{B} = \nabla \times \boldsymbol{A}$ as:

$$\begin{gathered} B_x = -\frac{\partial A_s}{\partial y},\; B_y = \frac{\partial A_s}{\partial x}, \\ B_y(x,y) + iB_x(x,y) = B_0 \sum_{n=0}^{\infty}(b_n + ia_n)(x+iy)^n. \end{gathered} \tag{2.29}$$

The value of n defines the order of the multipole. For instance, $n = 0$ corresponds to a dipole, $n = 1$ to a quadrupole and $n = 2$ to a sextupole. Figure 2.2 illustrates the field in a normal (left) and skew (right) dipole (top), quadrupole (middle) and sextupole (bottom). The field in a dipole is uniform, in a quadrupole it increases linearly with the distance from the center and in the case of a sextupole it increases quadratically.

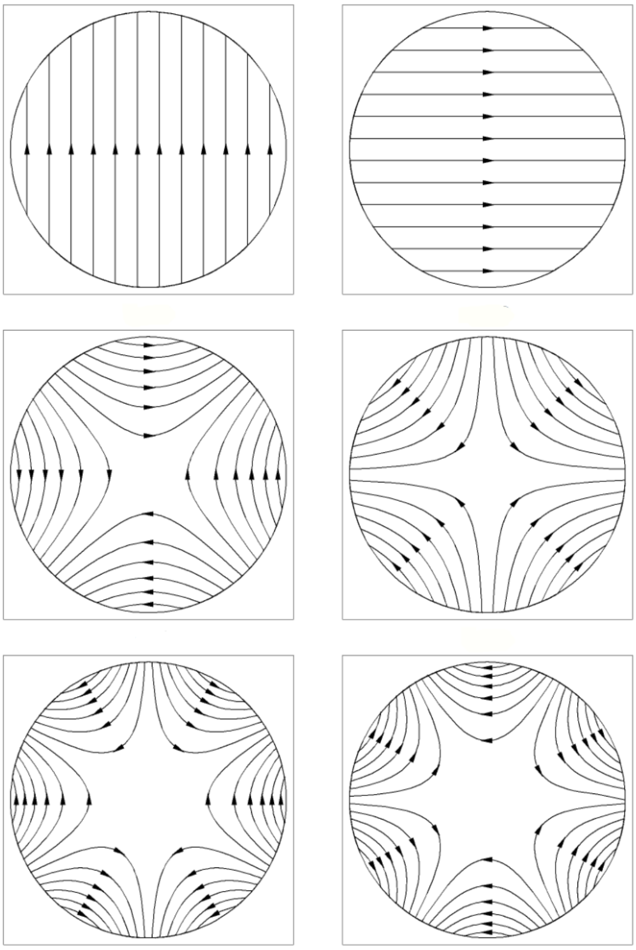

Figure 2.2: Pure multipole fields for the dipole (top), the quadrupole (middle) and the sextupole (bottom) for normal (left) and skew (right) fields [47].

2.2 Symplecticity and Liouville theorem

Neglecting effects such a synchrotron radiation, acceleration and the interactions between particles, the evolution of the particles motion between two points in phase space can be represented with a *transfer map*. The transfer map M of a dynamical system from an initial position s_0 to a position s is a canonical transformation from the original variables $(\boldsymbol{p}, \boldsymbol{q})$ to $(\boldsymbol{P}, \boldsymbol{Q})$. Maps that are obtained as a solution to Hamilton's equations are called *symplectic*, i.e., the following property is satisfied:

$$M^T S M = J^T S J = S, \tag{2.30}$$

where J is the Jacobian $J_{ij} = \frac{\partial X_i}{\partial x_j}$ and:

$$S = \begin{pmatrix} 0 & 1 \\ -1 & 0 \end{pmatrix}. \tag{2.31}$$

It follows that for a symplectic matrix $\det M = \det J = 1$. The product of symplectic matrices, which represents the evolution of the system between the two positions, is also symplectic. *Liouville's theorem* states that under symplectic transformation phase-space volume is preserved:

$$\prod_{i=1}^{N} dp_i dq_i = \det J \prod_{i=1}^{N} dP_i dQ_i, \tag{2.32}$$

$$d\omega = d\Omega, \tag{2.33}$$

where ω, Ω represent the initial and final volume in phase space, respectively and the phase space density ρ is conserved:

$$\frac{d\rho}{\mathrm{dt}} = \frac{\partial \rho}{\partial t} + \sum_{i=1}^{N} \frac{dq_i}{\mathrm{dt}} \frac{\partial \rho}{\partial q_i} + \frac{dp_i}{\mathrm{dt}} \frac{\partial \rho}{\partial p_i} = 0. \tag{2.34}$$

Liouville's theorem is particularly important for accelerators as it implies that a reduction of the size of the beam through focusing leads to an increase in divergence so that the area in phase space is preserved.

2.3 Linear beam optics

The dynamics of the motion in accelerator components such as drifts, dipoles and quadrupoles can be represented by linear approximations. Through the paraxial approximation $a\sqrt{1 - \frac{b^2+c^2}{a^2}} \approx a - \frac{b^2+c^2}{2a}$ where a, b, c arbitrary functions, the Hamiltonian in Eq. (2.27) is expanded to second order in the momenta:

$$H = -\left(1 + \frac{x}{\rho}\right)\left[p - \frac{(p_x - qA_x)^2 + (p_y - qA_y)^2}{2p} + qA_s\right], \tag{2.35}$$

where $p = \frac{(E-qV)^2}{c^2}$. From Hamilton's equations (Appendix A.2):

$$u' = \frac{du}{\mathrm{ds}} = \frac{\partial H}{\partial p_u}, \; p_u' = \frac{dp_u}{\mathrm{ds}} = -\frac{\partial H}{\partial u}, \tag{2.36}$$

with $u = (x, y)$. Combining the Hamiltonian of Eq. (2.35), the Maxwell equation for the magnetic field and the vector potential of Eq. (2.29) and the expression of the beam rigidity given in Eq. (2.3), neglecting higher-order terms, the equations of motion are:

$$\begin{aligned} x'' - \frac{\rho + x}{\rho^2} &= -\frac{B_y}{B\rho}\frac{p_0}{p}\left(1 + \frac{x}{\rho}\right)^2, \\ y'' &= \frac{B_x}{B\rho}\frac{p_0}{p}\left(1 + \frac{x}{\rho}\right)^2, \end{aligned} \tag{2.37}$$

where p_0 is the momentum of the reference particle. For a linear lattice, the magnetic field to first order is:

$$B_y = -B_0 + \frac{\partial B_y}{\partial x}x = B_0 + B_1 x, \;\; B_x = \frac{\partial B_y}{\partial x}y = B_1 y, \tag{2.38}$$

where B_0 is the dipole field and B_1 is the quadrupolar gradient function at the reference orbit. Expanding Eq. (2.37) to first order and setting $\delta = \left(\frac{p-p_0}{p_0}\right)$ and $K_1(s) = \frac{1}{B\rho}\frac{\partial B_y}{\partial x} = \frac{B_1}{B\rho}$ yields:

$$\begin{aligned} x'' + \left(\frac{1-\delta}{\rho^2(1+\delta)} + \frac{K_1(s)}{1+\delta}\right)x &= \frac{\delta}{\rho(1+\delta)}, \\ y'' - \left(\frac{K_1(s)}{1+\delta}\right)y &= 0. \end{aligned} \tag{2.39}$$

For on-momentum particles ($\delta = 0$), the equations of motion are reduced to the equation of a harmonic oscillator, called the *Hill's equation*:

$$u'' + K_u(s)u = 0, \tag{2.40}$$

where $u = (x, y)$ and $K_x(s) = \frac{1}{\rho^2} + K_1(s)$, $K_y(s) = -K_1(s)$. The solutions can be expressed in the form of a matrix:

$$\begin{pmatrix} u \\ u' \end{pmatrix}_s = \begin{pmatrix} C_u(s) & S_u(s) \\ C_u'(s) & S_u'(s) \end{pmatrix} \begin{pmatrix} u \\ u' \end{pmatrix}_{s_0} = M_u(s|s_0)\begin{pmatrix} u \\ u' \end{pmatrix}_{s_0}, \tag{2.41}$$

where M is the transfer matrix from the position s_0 to s. In a drift space of length l, where no electromagnetic fields are present ($K_u = 0$), the transfer matrix in the relativistic regime reduces to:

$$M_{\mathrm{drift}} = \begin{pmatrix} 1 & l \\ 0 & 1 \end{pmatrix}. \tag{2.42}$$

From the transfer matrix of the drift, it can be seen that the particle's offset changes in the case of a non-vanishing initial slope, while the momentum is unaffected. For a quadrupole of length l and a strength K_u, the transfer matrix in the focusing plane is equal to:

$$M_F = \begin{pmatrix} \cos\zeta & \frac{1}{\sqrt{K_u}}\sin\zeta \\ -\sqrt{K_u}\sin\zeta & \cos\zeta \end{pmatrix}, \tag{2.43}$$

where $\zeta = \sqrt{K_u}l$. Similarly, in the defocusing plane:

$$M_D = \begin{pmatrix} \cosh\zeta & \frac{1}{\sqrt{|K_u|}}\sinh\zeta \\ \sqrt{|K_u|}\sinh\zeta & \cosh\zeta \end{pmatrix}, \tag{2.44}$$

where $\zeta = \sqrt{|K_u|}l$. In the *thin-lens approximation*, i.e., $l \to 0$ and defining $f = \lim_{l\to 0}\frac{1}{|K_u|l}$ the *focal length*:

$$M_F = \begin{pmatrix} 1 & 0 \\ -\frac{1}{f} & 1 \end{pmatrix} = \begin{pmatrix} 1 & 0 \\ -K & 1 \end{pmatrix}. \tag{2.45}$$

For a pure sector dipole of length l and bending radius ρ the transfer matrix is:

$$M_F = \begin{pmatrix} \cos\theta & \rho\sin\theta \\ -\frac{1}{\rho}\sin\theta & \cos\theta \end{pmatrix}, \tag{2.46}$$

where $\theta = \frac{l}{\rho}$.

The transfer matrix of a periodic lattice with n elements is derived from the product of the transfer matrices M_i of all the constituent elements in this interval:

$$M(s) = M_n M_{n-1}..M_2 M_1. \tag{2.47}$$

2.3.1 Courant-Snyder parameters

The transfer matrix M of the uncoupled transverse motion can be written as:

$$M = I\cos\psi + SA\sin\psi, \tag{2.48}$$

where S is defined in Eq. (2.31), I is the identity matrix, ψ is the phase advance and:

$$A = \begin{pmatrix} \gamma & \alpha \\ \alpha & \beta \end{pmatrix}, \tag{2.49}$$

with α, β, γ the *Courant-Snyder parameters*. Substituting Eq. (2.48) to the symplectic condition of Eq. (2.30) yields:

$$1 + \alpha^2 = \beta\gamma. \tag{2.50}$$

The transfer matrix can then be expressed as a function of the Courant-Snyder parameters as:

$$M = \begin{pmatrix} \cos\psi + \alpha\sin\psi & \beta\sin\psi \\ -\gamma\sin\psi & \cos\psi - \alpha\sin\psi \end{pmatrix}. \tag{2.51}$$

For the stability of the particle's motion, the following expression must be satisfied:

$$|\mathrm{Trace}(M)| \leq 2. \tag{2.52}$$

The transfer matrix in a linear beam transport line between two positions s_1 and s_2 is equal to:

$$M(s_1|s_2) = \begin{pmatrix} \sqrt{\frac{\beta_2}{\beta_1}}(\cos\psi + \alpha_1\sin\psi) & \sqrt{\beta_1\beta_2}\sin\psi \\ -\frac{1+\alpha_1\alpha_2}{\sqrt{\beta_1\beta_2}}\sin\psi + \frac{\alpha_1-\alpha_2}{\sqrt{\beta_1\beta_2}}\cos\psi & \sqrt{\frac{\beta_1}{\beta_2}}(\cos\psi - \alpha_2\sin\psi) \end{pmatrix}, \tag{2.53}$$

where $\beta_1, \alpha_1, \gamma_1$ and $\beta_2, \alpha_2, \gamma_2$ are the Twiss parameters at the locations s_1, s_2 respectively and $\psi = \psi(s_2) - \psi(s_1)$ is the betatron phase advance between the two locations.

2.3.2 Action angle variables

In the absence of coupling, the canonical conjugate variables (u, u') form an ellipse in phase space with an area equal to $2\pi J_u$, where J_u is called the *action variable*. The action is an invariant of motion under symplectic transformation and is equal to:

$$J_u = \frac{1}{2}(\gamma_u u^2 + 2a_u uu' + \beta_u u'^2), \tag{2.54}$$

where $u = (x, y)$ and (a, β, γ) the Courant-Snyder parameters. Therefore, these parameters define the geometrical shape of the invariant ellipse. The phase space in the horizontal plane is depicted in Fig. 2.3.

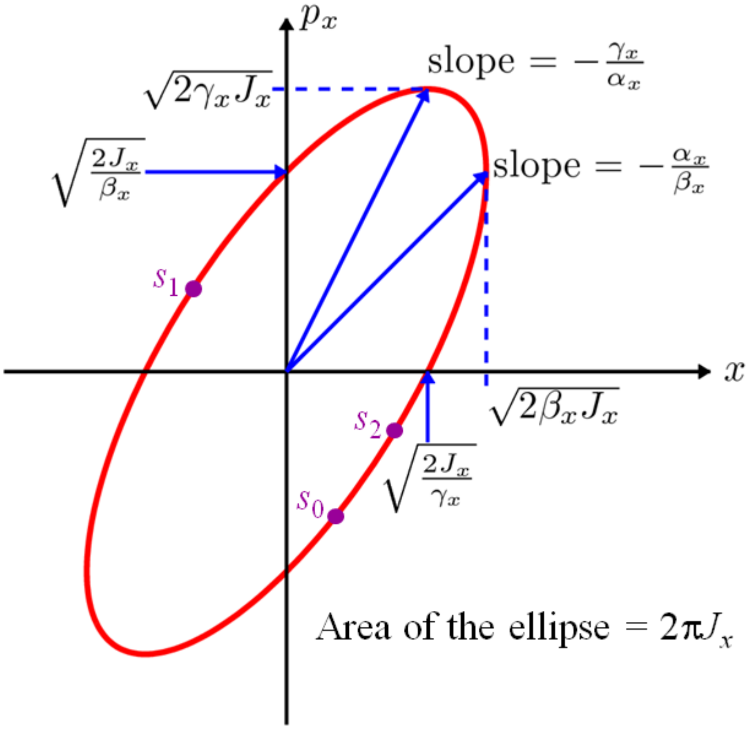

Figure 2.3: The ellipse in phase space from the canonical conjugate variables in the horizontal plane and the dependence of the geometry on the Courant-Snyder parameters [48].

The *angle variable* ϕ_u is defined as:

$$\tan\phi_u = -\beta_u \frac{u'}{u} - \alpha_u. \tag{2.55}$$

By employing the following generating function of the first kind with the old variables (x, y) and the new angle (ϕ_x, ϕ_y) (Appendix A.1):

$$F_1(x, y, \phi_x, \phi_y; s) = -\frac{x^2}{2\beta_x}(\tan\phi_x + \alpha_x) - \frac{y^2}{2\beta_y}(\tan\phi_y + \alpha_y), \tag{2.56}$$

the solutions to Hill's equations are:

$$u = \sqrt{2\beta_u J_u}\cos\phi_u, \;\; u' = -\sqrt{\frac{2J_u}{\beta_u}}(\sin\phi_u + \alpha_u\cos\phi_u). \tag{2.57}$$

The new Hamiltonian for a linear lattice in action-angle variables is:

$$H(J_x, J_y; s) = \frac{J_x}{\beta_x} + \frac{J_y}{\beta_y}. \tag{2.58}$$

Applying Hamilton's equations yields (Appendix A.2):

$$\frac{d\phi_u}{\mathrm{ds}} = \frac{\partial H}{\partial J_u}, \tag{2.59}$$

$$\frac{dJ_u}{\mathrm{ds}} = -\frac{\partial H}{\partial \phi_u} = 0. \tag{2.60}$$

Integrating Eq. (2.59) and substituting with Eq. (2.58) leads to the expression of the betatron phase advance in a linear machine:

$$\Delta\phi_u = \phi_u(s_1) - \phi_u(s_0) = \int_{s_0}^{s_1} \frac{\partial H}{\partial J_u}\mathrm{ds} = \int_{s_0}^{s_1} \frac{\mathrm{ds}}{\beta_u}. \tag{2.61}$$

The betatron tune is defined as the number of betatron oscillations per turn:

$$Q_u = \frac{\phi_u}{2\pi} = \frac{1}{2\pi}\int_0^{C_0} \frac{\mathrm{ds}}{\beta_u(s)} \tag{2.62}$$

and from Eq. (2.51), the transfer one-turn matrix is:

$$M_u = \begin{pmatrix} \cos(2\pi Q_u) + \alpha_u \sin(2\pi Q_u) & \beta_u \sin(2\pi Q_u) \\ -\gamma_u \sin(2\pi Q_u) & \cos(2\pi Q_u) - \alpha_u \sin(2\pi Q_u) \end{pmatrix}. \tag{2.63}$$

From Eq. (2.60) it follows that J_u is a constant of motion. The Hamiltonian for a linear lattice is *integrable*, i.e., angle independent. Defining $\vec{J_u}$ as:

$$\vec{J_u} = \begin{pmatrix} \sqrt{2J_u}\cos\phi_u \\ -\sqrt{2J_u}\sin\phi_u \end{pmatrix}. \tag{2.64}$$

The transformation to Cartesian co-ordinates is:

$$\vec{u} = N_u^{-1}\vec{J_u}, \tag{2.65}$$

where $N_u^{-1} = \begin{pmatrix} \sqrt{\beta_u} & 0 \\ -\frac{\alpha_u}{\sqrt{\beta_u}} & \frac{1}{\sqrt{\beta_u}} \end{pmatrix}$ is the *normalising matrix*. From position s_0 to s_1 with a transfer map R:

$$\vec{u_{s_1}} = M(s_0|s_1)\vec{u_{s_0}}, \tag{2.66}$$

$$\vec{J_{s_1}} = N_u M(s_0|s_1) N_u^{-1} \vec{J_{s_0}} = \begin{pmatrix} \cos\mu_u & \sin\mu_u \\ -\sin\mu_u & \cos\mu_u \end{pmatrix}, \tag{2.67}$$

where μ is the phase advance over one turn and the final transfer map corresponds to a pure rotation. For linear systems, this transformation replaces elliptical motion in phase space with a circular trajectory.

Finally, the Hamiltonian in Eq. (2.58) varies with $\frac{1}{\beta_u(s)}$ and to remove the dependence on s the following generating function is employed (Appendix A.1):

$$F_2(\phi_u, \tilde{J}_u) = \left(\phi_u - \int_0^s \frac{\mathrm{ds}}{\beta_u} + Q_u \frac{s}{R}\right) \tilde{J}. \tag{2.68}$$

The new conjugate co-ordinates are expressed as:

$$\tilde{J}_u = J_u, \quad \tilde{\phi_u} = \phi_u - \int_0^s \frac{\mathrm{ds}}{\beta_u} + Q_u \frac{s}{R} \tag{2.69}$$

and the new Hamiltonian:

$$\tilde{H}(J_u) = \frac{Q_u}{R} J_u. \tag{2.70}$$

2.3.3 Emittance

A bunch is composed by a distribution of particles. Therefore, it is necessary to derive statistical averages over the positions of all particles. The statistical average of x^2 from Eq. (2.57) is equal to:

$$\langle x^2 \rangle = 2\beta_x \langle J_x \cos^2 \phi_x \rangle. \tag{2.71}$$

Assuming that all positions are uncorrelated and that the angle variables are uniformly distributed:

$$\langle x^2 \rangle = \beta_x \epsilon_x, \tag{2.72}$$

where ϵ_x is the *geometric emittance* and it is equal to average of the actions of all the particles included in the bunch. Similarly:

$$\langle x p_x \rangle = -\alpha_x \epsilon_x, \tag{2.73}$$

$$\langle p_x^2 \rangle = \gamma_x \epsilon_x. \tag{2.74}$$

The Σ-*matrix* is computed from the previous statistical averages:

$$\Sigma = \begin{pmatrix} \langle x^2 \rangle & \langle x p_x \rangle \\ \langle p_x x \rangle & \langle p_x^2 \rangle \end{pmatrix}. \tag{2.75}$$

Generally, the geometric emittance is computed as:

$$\mathrm{eigenvalues}(\Sigma S) = \pm i \epsilon_x. \tag{2.76}$$

For the uncoupled horizontal motion, the emittance is equal to:

$$\epsilon_x = \sqrt{\langle x^2 \rangle \langle p_x^2 \rangle - \langle x p_x \rangle}. \tag{2.77}$$

The geometric emittance is not an invariant when the energy of the particles changes. Subsequently, the *normalised emittance* is defined as:

$$\epsilon_N = \beta\gamma\epsilon, \tag{2.78}$$

where β, γ are the relativistic factors.

2.3.4 Dispersion

In the absence of errors, the trajectory that passes through the center of the quadrupoles defines the *design orbit*. On-momentum particles with vanishing initial conditions will remain in the closed orbit $x_{co}(s)$ and return to their initial position after one turn. In the case of non-zero initial conditions, particles with the reference momentum will undergo betatron oscillation around the closed orbit $x_\beta(s)$. On the contrary, particles with a small momentum deviation from the reference particle will travel along different paths in the accelerator due to the dependence of the bending angle on the particle energy, called *dispersion*. These particles will perform betatron oscillations around a different closed orbit, which is derived from the non-homogeneous differential Eq. (2.39). The solution of the particle's motion in the horizontal plane with a momentum deviation δ in the presence of dispersion D_x is expressed as:

$$x(s) = x_{co}(s) + D_x(s)\delta + x_\beta(s). \tag{2.79}$$

Figure 2.4 illustrates the concept of closed orbit in the presence of dispersion. In particular, the dispersion function represents the orbit of a particle with $\delta = 1$ that satisfies the equation:

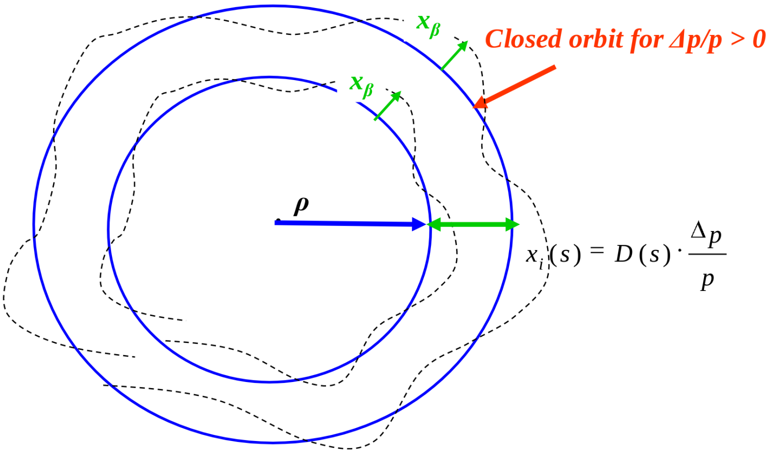

Figure 2.4: The betatron oscillation and the closed obit in the presence of dispersion [49].

$$D'' + K_x(s)D = \frac{1}{\delta}. \tag{2.80}$$

Due to the periodicity of the lattice, the dispersion function is also periodic. The form of the transfer function that also takes into account the dispersion is:

$$\begin{pmatrix} x \\ x' \\ \delta \end{pmatrix} = \begin{pmatrix} M_{11} & M_{12} & D \\ M_{21} & M_{22} & D' \\ 0 & 0 & 1 \end{pmatrix} \begin{pmatrix} x \\ x' \\ \delta \end{pmatrix}_0 . \tag{2.81}$$

The expression for the dispersion given by:

$$D(s) = M_{22}(s) \int_{s_0}^{s} \frac{1}{\rho} M_{11}(s')\text{ds'} - M_{11}(s) \int_{s_0}^{s} \frac{1}{\rho} M_{22}(s')\text{ds'}. \tag{2.82}$$

For a dipole magnet, Eq. (2.46) yields:

$$D(s) = \rho\left(1 - \cos\left(\frac{l}{\rho}\right)\right). \tag{2.83}$$

Comparing the revolution period of the on-momentum and off-momentum particles:

$$\frac{\Delta T}{T_0} = \frac{\Delta C}{C} - \frac{\Delta u}{u} = (a_c - \frac{1}{\gamma^2})\frac{\Delta p}{p_0} = \eta\delta, \tag{2.84}$$

where:
T_0 is the revolution period of the reference particle,
C is the circumference of the accelerator,
u is the velocity of the on-momentum particle,
γ is the Lorentz factor,
a_c is the *momentum compaction factor*, i.e., the ratio of the relative path length to the relative difference in momentum,
η is the *phase slip factor* equal to:

$$\eta = \alpha_c - \frac{1}{\gamma^2} = \frac{1}{\gamma_T^2} - \frac{1}{\gamma^2}, \tag{2.85}$$

where γ_T is the *transition energy*. The increase of the particle's energy leads to the increase of its velocity and its path length due to dispersion. Below the transition energy, particles with larger energy perform a revolution around the ring with a higher frequency. On the contrary, in the ultra-relativistic regime, the change in the path length dominates over the increase of the velocity and thus, the revolution frequency decreases. The transition energy defines the limit of the interplay between velocity and path length and determines whether off-momentum particles will perform a faster or slower revolution around the ring.

2.3.5 Linear imperfections

Dipolar field error

A particle with vanishing initial conditions injected at the closed orbit will repeat the same trajectory on every revolution. However, in the presence of a dipolar field error, at the location of the perturbation, the reference particle will experience a kick θ and the closed orbit will be perturb. For the new closed orbit at the location of the error, the following expression must be satisfied:

$$I\begin{pmatrix} x \\ x' \end{pmatrix}_{co} = M\begin{pmatrix} x \\ x' \end{pmatrix}_{co} + \begin{pmatrix} 0 \\ \theta \end{pmatrix}, \tag{2.86}$$

where I is the identity matrix and M the transfer matrix described in Eq. (2.63). Equation (2.86) yields:

$$(M - I)\begin{pmatrix} x \\ x' \end{pmatrix}_{co} = \begin{pmatrix} \cos(2\pi Q_x) + \alpha\sin(2\pi Q_x) - 1 & \beta\sin(2\pi Q_x) \\ -\gamma\sin(2\pi Q_x) & \cos(2\pi Q_x) - \alpha\sin(2\pi Q_x) - 1 \end{pmatrix}\begin{pmatrix} x \\ x' \end{pmatrix}_{co}. \tag{2.87}$$

Solving Eq. (2.87):

$$x = \frac{\beta\theta}{2}\left(\cot(\pi Q_x)\right), \; x' = \frac{\theta}{2}\left(1 - \alpha\cot(\pi Q_x)\right). \tag{2.88}$$

Equation (2.88) shows that in the presence of a dipole field error, an integer value of the tune will lead to an unstable closed orbit and hence, must be avoided. Similarly, a kick at the location s_1 will produce an offset at the location s_2 equal to:

$$x_2 = \frac{\theta\sqrt{\beta_1\beta_2}}{2\sin(\pi Q_x)}\cos(y_{12} - \pi Q_x), \tag{2.89}$$

where β_1, β_2 are the β-functions in the locations s_1, s_2 respectively and y_{12} is the phase advance between the two positions. In the presence of multiple independent dipole field errors:

$$x = \frac{\sqrt{\beta_s}}{2\sin(\pi Q)}\sum_{n=i}^{N_{error}}\sqrt{\beta_n}\theta_n\cos\left((y_s - y_n) - \pi Q\right). \tag{2.90}$$

Quadrupolar field error

Assuming a small gradient error of the form:

$$M_{err}(s) = \begin{pmatrix} 1 & 0 \\ -\Delta K(s)\mathrm{ds} & 1 \end{pmatrix}, \tag{2.91}$$

the final transfer matrix takes the form:

$$\tilde{M}(s) = M(s)M_{err}(s), \tag{2.92}$$

where M is given in Eq. (2.51). The matrix multiplication yields:

$$\tilde{M}(s) = \begin{pmatrix} \cos\phi + \alpha\sin\phi - \beta\sin\phi\Delta K(s)\mathrm{ds} & \beta\sin\phi \\ -\gamma\sin\phi - \Delta K(s)\mathrm{ds}\left(\cos\phi - \alpha\sin\phi\right) & \cos\phi - \alpha\sin\phi \end{pmatrix}. \tag{2.93}$$

From Eq. (2.52), the phase advance $\tilde{\phi}$ including the perturbation is equal to:

$$\cos\tilde{\phi} = \cos\phi - \frac{1}{2}\beta\sin\phi\Delta K(s)\mathrm{ds}, \tag{2.94}$$

which yields:

$$\Delta\phi = \frac{\beta\Delta K}{2}\mathrm{ds}, \;\; \Delta Q = \frac{\beta\Delta K}{4\pi}\mathrm{ds}. \tag{2.95}$$

In the presence of distributed gradient errors:

$$\Delta Q = \frac{1}{4\pi}\oint\beta\Delta K\mathrm{ds}. \tag{2.96}$$

Equation (2.96) indicates that the strength of the perturbation arising from a variation in the current of a quadrupole is proportional to the β function at its location. Therefore, it is necessary to avoid such effects in high β regimes such as the Inner Triplet. Apart from the tune shift, quadrupole errors induce changes in the β-function. The β-*beating* due to distributed gradient errors Δk is (proof Appendix A.3):

$$\frac{\Delta\beta_u(s)}{\beta_u(s)} = -\frac{1}{2\sin(2\pi Q_u)} \int_s^{s+C} \beta_u(s_1)\Delta k_u(s_1)\cos\left[2(y_u(s) - y_u(s_1)) - 2\pi Q_u\right]\mathrm{ds}. \quad (2.97)$$

From Eq. (2.97) it can be seen that for stable operation the half integer tune must be avoided.

2.4 Non-linear beam dynamics

2.4.1 Chromaticity

Off-momentum particles are also subjected to a different focusing strength from the quadrupoles, an effect known as *chromaticity*. Chromaticity is equivalent to a gradient error arising from the momentum deviations of the particles. The integrated quadrupole gradient over a length l is equal to:

$$K = \frac{q}{P_0}\int_0^l \frac{\partial B_y}{\partial x}\mathrm{ds}. \quad (2.98)$$

Differentiating Eq. (2.98) yields:

$$\frac{dK}{dP_0} = -\frac{K}{P_0}. \quad (2.99)$$

A small variation of the reference momentum ΔP_0 can be considered as a gradient error with $\Delta K = -K\frac{\Delta P_0}{P_0}$. From Eq. (2.96), the chromaticity is defined as:

$$Q\prime = \frac{\Delta Q}{\Delta P_0/P_0}. \quad (2.100)$$

and the *relative chromaticity*:

$$\xi = \frac{Q\prime}{Q}. \quad (2.101)$$

Therefore, chromaticity is the dependence of the quadrupolar focusing strength on the particle energy and it leads first to a change of the focal length and eventually to the variation of the betatron tunes for off-momentum particles.

The natural chromaticity has a large negative value that leads to a considerable tune shift and its compensation is necessary. This is achieved by installing sextupole magnets in regimes of non-vanishing dispersion. As the sextupole field gradient scales with the transverse offset, off-momentum particles with dispersive trajectories experience a stronger focusing, while the motion of particles with the nominal momentum is unaffected. The dependence of the focusing on the momentum deviation results in the same focal length for all particles and hence, the chromatic aberrations are compensated.

It must be underlined that the description of the dynamics in the linear approximation does not include any chromatic effects since chromaticity is a higher-order effect. In addition, the incorporation of sextupoles to correct chromatic aberrations introduces non-linear fields. Subsequently, the limitations of the linear approximation become evident. To this end, the next section introduces perturbation methods for treating non-linearities.

2.4.2 Canonical Perturbation Theory

The motion of the particles in the normalized phase space is equivalent to a harmonic oscillation, with non-linear effects appearing as perturbations. In the case of non-integrable systems, canonical perturbation theory can be employed in order to treat the perturbative terms in the Hamiltonian that distort the shape of the phase space. Through a canonical transformation to new dynamical variables, the dependence of the Hamiltonian on $\boldsymbol{\phi}$ is removed up to some order, while higher orders of the perturbation are neglected. As the approximation is done to the Hamiltonian and not to the solutions of Hamilton's equations, symplecticity is preserved. The generating function is then used is order to return to the original variables. In the presence of non-linearities, a Hamiltonian in N degrees of freedom can be expressed as:

$$H(\boldsymbol{J},\boldsymbol{\phi};s) = H_0(\boldsymbol{J};s) + \epsilon H_1(\boldsymbol{J},\boldsymbol{\phi};s), \tag{2.102}$$

where s is the independent variable, H_0 is the un-perturbed integrable Hamiltonian, i.e., that does not depend on $\boldsymbol{\phi}$, ϵ is a small parameter and H_1 is a function that represents the perturbation. It must be underlined that H_0 can include higher-order terms of $\boldsymbol{J}$ that represent the tune shift with amplitude. The scope of the perturbation theory is to define a canonical transformation that removes the dependence of the perturbed Hamiltonian on the angle $\boldsymbol{\phi}$ up to first order. By employing a mixed-variable generating function of the second kind that connects the old $\boldsymbol{\phi}$ and new $\tilde{\boldsymbol{J}}$ variables:

$$F_2(\tilde{\boldsymbol{J}},\boldsymbol{\phi};s) = \boldsymbol{\phi}\tilde{\boldsymbol{J}} + \epsilon G(\tilde{\boldsymbol{J}},\boldsymbol{\phi};s), \tag{2.103}$$

where G is a function to be defined. From the rules of the canonical transformation of the second kind (Appendix A.1):

$$\boldsymbol{J} = \frac{\partial F_2}{\partial \boldsymbol{\phi}} = \tilde{\boldsymbol{J}} + \epsilon\frac{\partial G}{\partial \boldsymbol{\phi}}, \tag{2.104}$$

$$\tilde{\boldsymbol{\phi}} = \frac{\partial F_2}{\partial \tilde{\boldsymbol{J}}} = \boldsymbol{\phi} + \epsilon\frac{\partial G}{\partial \tilde{\boldsymbol{J}}}. \tag{2.105}$$

The new Hamiltonian H_2 is:

$$H_2 = H + \frac{\partial F_2}{\partial s} = H + \epsilon\frac{\partial G}{\partial s}. \tag{2.106}$$

Combining Eq. (2.102), (2.104) and (2.106) yields:

$$H_2 = H_0(\tilde{\boldsymbol{J}} + \epsilon\frac{\partial G}{\partial \boldsymbol{\phi}};s) + \epsilon H_1(\tilde{\boldsymbol{J}} + \epsilon\frac{\partial G}{\partial \boldsymbol{\phi}},\boldsymbol{\phi};s) + \epsilon\frac{\partial G}{\partial s}. \tag{2.107}$$

By expanding the Hamiltonian H_0 and H_1 as shown in Appendix A.4 and re-grouping based on the order of ϵ::

$$H_2 = H_0(\tilde{\boldsymbol{J}}) + \epsilon H_3(\tilde{\boldsymbol{J}},\boldsymbol{\phi};s) + \epsilon^2 H_4(\tilde{\boldsymbol{J}},\boldsymbol{\phi};s) + O(\epsilon^3), \tag{2.108}$$

where:
$H_3(\tilde{\boldsymbol{J}};\boldsymbol{\phi}) = \frac{\partial G}{\partial \boldsymbol{\phi}}\frac{\partial H_0(\tilde{\boldsymbol{J}})}{\partial \tilde{\boldsymbol{J}}} + H_1(\tilde{\boldsymbol{J}};\phi;s) + \frac{\partial G}{\partial s}$ and

$H_4(\tilde{\boldsymbol{J}};\boldsymbol{\phi};s) = \frac{1}{2}(\frac{\partial G}{\partial \boldsymbol{\phi}})^2 \frac{\partial^2 H_0(\tilde{\boldsymbol{J}};s)}{\partial^2 \tilde{\boldsymbol{J}}} + \frac{\partial G}{\partial \boldsymbol{\phi}} \frac{\partial H_1(\tilde{\boldsymbol{J}},\phi;s)}{\partial \tilde{\boldsymbol{J}}}$. Selecting a generating function so that $H_3 = 0$, first order perturbation theory leads to:

$$H_2 \approx H_0(\tilde{\boldsymbol{J}}) + O(\epsilon^2). \tag{2.109}$$

By neglecting higher-order terms, the Hamiltonian becomes integrable. Substituting the expression for H_3 in the Hamiltonian, the final expression is:

$$H_2 = H_0(\tilde{\boldsymbol{J}}) + \frac{\partial G}{\partial \boldsymbol{\phi}} \frac{\partial H_0(\tilde{\boldsymbol{J}})}{\partial \tilde{\boldsymbol{J}}} + H_1(\tilde{\boldsymbol{J}};\phi;s) + \frac{\partial G}{\partial s}. \tag{2.110}$$

Imposing a periodic condition for H_1 and G, the Fourier expansion is:

$$H_1(\tilde{\boldsymbol{J}},\boldsymbol{\phi};s) = \sum_{\boldsymbol{m}} \tilde{H}_1(\tilde{\boldsymbol{J}};s)\mathrm{e}^{i\boldsymbol{m}\boldsymbol{\phi}}, \tag{2.111}$$

$$G(\tilde{\boldsymbol{J}},\boldsymbol{\phi};s) = \sum_{\boldsymbol{m}} \tilde{G}(\tilde{\boldsymbol{J}};s)\mathrm{e}^{i\boldsymbol{m}\boldsymbol{\phi}}, \tag{2.112}$$

where $\tilde{H}_1$ and $\tilde{G}$ the Fourier coefficients. Imposing H_3 to be equal to zero and substituting with the Fourier expansion yields:

$$i\boldsymbol{m}\frac{\partial H_0}{\partial \tilde{\boldsymbol{J}}}\tilde{G} + \frac{\partial \tilde{G}}{\partial s} = -\tilde{H}_1. \tag{2.113}$$

The periodic solution that eliminates in the first order the dependence on the angle is equal to:

$$G(\tilde{\boldsymbol{J}},\boldsymbol{\phi};s) = \sum_{\boldsymbol{m}} \frac{i}{2\sin(\pi \boldsymbol{m}\boldsymbol{Q})} \int_s^{s+2\pi} \mathrm{e}^{i\boldsymbol{m}(\boldsymbol{\phi}+\boldsymbol{Q}(s'-s-\pi))}\tilde{H}_1(\tilde{\boldsymbol{J}};s')\mathrm{ds'}. \tag{2.114}$$

As an example, in the presence of a quadrupolar gradient error Δk, the Hamiltonian in one degree of freedom is:

$$H = \frac{J_y}{\beta_y} - \Delta k \frac{y^2}{2}. \tag{2.115}$$

By replacing $y = \sqrt{2J_y\beta_y}\cos\phi_y$:

$$H(J_y,\phi_y;s) = H_0(J_y) + H_1(J_y,\phi_y;s) = \frac{J_y}{\beta_y} - \frac{1}{2}\beta_y J_y \Delta k - \frac{1}{2}\beta_y J_y \Delta k \cos(2\phi_y), \tag{2.116}$$

which will introduce a tune shift:

$$Q_y = Q_0 + \Delta Q_y = \frac{1}{2\pi}\int_s^{s+C_0} \frac{\partial H_0}{\partial J_y}\mathrm{d}s = \frac{1}{2\pi}\int_s^{s+C_0} \frac{\mathrm{ds'}}{\beta_y} - \frac{1}{4\pi}\int_s^{s+C_0} \beta_y \Delta k \mathrm{ds'}. \tag{2.117}$$

Equation (2.117) is equivalent to the tune shift derived in section 2.3.5.

2.4.3 Resonances

The Hamiltonian in Eq. (2.110) can also be expanded as a double Fourier series:

$$H_1(\tilde{\boldsymbol{J}},\boldsymbol{\phi};s) = \sum_{\boldsymbol{m},n} \tilde{H}_{mn}(\tilde{\boldsymbol{J}})\mathrm{e}^{i(\boldsymbol{m}\boldsymbol{\phi}-ns)}, \tag{2.118}$$

where $\tilde{H}_{mn}$ the Fourier coefficients of the n, m modes. In this case, the form of the generating function can be computed from Eq. (2.113):

$$G(\tilde{\boldsymbol{J}}, \boldsymbol{\phi}; s) = i \sum_{\boldsymbol{m},\boldsymbol{n}} \frac{\tilde{H}_{\boldsymbol{mn}}(\tilde{\boldsymbol{J}}) \mathrm{e}^{i(\boldsymbol{m\phi} - ns)}}{\boldsymbol{mQ} - n}. \tag{2.119}$$

The previous result implies that in the vicinity of a *resonance*, where the denominator approaches to zero, the perturbation will have a significant impact on the particle trajectories. At each turn the kick seen by the particles due to the perturbation accumulates, which leads to a large change in the betatron action. The transformation required to eliminate the perturbation is large and the approximate integrals of motion cannot be constructed. In the case of a large perturbation, first order perturbation theory is not sufficient and higher-order terms cannot be neglected as the effect on the particle motion is more pronounced. In this case, all resonances can be potentially excited and the behavior may become chaotic. In two degrees of freedom, the *resonance conditions* is:

$$m_x Q_x + m_y Q_y = n, \tag{2.120}$$

with m_x, m_y, n integers and the order of the resonance equal to $|m_x| + |m_y|$. Lower order resonances are more critical as the amplitude of the corresponding term in the generating function decreases with increasing order, as long as the betatron actions are sufficiently small. For even and odd values of $|m_y|$ the resonances are characterized as *normal* and *skew*, respectively. In the presence of synchrotron motion Q_s and additional modulation sources Q_p, the resonance condition is:

$$m_x Q_x + m_y Q_y + m_s Q_s + m_p Q_p = n, \tag{2.121}$$

with m_x, m_y, m_s, m_p, n integers. Figure 2.5 illustrates the resonance diagram as described in Eq. (2.120) up to the sixth order (left) and in the presence of a tune modulation at $Q_p = 0.053$ (right). The solid and dashed lines represent the normal and the skew resonances, respectively while the red lines represent the resonances which are excited due to the modulation.

In the vicinity of a single resonance in one degree of freedom, the perturbation will be dominated by one term and all the non-resonant terms can be neglected. The Hamiltonian in a ring of circumference C is then expressed as (Appendix A.5):

$$H = H_0(J) + f(J)\cos(m\phi - \frac{2\pi n}{C} s), \tag{2.122}$$

with $f(J) \sim J^{p/2}\beta^{p/2}$, where p is the order of the perturbation as given in Eq. (A.15) , β is the β-function at the location of the perturbation and m, n are integers that define the order of the resonance. In order to eliminate the dependence on the longitudinal position s, a mixed-variable canonical transformation of the second kind is used from variables (ϕ, J) to $(\tilde{\phi}, \tilde{J})$:

$$F_2(\phi, \tilde{J}; s) = \phi\tilde{J} - \frac{2\pi n s}{mC}\tilde{J}. \tag{2.123}$$

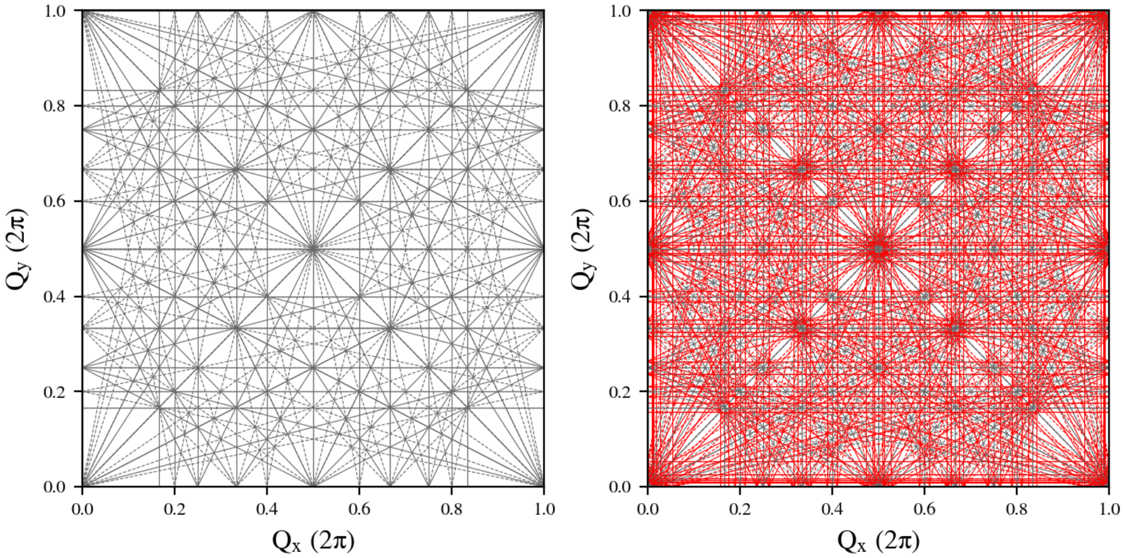

Figure 2.5: The resonance diagram up to the sixth order (left) and in the presence of a tune modulation at $Q_p = 0.053$ (right).

From the rules for the generating function of the second kind (Appendix A.1):

$$J = \frac{\partial F_2}{\partial \phi} = \tilde{J} \quad , \quad \tilde{\phi} = \frac{\partial F_2}{\partial \tilde{J}} = \phi - \frac{2\pi n s}{mC} \tag{2.124}$$

and the new Hamiltonian is:

$$\tilde{H} = H + \frac{\partial F_2}{\partial s} = \delta \tilde{J} + a(\tilde{J}) + f(\tilde{J}) \cos(m\tilde{\phi}), \tag{2.125}$$

where $a(\tilde{J})$ are the higher order of the action in the integrable Hamiltonian H_0 and $\delta = \frac{2\pi}{C}(Q - \frac{n}{m})$. *Fixed points* are defined as the points in the phase space where the dynamical variables are constant:

$$\frac{\partial \tilde{H}}{\partial \tilde{J}} = \frac{d\tilde{\phi}}{\mathrm{ds}} = 0 \quad \text{and} \quad \frac{\partial \tilde{H}}{\partial \tilde{\phi}} = \frac{d\tilde{J}}{\mathrm{ds}} = 0. \tag{2.126}$$

Replacing Eq. (2.125) to Eq. (2.126) yields:

$$\sin(m\tilde{\phi}) = 0 \text{ and } \ \delta + a'(\tilde{J}) + f'(\tilde{J}) \cos m\tilde{\phi} = 0, \tag{2.127}$$

where the prime notation indicates differentiation with respect to the action. Fixed points where the particle motion is elliptical ($\cos m\tilde{\phi} = -1$) or hyperbolic ($\cos m\tilde{\phi} = 1$) are the *stable* and *unstable* fixed points, respectively. The tori that pass through unstable fixed points define the *separatrices*, i.e., the limit of stable motion. Around the stable fixed points, islands of stable motion appear. Particles trapped in an island, will advance from island to island between successive turns. By keeping the lowest-order terms of the amplitude detuning and dropping the symbols of the new variables after the canonical transformation, the Hamiltonian is:

$$H = \delta J + \frac{1}{2}aJ^2 + f(J)\cos m\theta. \tag{2.128}$$

In the vicinity of the island action J_r ($\delta \approx 0$), the Hamiltonian can be expanded around the fixed points with the linear transformation:

$$\phi = \phi_r + \theta \text{ and } J = J_r + I. \tag{2.129}$$

The final one-turn Hamiltonian for an isolated resonance model is found to be [50, 51]:

$$H = \frac{1}{2}aI^2 + f(J_r)\cos m\theta, \tag{2.130}$$

where J_r is the amplitude which yields an oscillation frequency at a resonance. For m turns and substituting $f(J_r)$ with some terms the m-turn Hamiltonian is:

$$H_m = \frac{m}{2}aI^2 + mV_m J_r^{m/2}\cos m\theta. \tag{2.131}$$

The fact that the Hamiltonian is a constant of motion in the island separatrix leads to the following expression for the *island half width*:

$$H^{SFP}(\theta = \pi/m, I = 0) = H^{UFP}(\theta = 0, I = \pm\Delta I), \tag{2.132}$$

$$\Delta I = 2J_r^{m/4}\sqrt{\frac{V_m}{a}}. \tag{2.133}$$

From Eq. (2.130), Hamilton's equations yield:

$$\dot{\theta} = maI \text{ and } \dot{I} = -m^2 V_m J_r^{m/2}\sin m\theta, \tag{2.134}$$

$$\ddot{\theta} + am^3 V_m J_r^{m/2}\sin(m\theta) = \ddot{\theta} + m(2\pi Q_I)^2\sin(m\theta) = 0. \tag{2.135}$$

In the small deviation approximation ($\sin(m\theta) \approx m\theta$), the *island tune* is equal to:

$$Q_I = \frac{m}{2\pi}J_r^{m/4}\sqrt{aV_m}. \tag{2.136}$$

In the previous derivations, the impact of a single resonance is considered. In the presence of multiple resonances, chaotic motion can be observed when the islands originating from the various resonances start to overlap. The *Chirikov overlap criterion* states that stable motion can only be achieved if the island widths are much smaller than the spacing between the resonance bands [52, 53].

Chapter 3

Methods of analysis

Tracking simulations are used to investigate the dynamical behavior of the particles in a lattice with various non-linear fields and errors, where the strong non-linearities cannot be accurately described using the analytical formalism presented in the previous chapter. By post-processing the tracking results, information regarding the stability of the particle trajectories can be extracted. Tracking simulations are particularly important for noise studies as they provide the means to understand and quantify the impact of several types of external noise on the beam dynamics. In this thesis, the LHC and HL-LHC studies, including noise effects, have been conducted using a symplectic 6D tracking code, SixTrack [54].

The following chapter introduces the methods used for the analysis of the tracking results and provides a first finsight on their application to noise studies. The aim of these tools is to extract information concerning important quantities such as the diffusion of the particles, the strength of the resonances and the beam lifetime. To illustrate their application, basic examples have been included in this section, although a detailed review and interpretation of the results is given in the next chapters.

In particular, section 3.1 presents the refined Fourier analysis developed by J. Laskar, which provides an accurate representation of the particles' motion in frequency domain. Based on this algorithm, section 3.2 describes the numerical method that illustrates the diffusion in a storage ring and allows for a better understanding of the mechanisms that cause particle losses. Next, section 3.3 is devoted to the determination of the area of stability through tracking. Finally, the tools developed for tracking distributions with a detailed representation of the tails of the beam distribution are discussed in section 3.4.

3.1 Numerical Analysis of Fundamental Frequencies

The Numerical Analysis of Fundamental Frequencies (NAFF) was originally developed for studies concerning the stability of the solar system from J. Laskar [55–57]. This algorithm can also be applied for investigating the stability of a quasi-periodic motion described by symplectic maps such as the motion of a particle in an accelerator. Specifically, it allows for a very precise determination of the betatron frequency, amplitude and phase with an accuracy that exceeds the capabilities of the Fast Fourier Transform (FFT) and a much faster convergence. An accurate representation of the particle motion in frequency domain can reveal important information concerning the excitation of resonances. This is mainly achieved through the use of a window function and an interpolation. A new implementation of the algorithm has been written in C++ with a Python interface [58].

The NAFF algorithm provides a quasi-periodic approximation of a complex signal $\psi(t)$ over a time interval $[0, T]$. As a first step, the Fast Fourier Transform (FFT) is computed using as an input the transverse position tracking data or measurements. With a simple peak-detection algorithm, a first approximation of the location of the main spectral component f is derived from the Fourier spectrum. Next, the Fourier integral is computed, which is expressed as:

$$\phi(f) = \langle \psi(t)\ ,\ e^{i2\pi f} \rangle = \frac{1}{T} \int_0^T \psi(t)\ e^{-i2\pi f t}\ x(t)\ dt \tag{3.1}$$

where $x(t)$ denotes a window function.

Figure 3.1 illustrates the Fourier integral with a rectangular window ($x(t) = 1$) for two simulated sinusoidal signals that consist of one (red curve) and two frequency components (black curve), respectively. The Fourier transform assumes that the input finite data set includes an integer number of periods in the given window length. If this condition is not satisfied, the endpoints of the signal form discontinuities. The discontinuities of the truncated signal multiplied by the rectangular window lead to the appearance of side-lobes. In the presence of multiple frequencies, the side-lobes cause *spectral leakage*, an effect that eventually leads to the observed frequency and amplitude displacement. Subsequently, an improvement on the determination of the spectral components can be achieved by including

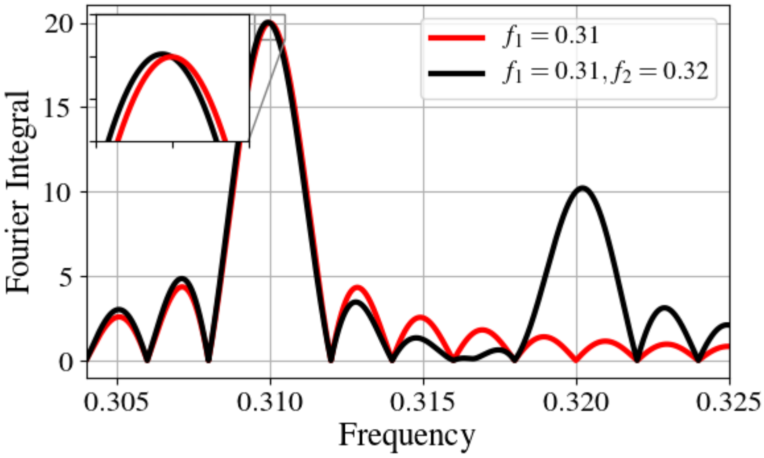

Figure 3.1: The concept of spectral leakage in the Fourier spectrum in the absence of a window function for a sinusoidal signal consisting of one (red) and two (black) frequency components.

a window function [59]. In particular, the window gradually reduces the amplitude of the signal in the edges of the finite time span to minimize the discontinuities thus, suppressing the side-lobes. The NAFF code employs the Hann window, which is defined as:

$$x_h(t) = \frac{2^h (h!)^2 (1+\cos \pi t)^h}{(2h)!} \tag{3.2}$$

where h is the power of the window, allowing to tune the ratio between side-lobe attenuation and main-lobe width. By increasing h the side-lobes are significantly reduced at the expense of a wider main lobe. On the contrary to the accuracy achieved by the FFT that is equal to $1/N$ where N is the window length, the accuracy of the NAFF algorithm scales with $1/N^{2h+2}$. Therefore, in the absence of noise and in the case of well separated frequency components, higher orders of the window lead to a better tune determination. On the contrary, in the presence of white noise or multiple frequency components that are separated by a small number of bins, low order windows should be selected that result in a sharper frequency peak. Figure 3.2 illustrates the convergence tests for various orders of the Hann window in the presence of two spectral peaks (left) and in the presence of white noise in the signal (left) that depicts the beneficial impact of lower order windows in the aforementioned cases.

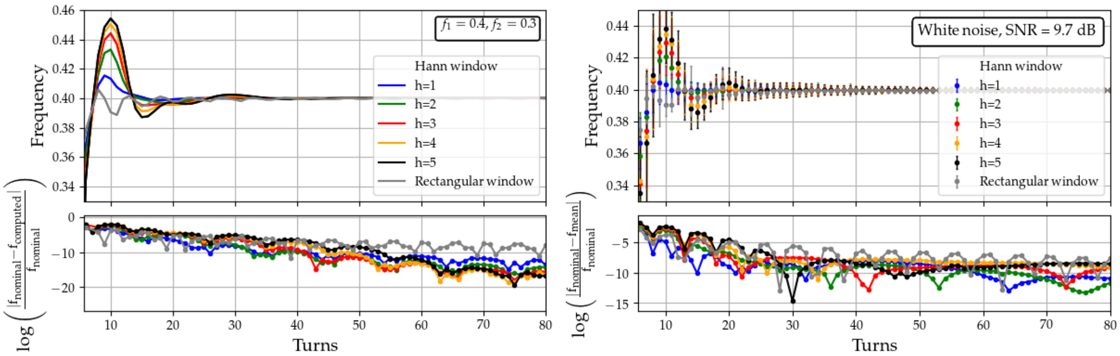

Figure 3.2: The convergence of different orders of the Hann window in the presence of multiple spectral components (left) and white noise (right).

The NAFF algorithm proceeds to the determination of the refined spectral component by maximizing the Fourier integral. For the numerical integration, Hardy's 6-point integration rule is employed. The refined frequency is then subtracted from the signal and the search is iterated for additional spectral components. From the second frequency onward, the new (u_i) and previous (u_j) components must be orthogonalised before the subtraction. In order to construct orthonormal basis functions, the modified Gram-Schmidt method is used:

$$u_i^{\perp} = u_i - \sum_{j=1}^{i-1} \mathrm{proj}_{u_j^{\perp}}(u_i) \tag{3.3}$$

The procedure is repeated until no relevant spectral components are present in the signal. Figure 3.3 depicts the tune determination of a distribution of particles, called *footprint*.

The tune shift in each case is the result of the different chromaticities, while the negative polarity octupoles are responsible for the amplitude detuning.

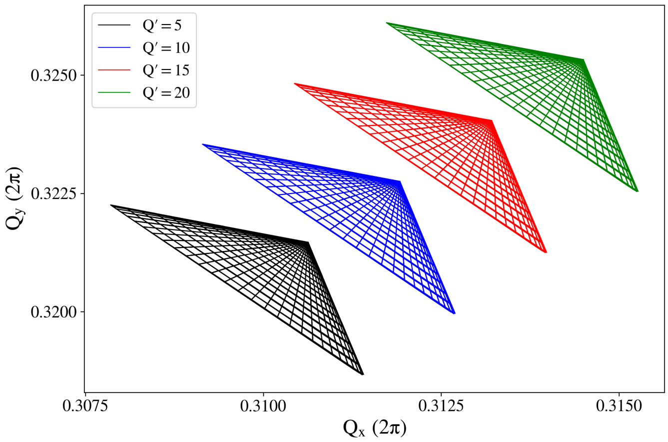

Figure 3.3: The use of the NAFF algorithm for the tune determination of a distribution of particles for a chromaticity equal to 5 (black), 10 (blue), 15 (red), 20 (green).

3.2 Frequency Map Analysis

The Frequency Map Analysis (FMA) is a powerful tool for the analysis of the beam dynamics in the presence of non-linearities [60–66]. Based on the NAFF algorithm, it provides information concerning the diffusion of the particles due the presence of strongly driven resonances in the vicinity of the working point. Such a tool provides an effective way to illustrate the irregular motion by identifying the variation of the tunes in time.

A distribution of particles, that is usually covering a polar grid in the configuration space up to 6 σ, is tracked around the accelerator lattice. Most often, the turn-by-turn position and momenta coordinates are divided into two equal time intervals. The coordinates are then used as an input for the NAFF algorithm and a precise determination of the tune of each particle in both intervals is achieved. The variation of the tunes during these two time spans defines the *diffusion*, which is expressed as:

$$D = \sqrt{(Q_x^1 - Q_x^2)^2 + (Q_y^1 - Q_y^2)^2} \tag{3.4}$$

where Q_u^1, Q_u^2 is the tune of each particle for the first and second interval, respectively, with $u = (x, y)$.

Figure 3.4 illustrates the concept of the FMA in the LHC lattice in the absence of synchrotron motion. Each point represents the tune in frequency domain (left) or the initial position in the configuration space (right) of a single particle. The shape of the footprint is the result of the interplay between several effects. In a linear machine and the absence of errors, the tunes of the on-momentum particles coincide with the working point. On the contrary, in the presence of non-linearities, the tunes depend on the amplitude and the momentum of the particles. In particular, the non-vanishing chromaticity leads to a tune shift from the working point and the presence of non-linear magnets in the lattice such as sextupoles and octupoles causes an action-dependent detuning. Furthermore, beam-beam effects have an important contribution to the tune spread observed, an effect which can be partially mitigated depending on the polarity of the octupoles. Due to the tune spread, some particles encounter strongly driven resonances (gray) and start to diffuse. Assigning a color-code to the logarithm of the diffusion allows to illustrate the areas of stable (blue) and irregular (yellow and red) motion. This allows to identify the dangerous resonances, to understand the mechanisms of beam losses and to determine the best working point for machine operation. Contrary to other tools that require tracking for a long amount of time, FMA is an early indicator of chaotic motion as only a few thousand turns of tracking are needed.

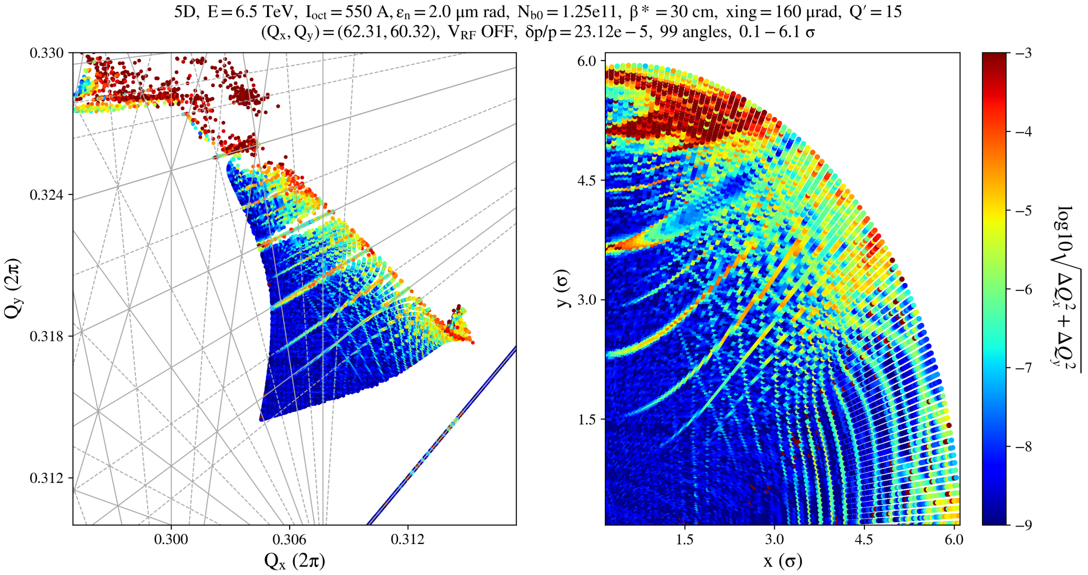

5D, $E = 6.5$ TeV, $I_{oct} = 550$ A, $\epsilon_n = 2.0$ μm rad, $N_{b0} = 1.25e11$, $\beta^* = 30$ cm, xing = 160 μrad, $Q' = 15$
$(Q_x, Q_y) = (62.31, 60.32)$, V_{RF} OFF, $\delta p/p = 23.12e-5$, 99 angles, $0.1 - 6.1\ \sigma$

Figure 3.4: The concept of Frequency Map Analysis for the LHC lattice in 5D.

3.3 Dynamic Aperture

Depending on the strength of the resonances, particles with actions beyond a certain threshold will not remain confined in phase space for an arbitrary amount of time. The limit between bounded and chaotic motion defines the *Dynamic Aperture* (DA). Particles with initial conditions outside the DA will follow unstable trajectories and will eventually be lost. Therefore, the DA defines the phase space volume of the initial conditions were stable motion is observed. To numerically determine the value of DA with SixTrack across several machine configurations, a distribution of particles is tracked, usually for 10^6 turns, that corresponds to approximately 90 s of LHC operation. The DA is then computed through a direct integration [67, 68]. Defining $\chi(x, p_x, y, p_y)$ a function that is equal to zero and one for unbounded and bounded motion, respectively yields in 4D:

$$\int\int\int\int \chi(x, p_x, y, p_y)\ dx\ dp_x\ dy\ dp_y \tag{3.5}$$

where x, y, dx, dy are the initial positions and momenta of the particles in the distribution. For vanishing initial momenta and with polar coordinates the integral is transformed to:

$$\int_0^{\pi/2}\int_0^{\infty} r\ dr\ d\alpha \tag{3.6}$$

where r, α are the radius and angle in the configuration space, respectively. Considering the last angle of stable motion $r(\alpha, N)$ after N turns, the volume of stable motion is equal to:

$$A_{\alpha,N} = \frac{1}{2}\int_0^{\pi/2}[r(\alpha, N)]^2 d\alpha \tag{3.7}$$

For K steps at each angle α, the DA is equal to:

$$r_{\alpha,N} = \left(\frac{1}{K}\sum_{k=1}^{K}[r(\alpha, N)]^2\right)^2 \tag{3.8}$$

Figure 3.5 illustrates an example of DA reduction in the presence of a harmonic dipolar field error in the horizontal plane at the injection configuration of the LHC. Each point corresponds to an independent study with the noise parameters defined from the combination of the amplitude and the frequency of the noise. A color-code is assigned to each study that represents the minimum value of the computed DA. By scanning several combinations of noise kicks and frequencies it is possible to define acceptable limits of noise for operation. The blue regime indicates that particles up to 6 σ survive, while increasing the amplitude of the noise and depending on the excitation frequency, a reduction of the DA is observed in the presence of noise.

The reduction of DA is translated into a degradation of the beam lifetime. For a Gaussian beam distribution the evolution of the beam intensity as a function of the DA is expressed as [69]:

$$\frac{I(N)}{I_0} = 1 - e^{-D^2(N)/2} \tag{3.9}$$

where N is the number of turns, D is the DA and I_0 represents the initial intensity. Equation 3.9 implies that there is a logarithmic scaling between DA and beam lifetime. Usually, optimizations are needed to reach a minimum target of 5 σ DA that has been shown to correspond experimentally to a burn-off corrected lifetime of around 100 h [70]. To this end, there are several modifications in the machine configuration that can contribute to the increase of DA such as tune optimization so that the beam distribution is less affected by resonances.

3.4 Weighted distributions

Quantifying the impact of non-linearities in terms of losses and emittance growth requires the tracking of 6D matched Gaussian distributions. In particular, if impacted by

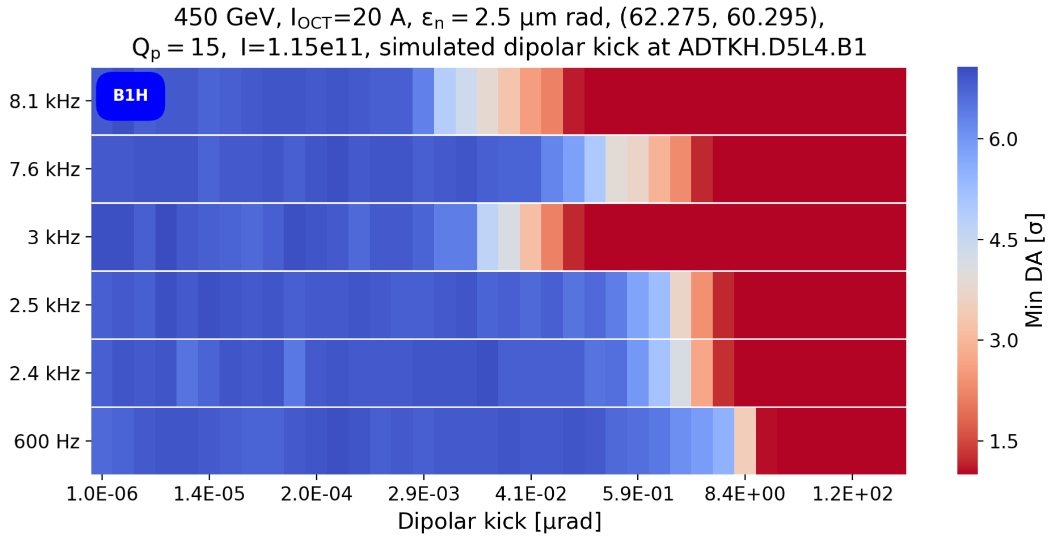

Figure 3.5: The minimum dynamic aperture for various dipolar excitation frequencies as a function of the amplitude of the noise in the horizontal plane at injection for LHC.

a resonance, particles at the tails of the distribution close to the limit of DA diffuse and will eventually be lost. Therefore, for the aforementioned studies a detailed representation of the tails of the distribution is needed. To achieve this goal, weighted distributions are employed. The initial distribution of particles is selected so that it forms a 4D round and uniform distribution up to 6 σ in the transverse plane, while the particles extend up to the limit of the RF bucket in the longitudinal plane. Then, during the post-processing of the data, weights are assigned to each particle according to their initial position in the configuration space. The weights are based on the probability density function of the simulated distribution as:

$$w_i = \prod_{j=1}^{6} \mathrm{pdf}(u_j) \tag{3.10}$$

where u are the normalized particles' coordinates in the 6D phase-space. For a Gaussian distribution with a standard deviation σ:

$$\mathrm{pdf}(u_j) = \frac{1}{\sqrt{2\pi\sigma^2}} e^{-\frac{u_j^2}{2\sigma^2}} \tag{3.11}$$

An additional step is that each weight must be normalized to the sum of the weights of all the particles. Based on the probability density function, particles which are at the core of the distribution will be assigned a larger weight than the ones at the tails and therefore, will have a more important contribution in the computations for emittance and losses. On the contrary to a simple Gaussian, the distribution contains an important number of particles at the tails with a small weight value and thus, a statistically significant representation of the tails can be achieved. In addition, as the weights are assigned during the post-processing, they can be modified accordingly to simulate different types of distributions, without the need to repeat the simulation. Furthermore, a mechanical aperture is defined at 5.5 $\sigma_{\text{collim.}}$ to simulate the collimators and particles with actions beyond this threshold are considered lost.

Figure 3.6 illustrates a typical study with weighted distributions in the presence of a tune modulation for the LHC configuration of 2017. Figure 3.6a shows the impact of an increasing modulation amplitude on the beam intensity and lifetime. For the computation of the lifetime an exponential fit is applied. The losses as a function of the modulation frequency are depicted in Fig. 3.6b and through this method the most dangerous frequencies can be identified. Finally, Fig. 3.6c depicts the horizontal emittance growth as a result of the excitation in a frequency close to the betatron tune.

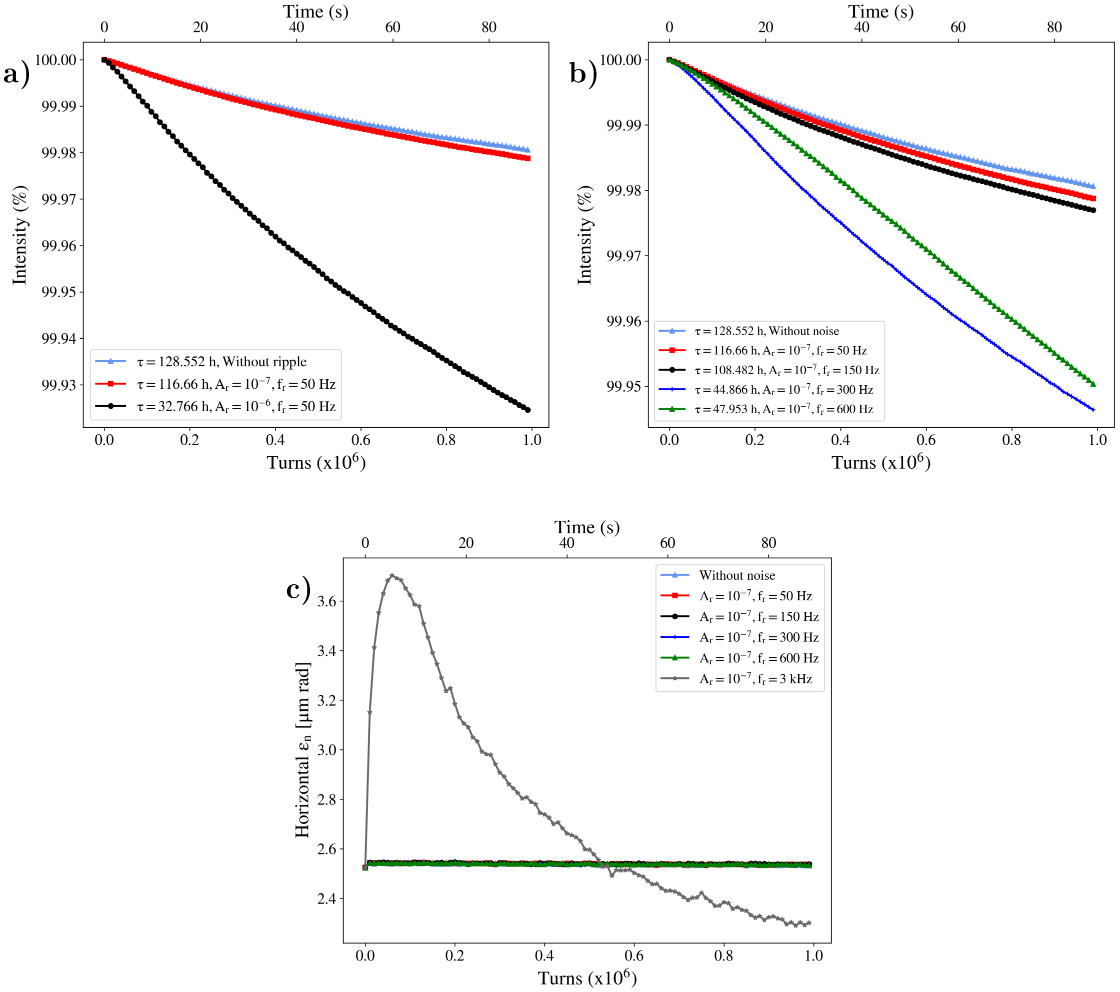

Figure 3.6: A tracking example that illustrates the use of weighted distributions in the presence of a tune modulation in the LHC configuration of 2017. The impact of the modulation depth (a) and frequency (b) are depicted, along with the emittance growth (c) in the horizontal plane for an excitation close in the vicinity of the betatron tune.

Chapter 4

50 Hz harmonics on the LHC beam spectrum

4.1 Introduction

In particle accelerators, studies of the beam spectrum can reveal important information concerning the existence of external noise sources that perturb the motion of the particles. Noise effects are an important issue for the single-particle beam dynamics in present and future accelerators. In the presence of non-linearities, depending on the spectral components and the nature of the source, noise can act as a diffusion mechanism for the particles in the beam distribution, through the excitation of additional resonances, an effect that can prove detrimental to the beam lifetime. This chapter focuses on the investigation of such a noise mechanism that has been observed in the beam spectrum of the LHC, which is contaminated by harmonics of 50 Hz [71–74].

Observations of harmonics of the mains power frequency in the beam spectrum with a dipolar nature have been reported in the past from several accelerators such as the Relativistic Heavy Ion Collider (RHIC) at Brookhaven National Laboratory (BNL) [75, 76], the Tevatron in Fermi National Accelerator Laboratory (FNAL) [31, 32] and SPS at CERN [28, 77]. In particular, the study conducted at RHIC demonstrated that high order harmonics (h>100) were visible in several unrelated instruments, as a result of a real beam excitation, rather than an artifact of the instrumentation system. To explore the origin of the perturbation, machine parameters such as the betatron tune and the coupling were modified and the source was identified as a dipolar field error. Through a set of experiments, a correlation with power converter noise was established and specifically, with the 12-phase main dipole power supply. During these tests, the phases of the 12-phase main dipole supply were modified, which led to distinct changes in the amplitude evolution of the lines. Studies in the SPS also excluded the factor of instrumentation noise and, by computing the phase evolution of the noise lines between two consecutive bunches, it was shown that the beam was excited by high order harmonics, mainly affecting the horizontal plane. It was proven that one source of the perturbation was the main dipoles, by injecting an external sinusoidal ripple on their power supply.

A similar mechanism of 50 Hz high order harmonics that perturb the beam spectrum is present in the LHC. Similarly to the aforementioned studies, the difficulty of the subject resides first, in proving that the noise lines originate from the beam, rather than spuriously entering the beam path and second, in establishing a correlation with the origin of the perturbation. First, an analytical formalism of the beam motion in the presence of a modulated dipolar field error is demonstrated (Section 4.2). Second, the methodology for the analysis of the bunch-by-bunch positions measurements that are acquired experimentally is depicted (Section 4.3). In the framework of this investigation, a thorough analysis of observations and dedicated experiments were conducted during the 2018 proton run. Based on the findings, the key observations that lead to the understanding that the harmonics are the result of a real beam excitation are presented in Section 4.4. A potential correlation with noise arising from the power converters of the Main Bends is investigated through parasitic observations and dedicated experiments. Furthermore, the impact of controlled dipolar excitations on the beam lifetime, conducted with the transverse damper, is described in Section 4.5, which provides a tool for the validation of the DA simulations in the presence of noise. The impact of the harmonics on the beam performance in terms of diffusion, DA and lifetime is discussed in the last section (Sec. 4.6), using on a lumped noise model and a realistic noise spectrum. The LHC spectrum is then used to make projections for the HL-LHC.

4.2 Analytical formalism of a modulated dipolar field error

In a circular accelerator, the kick related to a modulated dipolar field error Θ_p with a deflection θ_p and a frequency of Q_p oscillations per turn can be represented as:

$$\bar{P}_n = \begin{pmatrix} 0 \\ \Theta_p(n) \end{pmatrix} = \begin{pmatrix} 0 \\ \theta_p \cos\left(2\pi Q_p n\right) \end{pmatrix}, \tag{4.1}$$

where n is the turn considered. In the linear approximation, i.e., for a deflection much smaller than the beam size, considering only the horizontal motion in the normalized phase space and assuming that the noise source and the observation point are situated in the same location, the position of a given particle can be expressed as:

$$\bar{X}_N = \begin{pmatrix} \bar{x}_N \\ \bar{x}'_N \end{pmatrix} = \sum_{n=-\infty}^{N} M^{N-n} \bar{P}_n, \tag{4.2}$$

where $\bar{X}_N$ is the vector representation of the position and momentum at turn N and M is the linear rotation with:

$$M^N = \begin{pmatrix} \cos(2\pi QN) & \sin(2\pi QN) \\ -\sin(2\pi QN) & \cos(2\pi QN) \end{pmatrix}, \tag{4.3}$$

where Q is the machine betatron tune. Combining Eq. (4.1), (4.2) and (4.3) and assuming that the perturbation is present from $N \to -\infty$, it yields:

$$\begin{cases} \bar{x}_N = \sum_{n=-\infty}^{N} \Theta_p(n) \sin\left(2(N-n)\pi Q\right) \\ \bar{x}'_N = \sum_{n=-\infty}^{N} \Theta_p(n) \cos\left(2(N-n)\pi Q\right). \end{cases} \tag{4.4}$$

Combining Eq. (4.1) and (4.4) and computing the convergence of the series, the closed form expression of the offset induced by the modulated dipolar kick is:

$$\bar{x}_N = \frac{\theta_p \cos\left(2\pi N Q_p\right) \sin\left(2\pi Q\right)}{2\left(\cos\left(2\pi Q_p\right) - \cos(2\pi Q)\right)}. \tag{4.5}$$

In physical coordinates, the maximum offset observed at the position s is equal to:

$$|x_{max,N}(s)| = \left| \frac{\sqrt{\beta(s)\beta_p}\ \theta_p \sin\left(2\pi Q\right)}{2\left(\cos\left(2\pi Q_p\right) - \cos(2\pi Q)\right)} \right|, \tag{4.6}$$

where β_p is the β-function at the position of the perturbation. A comparison between the results of simulations and Eq. (4.6) is performed as a sanity check. A single particle is tracked in the LHC lattice, in the presence of a dipolar modulation. The amplitude of the kick is 1 nrad and the frequency varies across the studies. The offset is computed from the particle's spectrum for each study and is then compared to the analytical formula. Figure 4.1 illustrates the offset as a function of the frequency computed analytically (black) and from simulations (blue) and a very good agreement is found between the two. For a constant excitation amplitude, a resonant behavior is expected as the frequency approaches to $k \cdot f_{rev} \pm f_x$, where k is an integer.

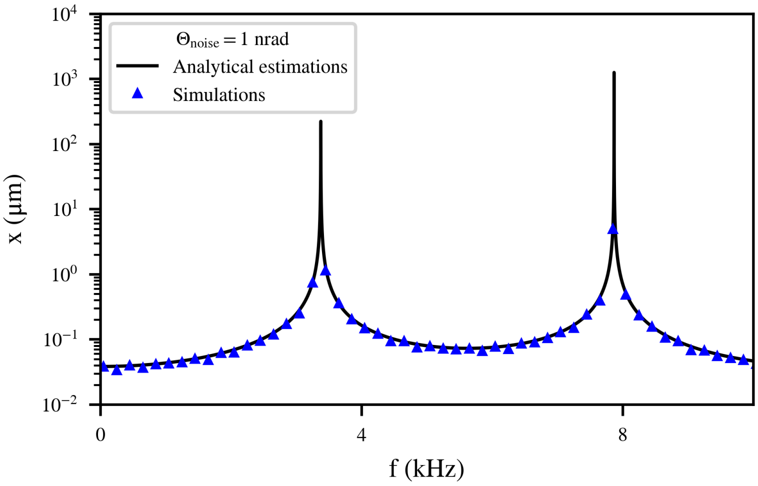

Figure 4.1: The offset as a function of the dipolar excitation frequency with $\theta = 1$ nrad as computed from the closed form (black) and from simulations (blue).

4.3 Beam spectrum from bunch-by-bunch acquisitions

In the presence of a regular filling scheme, the bunch-by-bunch and turn-by-turn position measurements from the transverse damper Observation Box (ADTObsBox) [78–80] can be combined to increase the effective bandwidth of the instrument. Signal averaging is not only needed to access the high-frequency components of the signal without aliasing, but also to reduce the noise floor of the spectrum compared to the single bunch case. In particular, averaging the signals of N_b bunches yields a $\sqrt{N_b}$ increase in the signal to noise ratio, in the presence of random noise with zero mean that is uncorrelated with the signal [81].

The spectrum of individual bunches and after averaging over all the bunches in the machine is shown in Fig. 4.2 for the horizontal plane of Beam 1, for a physics fill and a window length of $4 \cdot 10^4$ turns. The colored lines show the envelope of the spectra of several individual bunches, which is computed by setting a parametric peak threshold of $2 \cdot 10^{-3}$ σ. The single bunch noise floor is several orders of magnitude higher than the 50 Hz harmonics and thus, signal averaging is necessary.

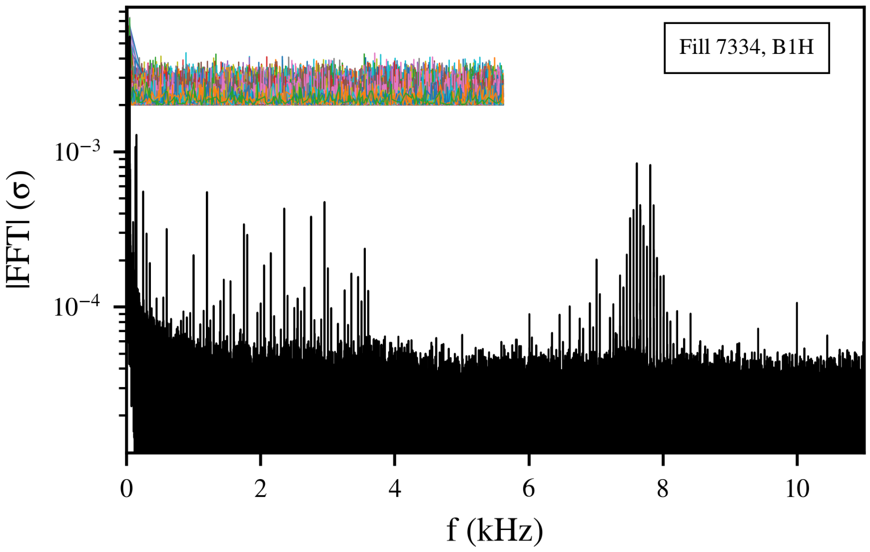

Figure 4.2: The spectral envelope of several individual bunches (colored lines) and the spectrum after averaging over all the bunches in the machine (black).

The time delay Δt_i of a trailing bunch i with respect to the first bunch in the machine, considered as the reference, results in a phase angle $\Delta\phi_i = 2\pi f \Delta t_i$, where f is the frequency under consideration. Consequently, the dephasing of the signals across the ring is proportional to the frequency and the longitudinal spacing of the bunches in the machine. To illustrate this effect, three trains of 48 bunches are considered in simulations with a dipolar excitation at 3 kHz. The bunch spacing is 25 ns and the trains are equally spaced in the LHC ring. The complex spectrum is computed for each bunch and the phase evolution of the 3 kHz line is extracted. Figure 4.3 depicts the phase evolution of the excitation for the three trains as a function of the bunch position in the ring. The color code represents the bunch number and the gray line is the expected phase evolution. The linear phase evolution of an excitation across the trains in the machine has been experimentally verified by injecting noise with the transverse damper kicker (see Section 4.5.1).

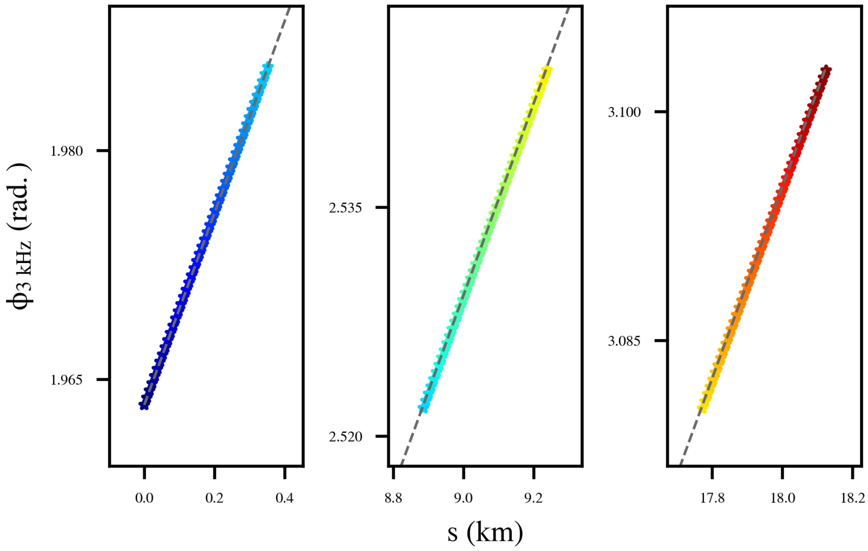

Figure 4.3: Phase evolution of the excitation at 3 kHz as a function of the bunch position for three trains of 48 bunches in the LHC ring. The dashed gray line represents the expected dephasing.

For frequencies much lower than the sampling frequency ($f \ll f_{\text{rev}}$), the dephasing is negligible and the bunch-by-bunch data can be directly averaged in time domain. For frequencies comparable to the revolution frequency, such as the high-frequency cluster, the dephasing between the bunches cannot be neglected. In this case, simply averaging the bunch-by-bunch information will lead to an error in the resulting metric. To illustrate this effect, the first bunches of the three trains are selected. Figure 4.4 illustrates the spectra for the first bunches (Fig. 4.4a) of the first (black), second (blue) and third (green) train, respectively, in the presence of a dipolar excitation at 3 kHz. The excitation results in an offset of 13.9 μm (red dashed line), while the second peak corresponds to the betatron tune. Then, the complex Fourier coefficients at 3 kHz are computed. Figure 4.4b presents the phase of the excitation for each bunch (left). For a filling scheme consisting of three trains located in azimuthally symmetric locations in the ring, the dephasing at 3 kHz is important. Averaging over the three vectors without correcting for the dephasing will lead to an error in the offset of the final spectrum. To this end, an algorithm that applies a phase correction has been implemented. The steps of the method are the following: first, the complex spectra $F_i(\omega)$ are computed for each bunch, where $\omega = 2\pi f$. Then, a rotation is applied which is proportional to the time delay Δt_i and the frequencies f of the spectrum.

The impact of the rotation is depicted in the second plot of Fig. 4.4b. Finally, the average over all bunches is computed. The procedure is described by the following expression:

$$F(\omega) = \frac{1}{N_b} \sum_{i=1}^{N_b} F_i(\omega) \mathrm{e}^{-j\omega\Delta t_i}. \tag{4.7}$$

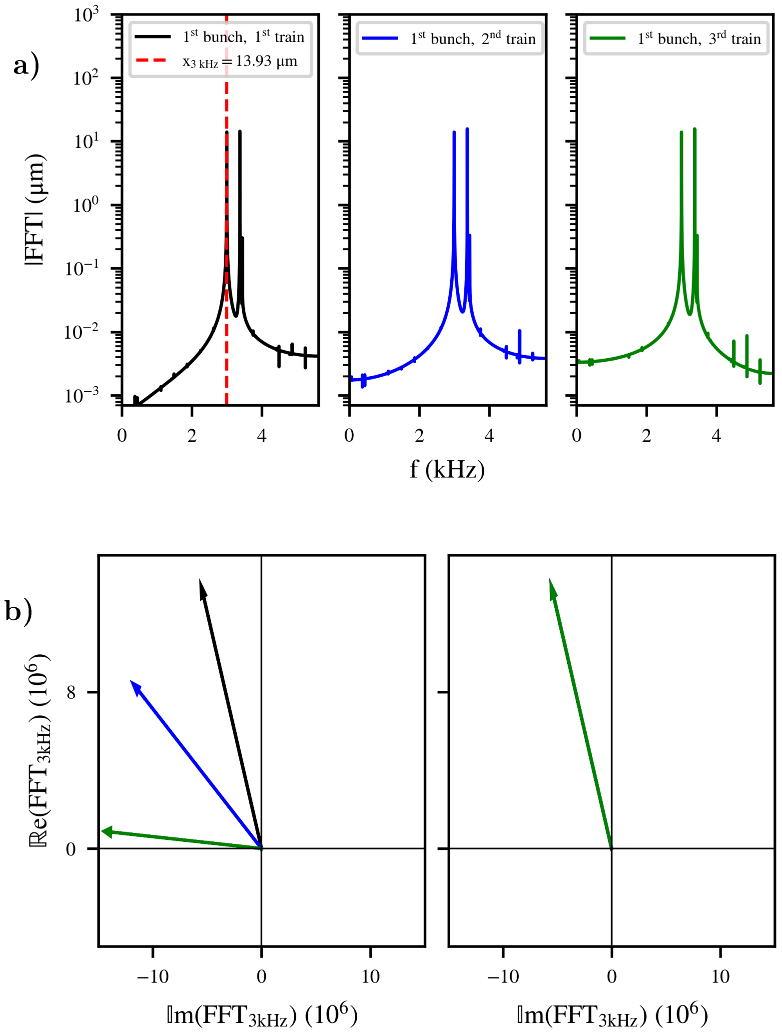

Figure 4.4: (a) Spectrum of the first bunches of the first (black), second (blue) and third (green) train in the presence of a dipolar excitation at 3 kHz (red dashed line). (b) Phase of the excitation for the three bunches before (left) and after (right) the correction.

4.4 Experimental observations

Throughout this study, the main observable is the representation of the beam signal in frequency domain as computed with the Fast Fourier Transform (FFT). Based on the Fourier analysis, information concerning the origin of the 50 Hz can be extracted. This can be achieved by following the evolution of the lines in frequency domain, both in terms of amplitude and phase, during normal operation, i.e., without any modification in the beam or machine parameters (Sections 4.4.1 to 4.4.5). In this context, general observations acquired from various instruments are presented, providing a first insight on the subject under study. The need for high bandwidth measurements is explained, the distinct signature of the harmonics in frequency domain is illustrated and definitive proof of the noise coupling to the betatron motion is presented. Then, the findings are further extended by observing the response of the harmonics during modifications in the beam or machine configuration. These modifications refer to changes, first, in the betatron motion with parameters such as the tune (Section 4.4.6), the phase advance (Section 4.4.7) and the beam energy (Section 4.4.8), second, in the power converters (Section 4.4.9) and last, in the settings of the transverse damper (Sections 4.4.10, 4.4.11).

4.4.1 End of Stable Beams

The first step is to illustrate the concept of the 50 Hz lines on the beam spectrum. To this end, the turn-by-turn data from the High Sensitivity Base-Band measurement system (HS BBQ) [82, 83] (stored in the CERN Accelerator Logging Service, CALS [84, 85]) are extracted. For instance, Fig. 4.5 depicts the spectrogram of the horizontal plane of Beam 1 (Fill 7056) for the last few minutes of the fill, extending up to the first few minutes of the beam dump (red dashed line). The Fourier analysis for each time interval in the horizontal axis is performed with a window length of 8192 consecutive turns and an overlap of 2048 turns between windows. The frequency range is zoomed close to the Beam 1 horizontal tune (≈3.49 kHz) to observe the 50 Hz harmonics in its proximity. A color code is assigned to the Power Spectral Density (PSD) to distinguish the main spectral components (yellow and red) from the noise baseline (blue).

The spectrum clearly shows that a sum of 50 Hz harmonics is present in the beam signal. The fact that the lines appear as multiples of 50 Hz and not as sidebands around the betatron tune indicates that the nature of the noise is dipolar. This conclusion will become more evident in the next sections of this chapter (see Section 4.4.6), where the behavior of the lines is studied during the trim of the betatron tunes at Flat Top. Furthermore, the harmonics are visible only in the presence of the beam. All signals acquired after the end of the fill are dominated by the noise of the instrument. A comparison between the signals prior and after the dump of the beam provides a first indication that the lines do not emerge as a result of instrumentation noise. To further support this hypothesis, the existence of the harmonics in the beam signal is also demonstrated in the next section with acquisitions from different unrelated beam instruments.

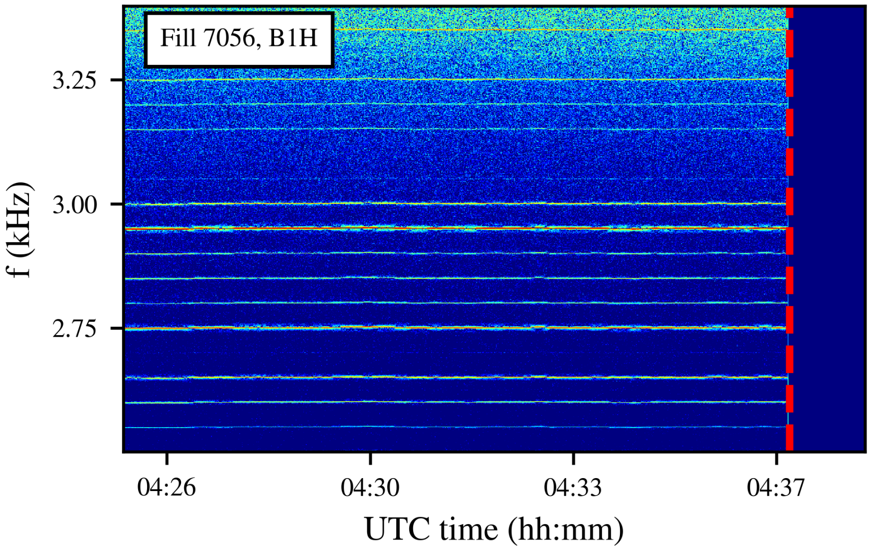

Figure 4.5: Horizontal HS BBQ spectrogram of Beam 1 at the end of a physics fill (Fill 7056), centered around the 3 kHz frequency. The red dashed line indicates the end of the fill and the start of the dump of the beam.

4.4.2 Spectra from multiple instruments

In an attempt to further exclude the factor of instrumental or environmental noise, the presence of these harmonics has been validated from different beam instruments. In this context, position measurements from multiple pickups, located in different positions in the LHC ring, are collected. The main observables are the HS BBQ, ADTObsBox, the Diode Orbit and Oscillation System (DOROS) [86, 87] and the Multi-Band Instability Monitor (MIM) [88, 89]. Measurements from all the aforementioned instruments are available for the Machine Development (MD) Fill 7343, dedicated to studies concerning the 50 Hz harmonics. Figure 4.6 shows the spectra for the HS BBQ (Fig. 4.6a), the ADTObsBox (Fig. 4.6b), the MIM (Fig. 4.6c) and the DOROS (Fig. 4.6d) for the horizontal plane of Beam 1, while the vertical gray lines represent the multiples of 50 Hz. As a reference, the sampling frequency and the number of turns $(\mathrm{f_s}, \mathrm{N})$ considered for each spectrum is $(\mathrm{f_{rev}},\ 9000)$, $(3 \cdot \mathrm{f_{rev}},\ 65536)$, $(16 \cdot \mathrm{f_{rev}},\ 65536)$, $(\mathrm{f_{rev}},\ 16384)$, respectively, where $\mathrm{f_{rev}} =$ 11.245 kHz.

From the review of the spectra, it is confirmed that this effect is visible across several unrelated instruments. It should be mentioned that the sampling rate, the window length, the noise floor and the frequency response of each pickup is different, which justifies the observed discrepancies between the spectra in terms of resolution. For a consistent comparison of the acquisitions, the frequency range is limited to approximately 5.6 kHz, which is the Nyquist frequency of the turn-by-turn acquisitions, assuming a single observation point across the machine $(\mathrm{f_s} = \mathrm{f_{rev}})$ [90]. Additional information concerning the high sampling rate measurements retrieved from the ADTObsBox and MIM are given in the next sections.

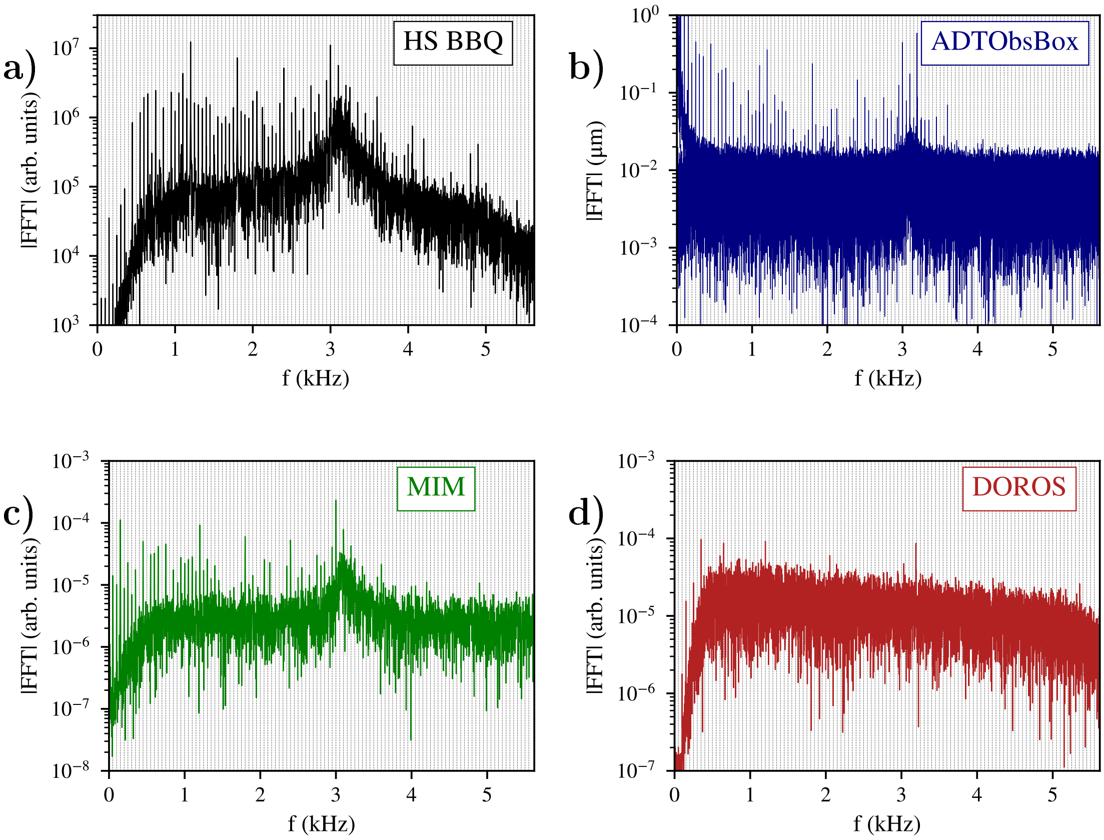

Figure 4.6: The horizontal spectrum of Beam 1 at injection energy during the MD Fill 7343 from the (a) HS BBQ, (b) ADTObsBox, (c) MIM and (d) DOROS. The vertical gray lines represent the multiples of 50 Hz.

4.4.3 Spectrum at Stable Beams

For this study, it is of interest to investigate the range of 50 Hz harmonics visible in the beam signal. As mentioned in the previous section, the turn-by-turn acquisitions, such as the ones from the HS BBQ and DOROS, allow accessing a frequency regime up to 5.6 kHz. If present in the signal, frequency components beyond this limit will be aliased in the spectrum.

On the contrary, the ADTObsBox and the MIM provide high sampling rate measurements. Specifically, the ADTObsBox instability buffer contains calibrated bunch-by-bunch position measurements for 65536 turns. Firstly, the fact that a calibrated metric is provided allows computing the offsets induced on the beam motion from the 50 Hz harmonics, which is particularly relevant for the next sections of this chapter. Secondly, the bunch-by-bunch information is needed to study the evolution of the 50 Hz in the cycle and to compute a high bandwidth spectrum, in the presence of a regular filling scheme. As shown in Section 4.3, the noise floor of the single bunch ADTObsBox spectrum exceeds the amplitude of the 50 Hz harmonics and therefore, a decrease of the noise baseline is necessary to study their evolution. To overcome this problem, a method to combine the information from several bunches has been developed, taking into account the dephasing of the spectrum (due to the time delay) across the different bunches (Section 4.3). Assuming a regular filling scheme (equal spacing between bunches), this signal averaging algorithm not only provides a reduction of the noise floor but also extends the measurable frequency range of the beam spectrum, while suppressing the aliases and preserving the signal metric. For all the reasons stated above, the ADTObsBox is the main observable in the next sections. As far as these studies are concerned, the main limitation of this instrument is that regular acquisitions were not available in the last LHC physics run. In particular cases where both consecutive acquisitions and a high bandwidth are required, the MIM measurements are used, at the expense of non-calibrated offsets. The sampling rate of the MIM is equal to 16 observations per revolution period and consecutive measurements are available for a limited number of fills in 2018.

The horizontal spectrum of Beam 2 is computed for the physics Fill 7334 during collisions, using the bunch-by-bunch and turn-by-turn acquisitions from the Q7 pickup of the ADTObsBox. Figure 4.7 illustrates the Fourier analysis, first, for a frequency range up to 10 kHz (Fig. 4.7a). From the review of the spectrum, two areas of particular interest are identified. The first regime (blue span) consists of 50 Hz harmonics extending up to 3.6 kHz. The second area (orange span) is a cluster of 50 Hz at 7-8 kHz. In particular, as will be described in Section 4.4.6, the cluster is centered at the frequency $\mathrm{f_{rev}} - \mathrm{f_x}$, where $\mathrm{f_x}$ is the horizontal betatron frequency (≈3.15 kHz at injection, ≈3.49 kHz at collision). In the frequency interval between the two clusters, either no harmonics are present in the signal or their amplitude is below the noise threshold of the instrument. Throughout this chapter, the two regimes of interest are referred to as the low and high-frequency cluster, respectively. It must be noted that the lowest order harmonics are excluded from the analysis as their amplitude is affected by the noise of the instrument. Then, the calibrated spectrum indicates that the harmonics of the high-frequency cluster are more important in terms of amplitude.

As the high-frequency cluster is situated at $\mathrm{f_{rev}} - \mathrm{f_x}$, the question that naturally arises is whether these frequency components emerge from aliasing. In fact, even in the case of a physics fill, the sampling rate is only approximately uniform as not all trains are equally spaced. This error can give rise to the aliasing of the low-frequency cluster around the revolution frequency. It must be noted however, that the beam revolution frequency is not a multiple of 50 Hz and therefore, the aliases can be distinguished from the excitations at 50 Hz. Figure 4.7b presents the spectrum centered around the high-frequency cluster. The red dashed lines represent the expected position of aliased 50 Hz harmonics ($\mathrm{f_{rev}} - \mathrm{f_{50}}$, where $\mathrm{f_{50}}$ are the harmonics of the low-frequency cluster), while the gray dashed lines illustrate the multiples of 50 Hz ($\mathrm{n} \cdot \mathrm{f_{50}}$, where n is a positive integer). As the spectral components of the high-frequency cluster coincide with the 50 Hz multiples, it is concluded that they are not aliased frequencies. It must be noted however, that the harmonics are not constantly exact multiples of 50 Hz due to the fact that their frequency evolution is affected by the stability of the 50 Hz mains of the electrical network as shown in the next section.

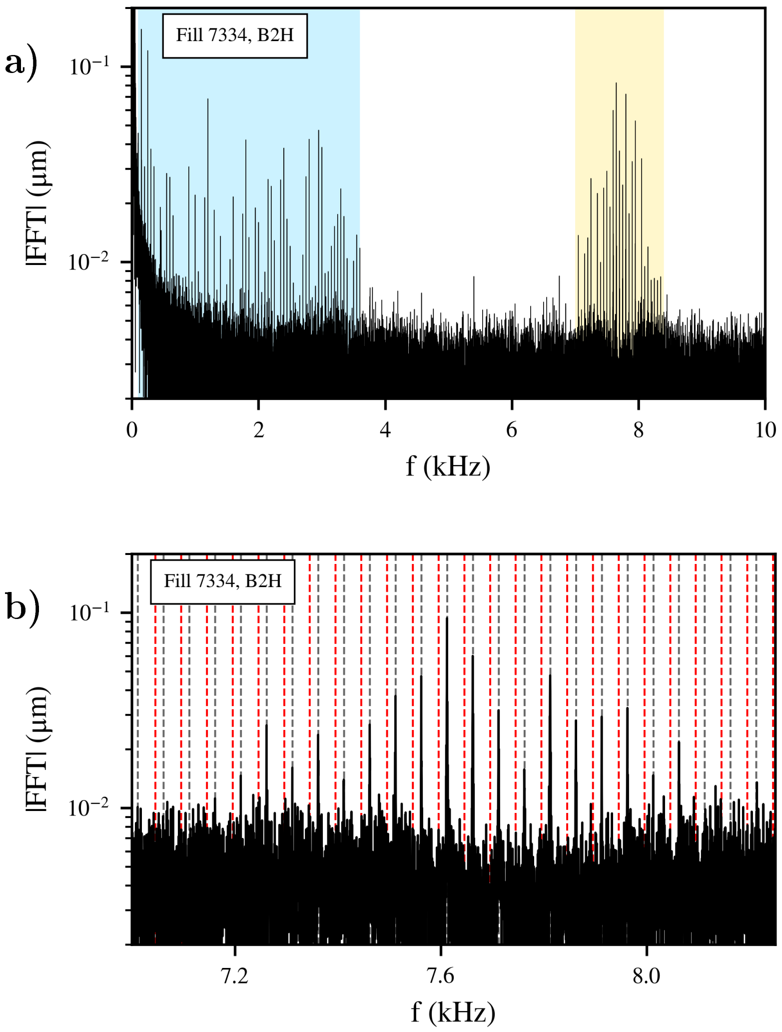

Figure 4.7: The horizontal spectrum of Beam 2 at top energy for a frequency range up to 10 kHz (a), with the low and high-frequency cluster indicated by the blue and orange span, respectively, and centered around the high-frequency cluster (b). The red and gray dashed lines represent the expected position of aliased and physical 50 Hz harmonics, respectively.

4.4.4 Frequency modulation of the harmonics

The time variation of the beam spectrum can reveal important information concerning the source of the perturbation. Due to the variation of the power grid load, the frequency of the mains power supply is not strictly 50 Hz. The following section is dedicated to the impact of the aforementioned drift on the frequency evolution of the 50 Hz harmonics in order to illustrate their distinct signature in the frequency domain. As stated in the previous section, consecutive measurements are required for a detailed representation of the spectrograms and thus, the analysis is based on the MIM and the HS BBQ acquisitions.

The spectrogram of the horizontal position of Beam 1 is computed from the MIM data for a time interval at Stable Beams in the physics Fill 7256. In Fig. 4.8, the horizontal axis represents the timestamp of each spectrum with a window length of 16384 turns, the vertical axis is centered around a value in the low (left panel) and high (right panel) frequency cluster and a color code is assigned to the PSD. An important finding is that, although the lines are harmonics of 50 Hz, a time variation of their frequency is observed. Specifically, all harmonics are affected by a similar frequency modulation, the amplitude of which is proportional to the order of the harmonic. For this reason, the aforementioned effect is more pronounced in the harmonics of the high-frequency cluster, an observation which provides yet another indication that these components are not aliases.

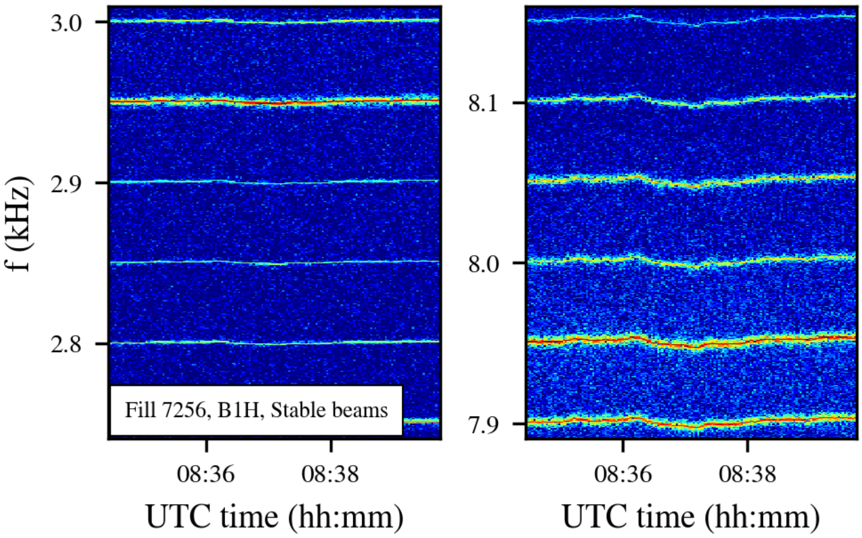

Figure 4.8: The horizontal spectrogram of Beam 1 in a regime of the low (left panel) and high (right panel) frequency cluster.

To illustrate quantitatively that the harmonics experience a similar frequency modulation, the amplitude of which scales with the order of the harmonic, an algorithm that can precisely follow their evolution has been implemented. The steps of the algorithm are the following: for each measured time interval the amplitude of the Fourier spectrum is computed. The algorithm focuses on a regime in the vicinity of a single harmonic and, by employing a maximization routine, an accurate determination of its frequency is achieved by detecting the local maximum. The algorithm returns the frequency and the amplitude of the harmonic at each time step. This procedure is repeated for all the time intervals in the spectrogram. An example of the routine's result is depicted in Fig. 4.9. The spectrogram is centered around the 2.95 kHz line and the black line represents the frequency determination from the aforementioned method. The agreement between the results of the algorithm and the spectrogram proves that the frequency evolution of the harmonic is very well determined.

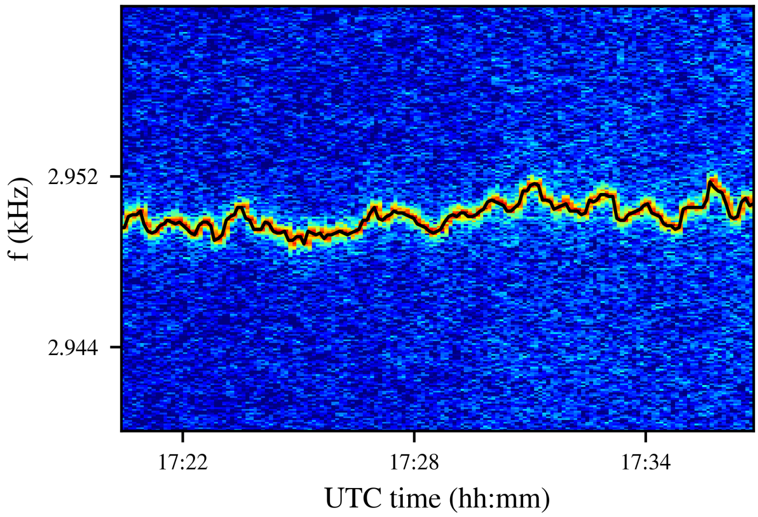

Figure 4.9: The horizontal spectrogram of Beam 1 centered around 2.95 kHz and the frequency evolution of the harmonic (black curve) as computed from the maximization algorithm.

Iterating over all the harmonics in the spectrum with the aforementioned algorithm validates the existence of a similar frequency modulation with an amplitude proportional to the order of the harmonic. Figure 4.10 shows the frequency evolution of all the harmonics (black) after individually subtracting the mean value, normalizing with the order of the harmonic and projecting to the fundamental frequency (50 Hz). The modulation of the fundamental frequency and its low order harmonics cannot be directly extracted from the beam spectrum without a more refined analysis due to the limited resolution and hence, these components have been excluded. The modulation is visible in both beams and planes, during all beams modes and across several unrelated instruments. The proportional relationship between the modulation amplitude and the harmonic order, observed both in the low and high-frequency cluster, suggests that they emerge from a common source (see Section B.1).

The origin of the modulation is clearly related to the stability of the 50 Hz mains from the electrical network, which then propagates to all the harmonics. This is validated by comparing the signals from various uncorrelated signals. First, signals from the eight independent Direct Current Current Transducers (DCCTs) of the main dipole power converters are collected [91, 92]. The DCCTs measure the converter output current with a sampling rate of 1 kHz. The sum of 50 Hz harmonics is also observed in their spectra with a similar frequency modulation. For the analysis of the DCCT signals, the fundamental harmonic (h=1) is selected. An accurate determination of the modulation directly at 50 Hz requires a more refined Fourier analysis to overcome the problem of limited resolution. For this reason, the implementation of the NAFF. The green curve of Fig. 4.10 presents the frequency evolution of the 50 Hz line, as observed in the DCCTs. All eight independent measurements reveal an oscillation which is synchronous in phase and equal in amplitude. The origin of this common drift, which is observed both in the eight DCCTs and the beam, is the stability of the 50 Hz mains from the power grid. This conclusion can also be verified by comparing the drift with unrelated signals acquired from other machines of the accelerator complex, such as the SPS, where the measured drift was identical to the one observed in the LHC signals.

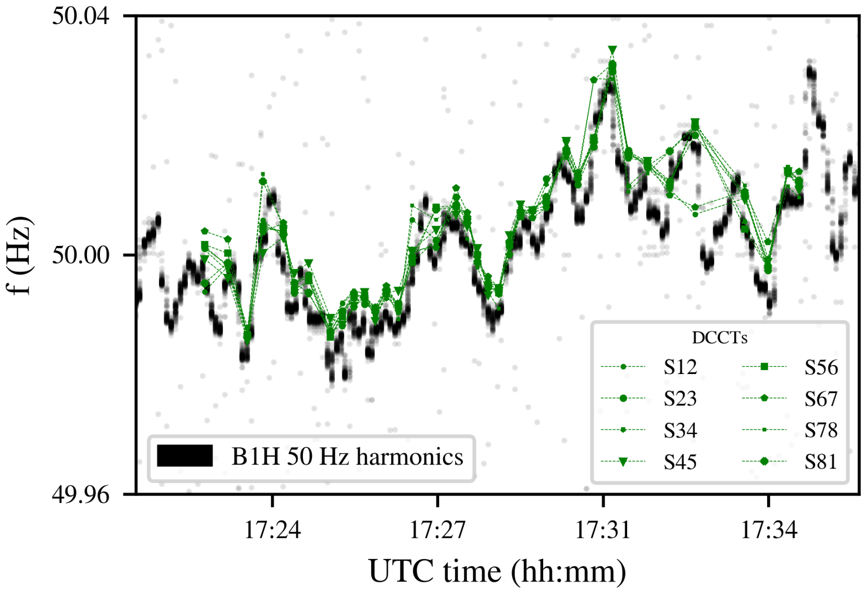

Figure 4.10: The frequency modulation of the harmonics observed in the eight DCCTs (green) and the ones of the beam spectrum (black).

To further support this conclusion, the beam spectrum is compared to the output voltage spectrum of the Main Bends power converter installed in sector 1-2. During the MD Fill 7343, voltage measurements of the power converter were collected every minute with a sampling rate of 50 kHz. The converter's spectrum consists of 50 Hz harmonics, extending up to 10 kHz. Figure 4.11 illustrates the voltage spectrogram for a regime in the low (left panel) and high (right panel) frequency cluster. Applying a similar analysis to the one used for the harmonics of the beam yields a similar frequency evolution of the 50 Hz components in the power converter. Figure 4.12 presents the modulation of the lines in the power converter (blue) and the beam (black) for the same time interval, after normalizing with the harmonic order. The strong correlation between the two enhances the hypothesis that the modulation originates from the stability of the mains. It is interesting to note that, at the end of the MD (6 am Central European Time), a frequency drift above the usual variation of the 50 Hz is visible in both spectra. To validate that this effect is reproducible, fills for the same time and different days have been analyzed, yielding similar

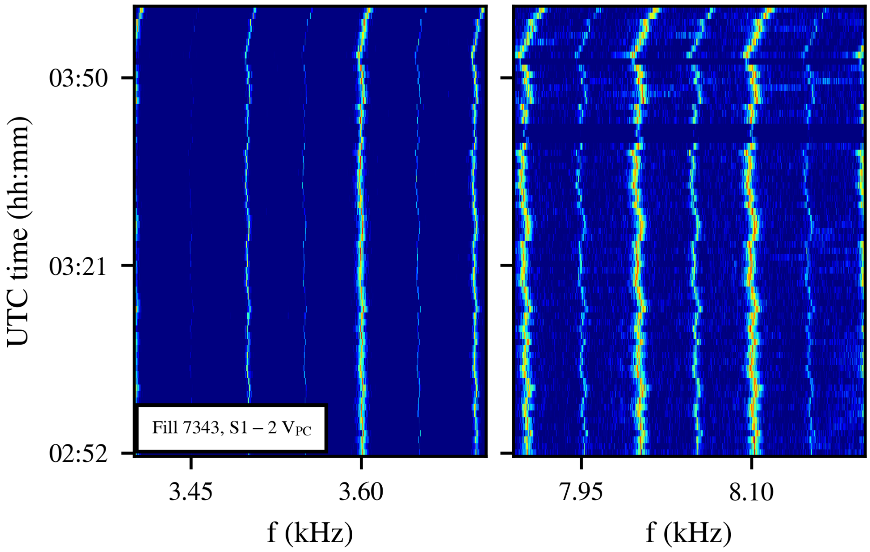

Figure 4.11: The voltage spectrum of the power converter of the Main Bends in sector 1-2 for the low (left panel) and high (right panel) frequency ranges.

results. These variations appear to be the result of the changing load of the power grid at this time of the day.

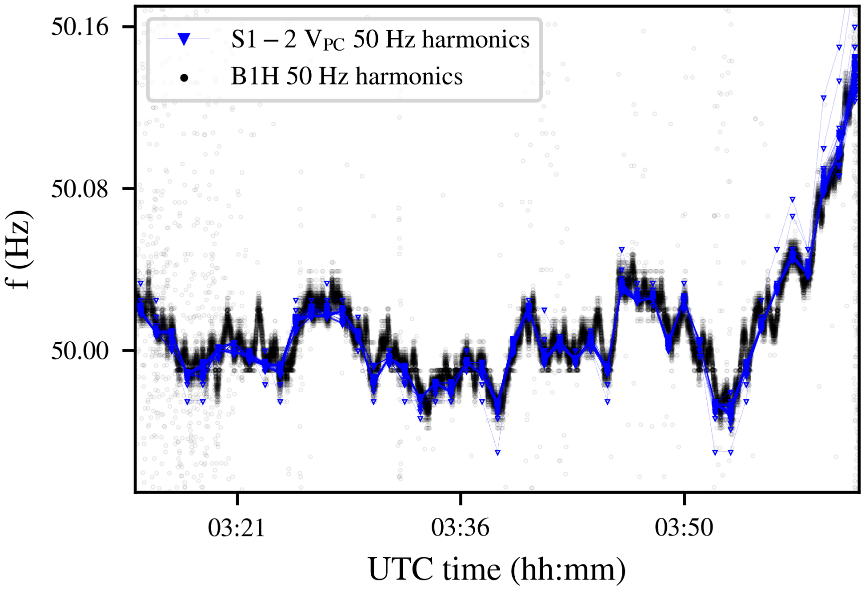

Figure 4.12: The frequency modulation of the harmonics observed in the voltage spectrum of the main dipoles power converter of sector 1-2 (blue) and the ones of the beam spectrum (black).

The previous findings are not used to establish a correlation between the dipole power converter in sector 1-2 and the beam. The importance of these observations resides on the fact that, if the 50 Hz harmonics are the results of a real beam excitation, their frequency domain signature points to a specific type of power converter as the noise source. In particular, the existence of multiple 50 Hz harmonics in combination with the frequency modulation induced by the mains suggests that the origin of these frequency lines are power converters that are based on commutated Thyristor Technology. This can be understood with a frequency analysis of the variation of the magnetic field (B-Train) in two other machines of the accelerator complex: the PS and the and SPS [93, 94]. In the B-Train system, a pickup up coil is installed in the aperture of the reference dipole magnets. The measured signals correspond to the rate of change of the magnetic field. Figure 4.13 shows the spectrogram of the magnetic measurements for the PS (Fig. 4.13a) and SPS (Fig. 4.13b). The PS spectrum reveals a strong component at 5 kHz, which is the frequency of some of its Switch-Mode power converters [95]. The switching of this type of power converter is regulated by a clock. Subsequently, a negligible variation in the frequency evolution of the line is observed. As the switching frequencies are well defined, they can be easily identified and no 50 Hz harmonics are present in the signal. On the contrary, in the SPS case, the power converter is a Silicon Controlled Rectifier (SCR). Hence, the 50 Hz harmonics are visible on the signal and the stability of the mains has an impact on the output current of the power converters. For the next sections, when the expected position of the 50 Hz harmonics is illustrated, the drift of the harmonics due to the modulation is taken into account.

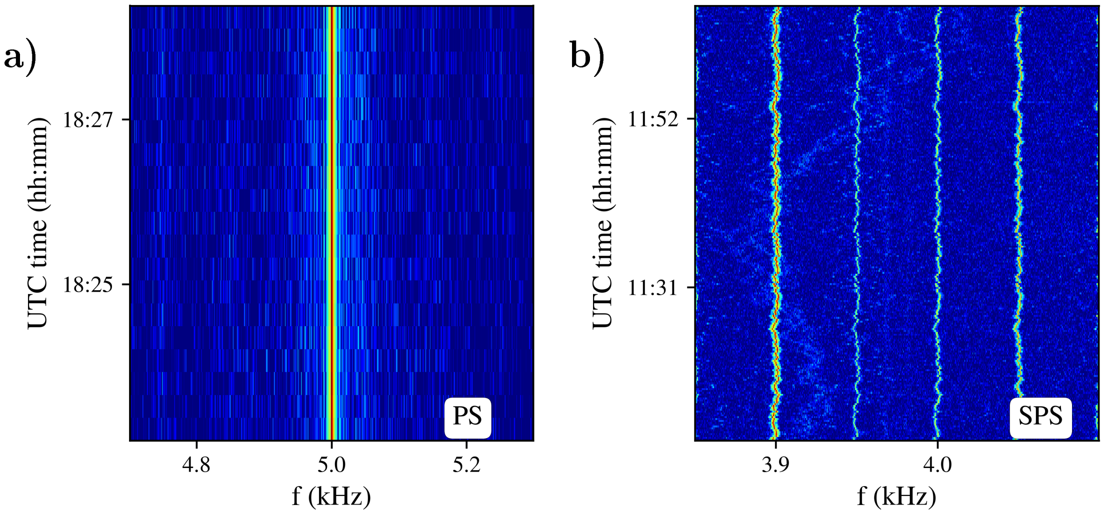

Figure 4.13: The spectrum of the B-Train in (a) PS and (b) SPS.

Therefore, if environmental noise is excluded as the origin of the perturbation, the signature of the 50 Hz harmonics in the beam spectrum suggests that the possible sources are limited to magnets with SCR power converters. The magnets with such types of power converters in the LHC are presented in Table 4.1 [91, 96]. To this end, the next sections focus on determining whether the 50 Hz harmonics are the result of a real beam excitation or external noise perturbing the beam signal.

Table 4.1: The SCR power converters in the LHC [91, 96].

Power converter	Use
RPTE	Main dipoles
RPTF	Warm quadrupoles (Q4, Q5)
RPTG	Dogleg dipoles (D1, D3, D4, spare)
RPTL	Alice compensator
RPTM	Septa
RPTI	Alice and LHCb dipoles
RPTN	LHCb compensator
RPTJ	CMS Solenoid
RPTH	Alice Solenoid
RPTK	RF Klystron

4.4.5 Betatron phase advance from Q7 to Q9

The phase evolution of the 50 Hz harmonics between two locations in the ring can clarify whether the noise lines are the result of a real beam excitation. To this end, their phase advance is measured between two closely separated pickups and is then compared to the betatron phase advance between the same pickups. For the validity of the comparison, the two observation points must be situated in a relatively close distance, so that the beam does not encounter a noise perturbation while crossing this path. If the harmonics are the result of a spurious signal entering the beam then their phase advance is not expected to correspond to the betatronic one. Furthermore, in general, an arbitrary dephasing between the low and high-frequency cluster should be observed. On the contrary, in the case of a real excitation, the noise phase advance must correspond to the betatronic one for all the harmonics present in the spectrum.

In the context of this investigation, two pickups of the transverse damper, referred to as Q7 and Q9, are selected for the analysis. At collision energy, the betatron phase advance between the two observation points is defined by the optics and is approximately equal to 110°. The first step is to compute the complex Fourier spectra for a single pickup and for each bunch in a physics fill to observe the dephasing of the lines across the full machine. As reported in the previous sections, with the present noise floor, the evolution of the lines cannot be determined with a single bunch. For this reason, the average signal is computed from five consecutive LHC trains, each one of which consists of 48 bunches. Then, the phase evolution of each harmonic is computed across the machine.

Figure 4.14 depicts the dephasing of a harmonic in the low (Fig. 4.14a) and high-frequency cluster (Fig. 4.14b) as a function of the train number for Q7 (blue) and Q9 (green). The gray dashed lines illustrate the expected dephasing, which is proportional to the frequency and the time delay of the trailing trains from the first train in the machine. It must be noted that by averaging over a few consecutive trains the signal is sub-sampled to f_{rev}, similarly to the single bunch case. Based on the above, the negative slope of the 7.8 kHz (h=156) shows that the phase evolution of the harmonic was computed through aliasing. The phase advance of each harmonic is the difference in the phase determination of the two pickups. In both cases, a correspondence to the betatron phase advance is found, an observation that clearly proves, for the first time, that the two excitations originate from the beam.

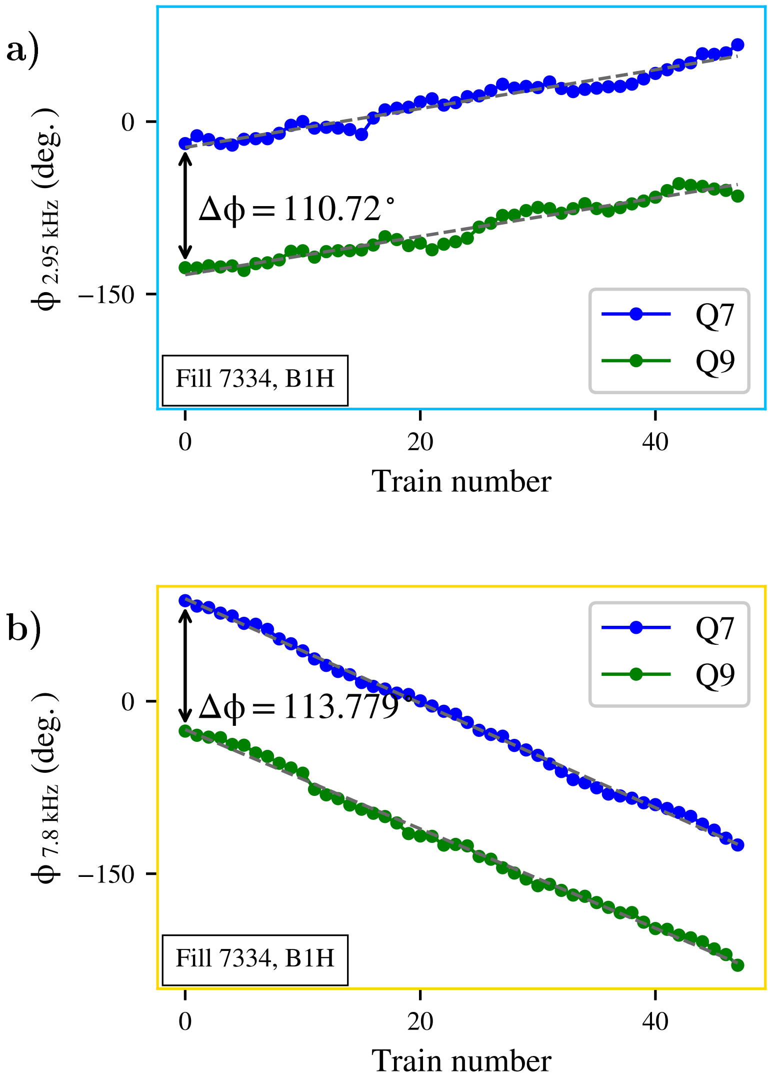

Figure 4.14: The phase evolution of the (a) h=59 and (b) h=156 harmonic as a function of the train number for Q7 (blue) and Q9 (green).

The reproducibility of the previous results must be verified for all the harmonics in the beam spectrum. It is also important to determine the standard deviation of these computations, as following the frequency drift of lower-amplitude harmonics can introduce uncertainties. To this end, the filling scheme of the physics Fill 7334 is divided in three groups of consecutive trains. Each group corresponds to approximately one-third of the total beam. The average value and the standard deviation of the dephasing between Q7 and Q9 are computed from the three groups for all the harmonics above noise level.

Figure 4.15 demonstrates the average phase advance for the harmonics in the low (blue) and high (orange) frequency cluster and the error bars represent one standard deviation. The gray dashed line indicates the betatron phase advance. From this observation it is concluded that, within the uncertainties of the analysis, all harmonics exhibit a phase advance that is compatible with the betatronic, thus proving that the observations are not instrumental. Following this conclusion, the next sections focus on identifying the origin of the perturbation by studying the response of the noise during changes in the beam or machine parameters, starting from the simplest modification, which is the change of tune.

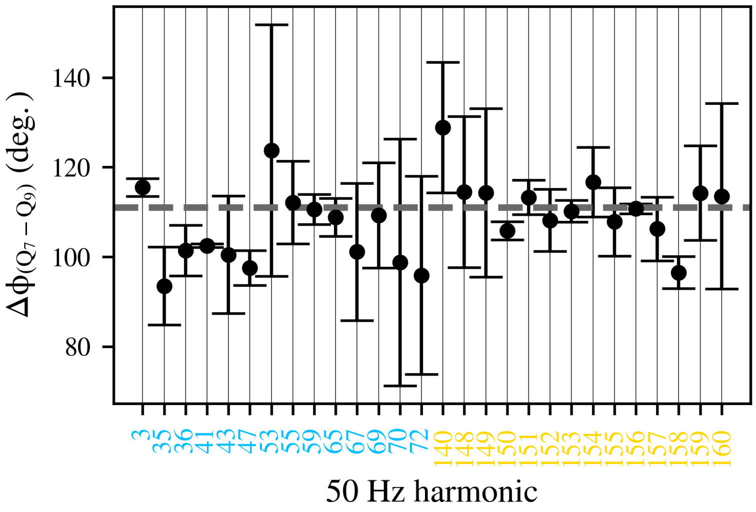

Figure 4.15: The average phase advance from Q7 to Q9 for the harmonics in the low (blue) and high (orange) frequency cluster. The error bars represent one standard deviation and the gray dashed line illustrates the betatron phase advance.

4.4.6 Change of betatron tune

The conclusions of the previous sections are based on parasitic observations with a static beam and machine configuration. This section investigates the response of the harmonics during a simple modification of the betatron motion such as the change of the tune at Flat Top. As previously mentioned, at this point in the beam cycle, the beam energy reaches the maximum value of 6.5 TeV and, after a few minutes at top energy, the decimal part of the horizontal tune is trimmed from approximately 0.28 to 0.31. Figure 4.16 presents the HS BBQ spectrogram for the horizontal plane of Beam 1 in the physics Fill 7056. The spectrogram is centered around the betatron tune for the whole duration of Flat Top and a color code is assigned to the PSD. The black dashed line represents an approximation of the horizontal tune evolution. First, one must observe that the frequencies of the lines are not affected by the tune change. This fact proves that the harmonics are the result of a dipolar field error rather than a tune modulation. Second, a comparison prior and after the trim leads to the conclusion that the amplitude of the lines in the vicinity of the betatron tune is strongly enhanced. This resonant behavior is in agreement with a dipolar perturbation, with an excitation frequency that approaches the betatron tune (see Section 4.2).

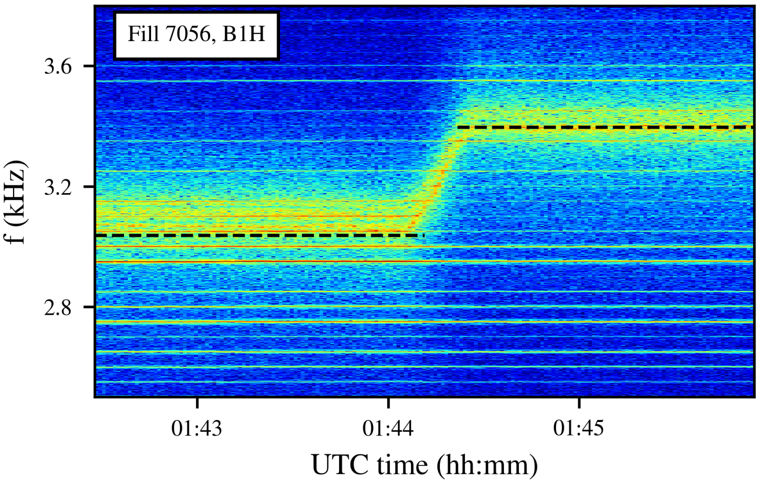

Figure 4.16: The horizontal spectrogram of Beam 1 at Flat Top. The black dashed lines represent an approximation of the injection and the collision tune.

Of particular interest is the impact of the tune change on the high-frequency regime. To investigate this effect, the high bandwidth spectrum is computed from the ADTObsBox prior and after the tune trim. Figure 4.17 shows the horizontal spectrum of Beam 2 up to 10 kHz (Fig. 4.17a) at top energy with the injection (blue) and collision (black) tune. Similarly to the HS BBQ, the closest harmonics to the tune of the low-frequency cluster are enhanced in terms of amplitude. It must be noted however, that a shift is also observed at the position of the high-frequency cluster. To further illustrate this effect, the spectrum is centered around the high-frequency cluster in Fig. 4.17b. Although the effect is dipolar in both cases (the harmonics coincide with the 50 Hz multiples indicated with the gray lines), this observation shows that, as stated in Section 4.4.3, the location of the cluster is at $\mathrm{f_{rev}} - \mathrm{f_x}$ and thus, depends on the tune. The fact that the changes in the beam configuration affect the amplitude of the noise lines provides further proof that the harmonics are the result of a real beam excitation. To complement these findings, the response of the harmonics is studied when another modification is applied to the betatron motion and specifically, to its phase advance, while the tune is constant.

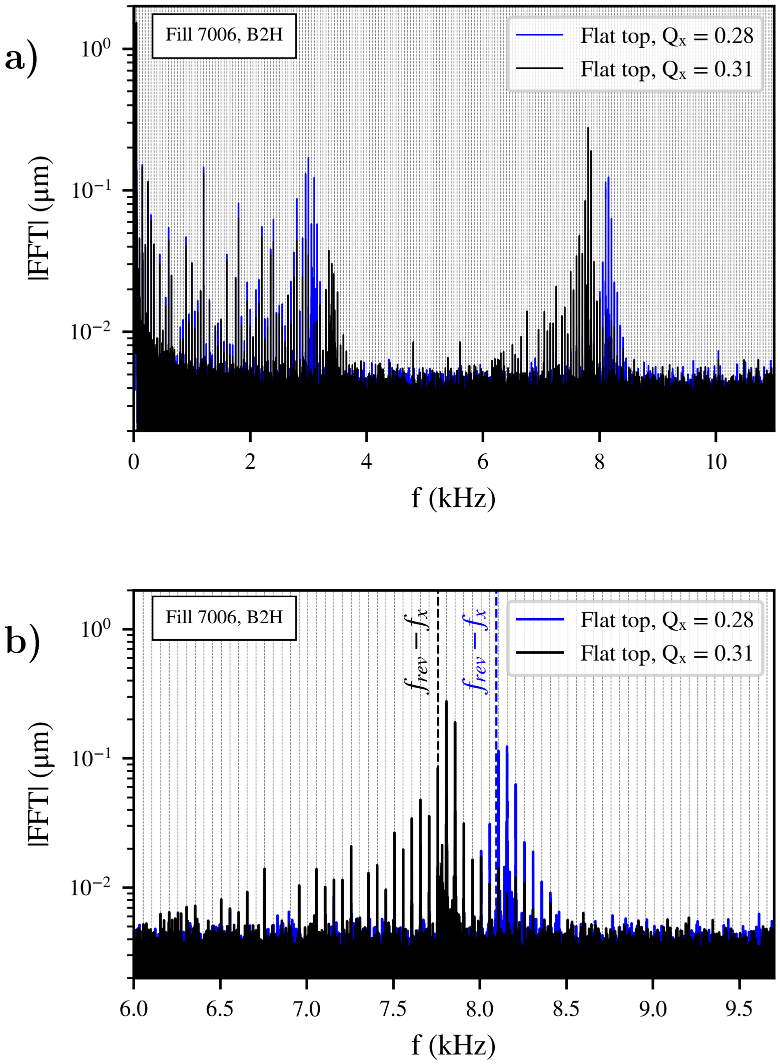

Figure 4.17: The horizontal spectrum of Beam 2 prior (blue) and after (black) the tune change (a) at Flat Top and (b) centered around the high-frequency cluster. The gray dashed lines represent the multiples of 50 Hz.

4.4.7 Change of phase advance between IP1 and 5

During the MD Fill 6984, the betatron phase advance between the IP 1 and 5 were modified [97]. This was achieved through the incorporation of a set of optics knobs, which allow scanning the phase between the two IPs, based on the ATS scheme [35]. In this case, the knobs lead to a trim in the current of the quadrupole families responsible for the control of the tune. Throughout these modifications, the betatron tune is constant.

To demonstrate the impact of the knob, Fig. 4.18 illustrates the converter current for a single quadrupole (red). The evolution of the current corresponds to a change of the phase advance within a range of ± 20° for the horizontal plane of Beam 1. During this time interval, the amplitude evolution of the harmonics is computed. Figure 4.18 also denotes the response of the h=12 harmonic (black curve). The amplitude evolution of the lines in the low-frequency cluster is clearly impacted by the variation of the betatron phase advance, an effect that provides definitive indications that they originate from the beam. As far as the high-frequency cluster is concerned, no impact is observed in their amplitude evolution throughout these tests. Following the change of the betatron tune and phase advance, we explore the evolution of the spectrum across different beams modes and thereby, different energies and optics.

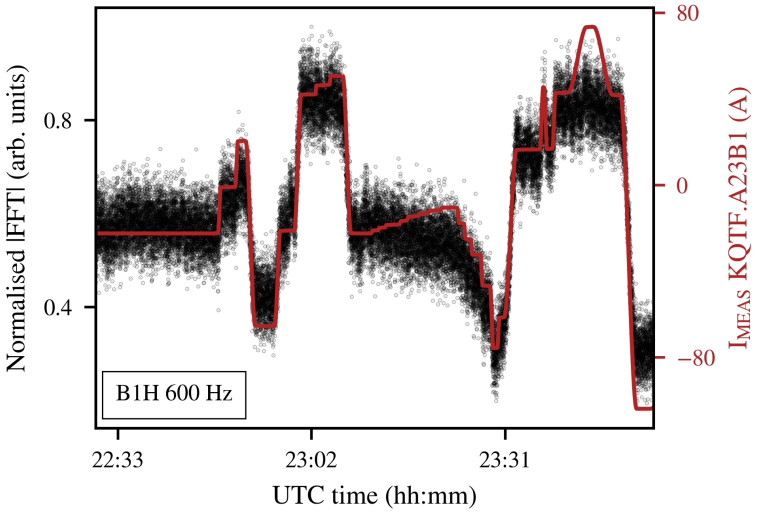

Figure 4.18: The amplitude evolution of the 600 Hz lines (black) during the change of the phase advance between IP1 and IP5. while the tune is kept constant. The red line represents the current in the quadrupole trims employed for the phase scan.

4.4.8 The spectrum evolution during the LHC cycle

Some of the magnets in Table 4.1 can be excluded as potential noise sources by observing the evolution of the spectrum across the cycle. For this reason, the horizontal spectrum of Beam 2 is computed for various beam modes (physics Fill 7033). For the comparison, we profit from the calibrated metric provided by the ADTObsBox. Figure 4.19 depicts the spectra, centered around the low (left panel) and high (right panel) frequency clusters. The beam modes of particular interest are Ramp (Fig. 4.19a and 4.19b) for two values of the energy, Flat Top prior to the change of tune (Fig. 4.19c), Squeeze (Fig. 4.19d) and Stable Beams (Fig. 4.19e and 4.19f) for two steps of the β^*-levelling.

First, due to the fact that the 50 Hz harmonics are systematically present in all beam modes and fills, the power converters of the spare magnets and the septa are excluded. Second, the amplitude of the noise lines does not significantly attenuate with increasing beam energy. Considering a non-ramping power converter as the source, a reduction of the angular deflection and thus, of the amplitude of the noise, should be observed with increasing beam rigidity. The absence of such an attenuation leads to the conclusion

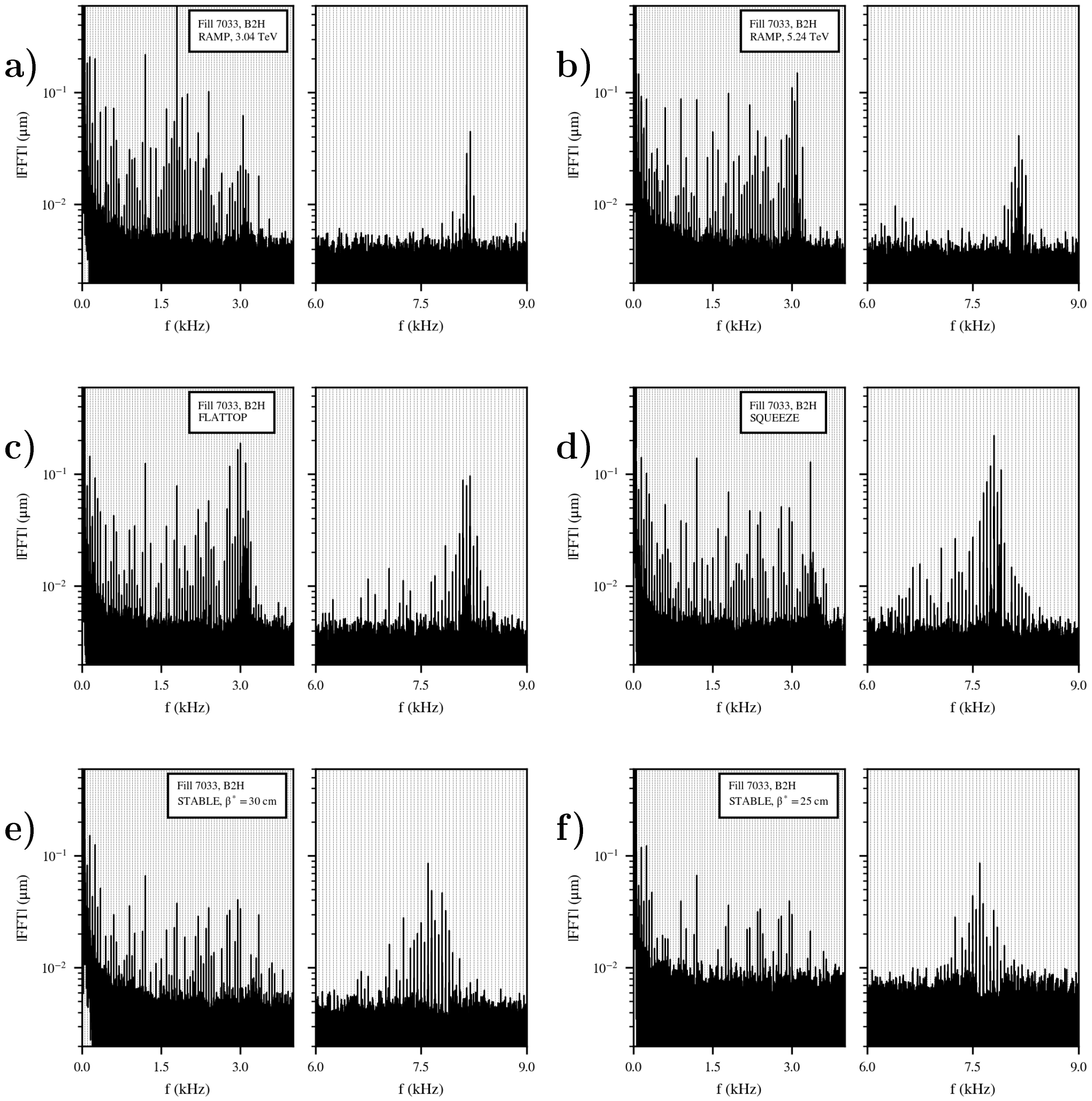

Figure 4.19: The horizontal beam spectrum of Beam 2 during Ramp (a,b), Flat Top (c), Squeeze (d) and Stable Beams (e,f).

that the noise is originating from a ramping power converter. Consequently, all non-ramping power converters can also be excluded. Through this process of elimination, the remaining candidates of Table 4.1 are the main dipoles and the warm quadrupoles. Combining this finding with previous indications of the dipolar nature of the source, the investigation focuses on the power converters of the Main Bends. The main dipoles have undoubtedly the highest filling coefficient in the machine and, as previously mentioned, the studies conducted in other machines have proved that the arc circuit was systematically the dominant contributor. To verify this assumption, a modification was applied in the power converters of the main dipoles and the beam response is presented and discussed in the next section.

Additionally, reviewing the spectrum at Ramp and Flat top yields a further excitation of the high-frequency cluster across the two beam modes. A comparison between Flat top (injection tune) and Squeeze (collision tune) illustrates the dependence of the position of the high-frequency cluster to the betatron tune, as discussed in the previous sections. Finally, the β^* reduction from 30 cm to 25 cm at Stable beams does not have an impact on the amplitude of the harmonics. The increase of the noise floor between the two spectra is due to the reduction of the beam intensity across the two observations.

4.4.9 Active filters of the main dipole power converters

Based on the previous findings, the pursued investigations focus on the main dipoles circuit. To establish a correlation between the harmonics of the beam and the ones in the output of their power converters, a modification in the configuration of the latter is needed. In this context, an important observation was made when the status of the active filters of the Main Bends, which are installed for the attenuation of the 50 Hz ripples [91, 98], was changed. During dedicated MD fills, the eight active filters were disabled sector-by-sector. The main observable throughout these tests is the amplitude evolution of the harmonics. First, the impact on one noise line is demonstrated and then the observations are extended to different beam energies and various harmonics.

Figure 4.20 illustrates the 3D spectrogram for the horizontal plane of Beam 1, as acquired from the MIM, for the time interval of the tests conducted at injection (Fill 7343). For a first demonstration, the frequency range is limited around 600 Hz. The projection of the spectrogram, which illustrates the amplitude evolution of the h=12 harmonic, is shown with the blue curve. Disabling the eight filters leads to abrupt changes in its amplitude evolution.

To clearly illustrate these results, the amplitude evolution of the h=12 harmonic is extracted from the 3D spectrogram. Figure 4.21 (top panel) presents the response of the 600 Hz line in Beam 1 (blue) and 2 (red) for two separate beam modes: a fill at injection (Fig. 4.21a) and at top energy (Fig. 4.21b). The status of the eight active filters is presented for the same time span (bottom panel) and a color code is assigned to each sector. The distinct changes in the amplitude coincide with the disabling of the filter of each sector. As a last step at injection, the filters were disabled simultaneously, which led to an important increase in the amplitude of the line.

The observations on the h=12 harmonic provide evidence that all eight power converters contribute to this effect. The question that arises is whether the most impacted sectors in terms of noise can be identified. Reviewing the results of Fig. 4.21 yields that the positive or negative impact of the filter compared to the baseline, which is defined as the amplitude of the harmonic prior to the test, depends on the sector. For instance, at injection in Beam 1, disabling the Filter of sector 1-2 leads to an increase of the ripple amplitude. Therefore, the filter, when active, suppresses the harmonic and its impact is characterized as positive. On the contrary, sector 5-6 has a negative contribution at injection. Then, comparing the same sector across the two beams reveals a different impact between the two (e.g., sector

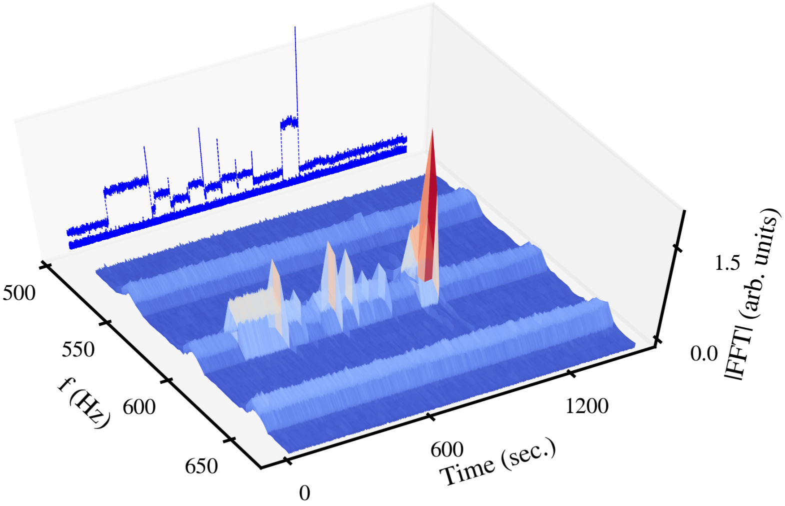

Figure 4.20: The horizontal spectrogram of Beam 1 during the tests of the active filters at injection centered around 600 Hz. The blue lines represent the amplitude evolution of the spectral components in this regime.

5-6 at injection). This can be possibly attributed to the different phase advance of the two beams in the ring. Finally, the contribution for the same beam and sector also depends on the beam energy (e.g., Beam 2, sector 3-4).

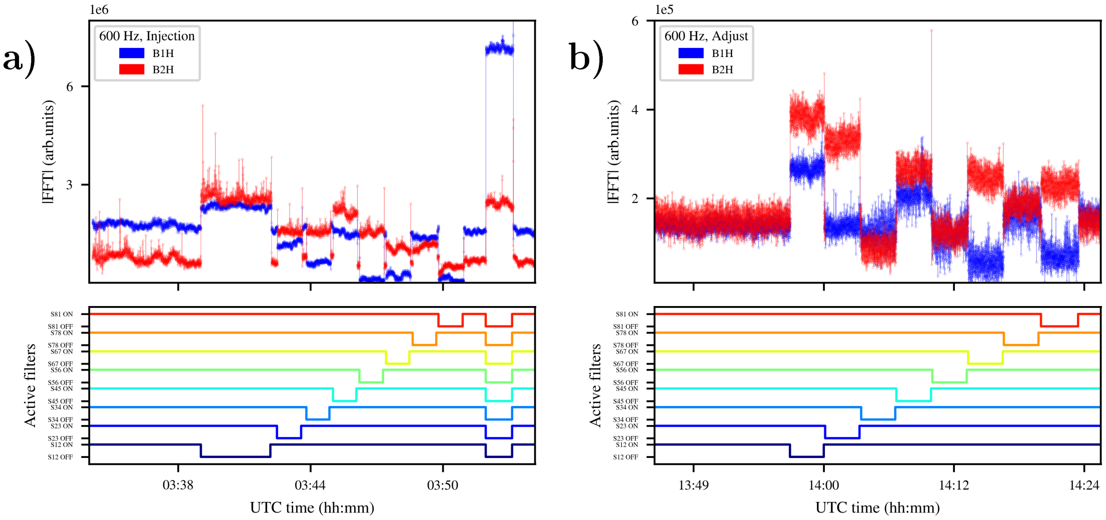

Figure 4.21: The response of the h=12 harmonic (top panel) during the tests with the active filters for Beam 1 (blue) and Beam 2 (red) (a) at injection and (b) top energy. The status of the active filters is color-coded with the sector number (bottom panel).

The correlation with the power converters is not only valid for the 600 Hz line, but for most of the 50 Hz harmonics included in the low-frequency cluster. Figure 4.22 shows the amplitude evolution of various harmonics at injection, represented with a different color code. The abrupt changes in the amplitude when disabling the active filter of each sector are reproduced for harmonics up to 3.6 kHz. In addition to the observations at 600 Hz, the contribution of each sector also varies across the harmonics.

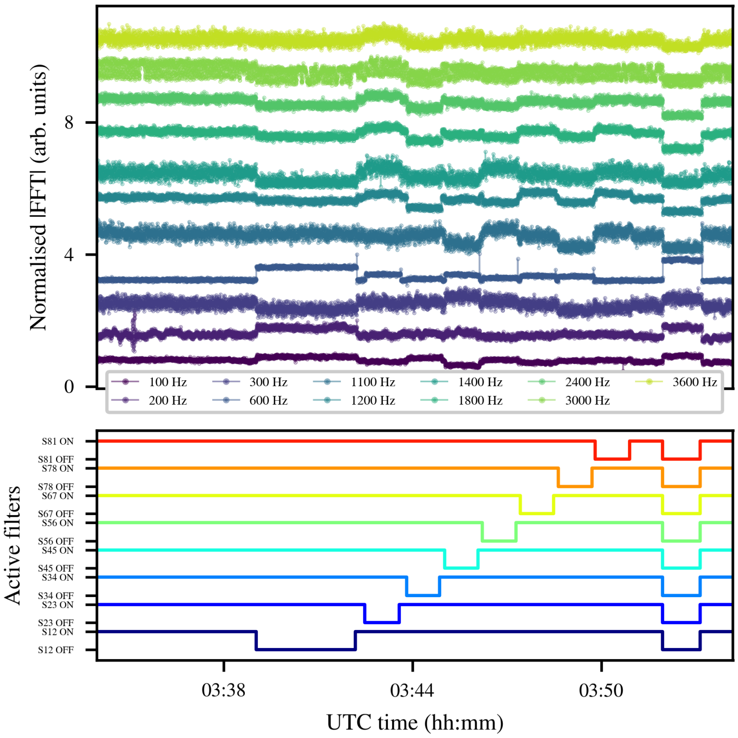

Figure 4.22: The amplitude evolution of the harmonics in the low-frequency cluster (up to 3.6 kHz) during the tests with the active filters.

To summarize, applying a simple modification in the configuration of the dipole power converters, such as modifying the status of the active filters, has a direct impact on the low-frequency cluster harmonics of the beam. These results provide evidence that the power converters of the main dipoles are at least a major contributor to the harmonics up to 3.6 kHz observed in the beam spectrum. It is the first time that such a correlation has been demonstrated in the LHC. Presently, no model exists to predict the impact of the active filters on the transverse spectra, as a function of the sector, the beam energy and the order of the harmonic and therefore, a classification of the sectors in terms of noise is not currently performed.

It must also be underlined that no change in the amplitude evolution of the harmonics in the high-frequency cluster is reported during these tests. A possible explanation is that, due to their limited bandwidth, the active filters are not acting in such a high-frequency regime and thus, no impact in the high-frequency cluster is expected. Figure 4.23 demonstrates the voltage spectrum of the power converter in one of the LHC sectors, first, when the active filter is enabled (Fig. 4.23a) and, then, disabled (Fig. 4.23b). In this case, the vertical lines represent the multiples of 600 Hz. The comparison of the spectrum prior and after the modification shows that the active filter is suppressing the harmonics up to approximately 3 kHz, while it enhances the high order harmonics. Additional observations concerning the high-frequency cluster are discussed in the next sections.

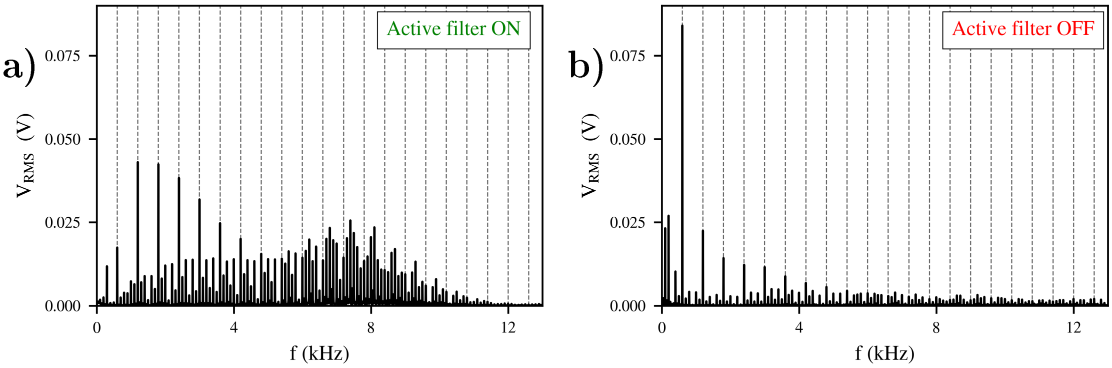

Figure 4.23: Voltage spectrum of the power converter of the main dipoles in one of the LHC arcs (Sector 1-2) with the active filter (a) enabled and (b) disabled. The vertical gray lines represent the multiples of 600 Hz.

4.4.10 Comparison of beams and planes

A comparison between the spectra of the horizontal and vertical plane provides yet another indication of the dipolar nature of the source. The spectra of both beams and planes are measured for the physics Fill 7334. As the pickups for the two beams and planes are located in different positions in the ring, the ADTObsBox calibrated spectra are normalised with the corresponding β-functions. Figure 4.24 demonstrates the spectra for the horizontal (magenta) and vertical (cyan) plane for Beam 1 (left) and 2 (right). Comparing the amplitudes of the spectral lines yields that the perturbation is mainly affecting the horizontal plane, an effect compatible with a dipolar field error. Due to the transverse coupling of the machine, an attenuated perturbation is also present in the vertical plane. To demonstrate that this effect results from the coupling, controlled excitations have been applied in the horizontal plane of Beam 1 using the transverse damper in a dedicated MD fill (see Section 4.5.1). In this case, although only the horizontal plane was excited, the oscillation was visible also in the vertical plane.

Furthermore, it must be highlighted that the maximum offset observed in the horizontal spectrum of Beam 1 is approximately 0.1 μm, which corresponds to $10^{-3}\ \sigma$. As shown in the Section 4.2, assuming a single dipolar perturbation, this value corresponds to a deflection of 0.09 nrad at a location with $\beta = 105$ m for an excitation frequency in the vicinity of the tune. Comparing the equivalent kick with the bending angle of a single dipole in the LHC (≈5 mrad) and neglecting additional effects (transverse damper, electron-cloud, transverse impedance) yields a field stability of $1.8 \cdot 10^{-8}$, a value which is well within the power converter specifications.

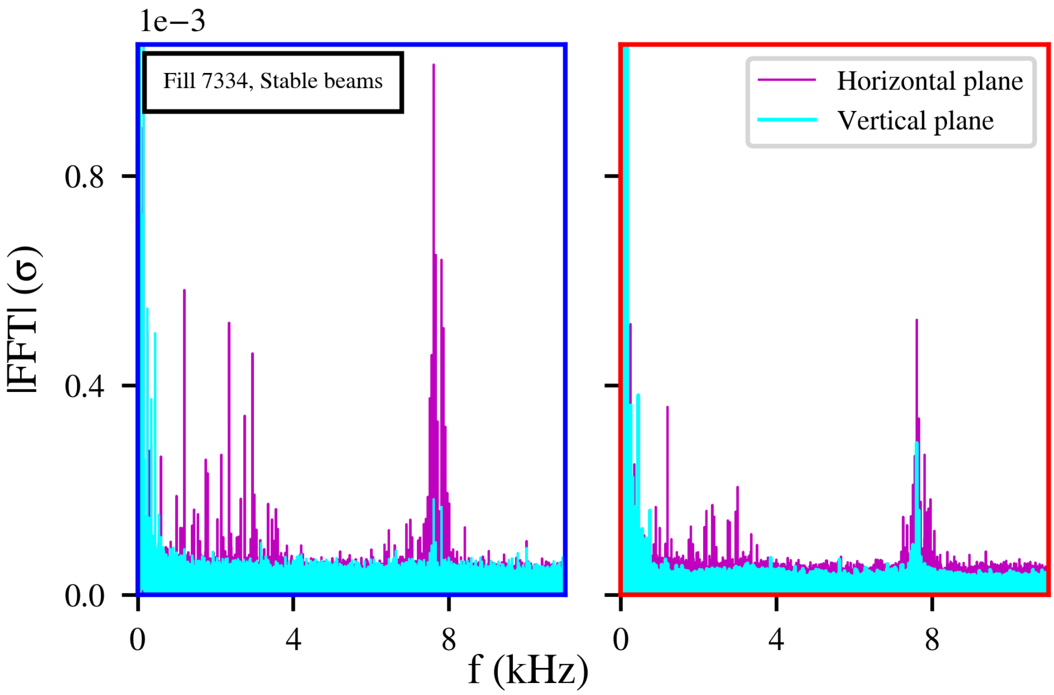

Figure 4.24: The spectrum of the horizontal (magenta) and vertical (cyan) plane of Beam 1 (blue) and 2 (red) in Stable Beams, normalized with the corresponding β-functions.

Comparing the spectra of the two beams yields an asymmetry in terms of noise between Beam 1 and 2. Based on the amplitudes of the spectral components, a more significant effect is visible in Beam 1. To verify the reproducibility of this observation, the spectra of both beams and planes are computed for all the proton physics fills of 2018. For each fill, the maximum offset induced by the 50 Hz harmonics is computed, which corresponds, in Stable Beams, to a frequency of 7.7 kHz. Figure 4.25 depicts the maximum amplitude observed in the spectrum as a function of the fill number for the horizontal (magenta) and vertical (cyan) plane in Beam 1 (blue) and 2 (red). The dashed lines represent the average offset over all the fills for each plane. These results confirm that the noise is systematically more pronounced in Beam 1 than Beam 2 by approximately a factor of two in the horizontal plane. It is particularly interesting to note that the amplitude of the noise is very regular across the fills, with a single exception in Fill 7035, an observation that is further analyzed in the next section.

4.4.11 Change of the ADT settings

The fill-by-fill analysis of the spectra reveals an increase of the noise in terms of amplitude in the physics Fill 7035. In this context, an additional parameter that has not been included in the analysis so far is the activity of the transverse damper and the interplay with the 50 Hz harmonics. In the nominal LHC cycle, the ADT settings are modified and

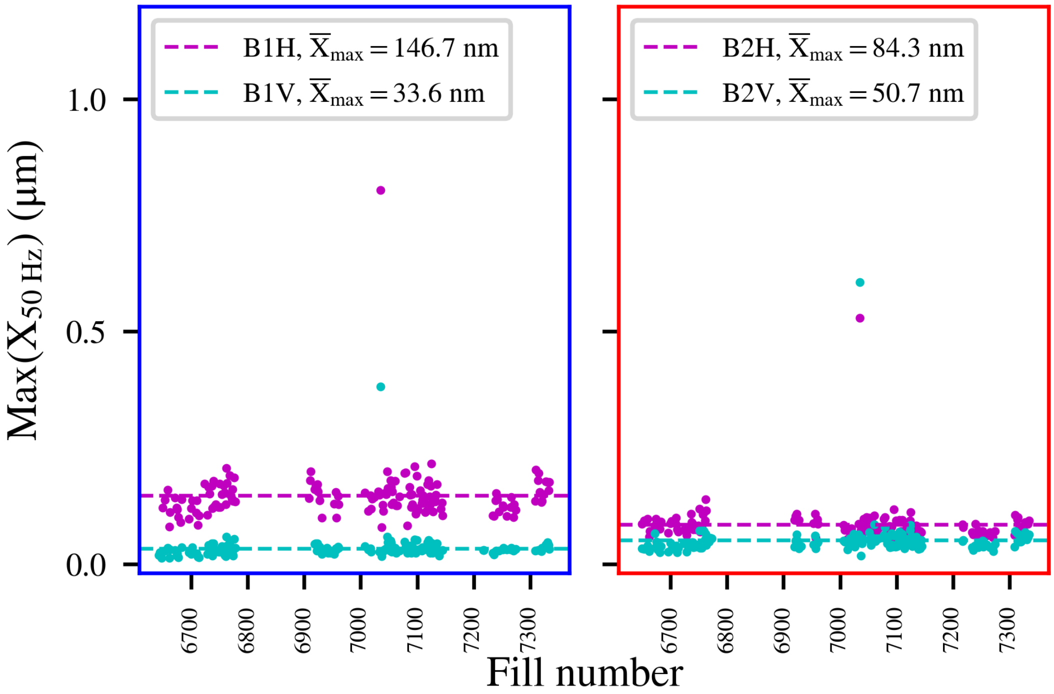

Figure 4.25: The maximum amplitude of the 50 Hz harmonics for the horizontal (magenta) and vertical plane (cyan) of Beam 1 (blue) and 2 (red) for all the proton physics fills of 2018.

in particular, the extended ADT bandwidth is changed to standard bandwidth at the end of Adjust [99, 100]. In the Fill 7035, this modification was not applied and the extended bandwidth was used at Stable Beams. Figure 4.26 illustrates the horizontal spectrum of Beam 2 at Stable Beams for the Fill 7033 (Fig. 4.26a) with the standard ADT bandwidth and for the Fill 7035 (Fig. 4.26b). Comparing the two spectra yields an increase in the amplitude of the 50 Hz harmonics in the regime above 3 kHz, which is particularly important for the high-frequency cluster. This observation indicates that the high-order harmonics are suppressed by the damper in normal operation. The impact of the ADT settings is also systematically observed in other beam modes of the machine cycle during which the bandwidth was modified such as the Adjust.

The importance of this finding resides on the fact that a strong asymmetry is present between the frequencies of the low and high cluster in terms of amplitude. In particular, these observations indicate that, in the absence of the damper, the amplitude of the harmonics in the high-frequency cluster is expected to be further enhanced compared to the values that have been observed experimentally. In contrast, Fig. 4.23a shows that the noise in the power converter voltage spectrum attenuates with increasing frequency. Furthermore, high-frequency perturbations such as the high-frequency cluster strongly exceed the cutoff frequency of the LHC main dipoles due to the shielding effect of the beam screen [101]. To this end, if the high-frequency cluster is driven by a direct excitation due to power

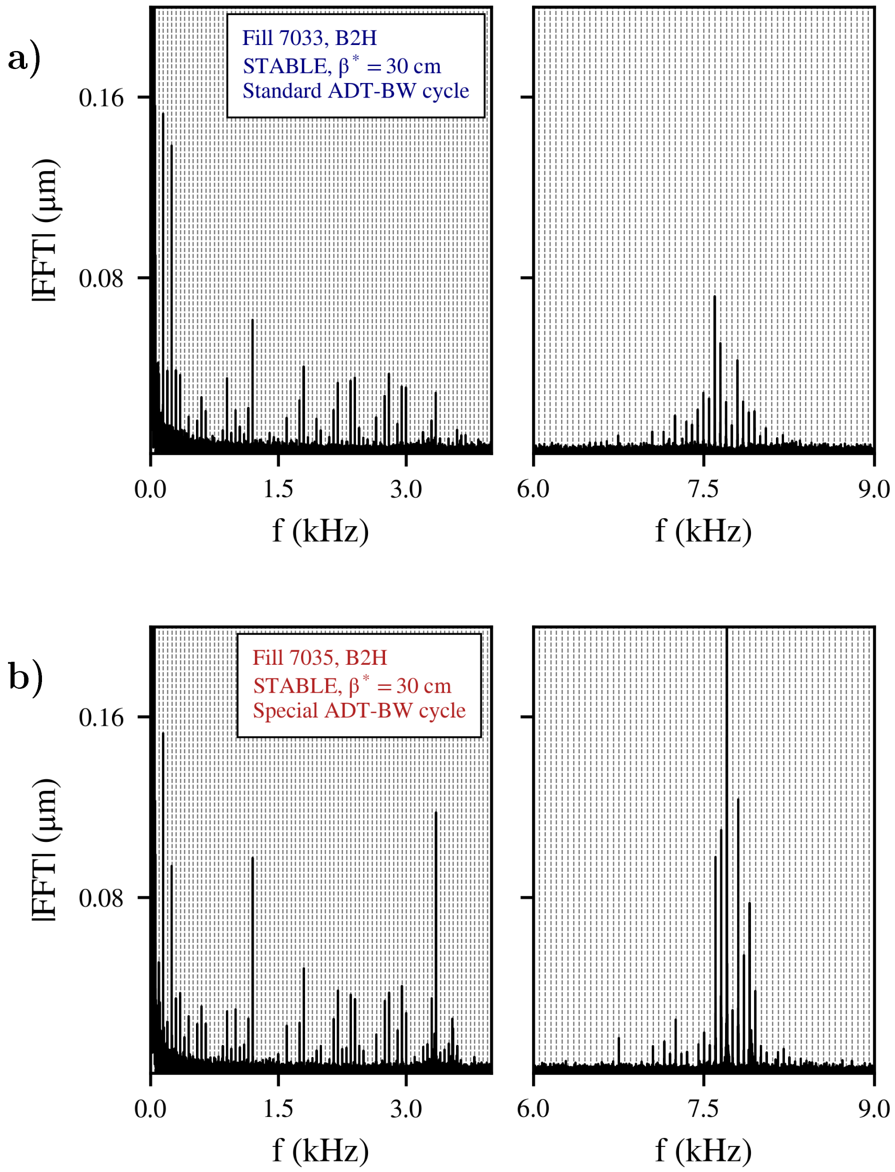

Figure 4.26: The horizontal spectrum of Beam 2 at Stable Beams centered around the low (left panel) and high (right panel) frequency cluster for a fill with (a) the standard (Fill 7033) and (b) extended (Fill 7035) ADT bandwidth.

converter noise, a significant attenuation of its amplitude should be observed compared to the low-frequency cluster, while experimentally we observed the opposite.

Additionally, it should be mentioned that the increase of the noise by a factor of two in Fill 7035 did not lead to an increase of losses or emittance growth compared to the rest of the fills. However, as the duration of the fill was limited to 40 minutes, the impact of the noise lines on the beam lifetime cannot be excluded.

4.4.12 Summary of observations and discussion

The beam transverse spectra, as computed from the ADTObsBox bunch-by-bunch acquisitions, reveal the existence of 50 Hz harmonic perturbations in two frequency regimes, namely the low and high-frequency clusters. Although many similarities have been identified between the low and high-frequency cluster, the need to distinguish the two regimes is justified by their different response when modifications in the machine configuration are applied. Comparing the amplitudes of the noise lines residing in each regime yields that larger excitation amplitudes are observed on the beam motion due to the high-frequency cluster. This section summarizes the findings, organizes the observations per cluster, discusses possible sources and presents the conclusions from the experimental observations. A summary of the most important findings can be found in Table 4.2.

Table 4.2: The summary of the observations for the low and high frequency cluster..

Low frequency cluster	High frequency cluster
Comb of 50 Hz	
Frequency modulation from the mains	
Phase advance Q7-Q9 compatible with betatronic	
Dipolar nature	
Mainly in the horizontal plane	
Higher amplitude in Beam 1	
Impact from IP1/5 phase scan	Impact from change of tune
Impact from Active filters	Impact from ADT settings

The analysis in frequency domain illustrates a common signature between the two clusters. Both regimes consist of a set of 50 Hz harmonics, that experience a frequency modulation induced by the mains. Several observations prove that both regimes are the result of a real beam excitation. Based on the fact that the harmonics are multiples of 50 Hz rather than sidebands around the tune, and that the horizontal plane is mainly affected, it is concluded that the nature of the source is dipolar. The signature of the harmonics in both regimes is compatible with a ramping SCR power converter. Comparing the spectra of the two beams shows that a larger impact is systematically observed in Beam 1 across all proton physics fills in 2018.

For the low-frequency cluster, it is reported that changing the betatron phase advance between IP1 and 5 had an impact on the amplitude evolution of these harmonics, which further proves that they are coupled to the beam. A correlation with the power converters of the main dipoles has been demonstrated. The status of the active filters has an impact on their amplitude evolution, an effect which proves that all eight sectors contribute to this effect. The response of the lines depends on the beam energy, the beam that is considered and the order of the harmonic. A model to quantify the beam response to each sector cannot be determined at the moment. From these experiments, it is concluded that the

50 Hz harmonics extending up to 3.6 kHz are the result of a direct excitation due to noise in the LHC main dipoles.

The amplitude of the beam oscillations in the high-frequency cluster is larger if compared to the low-frequency cluster, hence the importance to identify its origin. If both clusters emerge from a common source, the question that arises is what is the mechanism that allows these high-frequency components to excite the beam. In fact, oscillations at such high frequencies are expected to be significantly attenuated by the shielding effect of the beam screen in the dipole magnets [101]. A review of the power converter's spectrum in sector 1-2 (Fig. 4.23)reveals that there is a reduction of the noise with increasing frequency. To this end, the impact of the harmonics above 3.6 kHz was expected to be negligible compared to the low-frequency cluster. On the contrary, experimental observations indicate the presence of important spectral components in the frequency regime of $\mathrm{f_{rev}} - \mathrm{f_x}$. More interestingly, the amplitude increase of the lines when the ADT settings are modified indicates that, in normal operation, the high-frequency cluster is suppressed by the damper. This fact underlines that, in the absence of the damper, there is a significant asymmetry between the two clusters in terms of amplitude as the high-frequency cluster is expected to be even further enhanced. Furthermore, an important observation is that there is a dependence of the cluster's location on the betatron tune. A resonant behavior of noise lines around $\mathrm{f_x}$ and $\mathrm{f_{rev}} - \mathrm{f_x}$ is indeed expected from a direct dipolar excitation but it does not explain the higher sensitivity observed around $\mathrm{f_{rev}} - \mathrm{f_x}$ compared to $\mathrm{f_x}$. Combining these information suggests that, rather than a direct excitation, the high-frequency cluster is the result of the interplay between noise from the dipoles and a mechanism originating from the beam. In particular, the transfer function from the power converter voltage to the magnetic field seen by the beam indicates that the noise reduces with increasing frequency however, it does not consider the beam response. Therefore, the asymmetry between the two clusters can be explained if there is a higher sensitivity of the beam response in the regime $\mathrm{f_{rev}} - \mathrm{f_x}$, leading to important offsets from small noise perturbations. For instance, a potential candidate is the interplay of the beam with the machine transverse impedance, as the first unstable mode is at $\mathrm{f_{rev}} - \mathrm{f_x}$ [102]. Further observations and experiments are necessary to verify this hypothesis and to identify the exact mechanism that is responsible for the asymmetry between the two regimes. Finally, it should be mentioned that, regardless of the perturbation source, it has been demonstrated that the transverse damper can effectively suppress these harmonics. To this end, the capabilities of the transverse damper can be employed in the future as a mitigation measure against this noise perturbation, without the need to apply modifications on the power converters.

In the context of these studies, a general framework for the analysis of the experimental data has been developed and presented in the previous sections. These tools include computing high-bandwidth spectra from bunch-by-bunch acquisitions while preserving the signal metric and reducing the noise threshold, as well as methods to determine whether a frequency component in the beam spectrum is the result of a real excitation. The analysis presented in this study can be used to address other types of noise effects. Following the experimental observations, the next sections are dedicated to simulation studies.

4.5 Controlled excitations

To study the impact of dipolar noise at various frequencies and amplitudes, controlled dipolar excitations were applied with the transverse damper during dedicated MD time in Run II [103]. These excitations were conducted at injection energy for two Fills, consisting of a single bunch and three trains of 48 bunches placed azimuthally symmetric in the LHC ring, respectively. Such a filling scheme provides a uniform sampling rate for the Fourier analysis of the ADTObsBox data. The aim of this section is to validate the simulations with noise and to reproduce some of the effects presented in the previous sections in a controlled manner.

4.5.1 ADT excitations during MD4147

Figure 4.27 shows the horizontal spectrum of Beam 1 during a controlled excitation at 2.5 kHz (star-shaped marker) in a Fill that consists of a single bunch. The important parameters of the excitation such as the frequency and the offset are computed from the spectrum. Using Eq. 4.6, the equivalent kick at the location of one of the ADT kickers is determined, assuming an observations point at the location of the Q7 pickup.

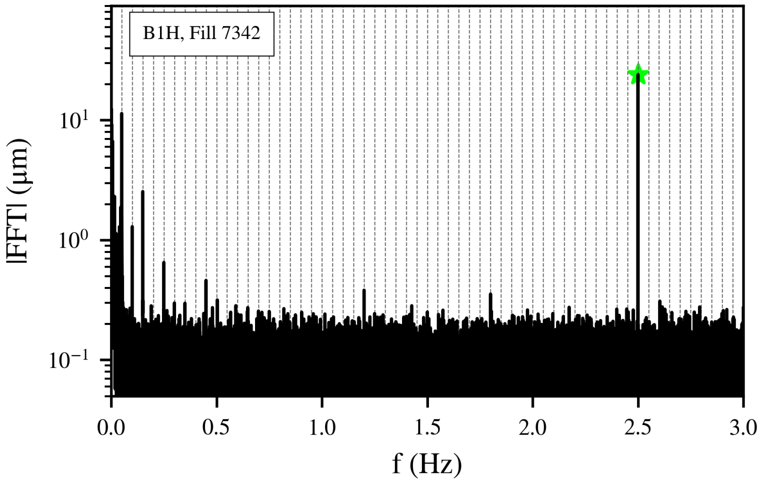

Figure 4.27: A controlled dipolar excitation at 2.5 kHz in the horizontal plane of Beam 1.

Iterating over all the excitations performed in the Fill, the values of the offsets, as well as the equivalent kicks, as a function of the excitation frequency are depicted in Fig. 4.28 (star-shaped markers). Furthermore, from the ADT parameters, the maximum deflection is computed which is then used to determine the maximum expected offset through Eq. 4.6. Both in the estimations of the deflections (left) and the impact on the transverse position (right), a discrepancy between the two is found by approximately a factor of 100.

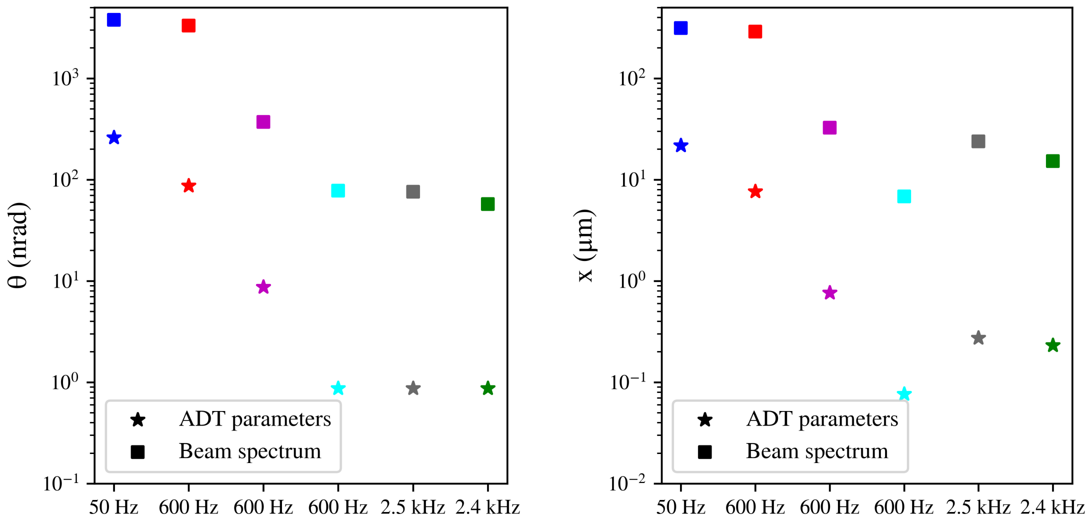

Figure 4.28: The maximum (star markers) and equivalent (square markers) deflections computed from the ADT parameters and the beam spectrum, respectively as a function of the excitation frequency (left). The offsets as observed in the beam spectrum (star markers) and as computed from the deflections based on the ADT parameters (square markers).

4.5.2 Validation of simulations

The impact of the excitations on the beam lifetime is compared against the DA thresholds computed with simulations in the presence of dipolar noise. To this end, simulations with the single-particle tracking code, SixTrack [54], have been performed. In the simulations, a distribution of particles, forming a polar grid in the configuration space, is tracked for 10^6 turns (≈90 seconds) in the LHC lattice at injection energy. The polar grid consists of nine angles and a radius from two to ten σ with a step of two σ. Furthermore, a horizontal modulated dipolar noise source is included at the location of one of the ADT kickers, while the observation point is located at the position of the Q7 pickup. The parameters used in the simulations are presented in Table 4.3. In each study, a different combination of the excitation frequency and amplitude is selected. In particular, considering a constant excitation frequency, the value of the kick is increased and the minimum DA is computed for each case. In this way, a noise amplitude threshold is defined and beyond this limit a reduction of DA is expected. Figure 4.29 presents the frequency of the excitation as a function of the deflection. A color code is assigned to the minimum DA to distinguish the regime where the noise has no significant impact (blue) from the one where a reduction of DA is expected (red).

Experimentally, some of the excitations lead to a significant reduction of the beam lifetime. To retrieve the initial deflection applied from the transverse damper, the offset and the frequency are extracted from the calibrated ADTObsBox beam spectrum. Then, based on these two parameters, the equivalent kick at the location of one of the ADT

Table 4.3: The LHC parameters at injection used in the simulations with dipolar noise.

Parameters (unit)	Values
Beam energy (GeV)	450
Bunch spacing (ns)	25
Betatron tunes (ν_x, ν_y)	(62.275, 60.295)
Normalised emittance (μm rad)	2.5
Chromaticity	15
Octupole current (A)	20
Bunch population (protons)	1.15e11
Horizontal β at Q7 (m)	130.9
Horizontal β at kick (m)	272.8

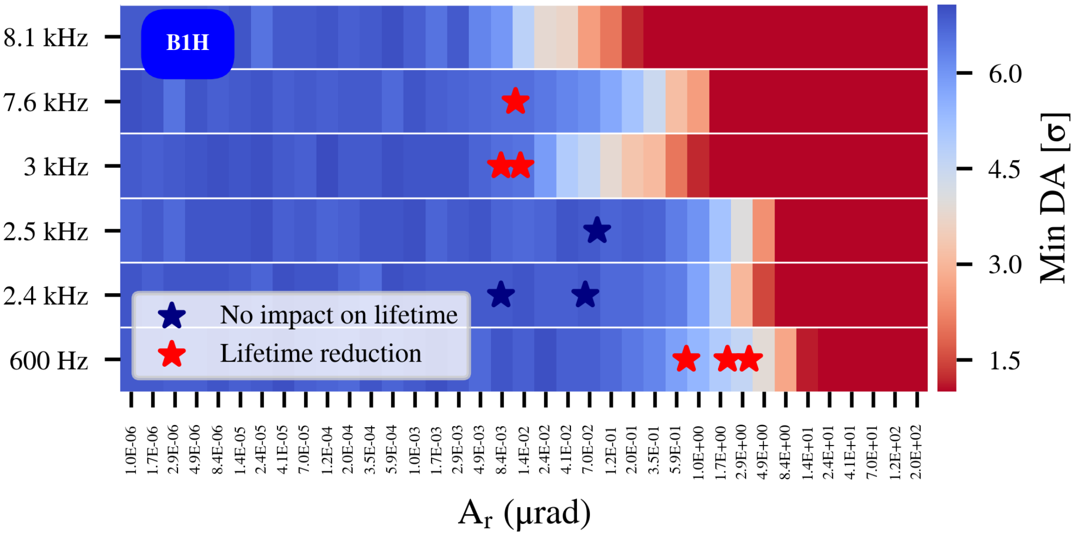

Figure 4.29: The frequency of the excitation as a function of the deflection. A color code is assigned to the minimum DA. The star shape markers present the equivalent kicks, as computed from the beam spectrum, during the controlled ADT excitations. The blue and red markers indicate whether a reduction of lifetime was or was not observed, respectively.

kickers is computed (see Section 4.5.1). In Fig. 4.29, the star-shaped markers illustrate the equivalent kicks and a color code is assigned to the markers that allows distinguishing the excitations that had no impact on lifetime (blue) from those that lead to proton losses (red). The comparison between experimental observations and the noise threshold defined by DA simulations yields that a good agreement is found between the two for the majority of the excitations.

It must be noted however, that the equivalent kick determined from the beam spectrum for an excitation at 600 Hz exceeds the maximum ADT kick strength (2 μrad at injection) [104, 105]. In particular, an important discrepancy is found between the maximum deflections retrieved from the ADT parameters and the ones computed from the beam spectrum for all the excitation frequencies (see Section 4.5.1). The offsets observed experimentally when exciting at multiples of 50 Hz are higher than the ones expected by a factor of approximately 100. Although the origin of this discrepancy has not been identified, this effect can be possibly attributed to the interplay between the controlled excitations at multiples of 50 Hz and the pre-existing 50 Hz harmonics that naturally arise in the spectrum due to power converter noise. Further experiments are required to validate this hypothesis.

Finally, both simulations and experimental observations indicate than an important impact on losses is observed in the presence of strong dipolar excitations at frequencies situated beyond the betatron tune spread such as the h=11 harmonic. This effect is due to the fact that a dipolar modulation, in combination with the non-linear elements of the LHC lattice, leads to a tune modulation through feed-down effects.

4.5.3 Horizontal and vertical coupling

The controlled excitations can improve the understanding of the role of the coupling in the presence of noise. Figure 4.30 illustrates the spectrum of the horizontal (magenta) and vertical (cyan) plane of Beam 1 during an excitation at 600 Hz. At this time interval, only the horizontal plane was excited, while the excitation is also visible in the vertical plane. This observation indicates that noise originating from a source that impacts only the horizontal plane, such as the main dipoles, is expected to also be present in the vertical plane. In particular, after normalizing the observed offsets with the corresponding β-functions, the comparison between the two planes yields a factor of 1.6% at injection energy.

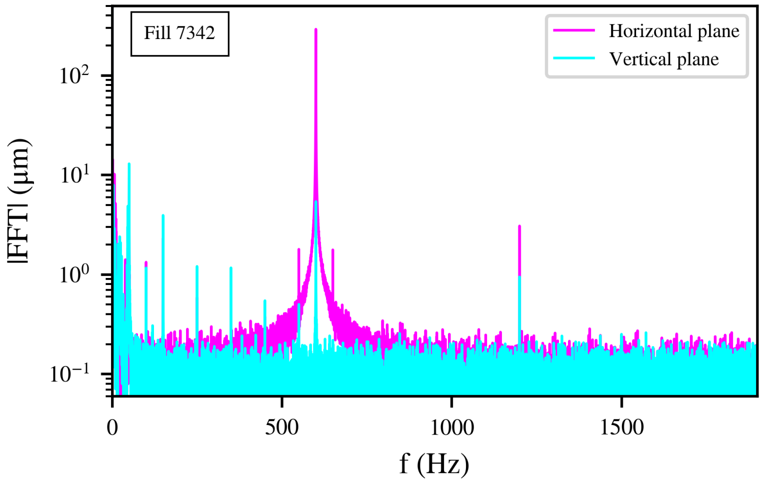

Figure 4.30: The impact of a horizontal controlled excitation at 600 Hz for the horizontal (magenta) and vertical (cyan) plane of Beam 1.

4.5.4 Coupling of Beam 1 and 2

Section 4.4.11 demonstrated that the bunch-by-bunch variations of one of the 50 Hz harmonics exhibit patterns compatible with beam-beam effects. To further investigate this observation, an excitation was applied at 600 Hz in the horizontal plane of Beam 1 with multiple trains injected in the machine. Based on the selected filling scheme, the two beams encounter at IP1 and 5. Figure 4.31 depicts the spectrum of Beam 1 (blue) and 2 (red) for the first bunch of the first train. Although the excitation was applied in Beam 1, it is also visible in Beam 2, an effect that was not observed during the single-bunch Fill.

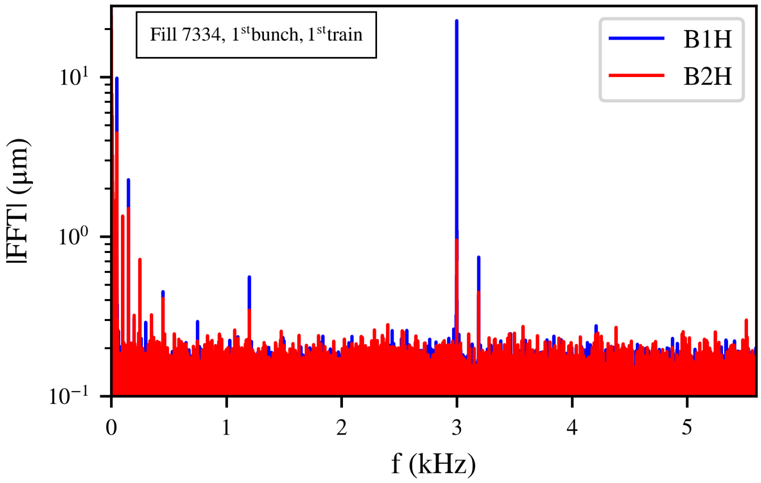

Figure 4.31: The horizontal spectrum of Beam 1 (blue) and 2 (red) during an excitation at 3 kHz, applied only in Beam 1, with a filling scheme consisting of multiple trains.

As the amplitude of the excitation exceeds the single-bunch noise baseline, the bunch-by-bunch variations of the injected noise can be computed. Figure 4.32 presents the amplitude evolution of the excitation as a function of the bunch position in the ring for Beam 1 (top) and 2 (bottom). The excitation is visible in Beam 2, although only Beam 1 was excited. The bunch-by-bunch variations observed in Beam 2 indicate that a maximum impact is observed at the center of the train, an effect that is consistent with the number of long-range encounters in IP1 and 5.

Furthermore, the amplitude evolution of the injected noise in Beam 1 yields that not all bunches experience the same offset, an effect that is also reported from the phase evolution of the noise (Section 4.5.5). The origin of these variations is yet to be identified, however it must be noted that these patterns are observed only in the presence of significant offsets. Reducing the amplitude of the injected noise leads to a reduction of the observed discrepancies between the bunches.

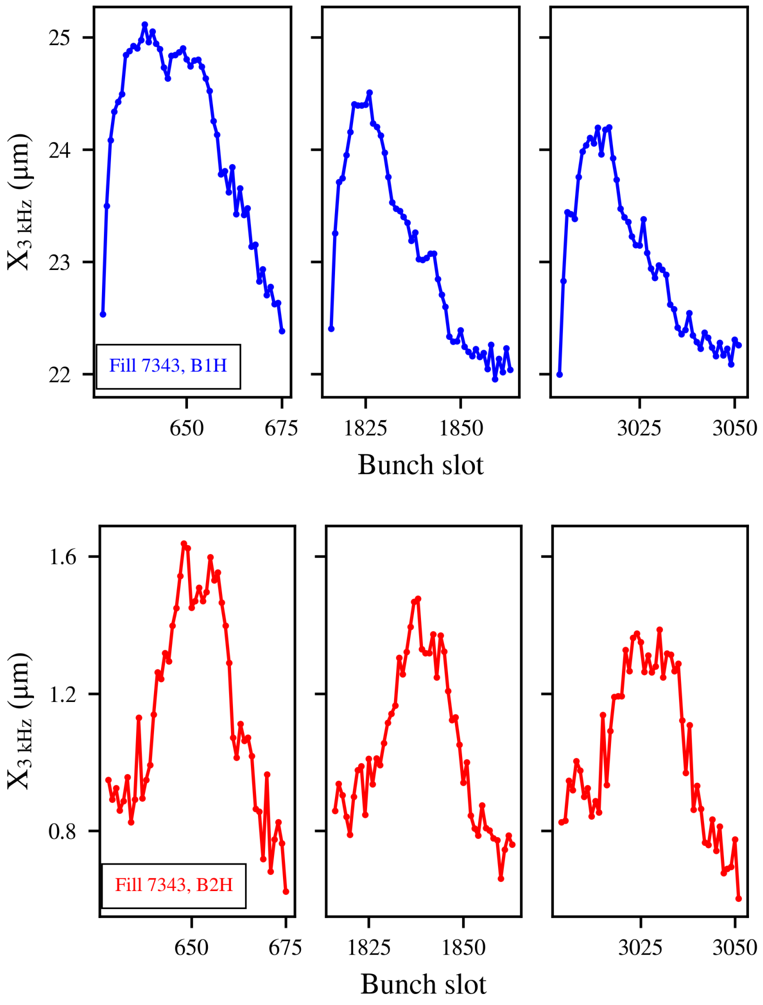

Figure 4.32: The bunch-by-bunch variations of the excitation at 3 kHz for Beam 1 (top) and 2 (bottom).

4.5.5 Phase evolution

The analysis method presented in Section 4.3 is based on the assumption that the dephasing of the bunch-by-bunch spectra is linearly proportional to the frequencies and the time delay of the trailing bunches compared to the reference i.e., the first bunch in the machine. Although this hypothesis has been validated with simulations, experimentally, with the present noise baseline, the bunch-by-bunch phase evolution of the harmonics cannot be directly computed. On the contrary, in the presence of a strong excitation, the determination of the bunch-by-bunch phase evolution is feasible as the amplitude of the noise line exceeds the noise floor of the single bunch spectrum. To this end, the bunch-by-bunch Fourier spectrum is computed during an excitation at 2.8 kHz in the horizontal plane of Beam 1, which resulted in an offset of 7.9 μm. Figure 4.33 demonstrates the phase evolution of the excitation across the three trains. A comparison with the expected phase evolution (gray dashed line) yields that a good agreement is found between experimental

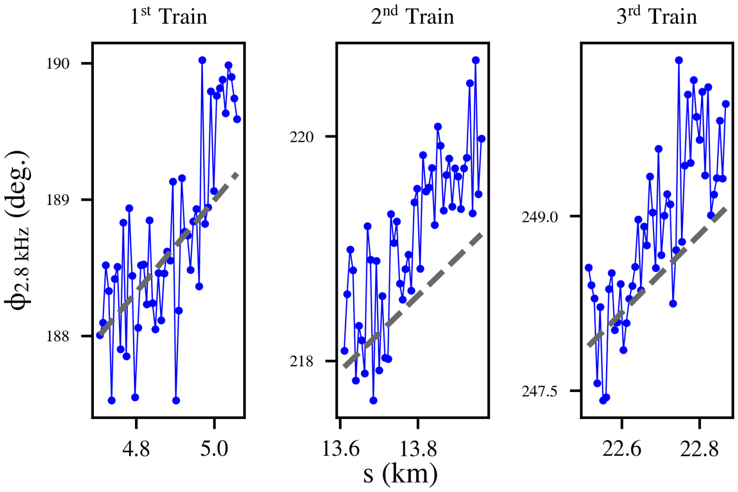

Figure 4.33: The bunch-by-bunch phase evolution of an excitation at 2.8 kHz and an offset of 7.9 μm as a function of the position of the trains in the ring. The expected dephasing is illustrated with the gray dashed line.

observations and predictions.

It must be noted however, that a discrepancy of a few degrees is observed during excitations that led to significant offsets. For instance, the phase evolution at 3 kHz is presented in Fig. 4.34 with an average offset of 23.9 μm. The mechanism that leads to these variations in terms of phase and amplitude (Fig. 4.32 top) is not yet identified. However, as the maximum excitations observed due to the 50 Hz are approximately 0.1 μm, this discrepancy is not expected to be an issue during normal operation.

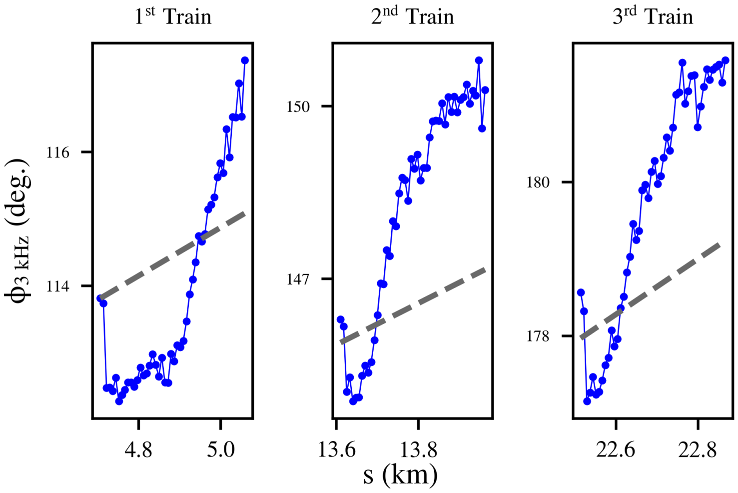

Figure 4.34: The bunch-by-bunch phase evolution of an excitation at 3 kHz and an offset of 23.9 μm as a function of the position of the trains in the ring. The expected dephasing is illustrated with the gray dashed line.

4.6 Simulations with noise

In the following section, the impact of modulated dipolar excitations on the LHC beam performance is discussed in terms of DA, diffusion and losses. The simulations are organized as follows. First, a scan in the noise parameter space $(\mathrm{f_r}, \mathrm{A_r})$ is performed, where $\mathrm{f_r}, \mathrm{A_r}$ represent the frequency and the amplitude of the noise, respectively. The aim of this study is to define the most dangerous tones of the low and high-frequency cluster, i.e., the frequencies that, for a constant excitation amplitude, have a maximum impact on the DA. In this context, the minimum amplitude of the excitation that leads to a reduction of DA is determined by considering individual tones. In the presence of multiple harmonics, similarly to the experimental observations, the impact on the beam performance is expected to be more significant. To this end, the offsets of the largest 50 Hz harmonics are extracted from the beam spectrum of a physics fill at Stable Beams. In Section 4.4.9, it was demonstrated that, as far as the low-frequency cluster is concerned, the noise is distributed in all eight sectors. An accurate representation of the noise propagation across the chains of the LHC dipoles requires a model of the transfer function as a transmission line for all the spectral components in the low-frequency cluster, similarly to the studies performed for the SPS [106]. Furthermore, as the exact mechanism of the high-frequency cluster is not yet identified, an accurate transfer function is not considered at the moment. To simplify these studies, a lumped noise model is employed. From the extracted offsets, the equivalent deflections are computed for a specific position in the LHC ring. In this way, the contribution of all the dipoles is represented by a single, equivalent kick and the offsets observed in the LHC spectrum are reproduced in the simulations.

The simulations are then repeated for the HL-LHC case. The need to perform projections for the HL-LHC is justified by the fact that no modifications are envisaged for the power converters of the main dipoles. Consequently, based on the source, the 50 Hz harmonic are expected to also be present in the HL-LHC era. In the following sections, the HL-LHC studies are based on the noise spectrum acquired experimentally from LHC, although the foreseen upgrade of the transverse damper system can lead to a more efficient suppression of the harmonics. The main parameters used in simulations for LHC and HL-LHC are presented in Table 4.4. The simulated conditions in the HL-LHC case correspond to the nominal operational scenario at the end of the β^*-levelling, taking place a few hours after the start of Stable Beams.

4.6.1 Impact of single tones on Dynamic Aperture

Similarly to Section 4.5, the DA simulations are performed for the LHC and HL-LHC lattice at collision energy. For each study, a different combination of the frequency and the amplitude of the excitation is selected. For each case, the minimum DA is compared to the value derived in the absence of noise. Figure 4.35 presents the results of the frequency scan as a function of the noise-induced offset for LHC (Fig. 4.35a) and HL-LHC (Fig. 4.35b). The offset is computed using Eq. (4.6) in the Section 4.2. Specifically, the harmonics of

Table 4.4: The LHC and HL-LHC parameters at Stable beams used in the simulations.

Parameters (unit)	LHC	HL-LHC
Beam energy (TeV)	6.5	7
Bunch spacing (ns)	25	25
Betatron tunes ($\nu_\mathrm{x}, \nu_\mathrm{y}$)	(62.31, 60.32/62.315)	(62.31/62.315, 60.32)
Normalised emittance (μm rad)	2.0	2.5
Chromaticity	15	15
Octupole current (A)	550	-300
Bunch population (protons)	1.25e11	1.2e11
IP1/5 Half crossing angle (μrad)	160	250
IP1/5 β^* (cm)	30	15
Horizontal β lumped noise (m)	105.4	102.3

the low and the high-frequency cluster that reside in the vicinity of $\mathrm{f_x}$ and $\mathrm{f_{rev} - f_x}$ have been selected for the analysis. A color code is assigned to the reduction of the minimum DA. From the scan, it is evident that the most dangerous frequencies are the ones that reside in the proximity of the tune and its alias. For the LHC, an offset threshold of 0.4 μm is defined, while this limit reduces to 0.2 μm for the HL-LHC. For comparison, the maximum excitation observed experimentally due to the 50 Hz lines is approximately 0.1 μm. The results of the simulations including a realistic noise spectrum with multiple tones are reviewed in the next section.

4.6.2 Frequency Map Analysis with a realistic noise spectrum

From the spectrum of a physics fill (Fill 7334), the offsets of the 40 largest 50 Hz harmonics are extracted. The equivalent kick at the location of the Q7 pickup is computed and used as an input for the noise simulations. Figure 4.36 shows the spectrum from the experimental observations (black) and the output of the simulations (green) after tracking a single particle at 0.1 σ and at an angle of 45 degrees for the low (left panel) and high (right panel) frequency cluster. The comparison of the two is a sanity check illustrating the good agreement between the simulated and the experimental beam spectrum. A similar agreement (between simulated and expected beam spectrum) is found for the HL-LHC case, were the equivalent kicks have been recomputed due to a small variation of the β-functions.

The studies have been organized in the following way: first, a study in the absence of noise is performed which defines the reference conditions. Second, the largest 50 Hz harmonics of the low-frequency cluster are considered. Then, a separate study is conducted including only the most important harmonics of the high-frequency cluster. Last, both regimes are included in the simulations. In the simulations, particles forming a polar grid in the configuration space from 0.1 to 6.1 σ with a step of 1 σ and 99 angles are tracked for 10000 turns in 5D. The turn-by-turn data are divided into two groups containing the

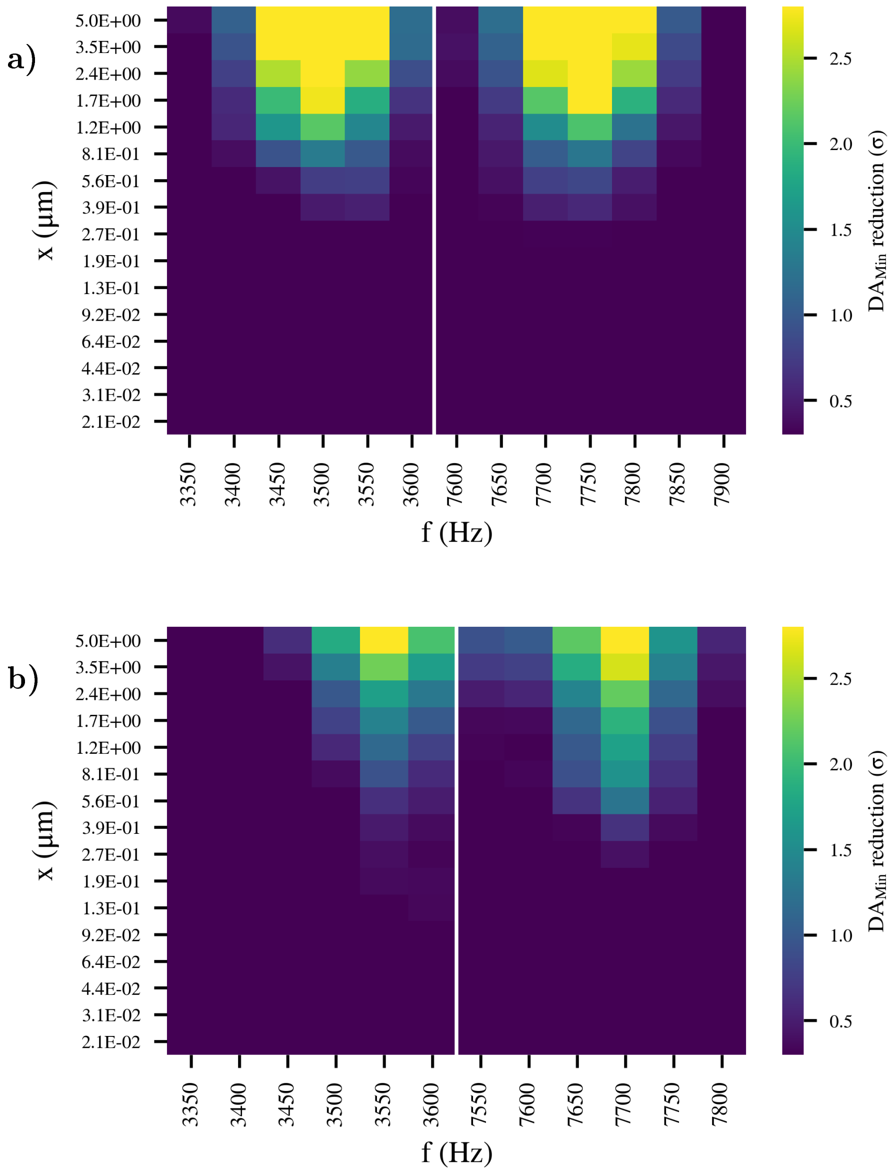

Figure 4.35: A scan of individual frequencies as a function of the offset for (a) LHC and (b) HL-LHC. A color code is assigned to the reduction of DA compared to the DA in the absence of noise.

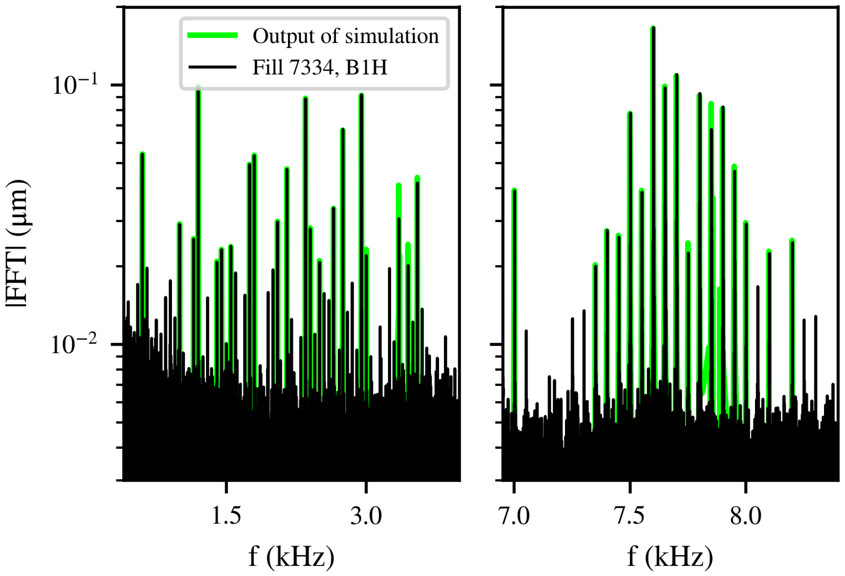

Figure 4.36: The spectrum for the low (left panel) and high (right panel) frequency clusters as acquired from the horizontal plane of Beam 1 for the physics Fill 7334 (black) and from tracking (green).

first and last 2000 turns, respectively. The tune of each particle is computed for each time interval using the NAFF algorithm. Comparing the variation of the tune of each particle across the two time spans reveals information concerning its tune diffusion. For the frequency map, the particle tunes of the second interval are plotted and a color code is assigned to the logarithm of the tune variations in the horizontal and vertical plane.

Figures 4.37 illustrate the frequency maps for the four studies in the LHC (Fig. 4.37a-4.37d) and the HL-LHC lattice (Fig. 4.37e-4.37h), respectively. The gray lines denote the resonances which intrinsically arise from the non-linear fields in the lattice. The second panel of each figure indicates the initial distribution in the horizontal and vertical x-y plane, which is color-coded with the diffusion. From the FMAs, it is observed that the dipolar noise results in an increase of the particles' diffusion through the excitation of additional resonances. In contrast to quadrupolar modulations, which lead to the excitation of sideband resonances, the location of the resonances in the presence of a modulated dipolar field error is equal to the frequency of the excitation. As the noise is injected in the horizontal plane, they appear as vertical lines in fixed positions for the low (black) and high (blue) frequency cluster. For the 50 Hz harmonics in the vicinity of the betatron tune and its alias, these additional resonances are located inside the beam's footprint. As shown in the x-y plane, the existence of such resonances impacts both the core and the tails of the distribution. These simulations indicate that the main contributor to the increase of diffusion are the spectral components in the high-frequency cluster. Furthermore, it must be noted that the simulations do not include effects such as electron-cloud and impedance, which have been experimentally observed in the LHC [107]. These non-linear fields lead to the excitation of additional resonances, as well, and the interplay between the two effects can lead to a further degradation of the beam performance than the one predicted in these simulations. The FMAs are an early indicator of the particle's stability and the increase of the diffusion due to noise suggests that a decrease of the beam's intensity may be observed. The next section is dedicated to the studies of the beam losses in the presence of noise.

4.6.3 Simulations of the beam losses

Quantifying the impact of the noise and the non-linearities on the beam intensity evolution requires the tracking of a 6D matched Gaussian distribution. In particular, if impacted by resonances as demonstrated in the previous section, particles at the tails of the distribution close to the limit of DA diffuse and will eventually be lost. Therefore, for these studies, a detailed representation of the tails of the distribution is needed.

To achieve this goal, weighted distributions are employed. The considered initial conditions of the tracked particles form a 4D round and randomly sampled distribution extending up to 6 σ both in the x-y and the xx'(yy')-plane. In the longitudinal plane, the momentum deviation of the particles is a uniform distribution that extends up to the limit of the bucket height. To reduce the statistical variations, 90000 particles are tracked in the LHC and HL-LHC lattice in 6D at collision energy for 10^6 turns. In the post-processing, a weight is assigned to each particle according to its initial conditions as computed from the probability density function (PDF) of a Gaussian distribution. In this way, significant statistics is achieved both for the core and the tails of the distribution. However, particles placed at the core of the distribution are assigned a larger weight than the ones at the tails and therefore, their contribution to the computations for losses is more important. Furthermore, a mechanical aperture is defined in the post-processing at 5 σ and particles beyond this threshold are considered lost.

Figure 4.38 presents the intensity evolution for the LHC (Fig. 4.38a) and HL-LHC (Fig. 4.38b) without noise (black), including the 50 Hz harmonics either of the low (blue) or high (orange) frequency cluster and considering both regimes (red). The results shows that, for the time span under consideration, the high-frequency cluster is the main contributor in the increase of losses. These simulations indicate that, based on a lumped transfer function of the noise, the 50 Hz harmonics lead to a reduction of the beam lifetime, which is already visible with a tracking equivalent to 90 seconds of operation. Considering the same noise spectrum for the HL-LHC case shows that a decrease in intensity is also observed. In both cases, the main contributor of proton losses is the high-frequency cluster.

Figure 4.39 illustrates the intensity evolution in the absence of noise (black), including the noise spectrum of Beam 1 (blue) and 2 (red). The fact that the noise spectrum of Beam 2 is lower by approximately a factor of two compared to Beam 1 results in an asymmetry of the intensity evolution between the two beams. In particular, by fitting the exponential decay of the intensity, a reduction of 23.2% and 6.6% in the lifetime of Beam 1 and 2, respectively, is observed compared to the reference conditions. This observation indicates

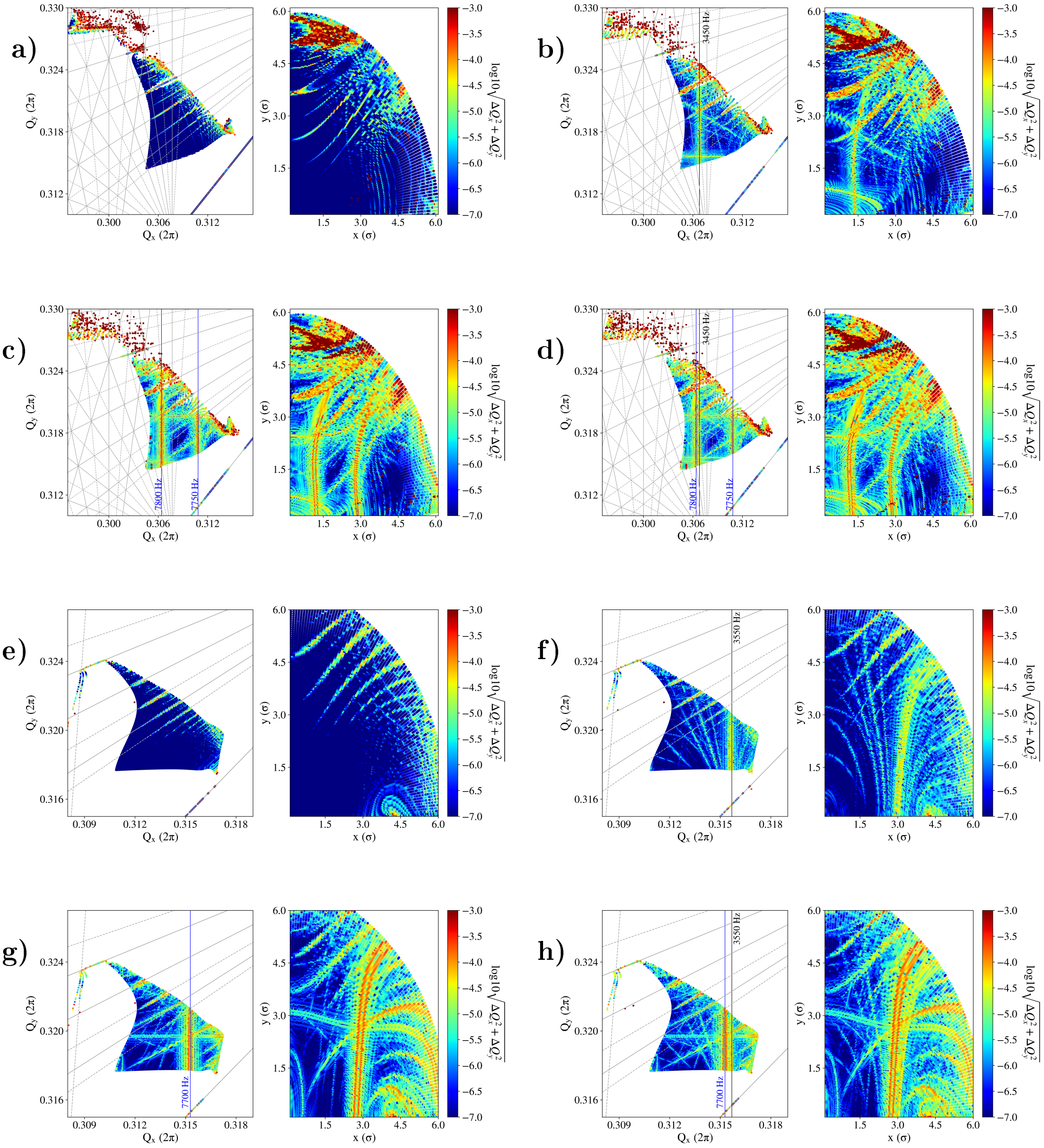

Figure 4.37: The frequency maps (left panel) and the initial configuration space (right panel) color-coded with the diffusion for the LHC (a) in the absence of noise , (b) with noise in the low and (c) high-frequency cluster and (d) combining both regimes. Similar studies are performed for HL-LHC ((e), (f), (g), (h)).

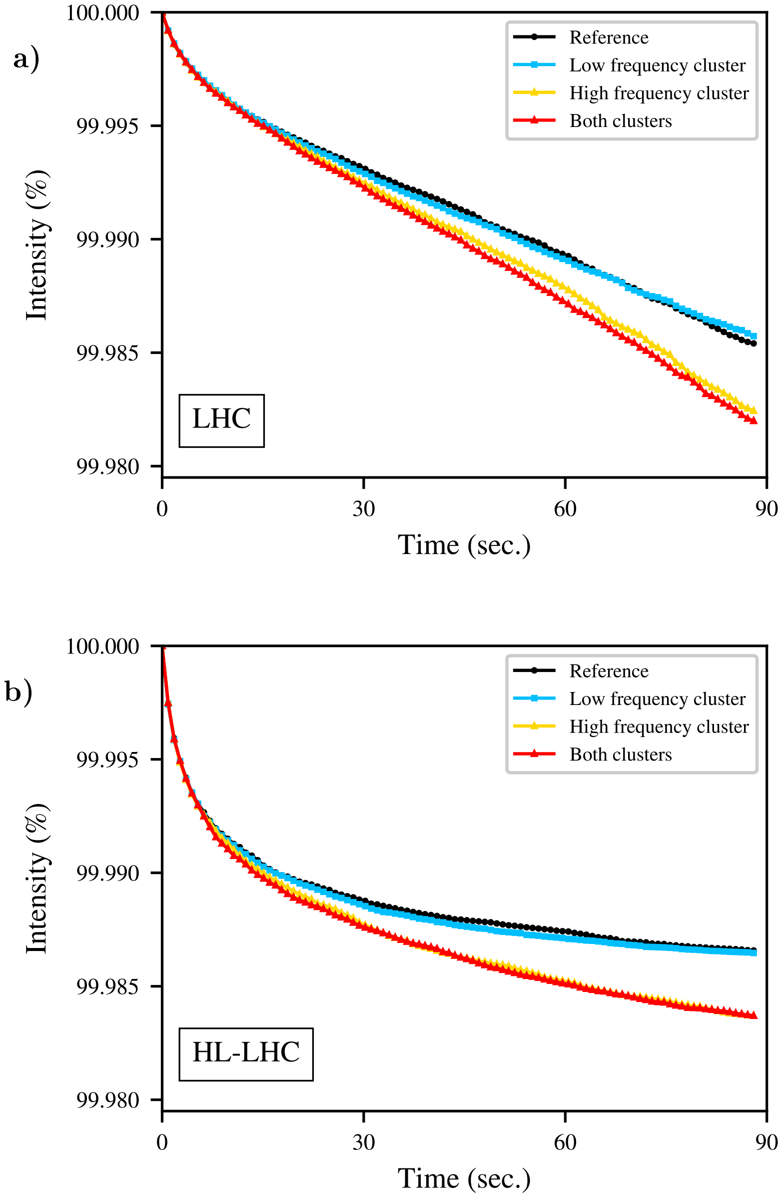

Figure 4.38: Intensity evolution for (a) the LHC and (b) the HL-LHC without noise (black), considering only the low (blue) or high (orange) frequency cluster and including the noise in both regimes (red).

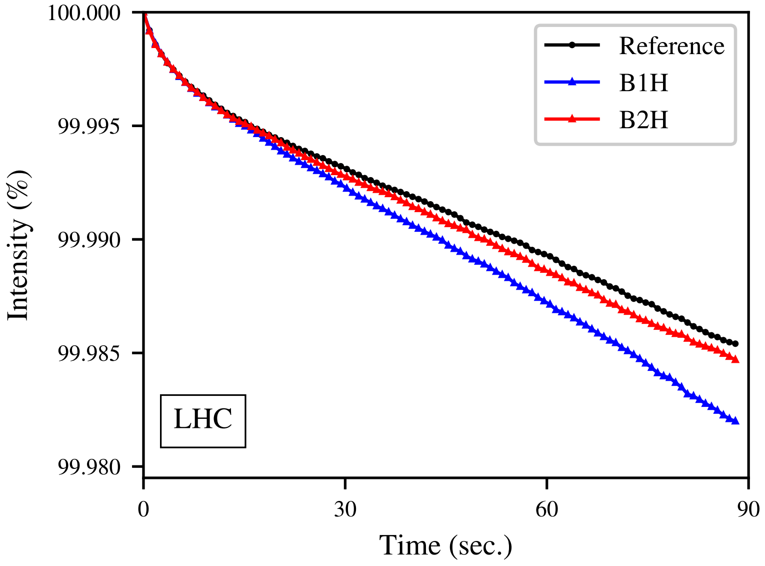

Figure 4.39: Intensity evolution for the LHC without noise (black), including the noise spectrum of Beam 1 (blue) and 2 (red).

that, amongst other effects, the noise contributes to the lifetime discrepancy between the two beams that has been observed experimentally.

Chapter 5

Tune modulation effects in the HL-LHC

5.1 Introduction

In order to optimize the performance of a high-energy particle collider such as the LHC, a thorough understanding of all the phenomena that can act as a luminosity degradation mechanism is required. A major concern for the transverse single-particle beam dynamics is the presence of noise, a mechanism that can impact the long term stability of the circulating particles. Noise can arise from various sources such as fluctuations of the magnetic fields, ground motion and the transverse feedback system. It has been previously reported that such a mechanism can cause emittance growth [21, 22, 24, 108], particle losses [23, 25] and eventually prove detrimental to the beam lifetime.

From the plethora of noise sources that are present in the accelerator, this chapter presents an approach to study the beam performance in the presence of a periodic perturbation in the strengths of the lattice magnets. Specifically, the analysis tools presented in this chapter are employed to investigate the implications of power supply ripple in the quadrupoles located in the high β-function regions. Ripples in the power supply voltage are converted into current ripples, depending on the magnet's impedance, which eventually leads to magnetic field perturbations through the magnet's transfer function (vacuum chamber, beam screen). As a result, these harmonic fluctuations induce a modulation in the normalized focusing strength of the quadrupoles. Depending on the frequency and the amplitude of the spectral components, a modulation of the betatron tune can arise with a modulation depth, i.e., the maximum tune variation from its unperturbed value, that is proportional to the β-function at the location of the perturbation. If present, this effect is combined with the tune modulation that intrinsically emerges for off-momentum particles from the coupling of the longitudinal and transverse plane through chromaticity [109]. In the presence of non-linearities, tune modulation effects may lead to the excitation of sideband resonances, that, depending on the modulation frequency, can either overlap, leading to chaotic trajectories [52, 53], or reach the tune footprint, thereby acting as an additional diffusion mechanism for the particles in the distribution [29]. In the latter case, the existence of such resonances critically limits the available space in frequency domain for an optimized, resonance-free working point. Subsequently, it is important to investigate whether the combination of the tune modulation induced by noise and synchro-betatron coupling will pose a limitation to the luminosity production of the future LHC upgrade, the HL-LHC.

Tune modulation effects have been reported in the past from several hadron synchrotrons and colliders. Simulations in the Tevatron, using a linear decoupled rotation and a weak-strong approximation of the beam-beam kick, showed that a tune modulation can lead to emittance growth [110]. In particular, the interplay between the resonances excited by the beam-beam interaction and the tune modulation led to emittance blowup for a modulation depth and period of 0.01 and 1000 turns, respectively. Additional chaotic trajectories were observed once the period of the modulation was increased, an effect which was correlated with the blow-up. In the SPS, the large tune spread observed experimentally was associated with the presence of power supply ripples [26, 28]. During dedicated experiments, a tune modulation was introduced at various frequencies in the presence of significant non-linearities. A critical modulation depth threshold below 10^{-3} was defined for acceptable performance. The combined effect of two modulation frequencies was experimentally proven to be more severe compared to a single frequency with an equivalent modulation depth. The presence of two modulation frequencies led to a more rapid lifetime decrease and to a shift of the chaotic boundary towards lower amplitudes. The increase of the losses and emittance growth was correlated with the overlap of multiple resonances [27]. The studies conducted at RHIC investigated the combined effect of synchrotron motion and power supply ripples on the DA. A linear correlation between the DA reduction and the synchrotron or gradient modulation depth was identified [111, 112]. By including in the simulations the voltage tones obtained from experimental observations, in combination with a modulation depth of 10^{-3} from synchro-betatron coupling, a DA reduction was observed for a variation of 10^{-5} in the quadrupolar current [76]. Furthermore, a tune modulation was also observed due to the difference in the Radio Frequencies (RF) of the two beams that led to a variation of the beam crossing location in the Interaction Region (IR), an effect that was not present once the RF were synchronized [75]. It was reported that a modulation depth of 10^{-3} had a detrimental impact on the beam lifetime. In HERA, a threshold of 10^{-4} in the modulation depth was defined from analytical derivations in the presence of both beam-beam effects and a high-frequency tune modulation, a limit which was also verified experimentally by injecting external noise [30]. A dependence of the particles' diffusion on the modulation frequency was shown. For the first time, a tune ripple feedback was employed for the compensation of the power supply ripples by injecting an additional modulation with the same amplitude and an opposite phase [29, 113]. During these experiments, the use of such a compensation scheme proved to be beneficial for the beam lifetime.

The upgrade of the LHC to the HL-LHC aims to reach an integrated luminosity of

250 fb^{-1} per year [114]. To achieve this goal, the LHC will be operating with low beam emittances, high intensities, an unprecedented $\beta^* = 15$ cm at the Interaction Points (IPs) of the high luminosity experiments (IP1 and 5), and thus the beams will be subjected to strong beam-beam interactions. In addition to the incoherent effects, the suppression of the coherent beam motion requires the operation of the machine in a high chromatic and octupolar current regime for the mitigation of the collective instabilities. This configuration results in to significant non-linearities. Furthermore, a key component in the HL-LHC project is the upgrade of the IRs around IP1 and 5. An important modification concerns in the inner triplet layout, which provides the final focusing of the beam in the two high-luminosity experiments. Reducing the beam size at the two IPs results in the increase of the maximum β-functions at the quadrupoles of the inner triplet, rendering the beam more sensitive to magnetic field fluctuations at this location. Due to the combined effect of the significant non-linearities that arise from this configuration and the higher β-functions, a larger sensitivity to noise effects is anticipated.

The unprecedented high-values of the maximum β-functions at these locations, in combination with the next triplet generation based on Nb_3Sn technology that is currently being developed, justifies the need to perform a complete analysis on the beam performance implications of a modulation in the quadrupole gradients. Therefore, our investigation focuses on the four quadrupoles, namely Q1, Q3 (MQXFA magnets) and Q2a, Q2b (MQXFB magnets), circuits which are electrically powered in series. Previous studies for the HL-LHC have revealed a dependence of the DA reduction on the modulation frequency and specifically, a more significant effect to noise at 300 Hz and 600 Hz [115]. In the context of this investigation, the aim of the present chapter is to explain the sensitivity to power supply ripples at particular frequencies and to quantify their impact with 5D and 6D single-particle tracking simulations, including beam-beam effects, in terms of tune diffusion, intensity evolution and DA.

This chapter is organized as follows. In Section 5.2 a simplified formalism with a linear decoupled rotation, a modulated quadrupole and non-linear elements is employed. Starting from the characterization of the single-particle spectrum and extending to a distribution of particles, the impact of the modulation in configuration space and frequency domain is reported. These observations are then validated with tracking simulations in the HL-LHC lattice, including noise in the inner triplets of the high luminosity experiments and/or synchro-betatron coupling in Section 5.3. The results of these studies are compared to the power converters specifications to determine whether noise in the triplet will be an issue of concern for the beam performance in the future operation. Further investigation is performed with frequency maps to understand the increased sensitivity to specific modulation frequencies. Finally, multiple voltage tones are included in the analysis and the expected impact on diffusion and intensity evolution is evaluated.

5.2 Modulated simplified map

The effect of a tune modulation in a one-dimensional non-linear Hamiltonian system has been extensively studied in the past [23, 51, 116]. These studies have shown that, depending on the modulation tune, Q_m, and modulation depth, ΔQ, the impact on the transverse motion varies. Through an analytical formalism, in the presence of a single resonance with an island tune Q_I and a tune modulation, four regimes of interest were identified in the tune modulation $(Q_m, \Delta Q)$ parameter space [23, 51, 116]. As an example, Fig. 5.1 illustrates the four regimes in the tune modulation parameter space for the sixth-order resonance. First, a low amplitude and frequency modulation causes a time variation of the particles' actions, without affecting their stability (*Amplitude modulation* regime). Second, increasing the frequency leads to the appearance of sideband islands around the resonance, in a distance equal to the modulation tune. For small depths, the islands occupy a limited portion of the phase space (*Frequency modulation*). As the modulation depth increases, the amplitude of the high-order sidebands becomes significant (*Strong sidebands*). The combination of a strong modulation in terms of amplitude and a frequency below a critical value, results in the overlap of the resonance islands, hence leading to chaotic motion (*Chaos*).

The existence of islands in the phase space originating from the strong non-linearities of the lattice was experimentally demonstrated through observations of persistent signals in the beam position measurements [31]. Then, by injecting noise that resulted in a tune modulation, the particles were driven outside of the resonance islands. Based on the beam response, the existence of the three out of four regimes in the tune modulation parameter space was experimentally verified [32]. In this context, the present study investigates the effect of power converters ripples in the voltage-controlled regime, which extends beyond a critical value of a few Hz [101]. Subsequently, the regimes of interest in the aforementioned parameter space are the *Frequency modulation, Strong sideband* and *Chaos*, where emittance growth and particle losses occur. The *Amplitude modulation* regime is not discussed in the present study as it mainly refers to low-frequency noise.

This section focuses on the description of the particles' motion under the influence of a modulated quadrupole using a simplified formalism based on a linear decoupled rotation and non-linear elements. As a starting point, a 2D model is employed to illustrate the modulation in frequency domain in the absence of non-linearities. The impact of the three regimes of interest in the tune modulation parameter space is then summarized by accounting for non-linearities. The transfer map is then extended to 4D to study the instantaneous variation of the tune footprint and the sideband resonances with frequency maps.

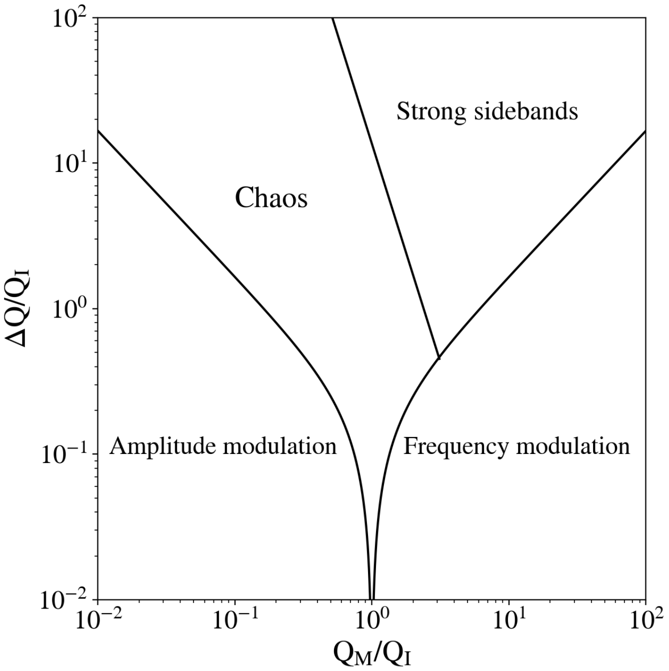

Figure 5.1: The four regime in the tune modulation parameter space for a modulation tune Q_m and depth ΔQ with an island tune Q_I [23, 51, 116].

5.2.1 Tune modulation in 2D

Instantaneous tune

As a first step, a single particle with a zero initial transverse momentum is tracked in a lattice that consists of a linear rotation and a modulated quadrupole (without including non-linearities). A tune modulation is induced by varying the quadrupolar strength turn-by-turn with a sinusoidal function at a single frequency, rather than directly modulating the tune in the rotation matrix. The variation of the tune, namely instantaneous tune, as a function of the turn number n is represented by:

$$Q_{inst}(n) = Q_0 + \Delta Q \cdot \cos(2\pi Q_m n), \tag{5.1}$$

where Q_0 is the unperturbed tune in the absence of the modulation, ΔQ and Q_m is the modulation depth and tune, respectively. The rotation is divided into eight segments with equal values of the betatron phase advance and the position measurements are retrieved after each segment. This method provides a uniform sampling for the analysis in frequency domain. In this way, the sampling rate increases by a factor of eight and an accurate tune determination with a limited number of turns is achieved using the implementation of the NAFF algorithm. An approximation of the instantaneous tune is computed with a sliding window of 30 turns in steps of one turn. Such a window length was found to be a good trade-off between time and frequency resolution for the tune determination.

The two parameters of interest are the modulation depth ΔQ and tune Q_m, the ratio of which defines the modulation index β_m. Figure 5.2 demonstrates the evolution of the instantaneous tune for an increasing value of the modulation depth (Fig. 5.2a), considering a constant frequency, and for several values of the modulation frequency with a constant depth (Fig. 5.2b), assuming the LHC revolution frequency ($f_{\mathrm{rev}} = 11.245$ kHz). The gray dashed line represents the unperturbed tune in the absence of a tune modulation. In particular, in the case of a tune modulation induced by noise in a quadrupole, the modulation depth is proportional to the β-function at the location of the perturbation and the maximum variation of the quadrupole normalized strength. Similarly, in the presence of synchro-betatron coupling, the modulation index depends on the chromaticity, the momentum deviation of the particle and, in this case, the synchrotron tune is the modulation frequency [117]. It must be noted however, that for a matched bunch, as all the particles in the distribution experience the same quadrupolar modulation, this coherent effect can be measured. On the contrary, due to the different momentum deviations of the particles in the distribution, synchro-betatron coupling is more difficult to measure experimentally.

Average single-particle spectrum

To illustrate the importance of the modulation index and its impact on the particle's motion, the tracking is extended to 10^4 turns. During this time span, the variation of the tune depicted in Fig. 5.2 is averaged over several modulation periods. As in every frequency modulated signal, considering the betatron motion as the carrier and the noise as the modulator, the particle's trajectory is represented in time domain by a sum of co-sinusoidal signals, weighted by the Bessel functions of the first kind [118]. By integrating Eq. (5.1), the frequency-domain representation of the betatron motion, after normalizing by the maximum amplitude, is:

$$\begin{aligned} |\tilde{X}(Q)| = \sum_{k=-\infty}^{\infty} J_k(\beta_m)[\delta(Q - Q_0 - k \cdot Q_m)+ \\ \delta(Q + Q_0 + k \cdot Q_m)], \end{aligned} \tag{5.2}$$

where $\beta_m = \frac{\Delta Q}{Q_m}$ is the modulation index, J_k are the Bessel functions of the first kind and δ is the Dirac function. Consequently, the spectrum consists of infinite harmonics of the modulation frequency around the betatron frequency with a relative amplitude that depends on the modulation index. In particular, the k-order Bessel function for a modulation index β_m determines the amplitude of the k-order sideband, with $k = 0$ representing the betatron tune. Figure 5.3 presents the Fourier spectrum as computed with the NAFF algorithm (black) and analytically from Eq. (5.2) (green). In the first four cases, the modulation depth is constant, while the frequency reduces from 800 Hz (Fig. 5.3a) to 400 Hz (Fig. 5.3b), 200 Hz (Fig. 5.3c) and 100 Hz (Fig. 5.3d). In each case, sidebands around the betatron tune (blue) are present in the spectrum at a distance equal to multiples of the modulation frequency. The distance of the first positive sideband from the betatron frequency is also depicted (red). Based on the fact that the modulation index

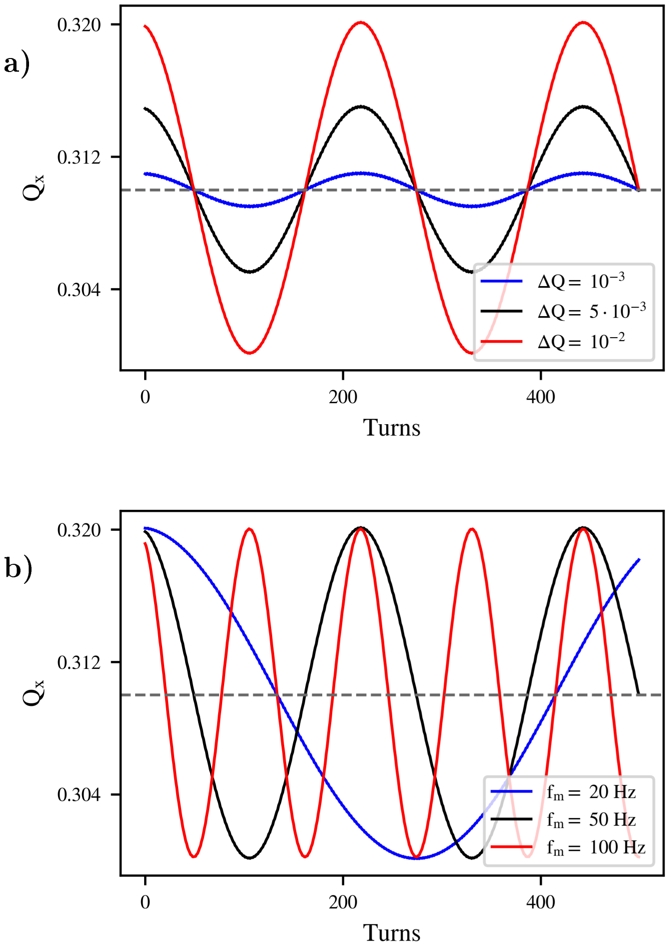

Figure 5.2: (a) (a) An approximation of the instantaneous tune in the presence of a modulated quadrupole for $f_m = 50$ Hz and $\Delta Q = 10^{-3}$ (blue), $\Delta Q = 5 \cdot 10^{-3}$ (black) and $\Delta Q = 10^{-2}$ (red). (b) An approximation of the instantaneous tune for $\Delta Q = 10^{-2}$ and $f_m = 20$ Hz (blue), $f_m = 50$ Hz (black) and $f_m = 100$ Hz (red). The horizontal gray line denotes the unperturbed betatron tune.

is inversely proportional to the frequency, decreasing the frequency for a constant depth leads to an increase of the modulation index. Subsequently, higher-order sidebands with larger amplitudes are visible in the spectrum for lower frequencies.

Then, for a constant modulation frequency at 100 Hz, the modulation depth is increased (Fig. 5.3d to 5.3f). Reviewing the spectra shows that for $\beta_m \geq$1.5, due to the strong modulation, the amplitude of the sidebands exceeds the one of the betatron tune (Fig. 5.3e) and for specific values of the modulation index the amplitude of the betatron peak can also be suppressed (Fig. 5.3f). In such cases, using a peak-detection algorithm that sorts the frequencies by decreasing amplitude, such as NAFF, will return the frequency determination of the sideband peak rather than the one of the betatron tune. To overcome this problem, in the presence of a strong modulation, the algorithm's frequency range of search should be limited in the vicinity of the betatron tune. This is not always possible as for small modulation frequencies, the limited resolution does not allow to disentangle the sideband from the betatron peak. For instance, in the LHC, the modulation induced by the synchrotron motion ($f_m \approx$20 Hz) to a particle which is placed in the limit of the bucket height ($\Delta p/p = 27 \cdot 10^{-5}$) and in the presence of a high chromaticity ($Q' = 15$) leads to a modulation index which exceeds the critical value of 1.5 ($\beta_m = 2.25$). For the purpose of the study presented in this chapter, the tracking is, in this case, performed either in 4D or 5D, i.e., neglecting the impact of the synchrotron motion or in 6D with a lower chromaticity and thus, a lower modulation depth.

Tune modulation and non-linearities

Non-linear fields are an important aspect of the accelerator's lattice, introduced for the correction of the chromatic aberrations and the action-dependent detuning of the particles. Of particular interest in this study is the interplay between non-linearities and the tune modulation. To illustrate this effect, first, an octupolar element is included in the map and the working point is moved in the vicinity of a horizontal sixth order resonance. A distribution of particles with linearly increasing horizontal actions is tracked in the simplified lattice. First, Fig. 5.4a shows the turn-by-turn phase space, which reveals that several particles are trapped in the resonance islands. Second, a modulated quadrupole is included, with a combination of noise parameters ($\mathrm{Q_m}, \Delta \mathrm{Q}$) that correspond to the *Frequency modulation* regime. For the Poincaré section, the stroboscopic technique is used, where the horizontal coordinates are plotted once per modulation period. The phase space depicted in Fig. 5.4b reveals the existence of sideband islands (red) in the vicinity of the ones presented in Fig. 5.4a. Finally, the parameters of the modulation in Fig. 5.4c correspond to the limit of the *Strong sideband* and *Chaos* regime. In this case, the simultaneous reduction of the modulation frequency and increase of the modulation depth results in overlapping higher-order sidebands (red), thus creating layers of chaotic motion.

Similarly, the action-angle variables are computed for each of the aforementioned cases. Furthermore, the tune of each particle is computed with the NAFF algorithm in order to illustrate the position of the sideband islands in frequency domain. Figure 5.5 depicts the

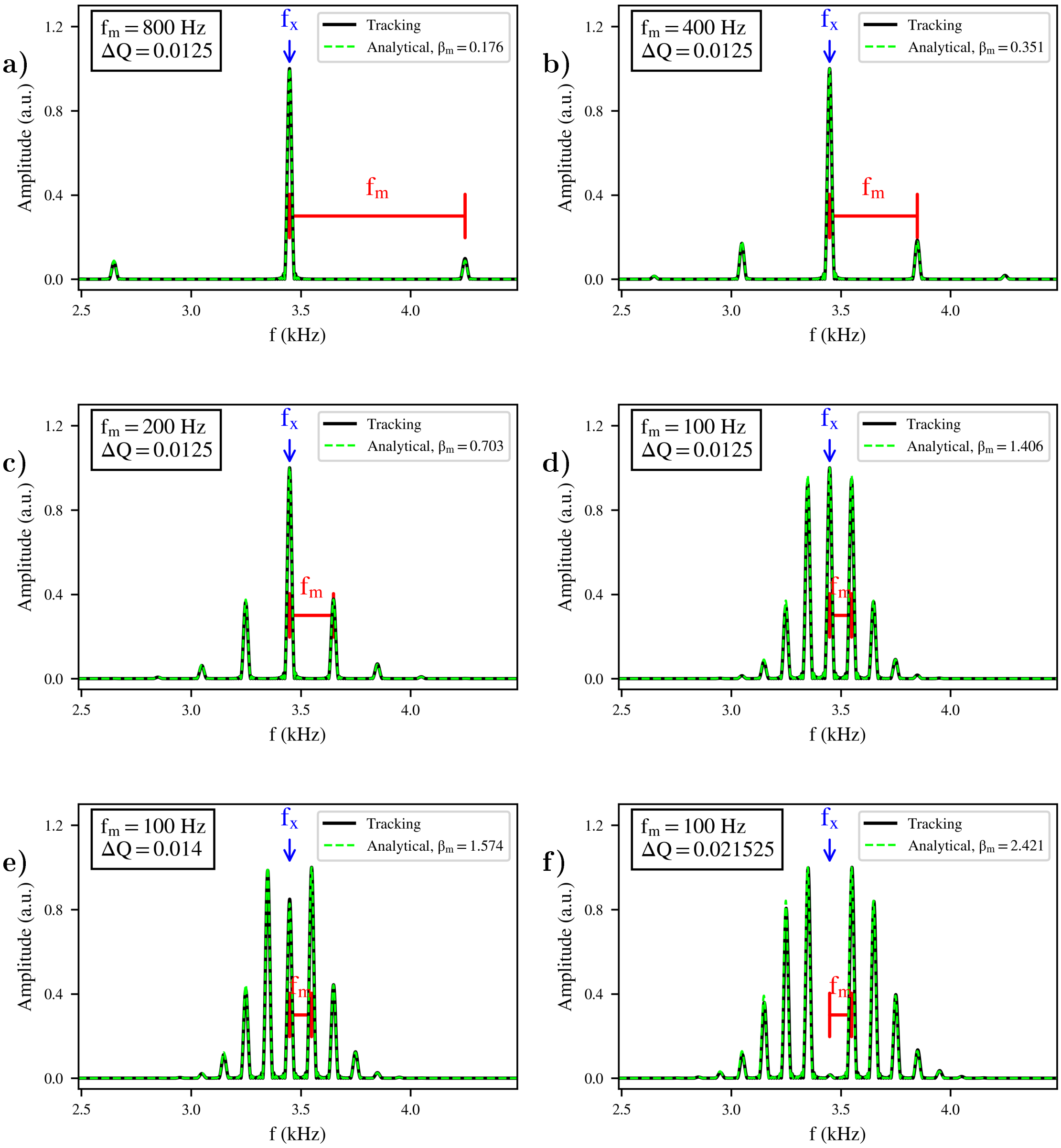

Figure 5.3: The normalised single-particle spectrum in the presence of a tune modulation at (a) 800 Hz, (b) 400 Hz, (c) 200 Hz and (d) 100 Hz and $\Delta Q = 1.25 \cdot 10^{-2}$ and with (e) $\Delta Q = 1.4{\cdot}10^{-2}$, (f) $\Delta Q = 2.2{\cdot}10^{-2}$ at 100 Hz. The green curve indicates the representation of the particle's motion with the sum of Dirac functions weighted with the Bessel functions of the first kind for the various modulation indexes. The betatron frequency (blue) and its distance from the first positive sideband (red) are also depicted.

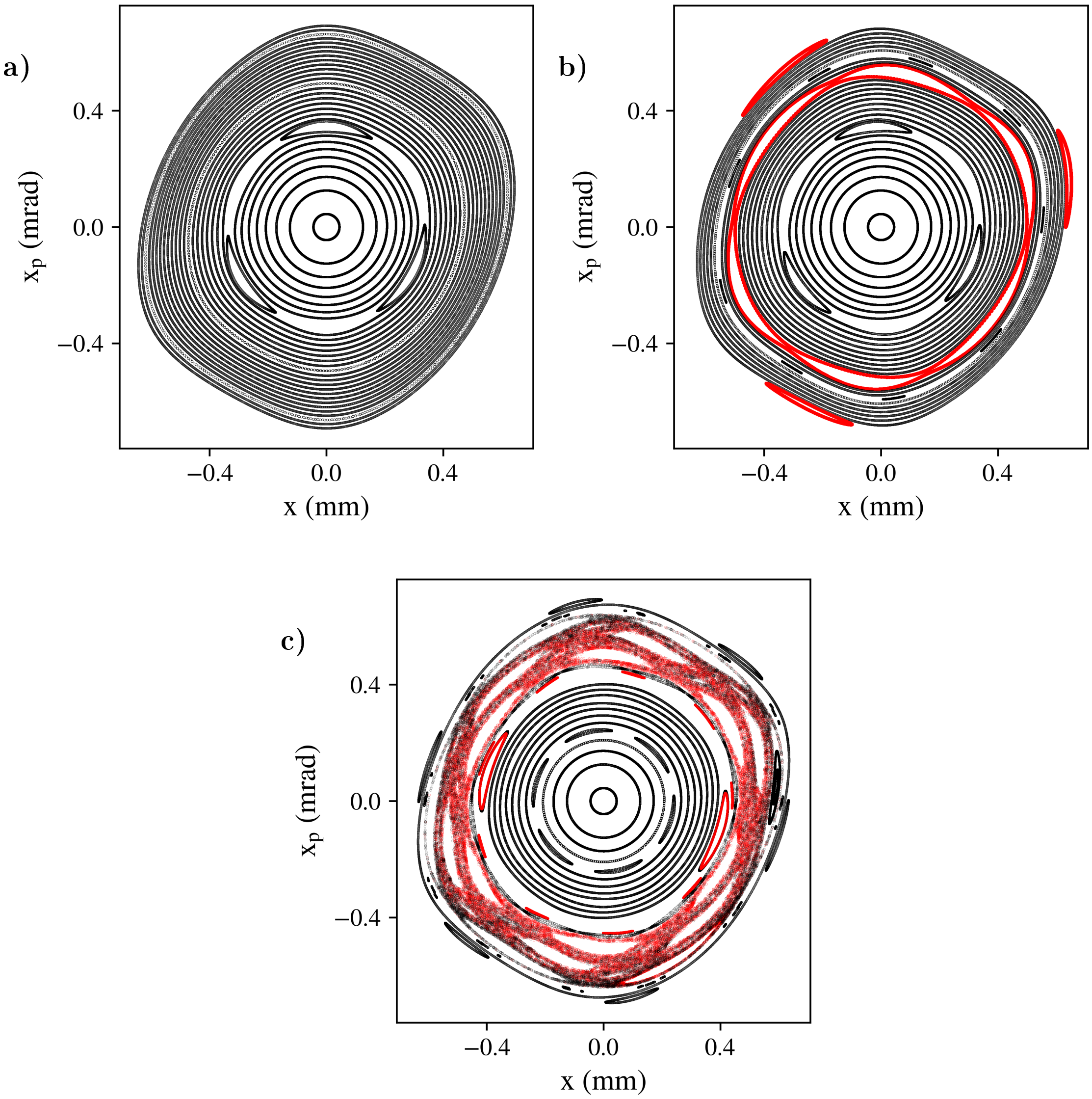

Figure 5.4: The phase space in the presence of non-linearities (a) without a tune modulation, (b) with a tune modulation in the *Frequency modulation* regime and (c) in the *Strong sidebands / Chaos* regime.

action-angle variables (left panel) and the tune as a function of the action (right panel). In the absence of a tune modulation (Fig. 5.5a), the islands correspond to the trapping of the particles in the sixth-order resonance (vertical gray line). In the *Frequency modulation* regime (Fig. 5.5b), the tune determination indicates that the additional resonances are the first and second-order sideband of the modulation frequency (red vertical lines). The additional resonances are located in a distance equal to multiples of the modulation frequency. In the last case (Fig. 5.5c), the particles are trapped up to the fifth-order sideband of the modulation frequency and the chaotic motion of the particles is also visible in their tune determination.

5.2.2 Tune modulation in 4D

Instantaneous tune footprint

The aim of this section is to extend the previous observations to additional degrees of freedom. In 4D and for a distribution of particles, the tune modulation of each particle is translated into a time variation of the footprint. To illustrate this effect with tracking, the initial conditions of the distribution form a polar grid in the configuration space up to 6 σ with vanishing initial transverse momenta. The map consists of a linear rotation, an octupole and a modulated quadrupole. The selected modulation frequency is 20 Hz, which corresponds to a modulation period of $\approx$560 turns in the LHC lattice. Such a frequency has been selected to simulate the impact of the synchro-betatron coupling for off-momentum particles in the LHC in the presence of a non-zero chromaticity, as the synchrotron frequency corresponds to approximately 20 Hz. In addition, the linear rotation is divided into eight segments to simulate the eight arcs of the LHC and the transverse coordinates are retrieved after each segment. Combining the data from the eight observation points, the sampling rate increases by a factor of eight compared to the case of a single observation per revolution. Then, an approximation of the instantaneous footprint is computed with a window length of 50 turns, which was found to be a good trade-off between time and frequency resolution for the tune determination of each particle. Figure 5.6 illustrates the instantaneous footprint for the first (left panel) and second (right panel) half of the modulation period and a step of 10 turns. The sequential color map represents the time evolution with the start and end of one modulation period shown in black and yellow, respectively. The maximum excursion of the footprint from its unperturbed position depends on the selected modulation depth. From the review of the instantaneous footprint, it can be seen that the particles cross several resonances (gray lines) during the modulation period, even if the selected working point is in a resonance-free area of the tune space.

Frequency Map Analysis with tune modulation

In Section 5.2.1 it was shown that, in the presence of non-linearities, the variation of the tune eventually leads to the excitation of sideband islands. Similarly, averaging the variation of the instantaneous footprint over several modulation periods leads to the

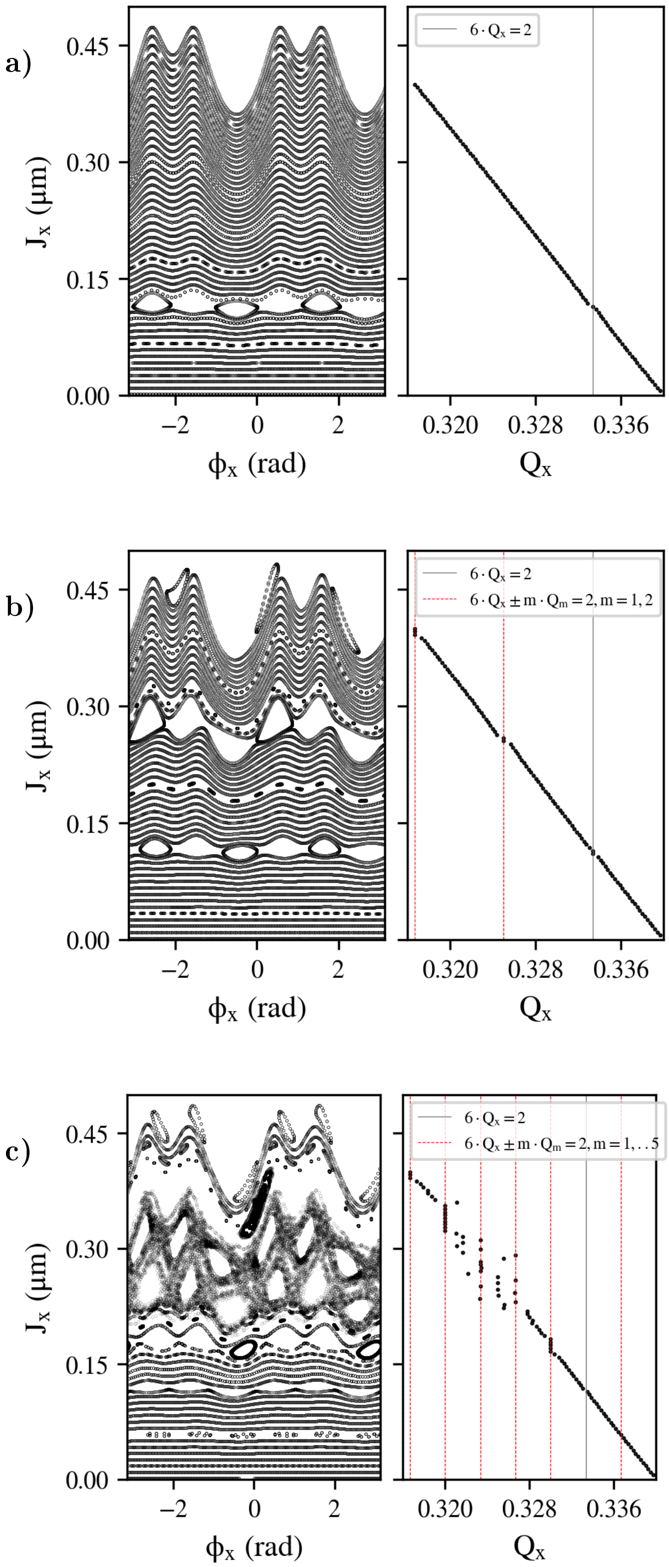

Figure 5.5: Action-angle variables (left panel) in the presence of non-linearities (a) without a tune modulation, with a tune modulation (b) in the *Frequency modulation* regime and (c) in the *Strong-sideband/Chaos* regime, next to the tune of each particle as a function of its action (right panel). The vertical lines represent the nominal (gray) and sideband (red) resonances.

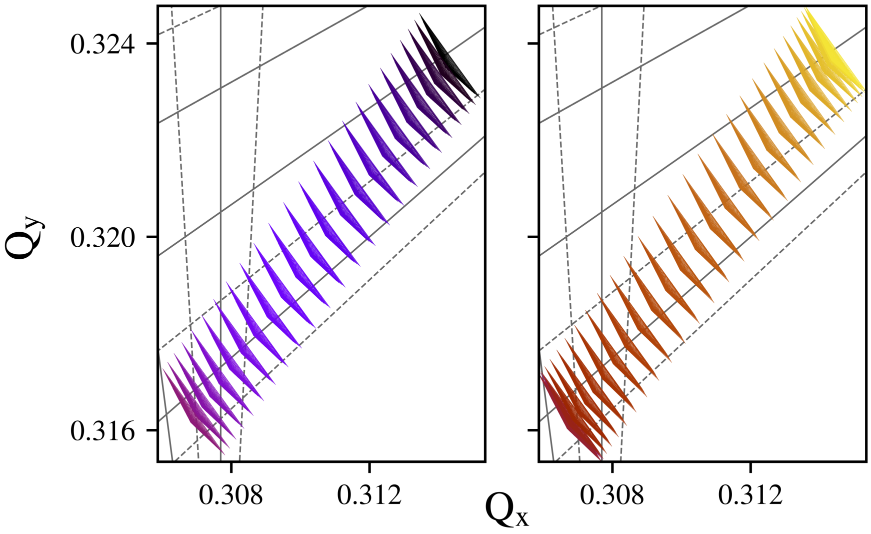

Figure 5.6: An approximation of the instantaneous footprint in the presence of a tune modulation for the first (left panel) and second (right panel) half of the modulation period. A color code is assigned to the turn number that indicates the first (black) and last (yellow) turns of one modulation period. The resonance diagram (gray lines) is also depicted.

excitation of sideband resonances in the vicinity of the ones driven by the lattice non-linearities. In particular, in the presence of a tune modulation with a single modulation tune $Q_m = f_m/f_{\text{rev}}$, where f_m and f_{rev} are the modulation and revolution frequency, respectively, the resonance diagram is computed as:

$$k \cdot Q_x + l \cdot Q_y + m \cdot Q_m = n \tag{5.3}$$

where k, l, m, n are integers and $|k| + |l|$ is the resonance order, while m is the sideband order. Figure 5.7 indicates the working point (black star-shaped marker) and the tune diagram of Eq. (5.3) for three different modulation frequencies: a modulation at 100 Hz (Fig. 5.7a), 600 Hz (Fig. 5.7b) and 800 Hz (Fig. 5.7c). The gray lines represent the nominal resonances, while the first-order sideband ($m = 1$) of the second (blue), third (cyan), fourth (green), fifth (orange) and sixth (red) order resonance is also depicted ($|k| + |l| \leq 6$). The solid and dashed lines illustrate the normal and skew resonances, respectively. The sidebands are always parallel to the main resonances and they are located in a distance that is proportional to the modulation tune, an effect that is clearly shown in Fig. 5.7a. As the modulation frequency increases, the sidebands, such as the ones of the second-order resonance (blue) in Fig. 5.7a, are driven further away from the working point. At the same time, sidebands of excited resonances that are not in the vicinity of the working point reach the betatron tune spread, such as the sideband of the third-order resonance (cyan) in Fig. 5.7b and Fig. 5.7c. Subsequently, depending on the selected working point, the lattice non-linearities and the modulation frequency, the sidebands of lower or higher-order resonances might reach the betatron tune spread and increase the particles' tune diffusion.

The existence and the impact of the sideband resonances described in Eq. (5.3) is validated by computing the tune of each particle from the turn-by-turn data that span over several modulation periods. As the aim of the present chapter is to study the dynamics of colliding beams that experience strong beam-beam interactions, a 4D beam-beam element is also included in the aforementioned one-turn map. The map of the 4D head-on beam-beam element used in the simulations is decribed in [36], assuming Gaussian and round beams with an intensity of $1.2 \cdot 10^{11}$ protons, a normalized emittance of 2.5 μm rad and a β-function of 100 m. Including such a non-linearity also allows for a more detailed review of the footprint as it leads to the excitation of several resonances and increases the betatron tune spread. The particles are tracked for 10^4 turns, the transverse position and momenta are retrieved turn-by-turn and they are then used to perform the Frequency Map Analysis (FMA) [60, 61, 64, 66]. In particular, the tune of each particle is computed for the first and last 3000 turns, using the NAFF algorithm. The variation of the transverse tunes between the two time intervals reveals information concerning its diffusion. Figure 5.8 shows the tune determination in the second time span (left panel) and the initial configuration space (right panel), color-coded with the logarithm of the diffusion for four studies: first, in the absence of a tune modulation, which is used as a reference (Fig. 5.8a), and in the presence of a tune modulation at 100 Hz (Fig. 5.8b), 600 Hz (Fig. 5.8c) and 800 Hz (Fig. 5.8d). As a reference, the typical values of the diffusion extend from 10^{-7} (blue) to 10^{-3} (red). The review of the frequency maps shows that for a tune modulation at 100 Hz (Fig. 5.8b) the first-order sideband of the second-order resonance (blue) has a clear impact on the diffusion of the particles. This observation underlines that there is a good agreement between Eq. (5.3) and the tracking results. Next, the increase of the modulation frequency at 600 Hz results in an important increase of the tune diffusion due to the first sideband of the third-order resonance (cyan). Although lower-order resonances are more critical, the configuration space (second panel) shows that this resonance affects a large portion of the phase space, an effect that explains the more critical impact compared to the modulation at 100 Hz. Finally, the same sideband affects the footprint during a modulation at 800 Hz, but due to the position of the sidebands, a lower impact is observed.

Overall, in the presence of a tune modulation, the impact on the particles' tune diffusion depends on the lattice non-linearities, the position of the sidebands, the sideband and resonance order (lower orders have a more critical impact), the working point and the actions of the affected particles. If the sidebands reach high amplitude particles rapid losses are observed in a limited amount of turns. Therefore, tune modulation effects introduce a frequency-dependent diffusion mechanism, the impact of which significantly depends on the selected working point and the non-linearities of the lattice. This fact underlines that some modulation frequencies are more critical for the beam performance than others for the selected working point. On the contrary to modulated dipolar perturbations, where a significant impact on the particle's motion is observed, to first order, when the frequencies

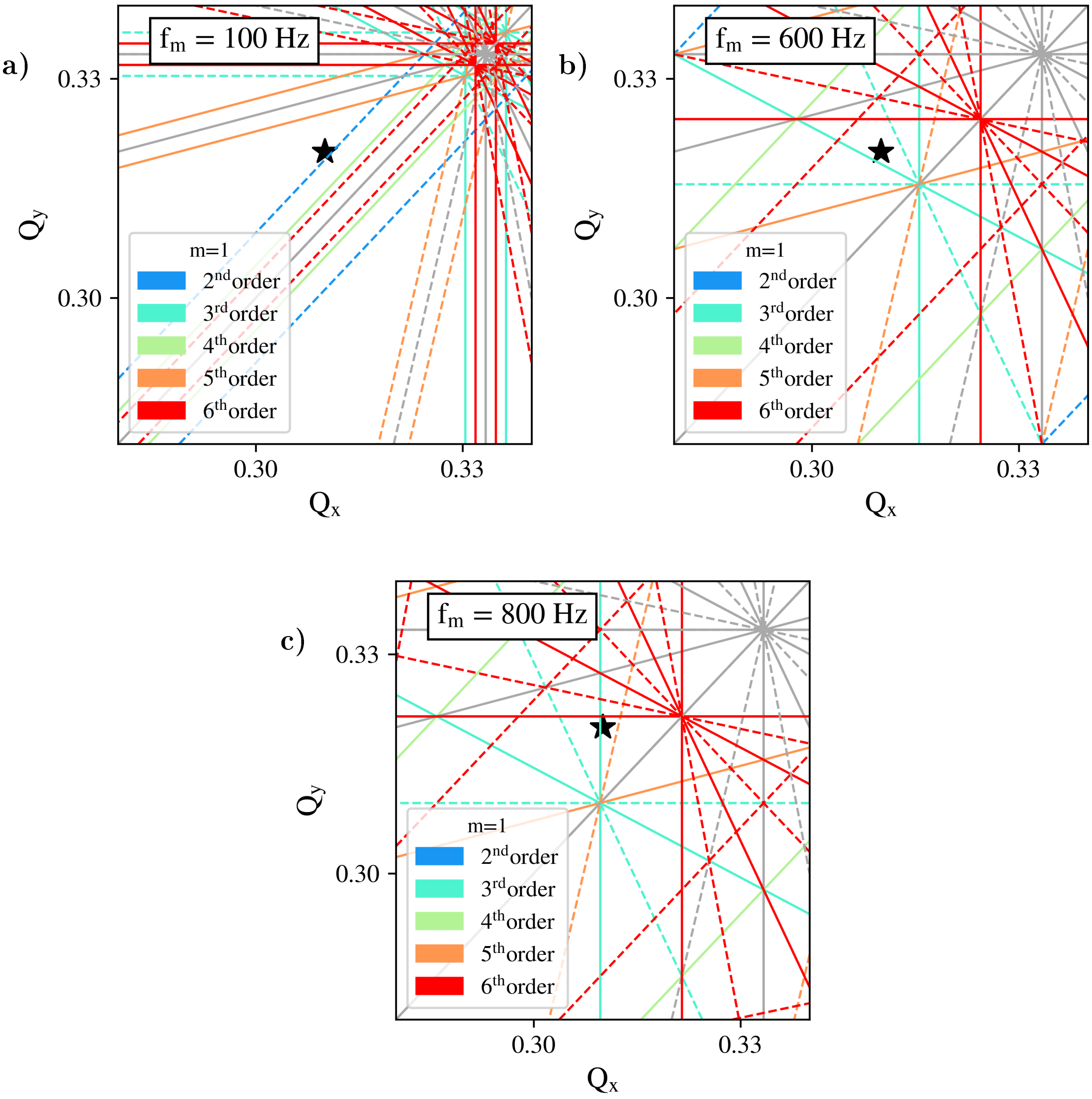

Figure 5.7: The tune diagram with the nominal resonances (gray) and the first-order sideband of the second (blue), third (cyan), fourth (green), fifth (orange) and sixth (red) order resonance for a tune modulation at (a) 100 Hz, (b) 600 Hz and (c) 800 Hz. The working point is also illustrated (black). The solid and dashed lines illustrate the normal and skew resonances, respectively.

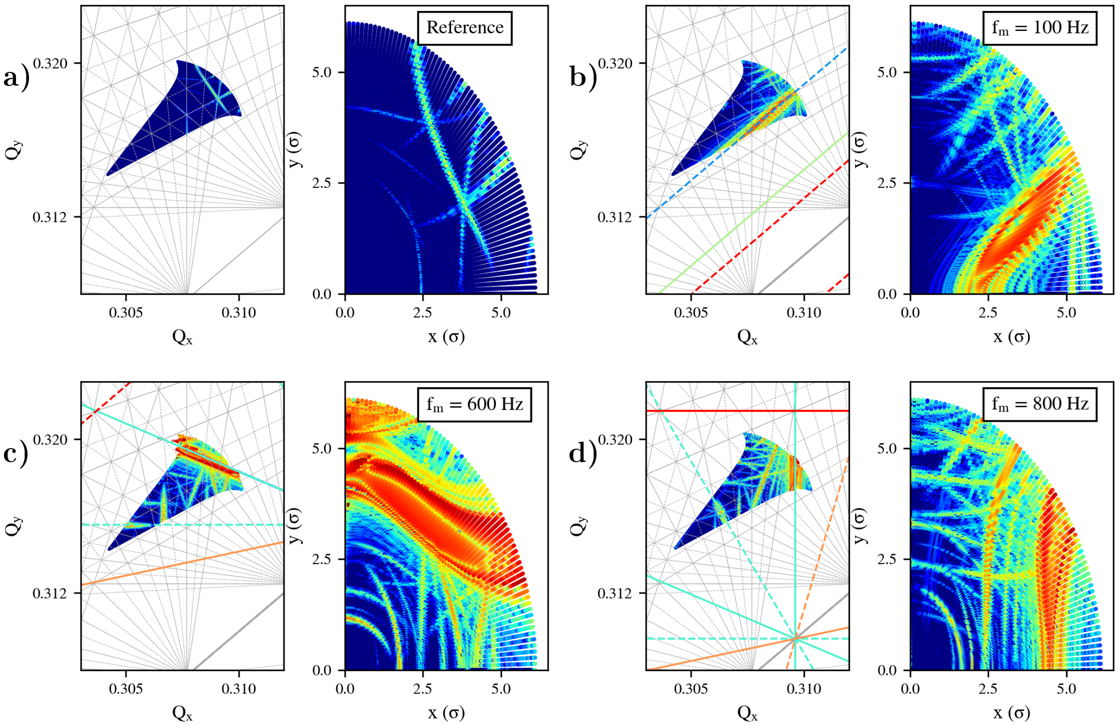

Figure 5.8: The FMAs (left panel) of the simplified model (a) in the absence of noise and in the presence of a tune modulation with a frequency at (b) 100 Hz, (c) 600 Hz and (d) 800 Hz, with the initial coordinates in configuration space color-coded with the tune diffusion (right panel). The gray lines depict the nominal resonances, while the colored lines illustrate the first sideband of the resonances up to the sixth order.

Table 5.1: The HL-LHC simulated parameters at the end of the luminosity levelling at top energy.

Parameters (unit)	HL-LHC v1.3 (values)
Beam energy (TeV)	7
Bunch spacing (ns)	25
Bunch length (m)	0.075
Betatron tunes (Q_x, Q_y)	(62.31/62.315, 60.32)
Normalised emittance (μm rad)	2.5
Chromaticity	15
Octupole current (A)	-300
Bunch population (protons)	1.2e11
IP1/5 Half crossing angle (μrad)	250
IP1/5 β^* (cm)	15
Crabbing angle (μrad)	190

of the spectral components are in the proximity of the betatron tune, power supply ripples in the quadrupoles can affect the distribution even if the modulation frequency is not in the vicinity of the working point.

5.3 Tune modulation in the HL-LHC

In the HL-LHC, luminosity levelling techniques are required to achieve a constant luminosity of 5×10^{34} cm^{-2}s^{-1}, as envisaged in the nominal scenario [114, 119]. The luminosity degradation, resulting from the intensity reduction from $2.2 \cdot 10^{11}$ to $1.2 \cdot 10^{11}$ protons per bunch due to the proton-proton collisions, will be compensated by reducing the beam size at the two high luminosity experiments, CMS and ATLAS, from β^*=64 cm to 15 cm with the ATS scheme [35]. In the context of these studies, the machine configuration at the end of the levelling is the most critical as the increase of the maximum β-functions in the inner triplet will act as an amplification factor for the noise in the quadrupoles. Therefore, simulations with power supply ripples in the inner triplet left and right of the two IPs are conducted for the simulated parameters shown in Table 5.1. As a first step, arbitrary modulation amplitudes and frequencies are employed to illustrate the impact of such a mechanism on the particles' motion either in 5D, i.e., without considering the synchrotron oscillations but with off-momentum particles or in 6D to depict the combined effect of the gradient and the synchrotron modulation. From this parametric investigation, the dependence on the modulation frequency is presented in terms of diffusion, intensity evolution and DA. The larger sensitivity to specific modulation frequencies is explained with frequency maps and a modulation depth threshold is defined as a function of the frequency.

Of particular importance is the fact that the quadrupoles in the inner triplet are powered by switch-mode power supplies [120]. In contrast to thyristor commutated technology, the voltage tones that are anticipated in the noise spectrum, in this case, are the switching frequency of the power converter and its harmonics, as well as a few low order 50 Hz harmonics, namely 50, 150, 300 and 600 Hz, without excluding the existence of others [121]. It must be noted that the envisaged switching frequencies of the main circuits in the triplet lie in the regime of 50-200 kHz [122]. Such high frequencies are not expected to perturb the beam motion as they will be strongly attenuated by the shielding effect of the beam screen [101]. Therefore, the following studies mainly focus on the potential impact of the low order harmonics in the spectrum or low switching frequencies in the trim circuits. As a realistic voltage spectrum is not presently available, the results of the parametric simulations are compared to the power converter specifications [121]. The specifications provide the maximum tolerated output voltage for an extended frequency bandwidth, without defining the actual amplitude and the voltage tones in the noise spectrum of the triplet. These values, in combination with the inductance and the current of the circuits, are used to compute the expected tune modulation from the four quadrupoles and the three trims left and right of the two IPs. Furthermore, the transfer function that converts the voltage ripples into variations of the magnetic field is approximated by a simple RL circuit and the beam screen attenuation [101] is not included, an approach which leads to the overestimation of the modulation depths in these studies.

The simulations are performed using the single-particle symplectic tracking code, SixTrack [54, 123]. Only one beam is tracked around the lattice, that corresponds to Beam 1, and the weak-strong approximation is used for the beam-beam effects, as the charge distribution of the strong beam is not varied. The normalized strengths of Q1, Q2a, Q2b and Q3 in the IRs left and right of IP1 and 5 are modulated with a sinusoidal function. The amplitude of the function defines the maximum variation of the strength while the polarity of each magnet is preserved. The absolute value of the amplitude is assumed to be equal for all the quadrupoles, without however leading to the same modulation depth due to variations of the $\beta-$functions. The phase of the injected noise is considered equal to zero for all the circuits. This approximation does not correspond to a realistic scenario, as the switching clocks of the power converters are not synchronized. Nevertheless, such a configuration is selected as it maximizes the overall impact of the noise. In fact, due to the anti-symmetric powering of the triplets left and right of the two IPs, the modulation of the circuits accumulates when equal phases are considered. To illustrate this effect, a single particle is tracked in the HL-LHC lattice for 10^4 turns. The simulations are performed in 5D to disentangle the contribution of the synchrotron motion from the noise. A low-frequency modulation is selected so that an approximation of the instantaneous tune can be derived from the turn-by-turn position information. The horizontal tune is computed with a sliding window of 50 turns with a step of 10 turns between intervals. Figure 5.9 presents the tune evolution for equal (blue) and random (black) phases in the circuits. In the latter case, the randomly selected phases act as a compensation scheme for the overall modulation compared to the former. The unperturbed horizontal tune is also depicted

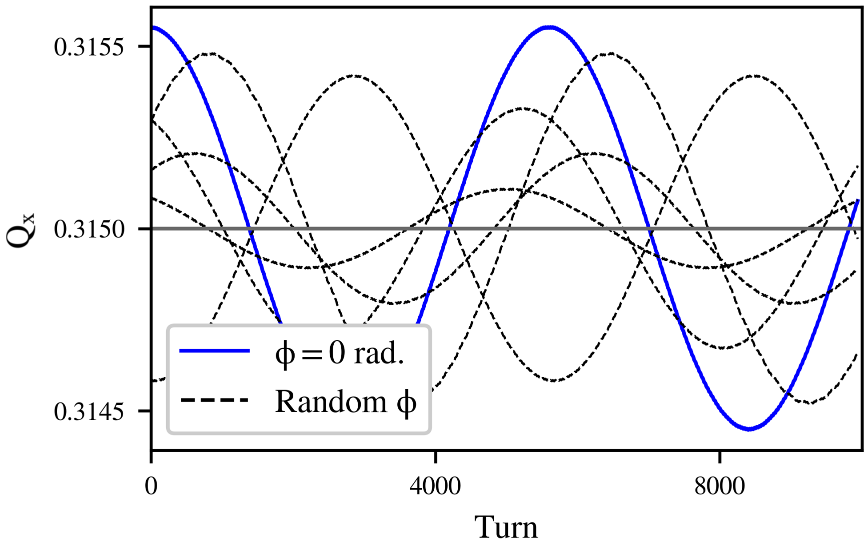

Figure 5.9: The horizontal instantaneous tune in the presence of a low-frequency modulation with a zero (blue) and a random (black) phase of the noise in the inner triplet quadrupoles left and right of IP1 and 5. The gray line represents the horizontal tune in the absence of a modulation.

(gray). Several studies are performed with random phases to validate this observation. Specifically, due to the betatron phase advance between the right and left circuits around the IPs, the modulation is minimized when their phase difference approaches $\Delta\phi = \pi$. Thereby, simulations show that there is a potential benefit of phasing conveniently the clocks of the power converters. The results of the above simulations are presented and discussed in the next sections.

5.3.1 Noise spectrum with a single tone

Frequency Map Analysis in 5D with noise

Similarly to the simplified model of Section 5.2, the FMAs are computed to depict the excitation of sideband resonances in the HL-LHC case due to noise effects. A distribution of particles is tracked in 5D for 10^4 turns in the lattice at the nominal working point. The initial conditions form a polar grid in the configuration space and vanishing initial momenta are selected. The grid consists of 99 angles and a radius extending from 0.1 to 6.1 σ and a step of 1 σ. Longitudinally, the particles are located at 3/4 of the bucket height. The turn-by-turn data are divided into two groups, consisting of the first and last 3000 turns, respectively. The diffusion of the particles is computed by comparing the variation of their tune determinations between the two time intervals. Figure 5.10 depicts the FMAs (left panel) and the initial configuration space (right panel), color-coded with the logarithm of the diffusion, for several modulation frequencies and equal depths. The gray lines represent the nominal resonances, while the colored lines illustrate the first sideband ($m = 1$) of the

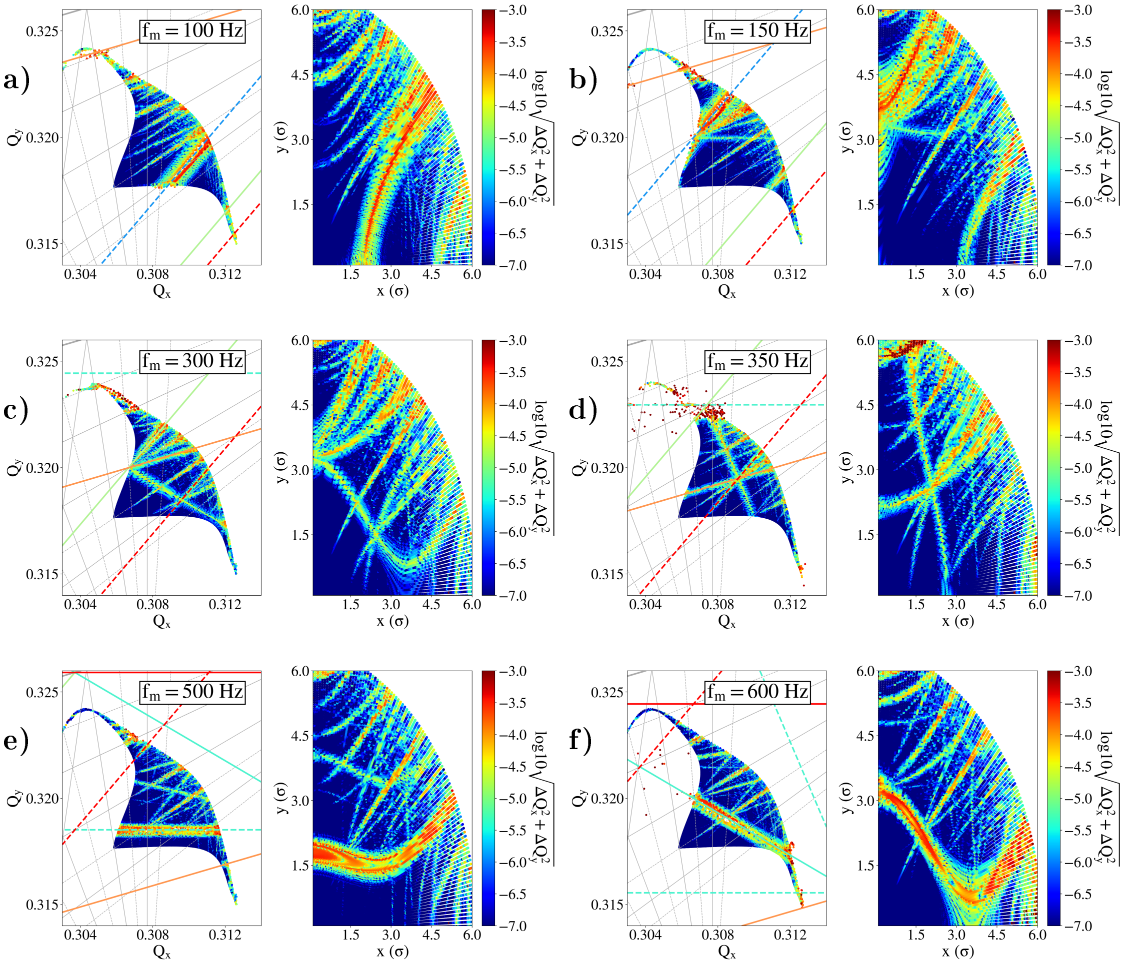

Figure 5.10: The 5D frequency map (left panel) and the initial configuration space (right panel) in the presence of a tune modulation in the inner triplet left and right of IP1 and 5 in the HL-LHC lattice for the nominal working point. The modulation depth is $\Delta Q = 5.5 \cdot 10^{-5}$ and the modulation frequency is (a) 100 Hz, (b) 150 Hz, (c) 300 Hz, (d) 350 Hz, (e) 500 Hz and (f) 600 Hz. A color code is assigned to the logarithm of the tune diffusion. The nominal (gray) lines and the first-order sideband of the second (blue), third (cyan), fourth (green), fifth (orange) and sixth (red) order resonance are indicated.

second (blue), third (cyan), fourth (green), fifth (orange) and sixth (red) order resonance ($|k| + |l| \leq 6$).

For a constant modulation depth, the impact of the tune modulation depends on the working point and the modulation frequency. First, for a modulation at 100 Hz (Fig. 5.10a) and 150 Hz (Fig. 5.10b) the first sideband of the second-order resonance (blue) leads to an increase of the diffusion. Second, for a modulation at 300 Hz (Fig. 5.10c), sidebands of higher-order resonances (fourth to sixth) are in the vicinity of the betatron tune. Next, a modulation at 350 Hz (Fig. 5.10d) leads to rapid losses due to the fact that the first sideband of the third-order resonance (cyan) reaches high-amplitude particles and overlaps with the nominal resonances (gray lines), as well as with the first sideband of the fourth-order resonance (green). Finally, for a modulation at 500 Hz (Fig. 5.10e) and 600 Hz (Fig. 5.10f) the excitation of the first sideband of the third-order resonance (cyan) is visible and the review of the configuration space shows that the core of the distribution is mainly affected. From the frequency maps, it is observed that there is a sensitivity to some modulation frequencies as the same depth leads to a higher diffusion increase. As previous studies have reported [115], for the working point and the non-linearities of the HL-LHC lattice, amongst the low-order harmonics that are anticipated in the spectrum (50,150,300 and 600 Hz), a higher sensitivity to 300 and 600 Hz is present. This is due to the fact that multiple sidebands are reaching the footprint. This effect is not observed with a modulation at 50 and 150 Hz as only the first sideband of the second-order resonance is in the vicinity of the betatron tune and it affects a small portion of the phase space.

Frequency Map Analysis in 6D

In a similar way, the coupling of the synchrotron and the betatron motion in the presence of a non-vanishing chromaticity leads to the variation of the instantaneous footprint with a modulation frequency equal to the synchrotron frequency ($\approx$20 Hz). As the synchrotron frequency in the LHC is much lower than noise frequencies under consideration, the tracking is extended to $2 \cdot 10^4$ turns to average over several modulation periods. The same distribution of particles is tracked in 6D in the nominal HL-LHC lattice, i.e., without injecting noise in the triplet. The momentum deviation of all the particles is equal to $3/4$ of the bucket height. It is important to note that, as shown in Section 5.2, the modulation index of each particle with a chromaticity of 15, a relative momentum deviation of $27 \cdot 10^{-5}$ and a synchrotron frequency at 20 Hz exceeds the critical value of 1.5. In this case, as presented in the previous section, due to the appearance of strong sidebands, the NAFF algorithm returns the frequency determination of the sideband and not the one of the betatron tune. Therefore, to illustrate the frequency map in 6D the chromaticity is reduced to 5. After the tracking, the turn-by-turn data are divided into two consecutive intervals of 10^4 turns and the diffusion of each particle is computed. Figure 5.11 demonstrates the 6D FMA (left panel) and the initial configuration space (right panel). The review of the frequency map shows that high order synchrotron sidebands ($m \leq 8$) of the second-order resonance (blue) are excited. Although considering constant momentum deviations for all

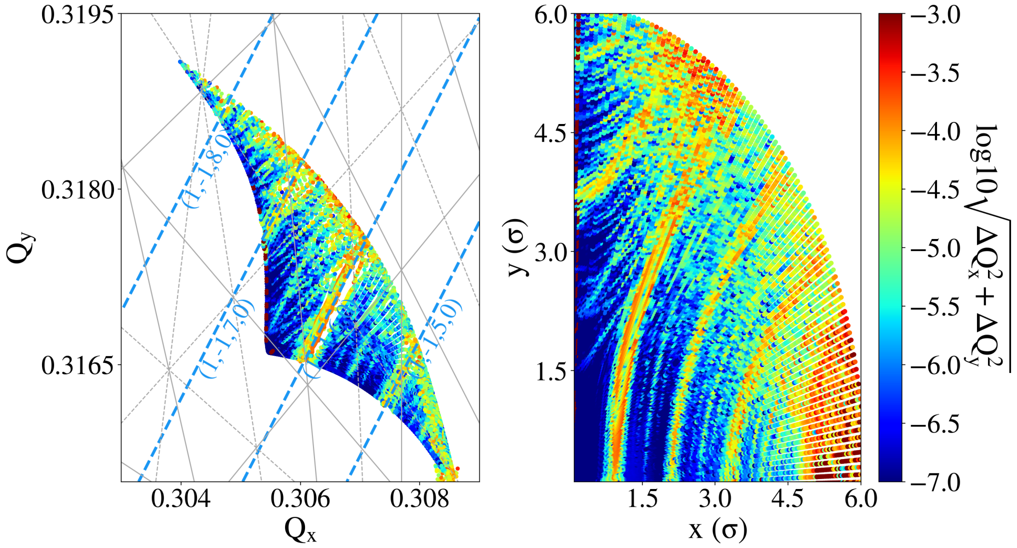

Figure 5.11: The 6D FMA with a chromaticity equal to 5 and for a momentum deviation of all particles at 3/4 of the bucket height. The blue lines depict the sidebands ($m \leq 8$) of the second-order resonance.

the particles in the distribution is essential to compute frequency maps, experimentally the initial longitudinal distribution extends over the whole bucket area. As the momentum deviation is not constant across all particles, the variation of the modulation index leads to the reduction of the average modulation. To this end, the next section focuses on the investigation of the intensity evolution in a more realistic configuration.

Simulations of beam losses

Studying the intensity evolution requires the tracking of a 6D matched distribution with momentum deviations that span over the whole bucket height. Due to the excitation of additional resonances from the slow (synchrotron motion) and fast (power converter noise) modulation, particles at the tails of the distribution diffuse and will eventually be lost. A detailed representation of the high amplitude particles is achieved by first, overpopulating the tails and then, assigning weights to the particles according to their initial position. Specifically, the initial conditions form a 4D round distribution in the transverse plane that extends up to 6 σ both in the configuration and the trace space. Longitudinally, the particles are uniformly placed in the bucket height extending up to its limit. Overall, $9 \cdot 10^4$ particles are tracked for 10^6 turns and the turn-by-turn position measurements are retrieved every 10^3 turns. Depending on the initial position of the particles in the transverse and longitudinal plane, a weight is assigned to each particle in the post-processing analysis. The weight defines the importance of each particle in the computations of the intensity. It is determined from the Probability Density Function (PDF) of the simulated distribution, which in this case is Gaussian in all planes. Instead of directly tracking a Gaussian distribution, an important number of particles are located at the tails of the distribution, to which a lower weight is assigned compared to the ones at the core. In this way, their contribution to the determination of the losses is less significant. Furthermore, a mechanical aperture is defined in the post-processing at 5 σ. Particles reaching this limit are considered lost and the corresponding weights are set to zero.

Figure 5.12 shows the intensity evolution as computed from the weighted distributions. First, the chromaticity and thereby, the modulation depth is increased in steps (Fig. 5.12a) from 0 to 15, which leads to a lifetime reduction. From the review of the intensity evolution, it is shown that the intensity degradation scales roughly linearly with the chromaticity increase, without however leading to a significant lifetime reduction. Then, for a chromaticity equal to 15 for both planes, the frequency of the tune modulation induced by power supply ripples is varied for a constant depth (Fig. 5.12b). The study focuses on the low-frequency tones that are expected to be present in the power converter (50, 150, 300 and 600 Hz) and that may perturb the beam motion. Although, for a constant depth, the modulation index decreases with increasing frequency, the impact on the intensity is much more severe 600 Hz compared to 50, 150 and 300 Hz. The beam lifetime is computed in each case with an exponential fit which yields a reduction from $\approx$ 1100 h for a modulation frequency at 50 Hz to $\approx$750 h for 300 Hz and $\approx$130 h when the frequency is increased to 600 Hz. As shown from the FMAs, the tune modulation introduces a frequency-dependent mechanism of diffusion, which, for the selected working point, renders these frequencies the most critical in terms of losses as with the same modulation depth a more significant impact on the intensity is observed.

Noise thresholds with parametric Dynamic Aperture scans

As the presence of voltage tones with frequencies beyond the ones already considered cannot be excluded, the DA dependency on the modulation frequency is explored. To this end, parametric 6D simulations are performed to estimate the impact of various modulation frequencies and depths. In the transverse configuration space, the initial distribution consists of five angles and a radius that extends from two to ten σ with a step of two σ. In the longitudinal plane, all particles are placed at 3/4 of the bucket height. The duration of the tracking is 10^6 turns, which corresponds to $\approx$90 seconds in operation. The working point is set to its nominal $(Q_x, Q_y) = (62.31, 60.32)$ and not the DA optimized $(Q_x, Q_y) = (62.315, 60.32)$ value [124]. For each study, a different combination of the excitation frequency and amplitude is selected in order to conduct a scan in the tune modulation parameter space. The frequency range spans over all 50 Hz harmonics up to 10 kHz. For each frequency, the amplitude of the excitation is increased and the total modulation depth due to the contribution of all the circuits is computed from the optics using MAD-X [125]. Then, the minimum DA across all the angles in the configuration space is computed. Figure 5.13 presents the modulation frequency as a function of the depth. Each point on the plot corresponds to an individual study and a color code is assigned to the minimum DA. The parametric scan defines the depth threshold for each modulation frequency beyond which a DA reduction is foreseen (white to red). As an average, a maximum limit in

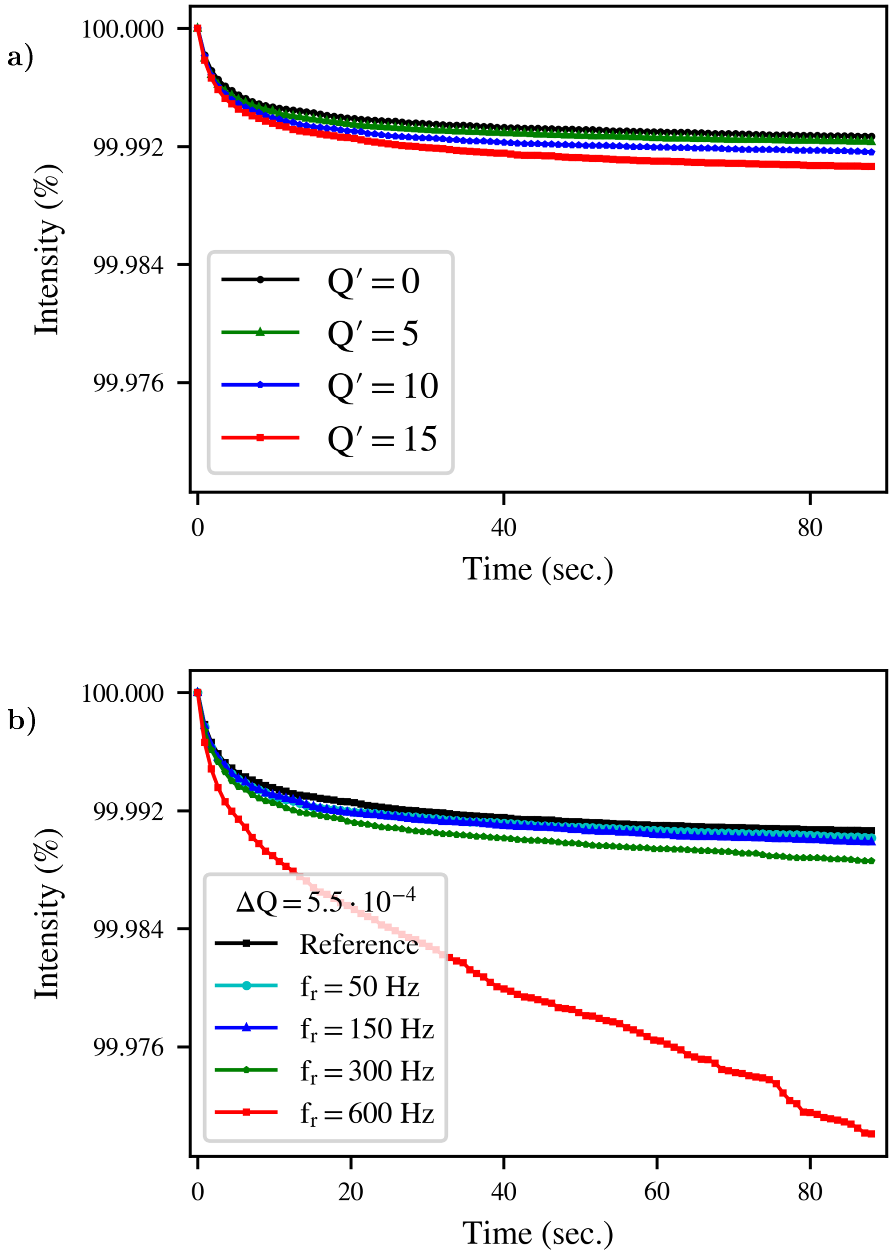

Figure 5.12: (a) Intensity evolution in the HL-LHC lattice for $Q' = 0$ (black), $Q' = 5$ (green), $Q' = 10$ (blue) and $Q' = 15$ (red). (b) Intensity evolution for Q′ = 15 without noise (black) and in the presence of a tune modulation with $\Delta Q = 5.5 \cdot 10^{-5}$ at 50 Hz (cyan), 150 Hz (blue), 300 Hz (green) and 600 Hz (red).

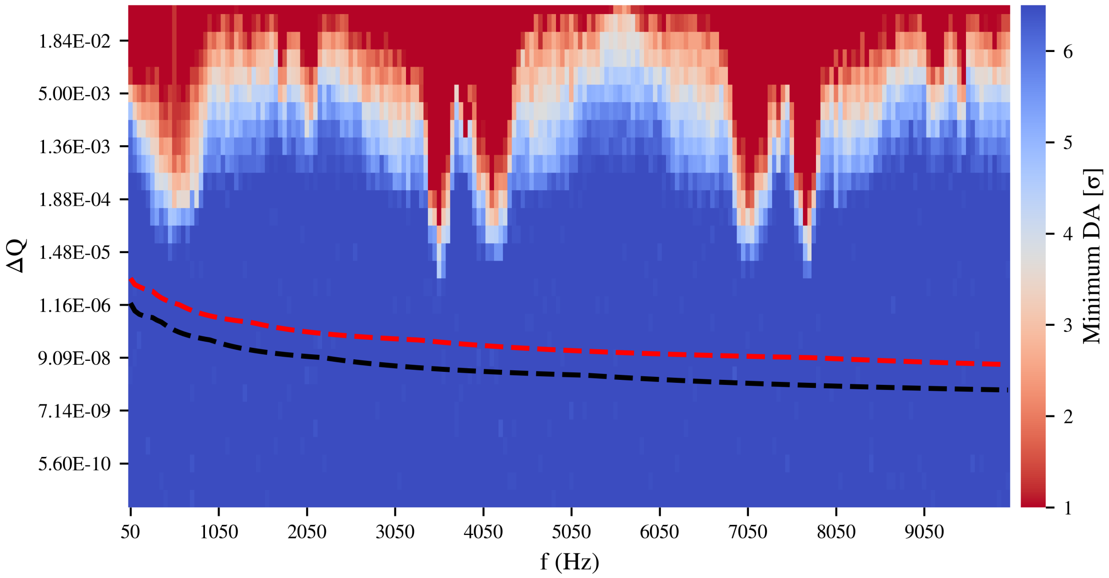

Figure 5.13: Modulation frequency as a function of modulation depth in the presence of noise in the inner triplet quadrupoles of the HL-LHC. The color code indicates the minimum DA. The red and black lines represent the sum and the root mean square of the contribution from all the circuits, respectively, computed from the maximum output voltage as defined in the power supply specifications.

the order of 10^{-4} in the modulation depths can be defined; however the strong dependency on the modulation frequency is evident and, as expected from the frequency maps, there are regimes with increased sensitivity to noise, which is further investigated in the following section. Furthermore, these simulations include the combined effect of noise in the triplet and high chromaticity for large momentum deviations.

Next, the modulation depth is computed from the maximum output voltage as defined in the power converter specifications. For each triplet, the contribution of the four main power supplies and the three trim converters are considered. Then, the sum (red dashed) and the root mean square (black dashed) modulation depth from the contribution of all the circuits are computed. It must be highlighted that these values correspond to the maximum acceptable and not the realistic voltage. The attenuation from the beam screen is not considered from which a further reduction of the modulation depth is expected for frequencies above ≈ 100 Hz [101]. In addition, summing the contribution of all the triplets corresponds to a scenario where the phase of the noise is synchronous and thus, overestimates the modulation depth even further. A comparison between the modulation depth from the specifications and the threshold defined by simulations through the scan of individual frequency indicates that there is a difference of several orders of magnitude between the two. Therefore, the much larger tolerances defined by the DA simulations suggest that, by considering individual tones, the ripples in the inner triplet, combined with large chromaticity values, will not a limitation for the beam performance.

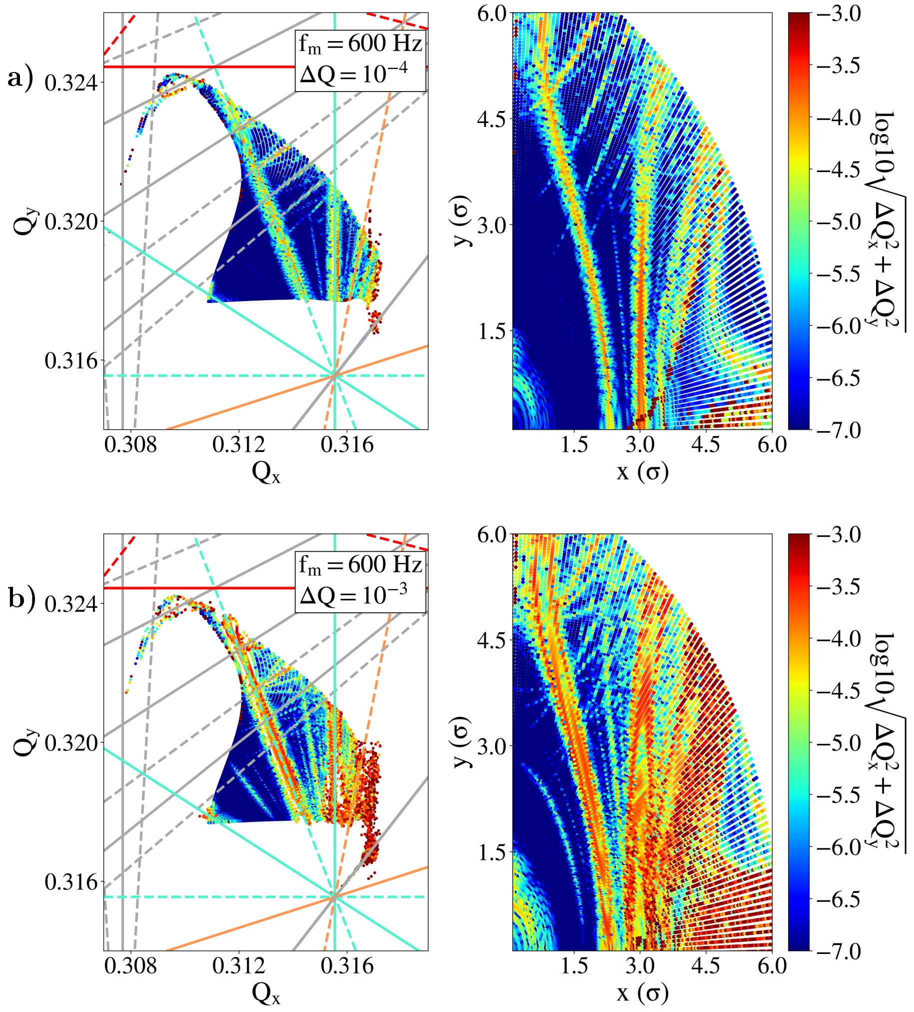

Figure 5.14: The 5D frequency maps for a tune modulation at 600 Hz with (a) $\Delta Q = 10^{-4}$ and (b) $\Delta Q = 10^{-3}$. The gray lines represent the nominal resonances, while the cyan lines the first sideband of the third-order resonance.

A review of the high-sensitivity noise regimes

Based on the heat-map of Fig. 5.13, a more detailed review is performed around the frequency regimes with a higher sensitivity to noise. First, to illustrate the repercussions of the modulation depth increase, two sets of noise parameters are selected, corresponding to a slight and a significant DA reduction, respectively. For both cases the modulation frequency is 600 Hz and the optimized working point is selected. Figure 5.14 depicts the 5D FMA for $\Delta Q = 10^{-4}$ (Fig. 5.14a) and $\Delta Q = 10^{-3}$ (Fig. 5.14b). The first-order sideband of the third (cyan), fifth (orange) and sixth (red) order resonance is depicted. The review of the frequency maps demonstrates that the critical impact on the DA when increasing the depth is observed due to, first, the increase of the sideband resonance strength and, second, the appearance of higher-order sidebands.

Secondly, a higher sensitivity is observed around the regime of the betatron frequency

(f_x ≈3.48 kHz) and its alias i.e., the folding of the betatron frequency around the revolution frequency ($f_{\mathrm{rev}} - f_x$ ≈7.76 kHz). This observation is attributed to the dipolar effect of the triplets through feed-down. In particular, as the particle trajectories are not aligned to the magnetic center of the quadrupoles, an orbit modulation is also observed. This statement is demonstrated by tracking a single particle in the HL-LHC lattice under the influence of a tune modulation at 600 Hz and 3.4 kHz. From the turn-by-turn data the Fast Fourier Transform (FFT) is computed as demonstrated in Fig. 5.15. In the former case (Fig. 5.15a), apart from the sidebands (red) around the betatron tune (black), a dipolar excitation is also visible (purple). As the excitation frequency is not in the vicinity of the betatron tune spread, the dipolar effect has no impact on the diffusion. In the second case (Fig. 5.15b), the frequency of one of the sidebands (≈6.89 kHz) exceeds the Nyquist frequency of the turn-by-turn acquisitions (≈5.62 kHz) and it is aliased into the spectrum (≈4.36 kHz). The dipolar excitation (purple) approaches the betatron tune spread and eventually, has an impact on the betatron motion.

The dipolar effect of the triplet eventually leads to the excitation of additional resonances for modulation frequencies close to the tune. These resonances appear in constant frequencies rather than as sidebands around the nominal. This conclusion can also be derived from Eq. (5.3) for $m = 1$, $l = 0$ and $k = 1$, which is the excitation due to the dipolar effect. Figure 5.16 illustrates the 5D FMA for a tune modulation at a frequency in the vicinity of the working point (3.5 kHz). In this case, the main contributor to the increase in tune diffusion is the first sideband of the first-order resonance and thus, the dipolar excitation.

A simple tool to predict frequency sensitivity

The parametric scan in the tune modulation parameter space presented in Fig. 5.13 is computationally challenging as it requires performing a large number of simulations. Moreover, the tracking must be repeated if the selected working point is modified. Although running the simulations up to 10^6 turns is essential to determine the minimum modulation depth that leads to a DA reduction, it is not required to identify, in a fast way, the safest modulation frequencies for operation. In this context, the aim of this section is to present a simple tool to predict the beam sensitivity to specific modulation frequencies based on the position of the sideband resonances. In fact, only the knowledge of the betatron tune spread is needed for the unperturbed case, i.e., the reference conditions without power supply ripples.

The working principle of the method is presented in Fig. 5.17, which shows the betatron tune spread (left panel) and the initial configuration space (right panel) in the absence of power supply ripples (black). Based on the modulation tune, the first-order sideband resonances ($m = 1$) from the first to the sixth resonance order ($|k| + |l| \leq 6$) are computed from Eq. (5.3). Similarly to the previous frequency maps, a different color code is assigned to each resonance order. For instance, Fig. 5.17a and Fig. 5.17b depict the sideband resonances in the vicinity of the footprint due to a modulation at 600 Hz and 3.55 kHz,

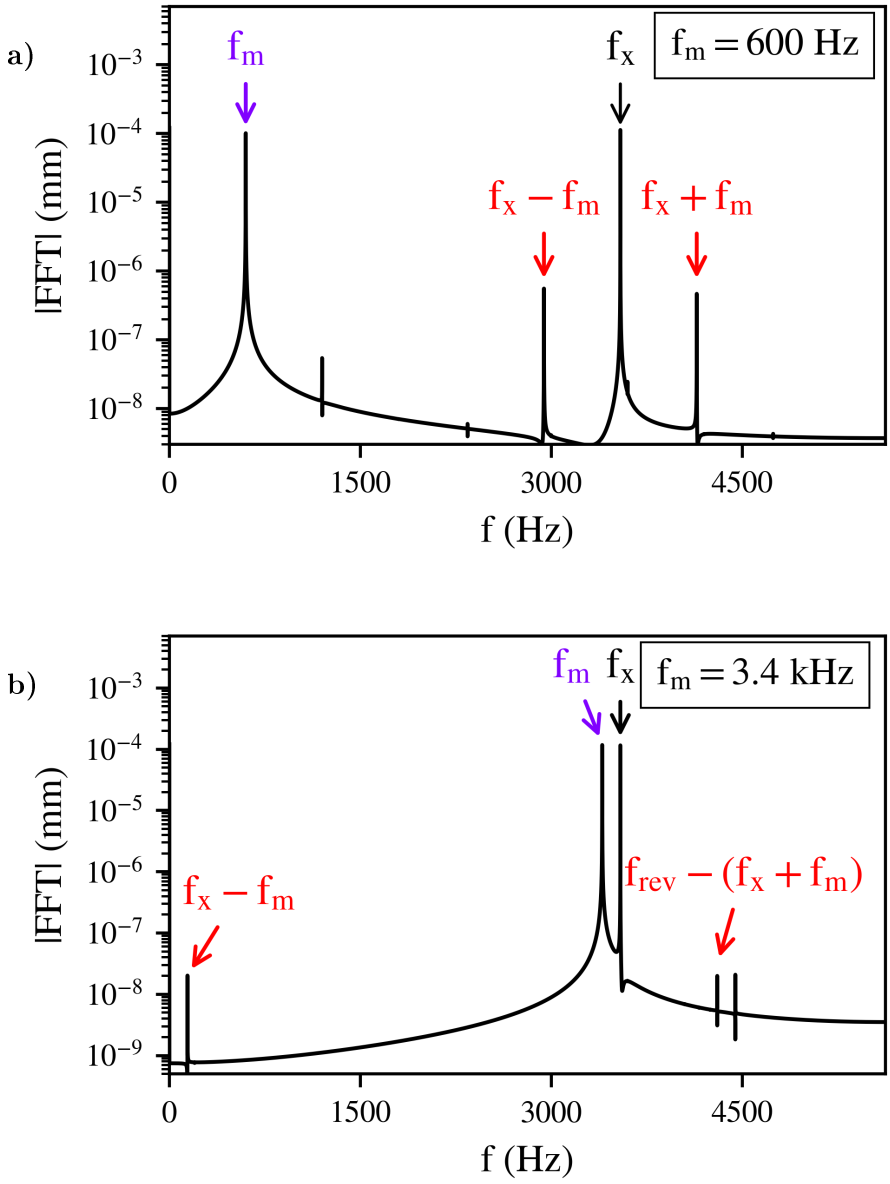

Figure 5.15: The FFT for a tune modulation at (a) 600 Hz and (b) 3.4 kHz that depicts the sidebands (red) around the betatron tune (black) and the dipolar excitation (purple) due to feed-down.

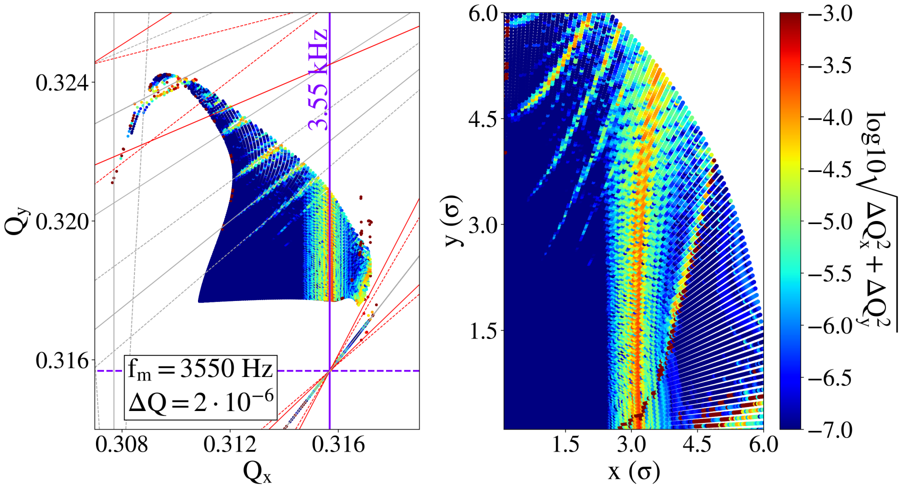

Figure 5.16: The 5D FMA for a tune modulation at 3.5 kHz. The purple line represents the first-order sideband of the first-order resonance, which is the dipolar excitation at 3.5 kHz in the horizontal plane.

respectively. For the selected working point, the first sideband of the third-order resonance (cyan) reaches the footprint for modulation at 600 Hz (Fig. 5.17a). The review of Fig. 5.17b shows that the first-order sideband of the first-order resonance (purple), which is the dipolar excitation at 3.55 kHz, will affect the footprint. As lower-order resonances have a more significant impact, a tune modulation at 3.55 kHz (first sideband of first-order resonance) is expected to be more detrimental to the beam performance than the modulation at 600 Hz (first sideband of third-order resonance). Then, depending on the amplitudes of the particles that are affected by the resonances in tune domain, a resonance map is performed from the tune domain to the configuration space (right panel). The representation of the resonances in configuration space allows us to more easily determine whether the resonance will affect the tails or the core of the distribution. For instance, a modulation at 3.55 kHz will mainly affect the tails of the distribution, while a modulation frequency of 600 Hz (Fig. 5.17a) will also have an impact on the core of the distribution. A comparison of the predictions of Fig. 5.17a to Fig. 5.14a, which is computed with tracking simulations, shows that there is a good agreement between the two. Similarly, a good agreement is found between Fig. 5.17b and Fig. 5.16. Therefore, using Eq. (5.3), determining whether the first sideband of the resonances up to a specific order will reach the footprint and mapping these sideband resonances in configuration space allows identifying the ones that will affect the beam depending on the modulation frequency.

As a next step, a similar analysis to Fig. 5.17 is performed for all the multiples of 50 Hz up to 10 kHz. Figure 5.18 presents the modulation frequency as a function of the resonance order ($|k| + |l|$) (bottom), while the heat-map of Fig. 5.13 (top) is also included for an easier comparison between the two. For each modulation frequency, the previously described procedure is repeated to determine whether the first or second-order sideband up to the sixth or second resonance order, respectively, is located in the vicinity of the

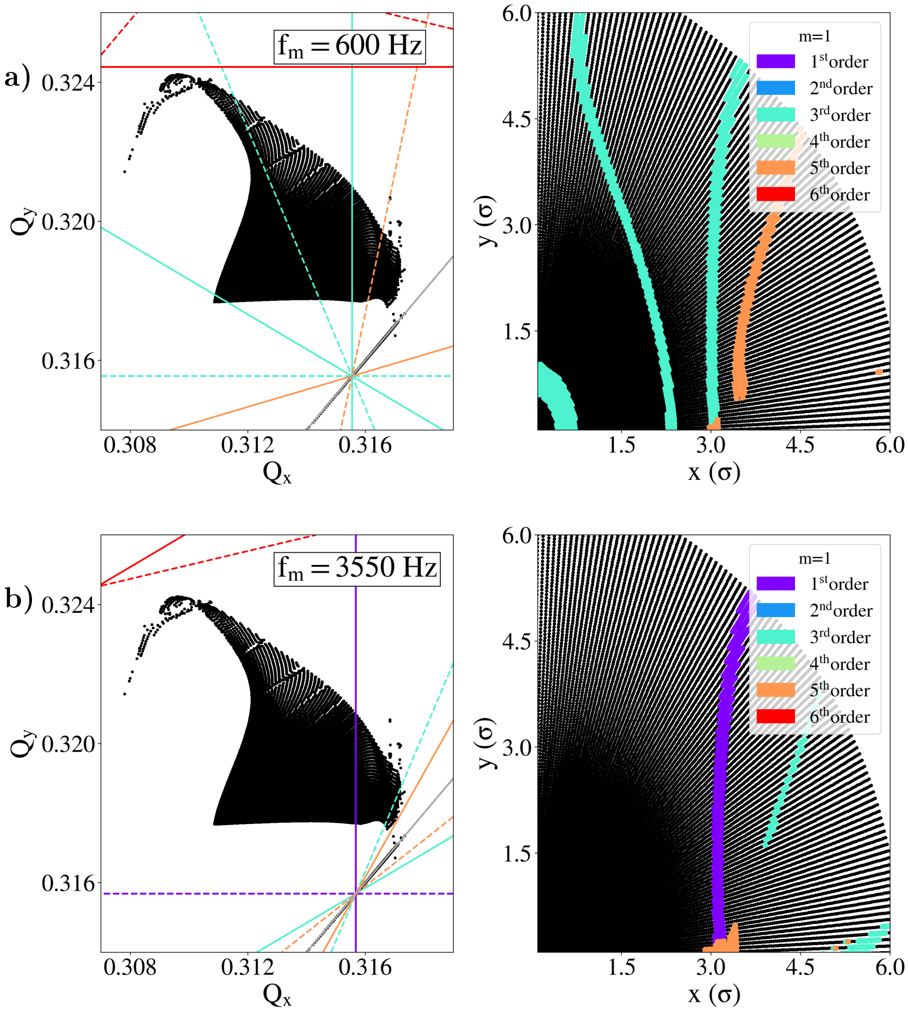

Figure 5.17: The footprint (left panel) and the initial configuration space (right panel) in the absence of power supply ripples. The first-order sideband ($m = 1$) of the first (purple), second (blue), third (cyan), fourth (green), fifth (orange) and sixth (red) order resonance ($|k| + |l|$) is illustrated for a modulation at (a) 600 Hz and (b) 3.55 kHz.

working point. Then, a color-code (bottom) is assigned depending on whether the first (red) or second (orange) order sideband will affect the distribution. The frequency regimes with a red color, especially for low order resonances, are the modulation frequencies with the largest impact on the beam and should, therefore, be avoided. The orange regimes illustrate the second-order sidebands and should be avoided only for large modulation depths. A blue color is assigned to the study if none of the resonances under consideration reach the footprint.

A comparison between the predictions (bottom) and the results of the tracking simulations (top) shows a good agreement between the two. In particular, it is evident that the large impact on DA close to the betatron tune and its alias is due to the first sideband of the first-order resonance. In the vicinity of the betatron tune (≈4.05 kHz) and its alias (≈7.05 kHz), there is an additional high-sensitivity regime due to the first sideband of the second-order resonance. In addition, the impact on DA for modulation frequencies around 50-1050 Hz is attributed to the first sidebands of the second and third-order resonance that reach the footprint for such modulation frequencies. Furthermore, for large modulation depths, a DA reduction is observed in the frequency region close to (≈2.05 kHz), which is due to the second-order sideband of the first and second-order resonance. Finally, no impact on the DA was observed from the tracking simulations around the regime of 6.05 kHz, which is explained by the fact that no sideband up to the sixth order affects the footprint for such modulation frequencies.

In this way, the modulation frequencies with sideband resonances that do not reach the footprint can be easily identified and they can be distinguished in a fast way from the modulation frequencies with a critical impact. This simple tool can guide the selection of the modulation frequencies such as the power supply switching frequencies for several working points. Although this method takes into account the position of the sidebands and the order of the resonance that affects the footprint due to the modulation, it does not consider the resonance overlap between the nominal and the sideband resonances. Due to this limitation, the simulations presented in the previous sections must be performed to identify the modulation frequencies with the most critical impact on the beam performance. In addition, this method is applicable for relatively small modulation depths as only the first and second-order sidebands of the modulation are considered but it can also be extended for a more aggressive power supply noise scenario.

5.3.2 Including a noise spectrum with multiple tones

As demonstrated from studies conducted in the past [29], the existence of multiple voltage tones in the noise spectrum is more critical than considering individual frequencies with an equivalent modulation depth due to the resonance overlap. To this end, the combined effect of the several voltage tones that are anticipated in the noise spectrum is computed. As mentioned in the previous sections, the envisaged power converter switching frequencies lie in a high-frequency regime and, as they are not expected to perturb the beam motion [101, 122], they are not considered in the following analysis. In this context, the

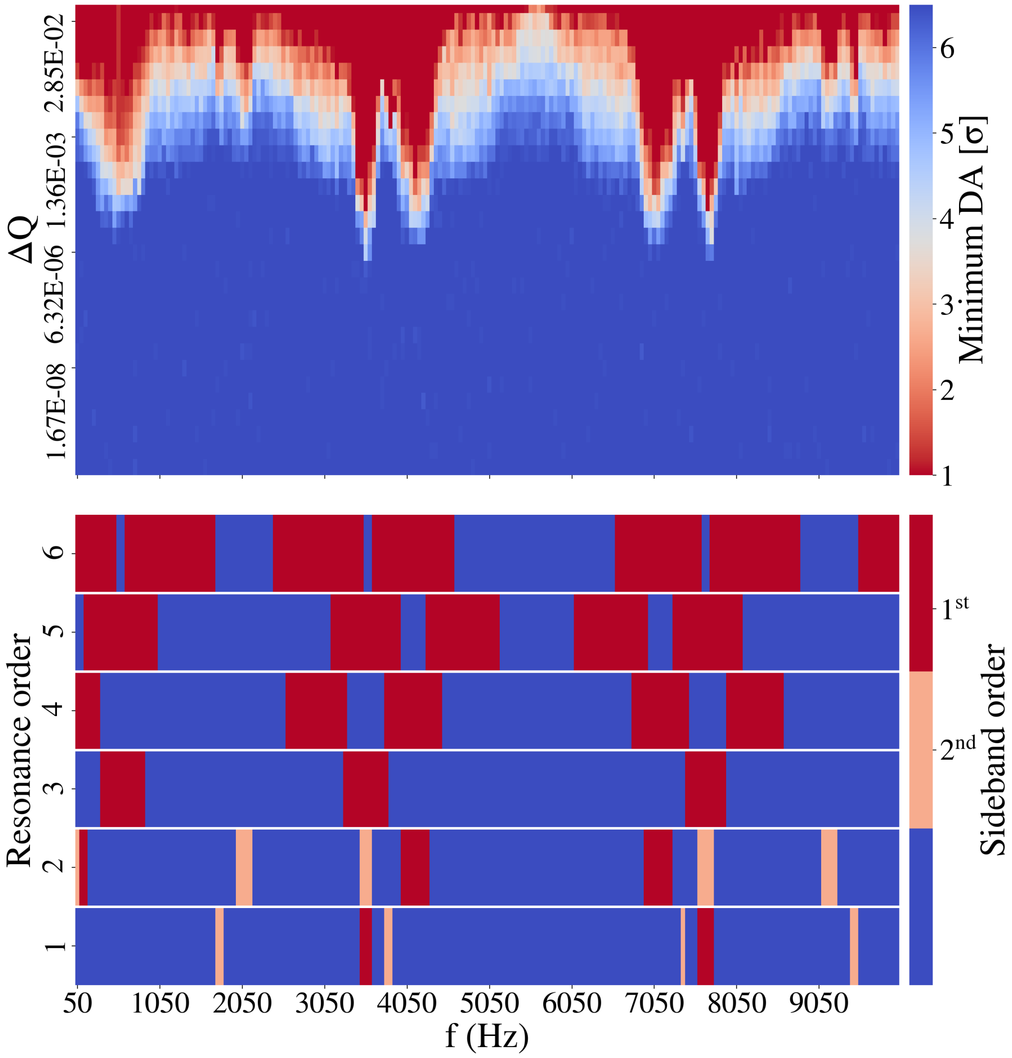

Figure 5.18: The tune modulation parameter space color-coded with the minimum DA (top) and the modulation frequency as a function of the resonance order (bottom). A color-code is assigned (bottom) depending on whether the first (red) or second (orange) order sideband of the resonance order reaches the footprint or not (blue) for each modulation frequency.

Table 5.2: The modulation depths of the low order 50 Hz harmonics as computed from the maximum output voltage of the power converter specifications.

Frequency (Hz)	$\Delta Q_{\mathrm{rms}}(\times 10^{-6})$	$\Delta Q_{\mathrm{max}}(\times 10^{-6})$
50	1.3	4.5
150	0.8	2.8
300	0.7	2.4
600	0.3	1.2

noise spectrum under consideration consists of the low-order 50 Hz harmonics. Table 5.2 shows the amplitude of each frequency as defined from the root mean square and the maximum modulation depth shown in Fig. 5.13 (dashed lines).

Figure 5.19 depicts the 5D FMAs for three studies: first, with the reference conditions, i.e., in the absence of noise (Fig. 5.19a), second, with amplitudes that correspond to the root mean square modulation depth (Fig. 5.19b) and last, using the maximum modulation depth (Fig. 5.19c) for each frequency as computed from the power converter specifications. From the review of the frequency maps the combined impact of the modulation at 50 Hz (blue, first sideband of the second-order resonance) and 600 Hz (cyan, first sideband of the third-order resonance) is visible. However, the increase in diffusion is small compared to the reference case.

Additional simulations are performed to estimate whether the slight increase in diffusion observed in the frequency maps can eventually enhance the particle losses. Figure 5.20 illustrates the intensity evolution for the three aforementioned studies. The results suggest that the considered noise spectrum (green and blue) has an insignificant impact on the intensity compared to the reference case (black) for tracking that corresponds to 90 seconds of operation. Based on these results, it is concluded that the combined effect of multiple voltage tones in the noise spectrum, with modulation depths that are extracted from the power converter specifications, will not affect the beam performance of the HL-LHC.

The present chapter depicts the results of the tracking simulations that include the most important non-linear fields in the machine such as the ones induced by beam-beam effects and non-linear magnets. Additional effects such as electron-cloud and magnet imperfections, which have been experimentally observed in the LHC, can potentially introduce additional non-linearities [107]. In this context, the interplay of such mechanisms with the noise should be further investigated in the future.

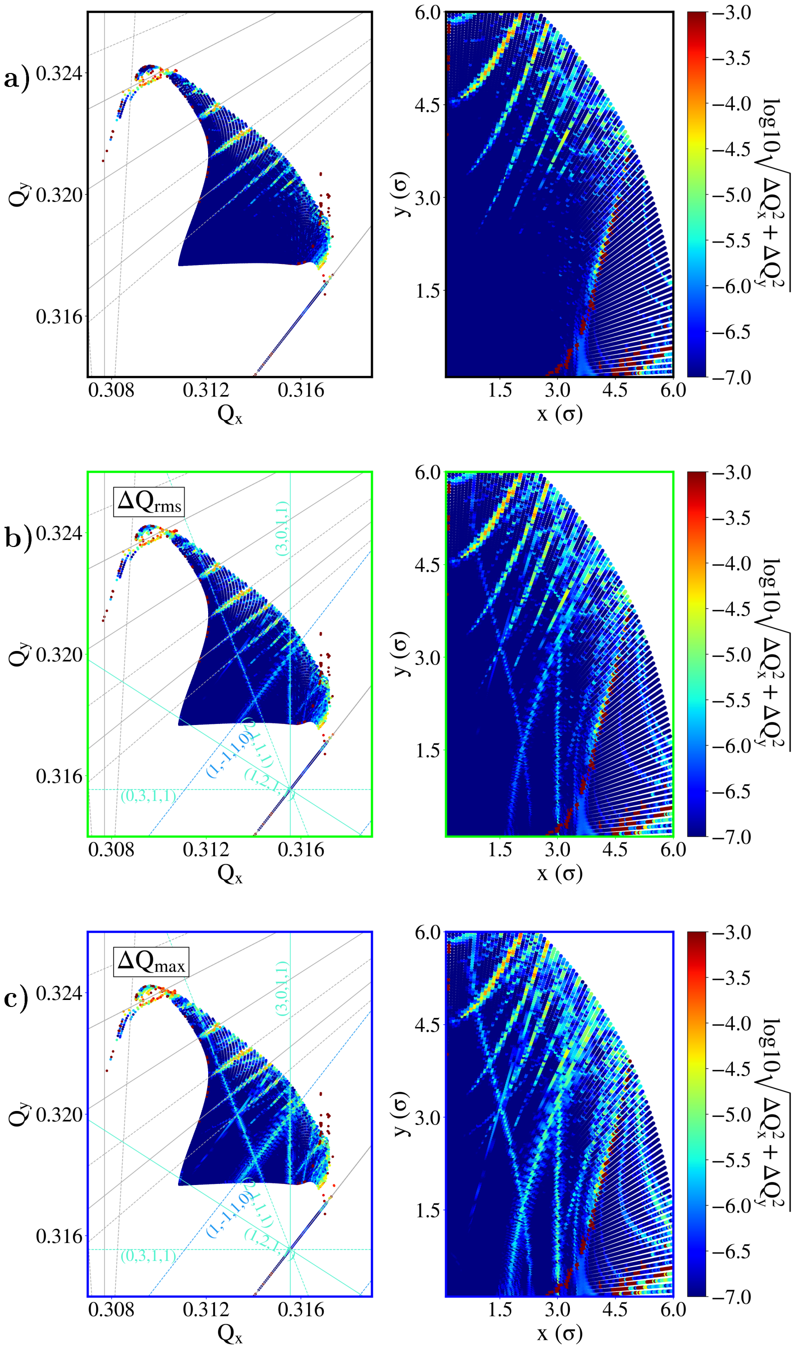

Figure 5.19: The 5D FMAs (left panel) and the initial configuration space (right panel) (a) in the absence of noise, including a tune modulation with spectral components at 50, 150, 300 and 600 Hz with (b) the root mean square and (c) the maximum modulation depth as computed from the power converter specifications. The first-order sidebands due to the combined effect of the tones at 50 Hz (blue lines, second-order resonance) and 600 Hz (cyan lines, third-order resonance) are shown.

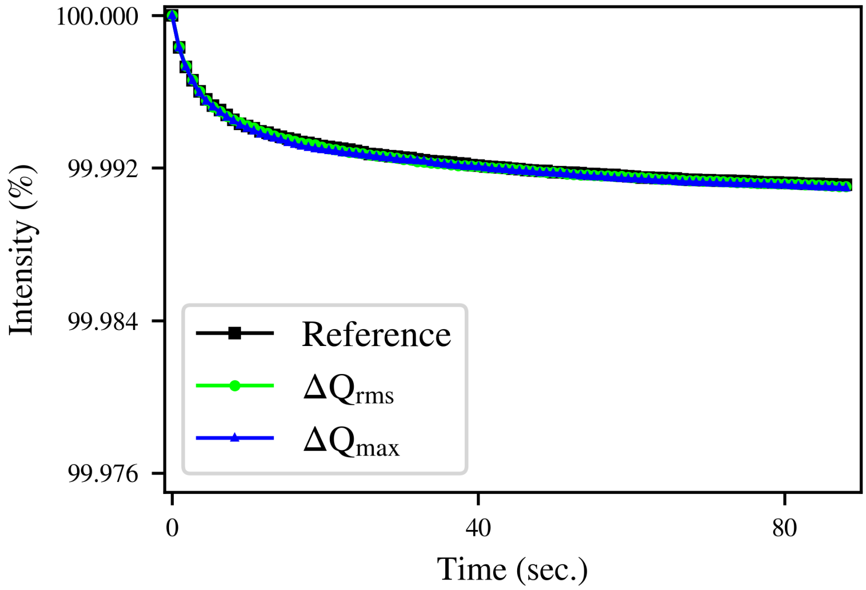

Figure 5.20: The intensity evolution in the absence of noise (black) and including a noise spectrum that consists of 50, 150, 300 and 600 Hz with the root mean square (green) and maximum (blue) modulation depth.

Chapter 6

Conclusions

In high-energy particle accelerators such as the LHC and its high-luminosity upgrade, a major concern for the transverse single-particle beam dynamics is the presence of noise, a mechanism that can impact the long term stability of the circulating particles and eventually prove detrimental to the beam lifetime. Among several noise sources present in the accelerator, this thesis investigated the impact of a periodic time variation in the strengths of the dipoles in the arcs and the quadrupoles in the inner triplet due to power converter noise.

The two phenomena under investigation present significant differences in terms of the power converter technology that is used in each case, the type of the magnet and the coupling mechanism of the noise spectrum to the beam motion. In particular, noise in a dipole leads to the appearance of additional frequency components in the beam spectrum at constant frequencies, which are equal to the excitation frequencies. These dipolar perturbations result in the excitation of additional resonances at constant frequencies in the tune diagram, an effect that was demonstrated in this thesis, for the first time, with frequency maps. On the contrary, the tune modulation that arises from quadrupolar noise leads to the appearance of sidebands around the betatron tune at a distance equal to multiples of the modulation frequency. In the presence of non-linearities, this mechanism causes the excitation of sideband resonances in the vicinity of the ones that intrinsically emerge from the lattice non-linearities. Although the concept of sideband resonances in the tune diagram has been introduced in the past, it is the first time that the excitation of additional resonances due to modulation effects was demonstrated with tracking simulations and frequency maps.

In the context of these studies, a general analysis framework of the experimental and simulation data has been developed. Although many differences are present between the two mechanisms under investigation, a similar analysis approach was adopted in both cases. This fact underlines that the methodology presented in this thesis can be generalized to also address several other types of noise effects.

The first section of this thesis was dedicated to the investigation of the 50 Hz harmonics that have been observed in the beam spectrum since the start of the LHC operation. A systematic analysis of the beam spectrum across several beam and machine configurations revealed the existence of 50 Hz harmonics in two regimes of the frequency domain: first, a cluster of harmonics extending up to approximately 3.6 kHz, namely the low-frequency cluster and second, the high-frequency cluster, centered around $\mathrm{f_{rev}} - \mathrm{f_x}$, where $\mathrm{f_{rev}}, \mathrm{f_x}$ represent the revolution and betatron frequency, respectively. The methodology devised in this thesis allowed us to identify, for the first time in the LHC operation, the existence of the high-frequency cluster on the beam signal.

The 50 Hz harmonics were observed in all beam modes, mainly affecting the horizontal plane and a larger impact was reported for Beam 1 by approximately a factor of two compared to Beam 2. In both cases, the observed effect indicates a dipolar nature of the source. This thesis showed definitive indications that both regimes are the result of a real beam excitation, rather than an artifact of the instrumentation system.

As far as the low-frequency cluster is concerned, a correlation with the eight SCR power converters of the main dipoles was clearly established during dedicated experiments. Specifically, changing the status of the power converter active filters led to distinct and abrupt changes in the amplitude evolution of the harmonics in the beam. These experiments showed that all eight power converters contribute to the existence of the low-frequency cluster on the beam spectrum. It is the first time that such a correlation has been demonstrated in the LHC.

The low and high-frequency clusters exhibit a similar signature in frequency domain: first, they consist of multiple 50 Hz harmonics and second, a common phase modulation is reported for all the harmonics, which originates from the stability of the electrical network mains. These findings indicate that the low and high-frequency clusters emerge from a common source. An amplitude asymmetry between the two clusters was identified. In particular, a more significant effect was reported in terms of amplitude for the high-frequency cluster, an observation that contradicts the expected attenuation of the power converter noise with increasing frequency. The amplitude asymmetry between the low and high-frequency cluster, suggests that the latter results from the interplay between noise from the dipoles and a mechanism originating from the beam, rather than a direct dipolar excitation. Therefore, future studies will concentrate on identifying the mechanism that increases the sensitivity of the beam to noise in the regime $\mathrm{f_{rev}} - \mathrm{f_x}$ compared to $\mathrm{f_x}$.

Single-particle tracking simulations, based on a realistic noise spectrum and a simplified lumped transfer function of the noise, indicate that these excitations increase the diffusion of the particles. From a tracking that corresponds to 90 seconds in operation, the excitation of additional resonances eventually led to proton losses, especially due to the high-frequency cluster. Based on these results, it is concluded that the 50 Hz harmonics had an impact on the beam performance during the LHC operation.

In addition, due to the discrepancy of the noise spectrum in Beam 1 and 2, the aforementioned simulations illustrated a clear differentiation in the intensity evolution of the two beams. An important lifetime asymmetry between the two beams has been observed since the beginning of run 2 and it is the first time that tracking simulations show that noise can contribute to this effect.

It must be noted that, neglecting the interplay with the transverse damper, the 50 Hz harmonics induced a beam offset in the order of 10^{-3} σ. The presence of such small excitations verifies that the stability of the power converters is well within the specifications and highlights the capabilities of the instrumentation systems. However, such small perturbations in the vicinity of the tune and its alias, combined with the non-linearities of the lattice, can indeed lead to a degradation of the beam lifetime.

Due to their origin, these harmonics are expected to be present in the future operation of the LHC. Therefore, the studies focus on extending the understanding of the mechanism that not only enables the high-frequency cluster to perturb the beam motion but that also leads to a more significant impact compared to the direct excitations of the low-frequency cluster. More importantly, regardless of the source, mitigation measures should be incorporated in the future operation to effectively suppress the 50 Hz harmonics from the beam motion.

For the HL-LHC noise studies in the inner triplet, the predictions presented in this thesis were based on simulated parameters that correspond to the end of the luminosity levelling. This is the most critical scenario in terms of noise due to the increase of the maximum β-functions in the quadrupoles at these locations. By individually scanning several modulation frequencies and depths, in the presence of strong non-linear fields such as beam-beam effects, the impact of the noise on the DA was computed, combined with the tune modulation induced by the coupling of the longitudinal and transverse plane through chromaticity. A comparison with the power converter specifications, without considering the shielding effects of the magnets that lead to a further attenuation of the ripples, yielded that the maximum expected noise level is several orders of magnitude lower than the DA reduction threshold.

The sensitivity of the beam performance to particular modulation frequencies, as shown with FMAs, results from the excitation of sideband resonances that affect the particles' diffusion, a mechanism that strongly depends on the working point and the lattice non-linearities. Contrary to dipolar excitations, quadrupolar noise can impact the beam performance even if the modulation frequency is not in the vicinity of the betatron frequency and it introduces a frequency-dependent mechanism of diffusion, an effect that was illustrated with frequency maps.

Considering a noise spectrum with several voltage tones and modulation depths extracted from the power converters' specifications, the impact on the beam performance was computed with simulations. A small increase of diffusion was reported, however, without leading to a lifetime degradation. Based on the simulation results, the combined effect of power converter noise in the inner triplet and synchro-betatron coupling during operation with high chromaticities is not expected to act as a luminosity degradation mechanism in the HL-LHC era.

As a next step, the DA tolerances defined by the simulations must be experimentally verified through controlled quadrupolar excitations. To improve the validity of the simulations, a realistic power converter spectrum must be included, in combination with a more accurate representation of the transfer function of the noise spectrum from the voltage to the magnetic field.

In conclusion, the analysis and the results of this thesis substantially improve our understanding of the noise effects that were present in the LHC and that are anticipated in the future operation of the accelerator.

Appendix A

A.1 Canonical transformations

The canonical transformations are needed to recast the initial conjugate variables (q, p) to a new set (Q, P) with a simpler form. The types of canonical transformations are:

$$G = F_1(q, Q; t),\ p = \frac{\partial F_1}{\partial q},\ P = -\frac{\partial F_1}{\partial Q},\ H_1 = H + \frac{\partial F_1}{\partial t}, \tag{A.1}$$

$$G = F_2(q, P; t),\ p = \frac{\partial F_2}{\partial q},\ Q = \frac{\partial F_2}{\partial P},\ H_2 = H + \frac{\partial F_2}{\partial t}, \tag{A.2}$$

$$G = F_3(p, Q; t),\ q = -\frac{\partial F_3}{\partial p},\ P = -\frac{\partial F_3}{\partial Q},\ H_3 = H + \frac{\partial F_3}{\partial t}, \tag{A.3}$$

$$G = F_4(p, P; t),\ q = -\frac{\partial F_4}{\partial p},\ Q = \frac{\partial F_4}{\partial P},\ H_4 = H + \frac{\partial F_4}{\partial t}. \tag{A.4}$$

A.2 Hamilton's equations

Hamilton's equations can be expressed as:

$$\dot{q_i} = \frac{\partial H}{\partial p_i}\ ,\ \dot{p_i} = -\frac{\partial H}{\partial q_i}\ ,\ \frac{\partial L}{\partial t} = -\frac{\partial H}{\partial t}, \tag{A.5}$$

where the overdot is the derivative with respect to the independent variable t. For $\vec{x} = (q_1, p_1, ..q_N, p_N)$ the form of Hamilton's equations is:

$$\frac{d\vec{x}}{dt} = S \cdot \nabla H, \tag{A.6}$$

with S an antisymmetric $2N$x $2N$ matrix with each of the N blocks given by:

$$S_N = \begin{bmatrix} 0 & 1 \\ -1 & 0 \end{bmatrix}. \tag{A.7}$$

A.3 Beta-beating due to gradient error

In the presence of a gradient error ΔK at the location s_1 in the ring, the perturbed transfer matrix can be represented as:

$$\tilde{M}(s|s+C) = M(s_1|s+C)M_{err}M(s|s_1) = \begin{pmatrix} \tilde{M_{11}} & \tilde{M_{12}} \\ \tilde{M_{21}} & \tilde{M_{22}} \end{pmatrix}, \tag{A.8}$$

where:
$M(s|s_1)$ is the transfer matrix from the position of observation s to the location of the perturbation s_1,
M_{err} is the quadrupole perturbation $M_{err} = \begin{pmatrix} 1 & 0 \\ -\Delta K \mathrm{d}s & 1 \end{pmatrix}$ and,
$M(s_1|s+C)$ is the transfer matrix from the location of the perturbation to the position of the observation. The gradient error results in a tune shift δQ and a variation of the $\beta-$function $\Delta\beta$. Then, from Eq. (2.63):

$$\tilde{M_{12}} = (\beta + \Delta\beta)\sin\left(2\pi(Q + \delta Q)\right), \tag{A.9}$$

where β is the initial β-function at the location s. For a small change in the tune, it follows that $\cos(2\pi\Delta Q) \approx 1$ and $\sin(2\pi\Delta Q) \approx 2\pi\Delta Q$. Assuming that the product $\Delta\beta\Delta Q$ is negligible:

$$\tilde{M_{12}} = \beta\sin(2\pi Q) + \Delta\beta\sin(2\pi Q) + 2\pi\delta Q\beta\cos(2\pi Q). \tag{A.10}$$

Replacing the rotation matrices from s_1 to $s+C$ and s to s_1 with Eq. (2.53) and performing the matrix multiplication of Eq. (A.8) yields:

$$\tilde{M_{12}} = \beta\sin(2\pi Q) - \beta\beta_{s_1}\sin(y)\sin(2\pi Q - y), \tag{A.11}$$

where y is the phase advance between s and s_1. From Eq. (A.9) and (A.11) and for multiple gradient errors around the lattice:

$$\frac{\Delta\beta(s)}{\beta(s)} = -\frac{1}{2\sin\left(2\pi Q\right)}\int_s^{s+C} \beta(s_1)\Delta k(s_1)\cos\left[2(y(s) - y(s_1)) - 2\pi Q\right]\mathrm{d}s_1. \tag{A.12}$$

A.4 Expansion of the Hamiltonian in canonical perturbation theory

The expansion of the Hamiltonian is:

$$H_0(\tilde{\boldsymbol{J}} + \epsilon\frac{\partial G}{\partial\boldsymbol{\phi}}; s) = H_0(\tilde{\boldsymbol{J}}) + \epsilon\frac{\partial G}{\partial\boldsymbol{\phi}}\frac{\partial H_0(\tilde{\boldsymbol{J}})}{\partial\tilde{\boldsymbol{J}}} + \frac{1}{2}\epsilon^2(\frac{\partial G}{\partial\boldsymbol{\phi}})^2\frac{\partial^2 H_0(\tilde{\boldsymbol{J}})}{\partial^2\tilde{\boldsymbol{J}}} + .., \tag{A.13}$$

$$\epsilon H_1(\tilde{\boldsymbol{J}} + \epsilon\frac{\partial G}{\partial\boldsymbol{\phi}}, \phi; s) = \epsilon H_1(\tilde{\boldsymbol{J}}, \phi; \theta) + \epsilon^2\frac{\partial G}{\partial\boldsymbol{\phi}}\frac{\partial H_1(\tilde{\boldsymbol{J}}, \phi; s)}{\partial\tilde{\boldsymbol{J}}} + \frac{1}{2}\epsilon^3(\frac{\partial G}{\partial\boldsymbol{\phi}})^2\frac{\partial^2 H_1(\tilde{\boldsymbol{J}}, \phi; s)}{\partial^2\tilde{\boldsymbol{J}}} + .. \tag{A.14}$$

A.5 Derivation of the Hamiltonian in the vicinity of a resonance

In two degrees of freedom, a perturbation can be expressed in the form:

$$H_1 = H_{p_x,p_y} x^{p_x} y^{p_y}, \tag{A.15}$$

where p_x, p_y positive integers that represent the order of the nonlinearity. Using the mixed-variable generating function of the first kind:

$$F_1(x, y, \tilde{\phi}_x, \tilde{\phi}_y) = -\frac{x^2}{2\beta_x}\left(\tan(\tilde{\phi}_x + W_x) + \alpha_x\right) - \frac{y^2}{2\beta_y}\left(\tan(\tilde{\phi}_y + W_y) + \alpha_y\right), \tag{A.16}$$

where:

$$W_u(s) = R\int_{s_0}^{s_1} \frac{ds}{\beta_u} - Q_u s, \tag{A.17}$$

with $u = (x, y)$. From the rules of generating function of the first kind (Appendix A.1):

$$\tilde{J}_u = \frac{\partial F_1}{\partial \tilde{\phi}_u} = \frac{u^2}{2\beta_u \cos^2(\tilde{\phi}_u + W_u)} \text{ and } p_u = \frac{\partial F_1}{\partial u} = -\frac{u}{\beta_u}\left(\tan(\tilde{\phi}_u + W_u + a_u)\right). \tag{A.18}$$

As a result:

$$u = \sqrt{2\tilde{J}_u\beta_u}\cos(\tilde{\phi}_u + W_u) = \sqrt{\frac{\tilde{J}_u\beta_u}{2}}\left(\mathrm{e}^{i(\tilde{\phi}_u+W_u)} + \mathrm{e}^{-i(\tilde{\phi}_u+W_u)}\right). \tag{A.19}$$

Substituting Eq. (A.19) to (A.15) and setting $p_x = j+k,\ m_x = j-k,\ p_y = l+m$ and $m_y = l-m$:

$$H_1 = \frac{1}{R}\tilde{J}_x^{\,p_x/2}\tilde{J}_y^{\,p_y/2}\sum_{j=0}^{p_x}\sum_{l=0}^{p_y} h_{jklm}\mathrm{e}^{i(m_x\tilde{\phi}_x + m_y\tilde{\phi}_y)}, \tag{A.20}$$

with:

$$h_{jklm} = \frac{H_{p_x,p_y}R}{2^{\frac{j+k+l+m}{2}}}\binom{p_x}{j}\binom{p_y}{l}\beta_x^{p_x/2}\beta_y^{p_y/2}\mathrm{e}^{i(m_xW_x + m_yW_y)}. \tag{A.21}$$

Re-naming $\tilde{\phi}_u = \phi_u$ and $\tilde{J}_u = J_u$, the linear part of the Hamiltonian is equal to:

$$H_0(J_x, J_y) = \frac{Q_x}{R}J_x + a(J_x) + \frac{Q_y}{R}J_y + a(J_y), \tag{A.22}$$

with $a(J_u)$ the higher order terms of the action. By imposing a periodic condition, the perturbation can be expanded into a Fourier series:

$$H_1(J_x, J_y, \phi_x, \phi_y; s) = \frac{1}{R}\sum_{j=0}^{p_x}\sum_{l=0}^{p_y}\sum_{n=-\infty}^{\infty} J_x^{p_x/2}J_y^{p_y/2}h_{jklmn}\mathrm{e}^{i(m_x\phi_x + m_y\phi_y - ns)}, \tag{A.23}$$

with h_{jklmn} the resonance driving terms that can be expressed as:

$$h_{jklmn} = \frac{1}{2^{\frac{j+k+l+m}{2}}}\begin{bmatrix} p_x \\ j \end{bmatrix}\begin{bmatrix} p_y \\ l \end{bmatrix}\frac{1}{2\pi}\int_{s_0}^{s_0+2\pi}\beta_x^{p_x/2}\beta_y^{p_y/2}H_{p_x,p_y}\mathrm{e}^{i[m_xW_x + m_yW_y + ns]}\mathrm{ds}. \tag{A.24}$$

In the vicinity of a resonance, the perturbation H_1 is dominated by the term:

$$V(J_x, J_y, \phi_x, \phi_y; s) = \frac{2}{R}|k|J_x^{m_x/2}J_y^{m_y/2}\cos(m_x\phi_x + m_y\phi_y - n\frac{s-s_0}{R}), \tag{A.25}$$

with $k = |k|\mathrm{e}^{i\phi_k} = h_{jklmp}$. The form of the new Hamiltonian is:

$$H = \frac{Q_x}{R}J_x + \frac{Q_y}{R}J_y + \frac{2}{R}|k|J_x^{m_x/2}J_y^{m_y/2}\cos(m_x\phi_x + m_y\phi_y - n\frac{s-s_0}{R}). \tag{A.26}$$

Appendix B

B.1 Frequency modulation and harmonics

This section presents the impact of a frequency modulation on a harmonic dipolar excitation, similar to the one observed in the 50 Hz harmonics. To simulate this effect, a single particle is tracked in the LHC lattice in the presence of a dipole field error. The dipole strength is modulated with the absolute value of a sinusoidal function at a frequency of 100 Hz. This perturbation mimics a non-linear transfer function exciting all the even harmonics of the fundamental frequency (100 Hz). Furthermore, an arbitrary low-frequency modulation is injected in the fundamental frequency. Figure B.1 illustrates the spectrogram for a frequency range up to 1.8 kHz, color-coded with the PSD. All harmonics experience a similar frequency modulation with a peak-to-peak variation proportional to the order of the harmonic.

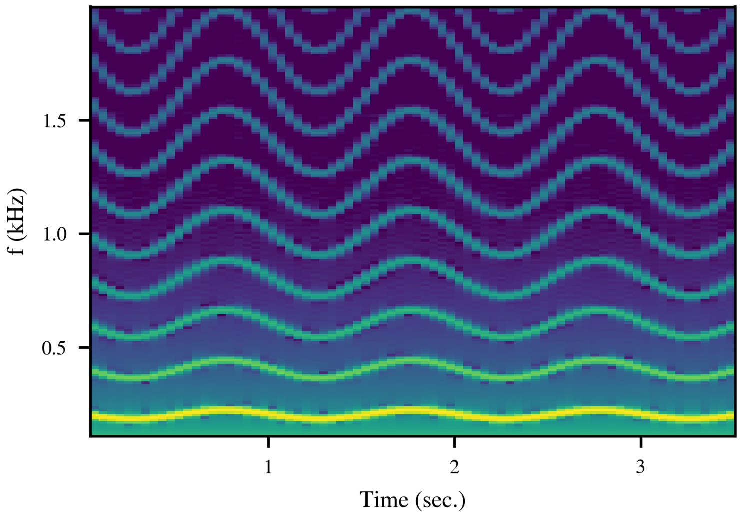

Figure B.1: The impact of a frequency modulation on a harmonic dipolar excitation.

B.2 Parameters for the modulation depth computations from the power converter specifications

Figure B.2 presents the maximum tolerated root mean square voltage ripple as a function of the frequency for all LHC power converters. Table B.1 illustrates the parameters used for the computation of the modulation depth from the modeling of the quadrupoles as RL circuits. In the computations the contribution from Q1, Q2a, Q2b, Q3 and the trims Q1, Q2a, and Q3 left and right of IP1 and IP5 are considered.

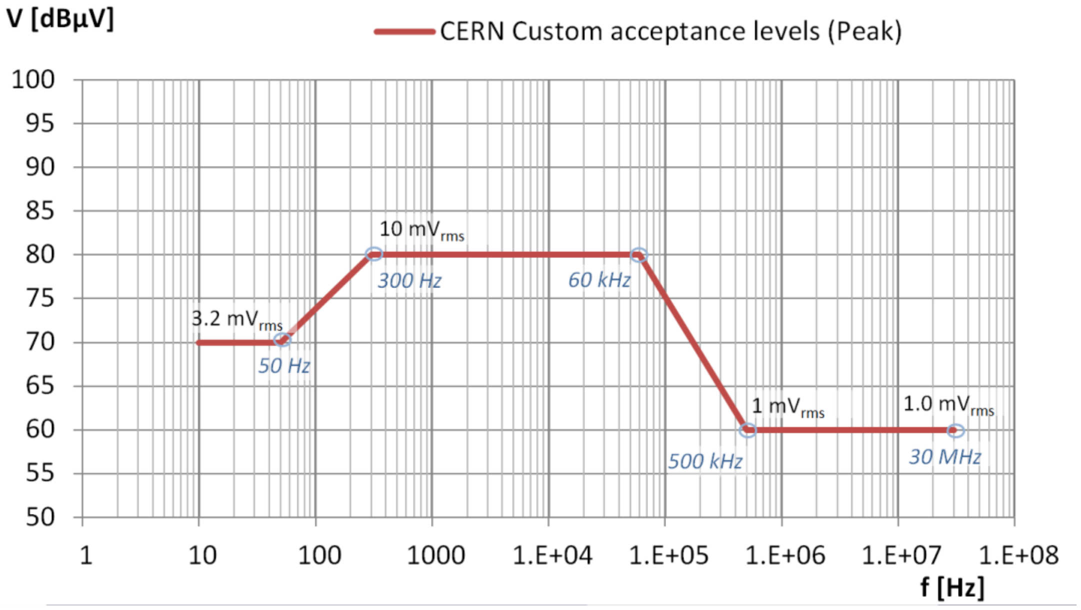

Figure B.2: The CERN Gabarit [126]. The maximum tolerated root mean square voltage ripple as a function of the frequency is illustrated.

Table B.1: The modulation depth, the current and the inductance of the circuits for Beam 1, at $\beta^* = 15$ cm and with round optics [121, 122, 127].

	$\frac{\Delta Q}{\Delta I/I_{rated}}$		
RQX.L1	80.500	RTQX3.L1	4.490
RQX.R1	62.790	RTQX3.R1	9.070
RQX.L5	79.160	RTQXA1.L5	0.060
RQX.R5	61.620	RTQXA1.R5	0.060
RTQXA1.L1	0.060	RTQX1.L5	2.670
RTQXA1.R1	0.060	RTQX1.R5	2.000
RTQX1.L1	2.700	RTQX3.L5	4.470
RTQX1.R1	2.010	RTQX3.R5	8.970

	L (mH)	I_{rated} (kA)
Q1/Q2a/Q2b/Q3	255	18
Trim Q1	69	2
Trim Q1a	34.5	0.035
Trim Q3	69	2

List of Figures

List of Tables

Bibliography

[1] S. L. Glashow, “Partial-symmetries of weak interactions”, *Nuclear Physics*, vol. 22, no. 4, pp. 579–588, 1961.

[2] S. Weinberg, “A Model of Leptons”, *Phys. Rev. Lett.*, vol. 19, pp. 1264–1266, 21 Nov. 1967. DOI: `10.1103/PhysRevLett.19.1264`. [Online]. Available: `https://link.aps.org/doi/10.1103/PhysRevLett.19.1264`.

[3] A. Salam and J. C. Ward, “Weak and electromagnetic interactions”, *Nuovo Cim.*, vol. 11, pp. 568–577, 1959. DOI: `10.1007/BF02726525`.

[4] M. Veltman *et al.*, “Regularization and renormalization of gauge fields”, *Nuclear Physics B*, vol. 44, no. 1, pp. 189–213, 1972.

[5] *CERN*, `https://home.cern/`, Accessed: 2019-09-03.

[6] S. Myers, *The LEP Collider, from design to approval and commissioning*, ser. John Adams’ Lecture. Geneva: CERN, 1991, Delivered at CERN, 26 Nov 1990. DOI: `10.5170/CERN-1991-008`. [Online]. Available: `https://cds.cern.ch/record/226776`.

[7] *ATLAS*, `https://home.cern/science/experiments/atlas`, Accessed: 2020-02-20.

[8] *CMS*, `https://home.cern/science/experiments/cms`, Accessed: 2020-02-20.

[9] *ALICE*, `https://home.cern/science/experiments/alice`, Accessed: 2020-02-20.

[10] *LHCb*, `https://home.cern/science/experiments/lhcb`, Accessed: 2020-02-20.

[11] G. Aad, T. Abajyan, B. Abbott, *et al.*, “Observation of a new particle in the search for the Standard Model Higgs boson with the ATLAS detector at the LHC”, *Physics Letters B*, vol. 716, no. 1, pp. 1–29, 2012.

[12] S. Chatrchyan, V. Khachatryan, A. M. Sirunyan, *et al.*, “Observation of a new boson at a mass of 125 GeV with the CMS experiment at the LHC”, *Physics Letters B*, vol. 716, no. 1, pp. 30–61, 2012.

[13] F. Englert and R. Brout, “Broken symmetry and the mass of gauge vector mesons”, *Physical Review Letters*, vol. 13, no. 9, p. 321, 1964.

[14] P. W. Higgs, “Broken symmetries and the masses of gauge bosons”, *Physical Review Letters*, vol. 13, no. 16, p. 508, 1964.

[15] G. S. Guralnik, C. R. Hagen, and T. W. Kibble, “Global conservation laws and massless particles”, *Physical Review Letters*, vol. 13, no. 20, p. 585, 1964.

[16] T. W. B. Kibble, "Symmetry Breaking in Non-Abelian Gauge Theories", *Phys. Rev.*, vol. 155, pp. 1554–1561, 5 Mar. 1967. DOI: 10.1103/PhysRev.155.1554. [Online]. Available: https://link.aps.org/doi/10.1103/PhysRev.155.1554.

[17] W. Herr and B. Muratori, "Concept of luminosity", in *Intermediate accelerator physics. Proceedings, CERN Accelerator School, Zeuthen, Germany, September 15-26, 2003*, 2003, pp. 361–377. [Online]. Available: http://doc.cern.ch/yellowrep/2006/2006-002/p361.pdf.

[18] F. Antoniou, M. Hostettler, G. Iadarola, S. Papadopoulou, Y. Papaphilippou, D. Pellegrini, and G. Trad, "Can we predict luminosity?", 125–132. 8 p, 2017. [Online]. Available: https://cds.cern.ch/record/2293678.

[19] F. Antoniou, G. Arduini, M. Hostettler, *et al.*, "LHC Luminosity Modeling for Run II", no. CERN-ACC-2016-268, TUPMW002. 4 p, 2016. DOI: 10.18429/JACoW-IPAC2016-TUPMW002. [Online]. Available: https://cds.cern.ch/record/2207357.

[20] S. Papadopoulou, F. Antoniou, I. Efthymiopoulos, M. Hostettler, G. Iadarola, N. Karastathis, S. Kostoglou, Y. Papaphilippou, and G. Trad, "Monitoring and Modelling of the LHC Emittance and Luminosity Evolution in 2018", in *Proceedings, 10th International Particle Accelerator Conference (IPAC2019): Melbourne, Australia, May 19-24, 2019*, 2019, WEPTS046. DOI: 10.18429/JACoW-IPAC2019-WEPTS046.

[21] V. Lebedev, "Emittance growth due to noise and its suppression with the feedback system in large hadron colliders", in *AIP Conference Proceedings*, AIP, vol. 326, 1995, pp. 396–423.

[22] V. Lebedev, "Computer simulation of the emittance growth due to noise in large hadron colliders", *Part. Accel.*, vol. 44, no. SSCL-Preprint-191, pp. 165–199, 1993.

[23] F. Zimmermann, "Emittance growth and proton beam lifetime in HERA", PhD thesis, Hamburg U., 1993. [Online]. Available: http://lss.fnal.gov/archive/other/desy-93-059.pdf.

[24] P. Baudrenghien and T. Mastoridis, "Transverse emittance growth due to rf noise in the high-luminosity LHC crab cavities", *Physical Review Special Topics-Accelerators and Beams*, vol. 18, no. 10, p. 101 001, 2015.

[25] W. Fischer, "An experimental study on the long-term stability of particle motion in hadron storage rings", PhD thesis, Hamburg U., 1995. [Online]. Available: https://cds.cern.ch/record/293621.

[26] X. Altuna, C. Arimatea, R. Bailey, *et al.*, "The 1991 dynamic aperture experiment at the CERN SPS", no. CERN-SL-91-43-AP. LHC-NOTE-171. CERN-LHC-Note-171, 16 p, Nov. 1991. DOI: 10.1063/1.42289. [Online]. Available: http://cds.cern.ch/record/231461.

[27] O. S. Brüning, "Diffusion In A Fodo Cell Due To Modulation Effects In The presence Of nonlinear Fields", *Part. Accel.*, vol. 41, no. DESY-HERA-92-20, 133–151. 13 p, Sep. 1992. [Online]. Available: `https://cds.cern.ch/record/1108270`.

[28] W. Fischer and M. Giovannozzi, "Dynamic aperture experiment at a synchrotron", *Physical Review E*, vol. 55, pp. 3507–3520, Mar. 1997. DOI: `10.1103/PhysRevE.55.3507`.

[29] O. S. Brüning and F. Willeke, "Diffusion-like processes in proton storage rings due to the combined effect of non-linear fields and modulational effects with more than one frequency", in *European Particle Accelerator Conference (EPAC 1994)*, Jul. 1994. [Online]. Available: `https://cds.cern.ch/record/271555`.

[30] O. S. Brüning, M. Seidel, K. Mess, and F. Willeke, "Measuring the effect of an external tune modulation on the particle diffusion in the proton storage ring of HERA", P00021147, Tech. Rep., 1994.

[31] A. Chao, D. Johnson, S. Peggs, *et al.*, "Experimental investigation of nonlinear dynamics in the Fermilab Tevatron", *Physical review letters*, vol. 61, no. 24, p. 2752, 1988.

[32] T. Satogata, T. Chen, B. Cole, *et al.*, "Driven response of a trapped particle beam", *Phys. Rev. Lett.*, vol. 68, pp. 1838–1841, 12 Mar. 1992. DOI: `10.1103/PhysRevLett.68.1838`. [Online]. Available: `https://link.aps.org/doi/10.1103/PhysRevLett.68.1838`.

[33] O. S. Brüning, P. Collier, P. Lebrun, S. Myers, R. Ostojic, J. Poole, and P. Proudlock, *LHC Design Report*, ser. CERN Yellow Reports: Monographs. Geneva: CERN, 2004. DOI: `10.5170/CERN-2004-003-V-1`. [Online]. Available: `http://cds.cern.ch/record/782076`.

[34] E. Mobs, "The CERN accelerator complex - 2019. Complexe des accélérateurs du CERN - 2019", Jul. 2019, General Photo. [Online]. Available: `https://cds.cern.ch/record/2684277`.

[35] S. Fartoukh, "Achromatic telescopic squeezing scheme and application to the LHC and its luminosity upgrade", *Phys. Rev. Spec. Top. Accel. Beams*, vol. 16, no. CERN-ACC-2013-0289, 111002. 33 p, Dec. 2013. DOI: `10.1103/PhysRevSTAB.16.111002`. [Online]. Available: `https://cds.cern.ch/record/1636178`.

[36] W. Herr and T. Pieloni, "Beam-Beam Effects", Jan. 2016. DOI: `10.5170/CERN-2014-009.431`.

[37] M. Hostettler, K. Fuchsberger, G. Papotti, Y. Papaphilippou, and T. Pieloni, "Luminosity scans for beam diagnostics", *Phys. Rev. Accel. Beams*, vol. 21, p. 102 801, 10 Oct. 2018. DOI: `10.1103/PhysRevAccelBeams.21.102801`. [Online]. Available: `https://link.aps.org/doi/10.1103/PhysRevAccelBeams.21.102801`.

[38] M. Giovannozzi, “Simple models describing the time-evolution of luminosity in hadron colliders”, no. CERN-ACC-2014-0086, 5 p, Jun. 2014. [Online]. Available: https://cds.cern.ch/record/1742039.

[39] M. Hostettler, “LHC Luminosity Performance”, Presented 21 Jun 2018, May 2018. [Online]. Available: https://cds.cern.ch/record/2319396.

[40] R. Alemany-Fernandez, E. Bravin, L. Drosdal, *et al.*, “Operation and Configuration of the LHC in Run 1”, Nov. 2013. [Online]. Available: https://cds.cern.ch/record/1631030.

[41] J. Wenninger, “Operation and Configuration of the LHC in Run 2”, Mar. 2019. [Online]. Available: https://cds.cern.ch/record/2668326.

[42] H. Damerau, A. Findlay, S. Gilardoni, and S. Hancock, “RF Manipulations for Higher Brightness LHC-Type Beams”, no. CERN-ACC-2013-0210, 3 p, May 2013. [Online]. Available: https://cds.cern.ch/record/1595719.

[43] O. Brüning and L. Rossi, *The High Luminosity Large Hadron Collider: the new machine for illuminating the mysteries of Universe*. World Scientific Publishing Company, 2015, vol. 24.

[44] A. Wolski, *Beam dynamics in high energy particle accelerators*. World Scientific, 2014.

[45] S.-Y. Lee, *Accelerator physics*. World scientific publishing, 2018.

[46] H. Goldstein, C. Poole, and J. Safko, *Classical mechanics*, 2002.

[47] A. Wolski, *Maxwell's equations for magnets*, 2011. arXiv: 1103.0713.

[48] A. Wolski, “Low-emittance Storage Rings”, no. arXiv:1507.02213. arXiv:1507.02213, 245–294. 50 p, Jul. 2015, Presented at the CERN Accelerator School CAS 2013: Advanced Accelerator Physics Course, Trondheim, Norway, 18-29 August 2013. DOI: 10.5170/CERN-2014-009.245. [Online]. Available: https://cds.cern.ch/record/1982424.

[49] B. Holzer, *Introduction to accelerator physics*, URL: https://indico.cern.ch/event/91711/attachments/1096595/1564350/Summer_Stud_Holzer_2010.pdf, 2010.

[50] R. D. Ruth, “Single-particle dynamics in circular accelerators”, in *AIP conference proceedings*, AIP, vol. 153, 1987, pp. 150–235.

[51] T. J. Satogata, “Nonlinear resonance islands and modulational effects in a proton synchrotron”, PhD thesis, Northwestern U., 1993. DOI: 10.2172/1372845. [Online]. Available: http://lss.fnal.gov/archive/thesis/1900/fermilab-thesis-1993-52.pdf.

[52] B. V. Chirikov, “Resonance processes in magnetic traps”, *The Soviet Journal of Atomic Energy*, vol. 6, no. 6, pp. 464–470, 1960.

[53] B. V. Chirikov, “Research concerning the theory of non-linear resonance and stochasticity”, CM-P00100691, Tech. Rep., 1971.

[54] *SixTrack*, http://sixtrack.web.cern.ch/SixTrack/, Accessed: 2019-11-26, 2019.

[55] J. Laskar, C. Froeschlé, and A. Celletti, “The measure of chaos by the numerical analysis of the fundamental frequencies. Application to the standard mapping”, *Physica D: Nonlinear Phenomena*, vol. 56, no. 2-3, pp. 253–269, 1992.

[56] J. Laskar, “Secular evolution of the solar system over 10 million years”, *Astronomy and Astrophysics*, vol. 198, pp. 341–362, 1988.

[57] J. Laskar, “The chaotic motion of the solar system: A numerical estimate of the size of the chaotic zones”, *Icarus*, vol. 88, no. 2, pp. 266–291, 1990.

[58] S. Kostoglou, N. Karastathis, Y. Papaphilippou, D. Pellegrini, and P. Zisopoulos, “Development of Computational Tools for Noise Studies in the LHC”, in *Proceedings, 8th International Particle Accelerator Conference (IPAC 2017): Copenhagen, Denmark, May 14-19, 2017*, 2017, THPAB044. DOI: 10.18429/JACoW-IPAC2017-THPAB044.

[59] F. J. Harris, “On the use of windows for harmonic analysis with the discrete Fourier transform”, *Proceedings of the IEEE*, vol. 66, no. 1, pp. 51–83, 1978.

[60] J. Laskar, “Introduction to frequency map analysis”, in *Hamiltonian systems with three or more degrees of freedom*, Springer, 1999, pp. 134–150.

[61] J. Laskar, “Application of Frequency map analysis”, in *The Chaotic Universe: Proceedings of the Second ICRA Network Workshop, Rome, Pescara, Italy, 1-5 February 1999*, World Scientific, vol. 10, 2000, p. 115.

[62] J. Laskar, “Frequency map analysis of an Hamiltonian system”, in *AIP conference proceedings*, AIP, vol. 344, 1995, pp. 130–159.

[63] Y. Papaphilippou and J. Laskar, “Frequency map analysis and global dynamics in a galactic potential with two degrees of freedom.”, *Astronomy and Astrophysics*, vol. 307, pp. 427–449, 1996.

[64] Y. Papaphilippou, “Detecting chaos in particle accelerators through the frequency map analysis method”, *Chaos: An Interdisciplinary Journal of Nonlinear Science*, vol. 24, no. 2, p. 024 412, 2014.

[65] Y. Papaphilippou, “Frequency maps of LHC models”, in *Proceedings of the 1999 Particle Accelerator Conference (Cat. No. 99CH36366)*, IEEE, vol. 3, 1999, pp. 1554–1556.

[66] J. Laskar, “Frequency map analysis and particle accelerators”, in *Proceedings of the 2003 Particle Accelerator Conference*, IEEE, vol. 1, 2003, pp. 378–382.

[67] E. Todesco and M. Giovannozzi, “Dynamic aperture estimates and phase-space distortions in nonlinear betatron motion”, *Physical Review E*, vol. 53, no. 4, p. 4067, 1996.

[68] A. Bazzani, M. Giovannozzi, E. Maclean, C. Montanari, F. Van der Veken, and W. Van Goethem, "Advances on the modeling of the time evolution of dynamic aperture of hadron circular accelerators", *Physical Review Accelerators and Beams*, vol. 22, no. 10, p. 104 003, 2019.

[69] M. Giovannozzi, "Proposed scaling law for intensity evolution in hadron storage rings based on dynamic aperture variation with time", *Phys. Rev. ST Accel. Beams*, vol. 15, p. 024 001, 2012. DOI: `10.1103/PhysRevSTAB.15.024001`.

[70] D. Pellegrini, G. Arduini, S. Fartoukh, G. Iadarola, N. Karastathis, Y. Papaphilippou, and G. Sterbini, "Incoherent beam-beam effects and lifetime optimisation", in *2017 Evian Workshop on LHC beam operations*, p. 93.

[71] M. Kuhn, G. Arduini, J. Emery, *et al.*, "LHC Emittance preservation during the 2012 run.", 161–170. 10 p, 2012. [Online]. Available: `https://cds.cern.ch/record/2302436`.

[72] S. Cettour Cave, R. De Maria, M. Giovannozzi, M. Ludwig, A. MacPherson, S. Redaelli, F. Roncarolo, M. Solfaroli Camillocci, and W. Venturini Delsolaro, "Non-linear beam dynamics tests in the LHC: measurement of intensity decay for probing dynamic aperture at injection", Apr. 2013. [Online]. Available: `https://cds.cern.ch/record/1543434`.

[73] G. Arduini, *50 Hz lines studies: First observations*, CERN, Aug. 5, 2015. [Online]. Available: `https://indico.cern.ch/event/436679/contributions/1085928/attachments/1136594/1627012/LMC05082015_50Hz_04082015.pdf`.

[74] R. De Maria, *Observation of 50Hz lines in the LHC BBQ system*, LHC Beam Operation Committee, Oct. 16, 2012. [Online]. Available: `https://lhc-beam-operation-committee.web.cern.ch/lhc-beam-operation-committee/minutes/Meeting51-16_10_2012/workoutline.pdf`.

[75] W. Fischer, P. Cameron, S. Peggs, and T. Satogata, "Tune Modulation from Beam-Beam Interaction and Unequal Radio Frequencies in RHIC", in *AIP Conference Proceedings*, AIP, vol. 693, 2003, pp. 252–255.

[76] W. Ficsher and T. Satogata, "A simulation study on tune modulation effects in RHIC", Brookhaven National Lab.(BNL), Upton, NY (United States), Tech. Rep., 1996.

[77] T. Linnecar and W. Scandale, "Phenomenology and causes of the 50 Hz spaced lines contaminating the Schottky signal", CERN, Geneva, Tech. Rep. CERN-SPS-DI-MST-TL-WS-EEK. CERN-SPS-Improvement-Report-203, Feb. 1986. [Online]. Available: `http://cds.cern.ch/record/1214909`.

[78] L. Carver, D. Valuch, M. Söderén, *et al.*, "Usage of the Transverse Damper Observation Box for High Sampling Rate Transverse Position Data in the LHC", 2017.

[79] M. Ojeda Sandonís, P. Baudrenghien, A. Butterworth, J. Galindo, W. Höfle, T. Levens, J. Molendijk, F. Vaga, and D. Valuch, "Processing High-Bandwidth Bunch-by-Bunch Observation Data from the RF and Transverse Damper Systems of the LHC", in *Proceedings, 15th International Conference on Accelerator and Large Experimental Physics Control Systems (ICALEPCS 2015): Melbourne, Australia, October 17-23, 2015*, 2015, WEPGF062. DOI: `10.18429/JACoW-ICALEPCS2015-WEPGF062`. [Online]. Available: `http://jacow.org/icalepcs2015/papers/wepgf062.pdf`.

[80] M. Söderén, G. Kotzian, M. Ojeda Sandonís, and D. Valuch, "Online Bunch by Bunch Transverse Instability Detection in LHC", in *Proceedings, 8th International Particle Accelerator Conference (IPAC 2017): Copenhagen, Denmark, May 14-19, 2017*, 2017, MOPAB117. DOI: `10.18429/JACoW-IPAC2017-MOPAB117`.

[81] U. Hassan and S. Anwar, "Reducing noise by repetition: Introduction to signal averaging", *European Journal of Physics*, vol. 31, p. 453, Mar. 2010. DOI: `10.1088/0143-0807/31/3/003`.

[82] M. Gasior, "Faraday cup award: High sensitivity tune measurement using direct diode detection", in *Conf. Proc.*, vol. 1204151, 2012, MOAP02.

[83] O. Jones, "LHC beam instrumentation", in *2007 IEEE Particle Accelerator Conference (PAC)*, IEEE, 2007, pp. 2630–2634.

[84] C. Roderick, G. Kruk, and L. Burdzanowski, "The CERN accelerator logging service-10 years in operation: a look at the past, present and future", Tech. Rep., 2013.

[85] K. Fuchsberger, J. Garnier, A. Gorzawski, E. Motesnitsalis, *et al.*, "Concept and prototype for a distributed analysis framework for lhc machine data", in *proc. of ICALEPCS*, 2013.

[86] T. Persson, J. M. Coello de Portugal, A. Garcia-Tabares, *et al.*, "Experience with DOROS BPMs for Coupling Measurement and Correction", in *7th Int. Particle Accelerator Conf.(IPAC'16), Busan, Korea, May 8-13, 2016*, JACOW, Geneva, Switzerland, 2016, pp. 303–305.

[87] J. Olexa, O. Ondracek, Z. Brezovic, and M. Gasior, "Prototype system for phase advance measurements of LHC small beam oscillations", CERN, Geneva, Tech. Rep. CERN-ATS-2013-038, Apr. 2013. [Online]. Available: `https://cds.cern.ch/record/1546401`.

[88] R. Steinhagen, T. Lucas, and M. Boland, "A Multiband-Instability-Monitor for High-Frequency Intra-Bunch Beam Diagnostics", Sep. 2013.

[89] T. Levens, T. Lefèvre, and D. Valuch, "Initial Results from the LHC Multi-Band Instability Monitor", in *Int. Beam Instrumentation Conf.(IBIC'18), Shanghai, China, 09-13 September 2018*, JACOW Publishing, Geneva, Switzerland, 2019, pp. 314–318.

[90] H. Nyquist, "Certain topics in telegraph transmission theory", *Transactions of the American Institute of Electrical Engineers*, vol. 47, no. 2, pp. 617–644, 1928.

[91] O. S. Brüning, P. Collier, P. Lebrun, S. Myers, R. Ostojic, J. Poole, and P. Proudlock, *LHC Design Report*, ser. CERN Yellow Reports: Monographs. Geneva: CERN, 2004, ch. Power converter system. DOI: 10.5170/CERN-2004-003-V-1. [Online]. Available: http://cds.cern.ch/record/782076.

[92] H. Thiesen, G. Hudson, D. Nisbet, V. Montabonnet, M. Bastos, S. Page, and Q. King, "High Precision Current Control for the LHC Main Power Converters", in *Conf. Proc.*, vol. 100523, 2010, WEPD070.

[93] M. Buzio, P. Galbraith, S. Gilardoni, D. Giloteaux, G. Golluccio, C. Petrone, L. Walckiers, and A. Beaumont, "Development of Upgraded Magnetic Instrumentation for CERN's Real-time Reference Field Measurement Systems", *Conf. Proc.*, vol. C100523, MOPEB016, 2010.

[94] T. Bohl *et al.*, "Functional specification for upgrade of SPS B-train", *CERN, Geneva, Switzerland, Rep. EDMS*, vol. 1689759, 2016.

[95] A. Huschauer, A. Blas, J. Borburgh, *et al.*, "Transverse beam splitting made operational: Key features of the multiturn extraction at the CERN Proton Synchrotron", *Phys. Rev. Accel. Beams*, vol. 20, p. 061 001, 6 Jun. 2017. DOI: 10.1103/PhysRevAccelBeams.20.061001. [Online]. Available: https://link.aps.org/doi/10.1103/PhysRevAccelBeams.20.061001.

[96] H. Thiesen and D. Nisbet, "Review of the Initial Phases of the LHC Power Converter Commissioning", in *Conf. Proc.*, vol. 806233, 2008, THPP132.

[97] N. Karastathis, S. Fartoukh, S. Kostoglou, Y. Papaphilippou, M. Pojer, A. Poyet, M. Solfaroli Camillocci, and G. Sterbini, "MD 3584: Long-Range Beam-Beam 2018", CERN, Tech. Rep., Jan. 2020. [Online]. Available: http://cds.cern.ch/record/2707081.

[98] A. Verweij, V. Baggiolini, A. Ballarino, *et al.*, "Performance of the Main Dipole Magnet Circuits of the LHC during Commissioning", *EPAC 2008 - Contributions to the Proceedings*, Jan. 2008.

[99] F. Dubouchet, W. Hofle, G. Kotzian, and D. Valuch, ""What you get" - Transverse damper", in *Proceedings, 4th Evian Workshop on LHC beam operation: Evian Les Bains, France, December 17-20, 2012*, CERN, Geneva: CERN, 2012, pp. 73–78.

[100] J. P. O. Komppula, G. Kotzian, S. Rains, M. Söderén, and D. Valuch, "ADT and ObsBox in LHC Run 2, plans for LS2", 2019.

[101] M. Morrone, M. Martino, R. De Maria, M. Fitterer, and C. Garion, "Magnetic frequency response of High-Luminosity Large Hadron Collider beam screens", *Phys. Rev. Accel. Beams*, vol. 22, p. 013 501, 1 Jan. 2019. DOI: 10.1103/PhysRevAccelBeams.22.013501.

[102] F. Ruggiero, “Single beam collective effects in the LHC”, *Part. Accel.*, vol. 50, pp. 83–104, 1995.

[103] S. Kostoglou, G. Arduini, C. Baccigalupi, *et al.*, “MD4147: 50 Hz harmonics perturbation”, Dec. 2019. [Online]. Available: `http://cds.cern.ch/record/2703609`.

[104] E. Gorbatchev, I. Ivanov, V. Kossoukhine, *et al.*, “Transverse damping systems for the future CERN LHC”, in *PACS2001. Proceedings of the 2001 Particle Accelerator Conference (Cat. No.01CH37268)*, vol. 2, Jun. 2001, 1237–1239 vol.2. DOI: `10.1109/PAC.2001.986639`.

[105] W. Höfle, J. Komppula, G. Kotzian, K. Li, and D. Valuch, “Transverse Feedback System for the CERN FCC-hh Collider”, in *Proceedings, 9th International Particle Accelerator Conference (IPAC 2018): Vancouver, BC Canada, April 29-May 4, 2018*, 2018, WEPAF072. DOI: `10.18429/JACoW-IPAC2018-WEPAF072`.

[106] P. Burla, D. Cornuet, K. Fischer, P. Leclere, and F. Schmidt, “Power supply ripple study at the SPS”, in *AIP Conference Proceedings*, AIP, vol. 326, 1995, pp. 167–196.

[107] A. Romano, O. Boine-Frankenheim, X. Buffat, G. Iadarola, and G. Rumolo, “Electron cloud buildup driving spontaneous vertical instabilities of stored beams in the Large Hadron Collider”, *Phys. Rev. Accel. Beams*, vol. 21, no. 6, p. 061 002, 2018. DOI: `10.1103/PhysRevAccelBeams.21.061002`.

[108] B. Baklakov, T. Bolshakov, A. Chupyra, A. Erokhin, P. Lebedev, V. Parkhomchuk, S. Singatulin, J. Lach, and V. Shiltsev, “Ground vibration measurements for Fermilab future collider projects”, *Physical Review Special Topics-Accelerators and Beams*, vol. 1, no. 3, p. 031 001, 1998.

[109] S. G. Peggs and R. Talman, “Nonlinear problems in accelerator physics”, *Annual Review of Nuclear and Particle Science*, vol. 36, pp. 287–325, 1986.

[110] D. Neuffer, A. Riddiford, and A. G. Ruggiero, “Study of Periodic Tune Modulation with the Beam-Beam Effect”, *IEEE Transactions on Nuclear Science*, vol. 30, no. 4, pp. 2433–2435, Aug. 1983, ISSN: 0018-9499. DOI: `10.1109/TNS.1983.4332838`.

[111] G. Parzen, “Tune modulation due to gradient ripple and the dynamic aperture”, Brookhaven National Lab., Upton, NY (United States), Tech. Rep., 1994.

[112] G. Parzen, “Tune modulation due to synchrotron oscillations and chromaticity, and the dynamic aperture”, in *Proceedings, 16th Particle Accelerator Conference and International Conference on High-Energy Accelerators, HEACC 1995: Dallas, USA, May 1-5, 1995*, 1994, pp. 2798–2800. DOI: `10.2172/10142134`.

[113] O. S. Brüning and F. Willeke, “Reduction of particle losses in HERA by generating an additional harmonic tune modulation”, in *Proceedings Particle Accelerator Conference*, vol. 1, May 1995, 420–422 vol.1. DOI: `10.1109/PAC.1995.504677`.

[114] G. Apollinari, I. Béjar Alonso, O. Brüning, P. Fessia, M. Lamont, L. Rossi, and L. Tavian, "High-Luminosity Large Hadron Collider (HL-LHC)", *CERN Yellow Rep. Monogr.*, vol. 4, pp. 1–516, 2017. DOI: 10.23731/CYRM-2017-004.

[115] M. Fitterer, R. De Maria, S. Fartoukh, and M. Giovannozzi, "Beam Dynamics Requirements for the Powering Scheme of the HL-LHC Triplet", in *Proceedings, 6th International Particle Accelerator Conference (IPAC 2015): Richmond, Virginia, USA, May 3-8, 2015*, 2015, TUPTY035. DOI: 10.18429/JACoW-IPAC2015-TUPTY035. [Online]. Available: http://accelconf.web.cern.ch/AccelConf/IPAC2015/papers/tupty035.pdf.

[116] T. Satogata and S. Peggs, "Is beta modulation more or less potent than tune modulation?", in *Conference Record of the 1991 IEEE Particle Accelerator Conference: Accelerator Science and Technology, May 6-9, 1991, San Francisco, California*, IEEE, 1991, p. 476.

[117] T. Suzuki, "Synchro-betatron resonances", *Part. Accel.*, vol. 27, no. KEK-89-116. KEK-PREPRINT-89-116, 157–164. 8 p, Sep. 1989. [Online]. Available: http://cds.cern.ch/record/201687.

[118] H. Roder, "Amplitude, phase, and frequency modulation", *Proceedings of the Institute of Radio Engineers*, vol. 19, no. 12, pp. 2145–2176, 1931.

[119] E. Metral, S. Antipov, F. Antoniou, *et al.*, "Update of the HL-LHC operational scenarios for proton operation", CERN, Tech. Rep., Jan. 2018. [Online]. Available: http://cds.cern.ch/record/2301292.

[120] E. Coulinge, J.-P. Burnet, and D. Dujic, "High-current low-voltage power supplies for superconducting magnets", in *2017 International Symposium on Power Electronics (Ee)*, IEEE, 2017, pp. 1–6.

[121] D. Gamba, G. Arduini, M. Cerqueira Bastos, J. M. Coello De Portugal - Martinez Vazquez, R. De Maria, M. Giovannozzi, M. Martino, and R. Tomas Garcia, "Beam dynamics requirements for HL–LHC electrical circuits", CERN, Geneva, Tech. Rep. CERN-ACC-2017-0101, Dec. 2017. [Online]. Available: https://cds.cern.ch/record/2298764.

[122] D. Gamba, G. Arduini, M. Cerqueira Bastos, J. M. Coello De Portugal - Martinez Vazquez, R. De Maria, M. Giovannozzi, M. Martino, and R. Tomas Garcia, "Update of beam dynamics requirements for HL-LHC electrical circuits", CERN, Geneva, Tech. Rep. CERN-ACC-2019-0030, Feb. 2019. [Online]. Available: https://cds.cern.ch/record/2656907.

[123] R. D. Maria, J. Andersson, V. K. B. Olsen, *et al.*, "SixTrack project: Status, runtime environment, and new developments", in *Proceedings, 13th International Computational Accelerator Physics Conference, ICAP2018: Key West, FL, USA, 20-24 October 2018*, 2019, TUPAF02. DOI: 10.18429/JACoW-ICAP2018-TUPAF02.

[124] N. Karastathis, R. De Maria, S. Fartoukh, Y. Papaphilippou, and D. Pellegrini, "Refining the HL-LHC Operational Settings with Inputs From Dynamic Aperture Simulations: A Progress Report", in *Journal of Physics: Conference Series*, IOP Publishing, vol. 1067, 2018, p. 022 005.

[125] *MAD-X*, `http://mad.web.cern.ch/mad/`, Accessed: 2019-12-13, 2019.

[126] *CERN TE-EPC-LPC Converter-Concepts/EMC*, `http://te-epc-lpc.web.cern.ch/te-epc-lpc/concepts/converters/emc/emc_emissions.stm`, Accessed: 2019-12-19.

[127] D. Gamba, private communication, Dec. 10, 2018.